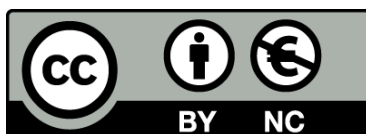




UNIVERSITAT DE
BARCELONA

Heterogeneous catalysis of green chemistry reactions on molybdenum carbide based catalysts

Sergio Posada Pérez



Aquesta tesi doctoral està subjecta a la llicència [Reconeixement- NoComercial 3.0. Espanya de Creative Commons](#).

Esta tesis doctoral está sujeta a la licencia [Reconocimiento - NoComercial 3.0. España de Creative Commons](#).

This doctoral thesis is licensed under the [Creative Commons Attribution-NonCommercial 3.0. Spain License](#).

Programa de doctorat en Química Teòrica i Computacional

Memòria presentada per **Sergio Posada Pérez** per a optar al grau de
Doctor per la Universitat de Barcelona

Heterogeneous catalysis of green chemistry reactions on molybdenum carbide based catalysts

Dirigida per:

Prof. Francesc Illas Riera

(Universitat de
Barcelona)

Dr. Francesc Viñes
Solana

(Universitat de
Barcelona)



UNIVERSITAT DE
BARCELONA

UNIVERSITAT DE BARCELONA

FACULTAT DE QUÍMICA

DEPARTAMENT DE CIÈNCIA DELS MATERIALS I QUÍMICA FÍSICA

INSTITUT DE QUÍMICA TEÒRICA I COMPUTACIONAL

Heterogeneous catalysis of green chemistry reactions on molybdenum carbide based catalysts

Sergio Posada Pérez

PhD Thesis

2018



UNIVERSITAT DE
BARCELONA



Institut de Química Teòrica
i Computacional
UNIVERSITAT DE BARCELONA

A tots els que heu aixecat les mans i m'heu donat la vostra energia

Us estimo

The work presented in this doctoral thesis has been carried out at the Materials Science and Physical Chemistry Department of the Chemistry Faculty of the University of Barcelona (UB), and within the Institute of Theoretical and Computational Chemistry (IQTCUB) and the Reference Network of Theoretical and Computational Chemistry of Catalunya (XRQTC).

This project has been possible in virtue of the financial support provided by the Spanish *Ministerio de Economía y Competitividad* (Grant CTQ2012-30751) and, in part, by Generalitat de Catalunya (grants 2014SGR97). Computer resources were provided by the Barcelona Supercomputing Center (*Red Española de Supercomputación*).

Agraïments

Saben aquell que diu que aquesta és la part més difícil d'escriure de la tesi? Postureo. En aquests moments finals d'estrés màxim es quan més present es tenen a les persones que han fet això possible. Així que allà vamos, sense revisió, sense correccions... el que aquí surt prové directament del cor.

En primer lloc vull agrair als meus directors de tesi, el Francesc Illas i el Francesc Viñes, la dedicació que han tingut en aquests quatre anys i l'aprenentatge rebut. M'heu ensenyat el que es investigar i tot el que hi ha darrere d'aquesta paraula, de veritat, gràcies. Molt especialment, vull agrair al Xino que hem dongués la oportunitat, sense coneixe'ns, de duu a terme una tesi doctoral quan ja estava a punt de deixar el camí de la investigació per entrar en qualsevol empresa química a fer altres tipus de feina, que segur, no eren tan satisfactories com investigar.

I must also thank the groups and researchers that have hosted me during my visit to Brookhaven National Laboratory and to Cardiff University. I am very grateful to Dr. José Rodriguez for giving me the chance to work with his group and visiting the BNL. I am very grateful to Dr. Ping Liu, Dr. Dario Stacchiola and Dr. Sanjaya Senanayake, who made me the visit more pleasant. Sanjaya, thank you for your friendship. Tambien me gustaria agradecerle a mi amigo Carlos su amistad durante esos meses en Nueva York, que me hizo la estancia mucho más agradable. I am also very grateful to Dr. Nora de Leeuw and Dr. Alberto Roldan for providing me the opportunity to work in their group. Thank you also David for your kindness, your help and your friendship.

M'agradaria donar les gràcies a tots aquells que han estat presents i que han ajudat directa o indirectament en aquesta tesi. Una menció important per als membres del "Computational Materials Science Laboratory", en especial al professors Carme, Iberio, Stefan, Konstantin, Ramón i Rosendo als quals tinc una gran estima. Tambien a Ángel, un tio cojonudo a pesar de ser del Madrid. Muchas gracias por tus consejos y tu ayuda. Als memebres que ja no hi son i tant m'han ajudat, com l'Albert Bruix, el Gian i el Sergey. No em vull oblidar dels tècnics de l'IQTC Jordi i Teresa, per la gran feina que fan i tots els cops de mà que m'han donat. Tambè, als professors amb els que he tingut el gran plaer de compartir classes, on he pogut aprendre molt d'ells, com la Carme Sousa, Pere Alemany, el Miquel Lluell, Xavi Gimenez i el Pablo Gamallo. Moltes gràcies al Jaime de Andres, amb qui vaig tenir el plaer d'iniciar la meva etapa com a professor associat, del que vaig aprendre molt i vaig gaudir enormement amb les seves anècdotes i humor maquiavelic (com ell deia) i que per desgracia no podrà llegir aquestes línies. Un record molt gran. No voldria oblidar la Merce, que tantes vegades m'ha ajudat amb la burocracia (i sempre amb un somriure), el Juan Novoa i el Jordi Ribas, perque formeu un grup molt macu i també al Juan Carlos Paniagua, per la seva gran i inestimable ajuda en els moments finals de la tesi.

Un no és pot oblidar dels començaments, i per tant vull agrair a tots els professors del grup de quàntica de la URV els coneixements i els fonaments que hem van donar, especialment el Josep Maria Poblet, l' Anna Clotet i el Xavi Aparicio. També a la Rosa Caballol, per insistir, insistir i insistir en que fèssim el master que finalment m'ha portat fins aquí. I si parlem de començaments, vull agrair als professors del departament de física i química del INS Baix Penedès de El Vendrell, a la Luisa, el Luís, el Salvador i la Josefina, que van ser els causants de que decidís estudiar química. Vau ser més que uns professors, vau ser amics. Luisa, esta tesis tiene un pedazo muy grande de ti, gracias por todo lo que me enseñaste.

Arribo a la part més difícil de resumir, parlar de les meves famílies, la que per sort m'ha tocat i les que he pogut escollir. Al grup de Bruixots i Bruixotes, gràcies per acompanyar-me en aquest camí. Començaré per elles: Almu ,gracias por tu cariño y tu amistad todos estos años y por miles de cosas más; Sonia, porque en ti siempre tendré un hombro para llorar; Noe, mi tita Herminia, gracias por todo; Julia, por esa amistad obligada que tenemos por la cual me he quedado con la custodia de tus futuros hijos; Cristina, por ser siempre un blanco (va con segundas) fácil para mis bromas (me encanta que me las devuelvas). Os quiero a todas. A vosotros, Oriol, por ser el mejor compañero de despacho que uno puede tener, a parte de una de las mejores personas que conozco, gracias por tu ayuda desde el principio; Raul, porque así como si nada te has convertido en un amigo TOP, eres un crack (y un tolai); Alberto, por motivos legales solo pondré palabras claves, (SECAT, IBIZA...) y tu ya sacas tus propias conclusiones... eres una gran persona y gran amigo. A les persones que en algun moment han format part d'aquest grup i que per desgracia han hagut de marxar, Felix, te echo mucho de menos, gracias por todos los momentos que vivimos y todas las frases que nos dejaste; Mikel por ser un tio cojonudo y KC, all of us miss you. No vull oblidarme d'aquelles persones que tot i no saber-ho, han sigut el pegament d'aquest grup i causant de molt bons moments (señor, acelga, terrorista, fashion victim, intensa, nen universitari, farlopera, caderas, chewbacca...).Tot i que aquest grup sigui molt gran, forma part d'un coto, *el coto de caza de Toni*, liderat pel senyor Toni Macià, un noi que val molt la pena tenir al costat. Gràcies per ser tan macu. Quiero agradecer tambien a Juanjo, por ser un gran compañero de despacho y un buen amigo y a Pablo, por ser un tio y un amigo genial. A les noves incorporacions, Lorena, Martí, Piqué, i Raul, sou molt grans. A la resta de doctorands del departament amb els que hem compartir més que xerrades de passadís (Manel, Hector, Gerard, Isaac...).Vull tenir un record també per a tots els companys que hem van acollir quan vaig entrar al grup de la URV, en especial a la Laura.

A les meves nenes, i ho dic sempre, el millor de la carrera ha estat compartir amb vosaltres aquells quatre anys. Gràcies Mireia, Laura, Natalia i Marta per tots aquells anys i per continuar la nostra amistat fora d'aquelles quatre parets. Es molt possible que no hagués arribat fins aquí sense vosaltres. Us estimo. Als amics fora del món acadèmic, Valeria/Miguel i Cristina/Oscar, gràcies per la vostra amistat i pels bons moments viscuts (i els que queden).

També un record pel meu amic Omar. Moltes gràcies a la Dana per tota la seva ajuda en els moments finals de la tesi, han valgut la pena totes les classes de repàs que he donat si al final coneixo persones com tu.

Finalment, a la meva família. A la meva mare Silvia i al meu pare José, per l'educació que m'han donat, per la seva formació i els seus consells i per sempre sacrificar-se per mi i per la meva germana. Sempre heu valorat més qualsevol assoliment dels vostres fills que qualsevol cosa que hàgiu fet vosaltres. Si avui estic aquí, es gracies a vosaltres. Gràcies per tot el que heu lluitat per la nostra família. Si els meus fills hem consideren la meitat de bon pare del que jo us considero a vosaltres, podré estar orgullós. Us estimo. A la meva germana Anna, la princesa de la casa, gràcies per existir. Vull que sàpigues i que entenguis que no necessites escriure un llibre com aquest per a ser algú en aquesta vida. Ser algú vol dir lluitar pels teus objectius, siguin quins siguin i a pesar de tots els obstacles i desgraciats que et trobaràs pel camí. Tu ets molt més gran que tot això i saps que sempre anirem de la mà. No perdis mai el somriure. A la resta de la meva família, (la família de el Vendrell, amb la Cristina, el Jaime, el Rubén i ara la Silvieta, la família de Molins, Yolanda, Álvaro i els nens, la part de la família encapçalada per la Pepa...) moltes gràcies per l'ajuda que ens heu donat als meus pares i a mi durant aquests anys difícils. Heu ajudat a que hem poguéssim centrar en la investigació. Un record pels meus avis, Jesús i Juan Leon, que no vaig tenir la sort de conèixer i gaudir-ne, i per a les meves iaies Rosaura i Anna, que vaig gaudir molt poc. Això va per vosaltres. Disfruté muy poco de mis abuelos, pero puedo sentirme muy afortunado porque yo he tenido seis, Rosita y Pepe, gracias por vuestro cariño y por haberme cuidado durante todos estos años. Habéis sido más que mis padrinos, y me habéis tratado siempre como un nieto.

Y por último tú. Porque necesitaría un libro entero solo para ti, pero esta vez, y solo por esta vez (no te acostumbres) seré breve. Gracias por la paciencia que tienes conmigo y por aguantar mis bromas y chascarrillos (buenísimos para mi, lamentables para ti). Gracias por los momentos que hemos vivido, los que estamos viviendo y sobre todo, los que nos quedan por vivir. Te quiero Sere.

TABLE OF CONTENTS

List of definitions and abbreviations	15
Chapter 1- Introduction	17
1.1 Brief history of catalysis.....	19
1.2 The importance of heterogeneous catalysis.....	21
1.3 Transition metal carbides.....	23
1.3.1 Catalytic properties.....	24
1.4 Environmental catalysis.....	27
1.4.1 Carbon dioxide: From harmful greenhouse gas to economical feedstock.....	27
1.4.2 Hydrogen as a new efficient and environmental friendly fuel.....	31
1.5 Motivation and outline of the thesis.....	33
1.6 References.....	36
Chapter 2- Theoretical background	41
2.1 The Schrödinger equation.....	43
2.2 The density functional theory (DFT).....	45
2.3 Exchange-correlation functionals.....	49
2.3.1 Local density approximation (LDA).....	49
2.3.2 General gradient approximation (GGA).....	50
2.3.3 Hybrid functionals.....	50
2.3.4 Dispersion correction.....	51
2.4 Plane waves and pseudopotentials.....	53
2.5 Solid state.....	55
2.5.1 Models for solids.....	55
2.5.2 The reciprocal lattice.....	58
2.5.3 Bloch's theorem.....	59
2.5.4 Miller indices.....	60
2.5.5 Periodic models.....	61
2.5.5.1 Surface models (slab).....	61
2.5.5.2 Nanoparticle model.....	63
2.6 Energy and free energy diagrams.....	64
2.6.1 Optimization of reactants, intermediates, and products.....	64
2.6.2 Diffusion.....	66
2.6.3 Transition state search.....	67
2.6.3.1 The nudged elastic band method.....	67
2.6.3.2 The dimer method.....	68
2.6.4 Vibrational frequencies.....	70
2.6.5 Zero-point energy correction.....	72
2.6.6 Gibbs free energy diagrams.....	73
2.7 Minima analysis.....	75
2.7.1 Density of states (DOS).....	75
2.7.2 Electronic localization function (ELF)	75
2.7.3 Bader charges.....	76
2.8 Kinetic study.....	77
2.9 Ab initio thermodynamics.....	80
2.10 Computational details.....	85

2.11 Experimental details.....	87
2.12 References.....	89
Chapter 3- Computational models for molybdenum carbide based systems.....	91
3.1 Introduction.....	93
3.2 Modeling concepts.....	96
3.3 Modeling bare molybdenum carbide surfaces.....	98
3.3.1 Previous works.....	98
3.3.2 Adsorption sites on Mo _n C (001) surfaces.....	101
3.3.3 Adsorption tests on Mo _n C (001) surfaces.....	102
3.4 Modeling metal clusters on molybdenum carbide surfaces.....	103
3.4.1 Cu nanoclusters supported on Mo _n C (001) surfaces.....	103
3.4.1.1 Isolated Cu nanoclusters.....	103
3.4.1.2 Supported Cu nanoclusters on β-Mo ₂ C (001) surfaces.....	107
3.4.1.3 Supported Cu nanoclusters on δ-MoC (001) surfaces.....	112
3.4.2 Au nanoclusters supported on δ-MoC (001) surfaces.....	117
3.4.2.1 Isolated Au nanoclusters.....	117
3.4.2.2 Supported Au nanoclusters on δ-MoC (001) surfaces.....	119
3.5 Conclusions.....	123
3.6 References.....	125
Chapter 4- Interaction of greenhouse related compounds with molybdenum carbide surfaces....	127
4.1 Introduction.....	129
4.2 Experimental results.....	131
4.3 CO ₂ study on (001) Mo carbide surfaces.....	134
4.3.1 CO ₂ adsorption and activation.....	134
4.3.2 CO ₂ dissociation.....	139
4.4 CO adsorption and dissociation.....	142
4.5 H ₂ study on (001) Mo carbide surfaces.....	146
4.5.1 H ₂ adsorption and dissociation.....	146
4.5.2 Full coverage surface hydrogenation.....	153
4.5.3 Relative stability of H-covered Mo _n C (001) surfaces.....	156
4.6 CH ₄ study on (001) Mo carbide surfaces.....	160
4.7 Conclusions.....	170
4.8 References.....	172
Chapter 5- CO₂ Hydrogenation on Orthorhombic β-Mo₂C and Cu/β-Mo₂C (001) Surfaces	175
5.1 Introduction.....	177
5.2 CO ₂ hydrogenation on bare β-Mo ₂ C (001)	180
5.3 CO ₂ hydrogenation on Cu/β-Mo ₂ C (001)	186
5.3.1 Experimental results.....	186
5.3.1.1 Interaction of CO ₂ with Cu/Mo ₂ C (001) surfaces.....	186
5.3.1.2 Hydrogenation of CO ₂ on Cu/Mo ₂ C (001) surfaces	187
5.3.2 DFT studies for CO ₂ hydrogenation on Cu/Mo ₂ C (001) surfaces.....	191
5.3.2.1 CO ₂ adsorption on Cu _n /Mo ₂ C (001) surfaces	191
5.3.2.2 CO ₂ hydrogenation mechanism on Cu ₄ /β-Mo (001) surfaces	194
5.3.2.3 CO ₂ hydrogenation mechanism on Cu ₄ /β-C (001) surfaces	197
5.4 Conclusions.....	199
5.5 References.....	201
Chapter 6- CO₂ Hydrogenation on cubic δ-MoC and Cu/δ-MoC (001) Surfaces.....	203

6.1 Introduction.....	205
6.2 CO ₂ hydrogenation on bare δ -MoC (001)	206
6.2.1 Experimental results.....	206
6.2.2 DFT results.....	207
6.3 CO ₂ hydrogenation on Cu/ δ -MoC (001) and Au/ δ -MoC (001)	212
6.3.1 Experimental results.....	212
6.3.2 DFT studies for CO ₂ hydrogenation on Cu/MoC (001).....	217
6.3.2.1 CO ₂ adsorption on Cu ₄ /MoC (001) surfaces	217
6.3.2.2 CO ₂ conversion to CO and MeOH on Cu ₄ / δ -MoC (001)	219
6.4 Conclusions.....	223
6.5 References.....	225
Chapter 7- Water gas shift reaction on cubic δ-MoC and Au/δ-MoC (001) Surfaces.....	227
7.1 Introduction.....	229
7.2 Experimental results.....	231
7.3 DFT study of WGS on bare δ -MoC (001)	236
7.4 DFT study of WGS on Au ₄ / δ -MoC (001)	243
7.4.1 Choice of model.....	243
7.4.2 Reaction mechanisms of WGS	246
7.5 Conclusions.....	251
7.6 References.....	253
Chapter 8- General conclusions.....	255
Resum en català.....	259
List of publications.....	295

List of Definitions and Abbreviations

1 electronvolt (eV) = 23.06035 Kcal mol⁻¹

AITD	<i>Ab initio</i> thermodynamics
Au_n	gold clusters
CSS	CO ₂ capture and storage
Cu_n	copper clusters
DFT	density functional theory
DFT-D2	density functional theory with the Grimme's dispersion correction
DOS	density of states
E_{adh}	adhesion energy
E_{ads}	adsorption energy
E_b	energy barrier
E_{br}	reverse energy barrier
E_{coh}	cohesion energy
E_F	energy of Fermi level
E_{slab}	slab energy
ELF	electronic localization function
GGA	general gradient approximation
LCAO	linear combination of atomic orbitals
IUPAC	International Union of Pure and Applied Chemistry
MeOH	Methanol

ML	monolayer
MOFs	metal organic frameworks
NEB	Nudged Elastic Band
θ	coverage
$\rho(r)$,	electron density
PAW	projected augmented wave pseudopotentials
PBE	Perdew-Burke-Enzerhof functional
TMCs	transition metal carbides
RWGS	reverse water gas shift reaction
TS	Transition state
UHV	ultra-high <i>vacuum</i>
VASP	Vienna Ab Initio Simulation Package
vdW	van der Waals dispersion
WGS	water gas shift reaction
XPS	X-ray photoelectron spectroscopy
ZPE	zero-point energy correction

CHAPTER ONE

Introduction

1.1 Brief history of catalysis

Catalysis is a phenomenon known from very ancient times, although its fundamental concepts were not known until 19th century. The oldest catalyzed reaction promoted by the humans was the wine fermentation, the art of producing alcohol from sugar, around 5000 b.C. In the Middle Ages, the alchemists observed that some "strange" elements in the reaction mixture lead to the procurement of useful products for humans. The alchemists named this matter as Philosopher's Stone because the substance which caused this incident was some kind of mineral. They believed that this substance was able to transform typical metals such as iron or lead to gold, the most valuable metal during this period. However, their investigations did not fructify despite many efforts, because the alchemists ignored that thermodynamic laws made the process unfeasible.

The first concept of catalysis was not introduced until 1836, by Berzelius, after the accounting of many chemical transformations and decompositions. He describes the term of catalysis as *"the property of some substance to awake affinities, which are asleep at a particular temperature, by their mere presence and not by their own affinity"*.¹ Berzelius used the term of catalysis to group together various phenomena which cannot be explained or associated with the concept of the chemical affinity. Some decades later, Ostwald redefined the term as we know it nowadays: *"catalysis is the acceleration of a slowly preceding chemical reaction through the presence of a foreign substance, which may participate intermediately but is not consumed by the reaction"*.² These substances were called catalysts and they are able to *"change the velocity of a reaction without the modification of the energy factors of the reaction"* which is already very similar to the present International Union of

Introduction

Pure and Applied Chemistry (IUPAC) definition for catalysts.[1] Indeed, as is exhibited in Figure 1.1, the role of catalysts is to interact with the reactants, products, or intermediates decreasing the activation energy (Figure 1.1a) or providing alternative reaction mechanisms (Figure 1.1b), with the goal to increase the velocity of the reaction to obtain certain products. Catalysts modify only the kinetics of the reaction, whereas the thermodynamic magnitudes remain invariable, since the reactants and products are the same for the catalyzed or uncatalyzed reaction.

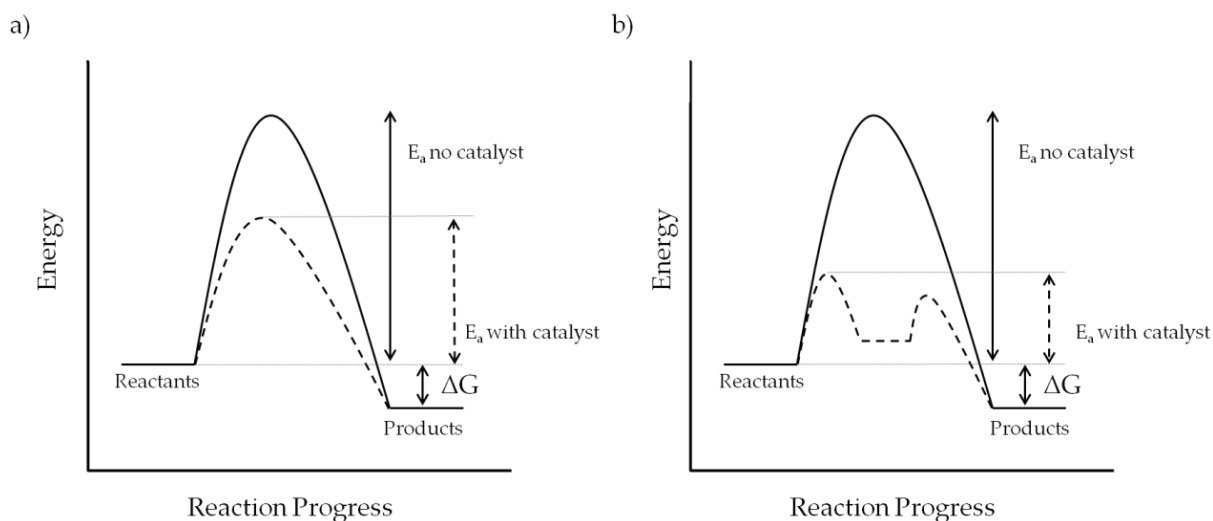


Figure 1.1: General representation of an arbitrary reaction profile for a catalyzed (dashed lines) and uncatalyzed (solid lines) reactions.

[1] "A substance that increases the rate of a reaction without modifying the overall standard Gibbs energy change in the reaction; the process is called catalysis. The catalyst is both a reactant and product of the reaction."

1.2 The importance of heterogeneous catalysis

Catalysis is called enzymatic, homogeneous, or heterogeneous as a function of the physical state of all involved substances and the catalyst's nature. In enzymatic catalysis, the reactions are accelerated by biological molecules (enzymes). In homogeneous catalysis, the reactants and catalyst are in the same physical state whereas the heterogeneous catalysis involves the studies of materials able to accelerate chemistry reactions in gas or liquid phase on solid catalysts. One of the advantages of heterogeneous catalysts respect to the homogeneous ones, is the facility to separate the catalyst and the final reaction products. Many efforts in the research of surface science have been focused towards the heterogeneous catalysis owing to its tremendous impact in our society. Most of the important industrial reactions, of the present and of the past, are/were catalyzed by heterogeneous catalysts as is summarized in Table 1.1. For example, the synthesis of ammonia (Haber-Bosch process)³ was the key reaction to avoid the famine suffered in the beginning of 20th century and consequently, the world population increased, since ammonia is/was used to produce fertilizers which nurture the farmlands.

Most of the catalysts used in the industry for a large number of reactions, use precious metal nanoparticles such as Pd or Pt as an active phase that are supported either on oxides or fine sulfides.⁴ Currently, one of the chief challenges in the field of catalysis is the design of a new cost-effective catalysts focused on the production of environmental friendly fuels and green chemistry reactions, in order to decrease the use of fossil fuels. Nevertheless, for many years, the design of these heterogeneous catalysts was performed by means of the "*trial and error*" methodology, which implies to test all the possibilities in a laboratory. Clearly, this technique is improvable since it does not consider the chemical reasoning.⁵ Fortunately, the last times, the fruitful collaboration between experiments and computational calculations have caused a

Introduction

forward leap in the knowledge of catalytic processes. The computational simulation of catalysis, either as a complement of experimental studies or as a predictive tool,⁶ is a useful technique in order to reduce the number of experiments and focus the efforts towards the appropriate predicted materials.

Table 1.1: Summary of the most relevant industrial catalytic reactions using heterogeneous catalysts

Year	Reaction Process	Catalysts
1875	Sulfuric acid: $\text{SO}_2 + 1/2\text{O}_2 \rightarrow \text{SO}_3$	V_2O_5 , Pt
1903	Nitric acid: $2\text{NH}_3 + 1/2\text{O}_2 \rightarrow 2\text{NO} + 3\text{H}_2\text{O}$	Pt gauze
1913	Ammonia synthesis: $\text{N}_2 + 3\text{H}_2 \rightarrow 2\text{NH}_3$	Fe/ Al_2O_3 / K_2O
1930	Fischer-Tropsch: $\text{CO} + \text{H}_2 \rightarrow \text{Hydrocarbons}$	Fe/K/CuO
1936	Petroleum cracking: $\text{C}_{20}\text{-C}_{30} \rightarrow \text{C}_8\text{-C}_{16}$	$\text{SiO}_2\text{-Al}_2\text{O}_3$
1937	Ethene oxidation: $\text{C}_2\text{H}_4 + \text{O}_2 \rightarrow \text{C}_2\text{H}_4\text{O}$	Ag/ Al_2O_3
1950	Naphta reforming: $\text{C}_7\text{-C}_{10} \rightarrow \text{iso-paraffins}$	Pt/ Al_2O_3
1960	Hydrodesulphuration: $\text{R-S} + 2\text{H}_2 \rightarrow \text{H}_2\text{S} + \text{RH}_2$	CoMo/ Al_2O_3
1980	NO reduction: $4\text{NH}_3 + 4\text{NO} + \text{O}_2 \rightarrow 4\text{N}_2 + 6\text{H}_2\text{O}$	VO_x TiO_2 , zeolites

1.3 Transition metal carbides

Transition metal carbides (TMCs) are formed when carbon atoms, produced for example by the decomposition of hydrocarbon molecules, are incorporated into the metal interstitial sites. TMCs have unique physical and chemical properties, which combine the characteristic features of three different classes of materials: They show the extreme hardness and brittleness of covalent solids, the high melting temperature and simple crystal structures, typical in ionic crystals, and electronic and magnetic properties similar to transition metals.⁷⁻⁹ Nowadays, the main applications of TMCs are based on the industrial use in cutting tools and wear-resistant parts. Although it may seem surprising, the study and knowledge of these materials is very new, despite of the fact that the excellent properties of steel (iron with a 0,03-2.14% of Carbon) were well-known.¹⁰ As is exhibited in Figure 1.2, the number of publications and citations related with TMCs were very low until the beginning of the 20th century.[2] What was the factor that changed this trend? The catalysis, of course! As I will put in context in the next section, in the current search for new catalysts,¹¹ TMCs have become a family of materials with an increasing role in heterogeneous catalysis in the last decades because of their chemical properties and low cost. One could think that the world economic crisis has played a prominent role in the increasing research of TMCs, given the imperative need to replace high cost catalysts with cheaper and equally efficient (or better) ones.

[2] *In the early 90's, there was an increase in the number of publications related with Silicium Carbide (SiC) due to its use in the field of semiconductors and electronic technology, although it is not included in the statistic because it is not a TMCs strictly speaking.*

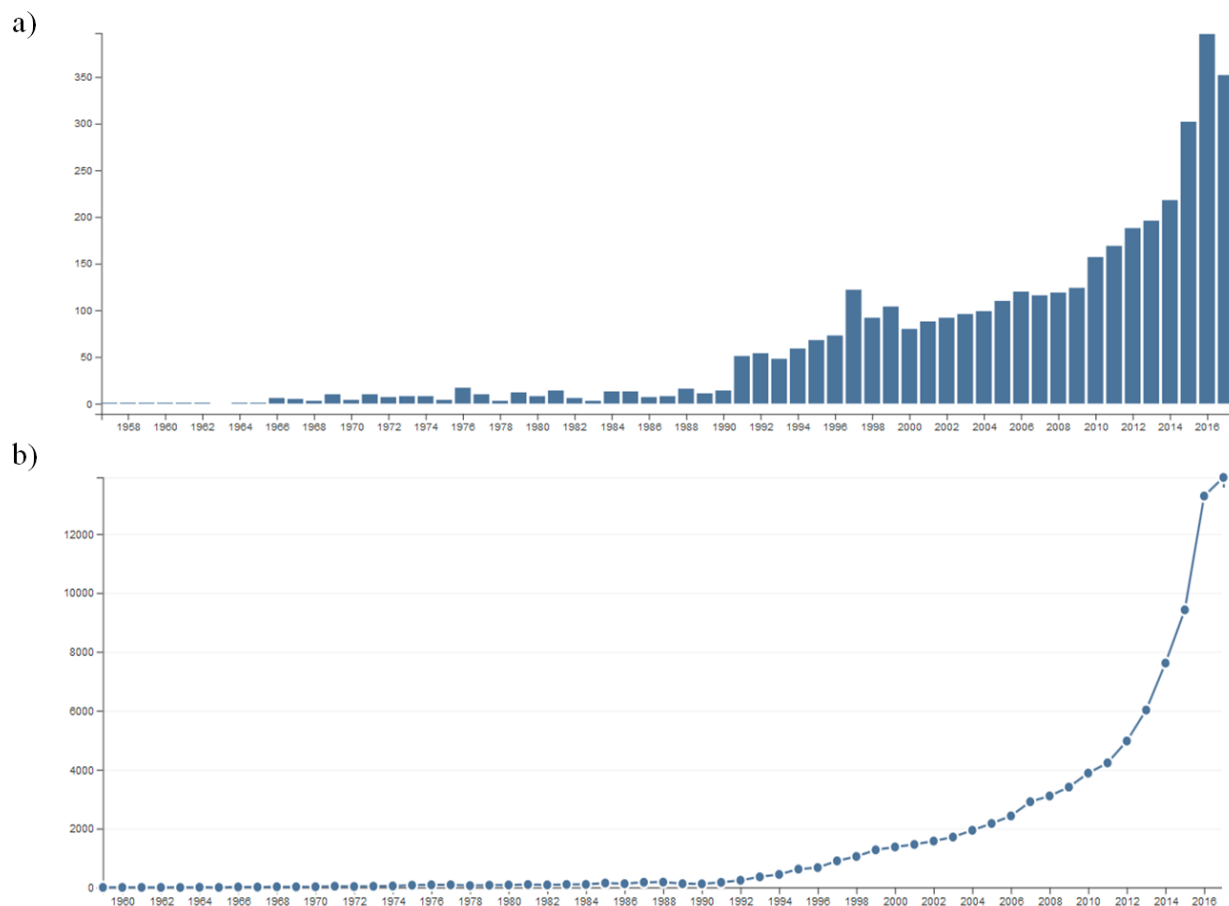


Figure 1.3: a) Number of published articles per year using the keyword "Transition metal Carbides" and b) Number of cites per year using the same keyword of a). Source: web of Science.

1.3.1 Catalytic properties

The first and key landmark in this topic was the work of Levy and Boudart, who suggested that tungsten carbides displayed Pt-like behavior in several catalytic reactions such as hydrogenation, dehydrogenation, isomerization, and desulfuration reactions.¹² Since the pioneer work of Levy and Boudart in the 1970s, the number of reactions catalyzed by TMCs has greatly increased.¹³⁻¹⁵ For instance, WC and W₂C were found to be potential catalysts for alcohol conversion,¹⁶ and electrocatalysts for direct alcohol fuel cells.¹⁷⁻¹⁹ Moreover, titanium carbide (TiC), one of the TMCs which has

1.3 Transition metal carbides

generated more interest in the latest times, was proposed as an excellent catalyst to dissociate H₂ molecule^{20,21} and oxidize CO.²²

From a catalytically point of view, TMCs exhibit some advantages respect to precious metals. The first one and probably the most important advantage, the cause of the vigorous increase number of publications in the last decade, is the price. TMCs are cost-effective materials whereas noble metals are very expensive since they are very limited. Of course, this fact would not matter if TMCs did not have a high catalytic power, similar or even higher to the precious metals. Another advantage is related to the Sabatier's principle, one of the most important qualitative concepts in catalysis. The Sabatier's principle reveals that the substrate-catalyst interactions must be neither too strong nor too weak, since strong interactions lead to the possible dissociation of the products²³ and weak interactions do not allow the reaction to take place. Precious metals are very active catalysts with strong adsorbate-catalyst interactions, which is not in agreement with Sabatier's principle. However, the presence of carbon on TMCs favor, on one hand, to modify the electronic structure of metal atoms due to a charge transfer from metal to carbon, and on the other hand, to reduce the number of metallic atoms on the surface (ensemble effect), *i.e.*, atoms in contact with the substrate, which reduces (positively) the catalytic activity of metallic atoms. Moreover, TMCs avoid the poisoning of carbon or sulfur, although they could be poisoned and, consequently deactivated, due to the oxygen adsorption and the subsequent oxycarbide formation,²⁴ which does not present the same catalytic activity as pure TMCs.²⁵ This is related with the fact that several TMCs surfaces have been found to easily dissociate molecular oxygen^{26,27} and they are particularly well-suited materials for the (electro)catalysis of oxygen-containing species,²⁸ which is likely to be related to the strong oxygen-carbide interaction.^{29,30}

One of the most promising properties of some TMCs is the capability to modify the electronic structure of small supported metal particles, and increase drastically their

catalytic activity through strong metal↔support interactions.³¹ Motivated by the initial work of Ono and Roldán-Cuenya on the catalytic activity of Au/TiC towards low temperature CO oxidation,³² many studies were performed about the interaction of Au with TiC (001), displaying that these systems are active for many reactions.³³⁻³⁹

Nevertheless, titanium carbide is a cumbersome support due to the difficulty of obtaining catalytically active supported nanoparticles on working conditions. In this sense, molybdenum carbides, in particular cubic (δ) MoC, orthorhombic (β) Mo₂C, and hexagonal (α) Mo₂C, have emerged as an excellent alternative because they are more active and do not require special conditions for their synthesis. Prior to the start of this thesis, molybdenum carbides were used as catalysts in different reactions: the orthorhombic β -Mo₂C was able to dissociate CO,⁴⁰ and it was proposed as a possible substitute to the commercial Cu-based catalyst used to carry out the Water-Gas-Shift (WGS) reaction^{41,42} and also as a highly beneficial support to Pt nanoparticles in the catalyzed WGS.⁴³ Moreover, β -Mo₂C was found to be, not only a good support to Ni nanoparticles, but also an active phase to the so-called Ni/ β -Mo₂C bifunctional catalyst used in methane dry reforming process. The catalytic activity of these systems was predicted based on density functional theory (DFT) calculations^{44,45} and also, a detailed mechanistic study was accomplished.⁴⁶ Furthermore, it was predicted that δ -MoC (001) can easily dissociate molecular oxygen⁴⁷ and DFT calculations showed the very high catalytic power of hexagonal α -Mo₂C on ammonia dehydrogenation.⁴⁸ Also, hexagonal α -Mo₂C (001) and orthorhombic β -Mo₂C phases were considered as catalyst for CO hydrogenation.⁴⁹⁻⁵¹

Thus, molybdenum carbides are promising multifunctional (and cost-effective) materials able to convert harmful substances for the environment to feedstocks and fuels, to avoid exploiting excessively the resources of nature, due to the disproportionate use of fossil fuels and obviating the damage of the environment, which is currently known as environmental catalysis.

1.4 Environmental catalysis

Environmental catalysis research is undergoing a transition from pollution abatement to pollution prevention. This term refers to catalytic technologies to reduce emissions of unacceptable and hazardous compounds⁵² in the environment and the conversion of these ones as feedstock by means of new and cleaner catalytic routes. Research for advanced fuel cells and catalytic combustion, both promise power generation with ultra-low emissions and are under intensive investigation worldwide.⁵³

1.4.1 Carbon dioxide: From harmful greenhouse gas to economical feedstock

Carbon dioxide (CO₂) is the second most abundant greenhouse gas in Earth's atmosphere (water is the most abundant) owing to the vast and exceeding emissions derived from human activities related to fossil fuels⁵⁴ with concomitant problems in the environment.⁵⁵ These anthropogenic emissions are considered to be the major contributor to climate change that may cause extreme events (high or low temperature, dryness,...) that are out of human control. Some technologies have been introduced in order to reduce the CO₂ emissions,⁵⁶ although, they have been increased since the sixties until a current level superior to 400 ppm (Figure 1.3). Moreover, the predictions indicate that CO₂ emissions will continue to increase in 2040⁵⁷ with devastating consequences for the environment.

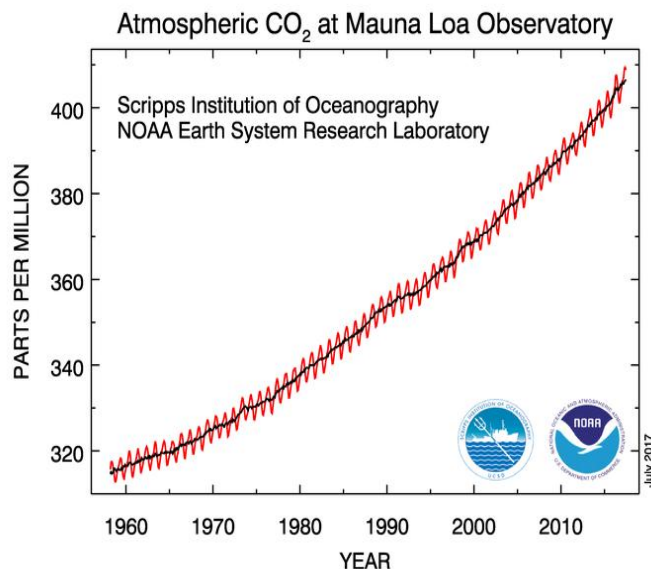


Figure 1.3: The steady increase in CO₂ concentrations in the atmosphere in the last sixty years. The red and black lines indicate the monthly mean values and the average *per* season, respectively. Adapted from <https://www.esrl.noaa.gov/gmd/ccgg/trends/full.html>

Thus, to mitigate the resulting harmful effects, CO₂ capture and storage (CCS), and specially, its conversion towards valuable fuels and precursors have become an urgent need. Many studies have been accomplished in order to provide an effective capture and sequestration of CO₂. A critical point is that the deployment of CCS schemes is a multifaceted problem that requires shared vision and efforts from governments, policy makers, and economists, as well as scientists, engineers and venture capitalists.^{58,59} The Intergovernmental Panel on Climate Change, estimates that CO₂ emissions to the atmosphere could be reduced by 80–90% for a modern conventional power plant equipped with carbon capture and storage technology.⁶⁰ The adsorption of CO₂ is considered one of the most promising technologies for CCS,⁶¹ where natural zeolites, metal organic frameworks (MOFs), and Fe₃O₄-graphene are the conventional adsorbents inasmuch as their capacity to adsorb CO₂ (222-2640 mg CO₂/g sorbent) at laboratory scale.⁶²⁻⁶⁶

1.4 Environmental catalysis

Nevertheless, it seems clear that the efforts must be routed towards the potential use of CO₂ as an economical feedstock,^{56,67} because the net amount of CO₂ mitigated by conversion with renewable energy is 20–40 times greater than sequestration over a 20 year span.⁶⁸⁻⁷⁰ To substantially reduce CO₂ emissions by catalytic conversion, only reactions which produce fuels or commodity chemicals can be considered as viable solutions. The demand for fine chemicals is simply not large enough to effectively reduce emissions through a CO₂ conversion process.⁷¹ Due to that, Figure 1.4 summarizes three ways for CO₂ conversion; CO₂ reduction has become an interesting option since the CO produced could be used as feedstock in the Fisher-Tropsch synthesis.⁷² This is an industrial catalytic process to produce synthetic hydrocarbons to be used as fuels known since the 40s, although it is worth pointing out that its economic viability is tightly related to the price of crude oil. Furthermore, CO is also a key ingredient of syngas, a mixture of CO, CO₂ and H₂ which is used in many industrial processes to produce tons of chemicals such as methane (CH₄)^{73,74} or methanol (MeOH).⁷⁵ In this sense, the CO₂ conversion to MeOH emerges as the most important way for CO₂ utilization since it is the most direct route for CO₂ utilization. Besides, MeOH is a fuel for batteries and a precursor to many interesting chemicals,⁷⁶ and it is very remarkable that the use of methanol as a transportation fuel presents economic advantages with respect to hydrogen based fuel cells⁷⁷ which, despite of the huge research efforts, have not been generalized in the automotive world yet, mainly because of the need to use Pt containing anodes as catalysts.⁷⁸ Finally, direct hydrogenation of CO₂ to alkanes species (CO₂-Fisher-Tropsch) is possible in one reactor since is thermodynamically easier than reverse Water Gas Shift Reaction because the overall process is exothermic.⁷⁹ This step is only the direct conversion of CO to hydrocarbons after the CO₂ reduction.

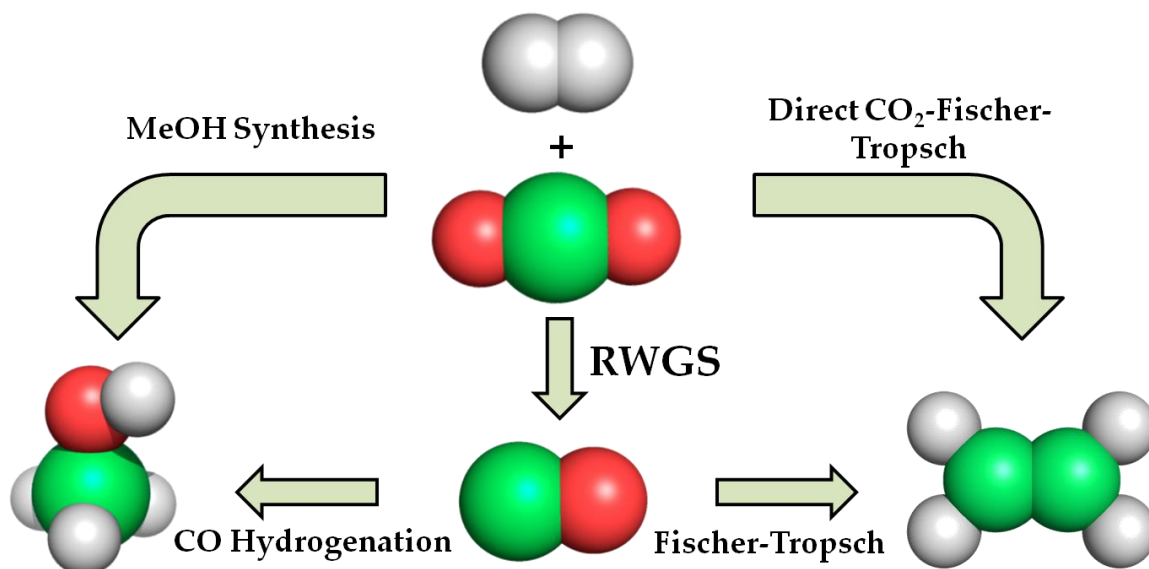


Figure 1.4: Scheme about different CO₂ hydrogenation pathways.

Deepening on the catalysts, the RWGS reaction ($\text{CO}_2 + \text{H}_2 \rightarrow \text{CO} + \text{H}_2\text{O}$) occurs on well dispersed nanoparticles supported on metal-oxides supports in order to maximize the interface area between particle and support.⁸⁰ Table 1.2 summarizes selected RWGS catalysts with a conversion superior to 20 %, (see Reference 72 to consult the full table).

Table 1.2: Summary of selected RWGS catalysts with a conversion superior to 20%, including reaction conditions.

Catalyst	H ₂ :CO ₂ ratio	Temperature (°C)	Pressure (MPa)	Conversion (%)	Selectivity (%)
NiO/CeO ₂ ⁸⁰	1:1	700	0.1	~40	~100
Cu/Al ₂ O ₃ ⁸¹	1:9	500	N/A	~60	N/A
Cu-Ni/ γ -Al ₂ O ₃ ⁸²	1:1	600	0.1	28.7	79.7
Fe-Mo/ γ -Al ₂ O ₃ ⁸³	1:1	600	1	~45	~100
Mo/ γ -Al ₂ O ₃ ⁸⁴	1:1	600	1	34.2	97
Pt/TiO ₂ ⁸⁵	1.4:1	400	N/A	~30	N/A
Pt/Al ₂ O ₃ ⁸⁵	1.4:1	400	N/A	~20	N/A
Ni-Mo ₂ C ⁸⁶	5:1	250	2	21	29
Co-Mo ₂ C ⁸⁶	5:1	250	2	23	24

1.4 Environmental catalysis

Regarding the MeOH synthesis, as is exhibited on Table 1.3, Cu/ZnO/Al₂O₃, the commercial catalyst for CO₂ hydrogenation towards MeOH,⁸⁷ shows the maximum space-time yield. Copper is an important metal to promote the MeOH synthesis, either as metallic catalyst or a supported particle, but the reducibility of Cu and the nature of the support material can also have a significant effect on the catalytic performance.⁸⁸

Table 1.3: Summary of selected MeOH synthesis catalysts with a conversion superior to 15%, sorted by space time yield, including reaction conditions. See Ref. 72 for more details.

Catalyst	H ₂ :CO ₂ ratio	Temperature (°C)	Pressure /MPa	Conversion /%	Selectivity /%	Space-time yield /g MeOH kg _{cat} ⁻¹ h ⁻¹
Cu-ZnO/Al ₂ O ₃ ⁸⁹	10:1	260	36.0	22.7	77.3	7729
Ga-Cu-ZnO- ZrO ₂ ⁹⁰	3:1	250	7.0	22.0	72.0	704
CuO/ZnO ⁹¹	3:1	240	3.0	16.5	78.2	550
Cu/Zn/Al/Y ⁹²	3:1	250	5.0	26.9	52.4	520
Pd-Ga/CNT ⁹³	3:1	250	5.0	16.5	52.5	512
Pd-ZnO/CNT ⁹⁴	3:1	270	5.0	19.6	35.5	343
CuO-ZnO/Al ₂ O ₃ ⁹⁵	3.89:1	280	5.0	19.5	37.0	311
CuO-ZnO/ZrO ₂ ⁹⁶	3:1	240	3.0	18.0	51.2	305
CuO-ZnO/CeO ₂ ⁹⁵	3.89:1	280	5.0	12.8	37.0	210
Cu/ZnO-ZrO ₂ ⁹⁷	3:1	220	8.0	21.0	68.0	181
Pd/Ga ₂ O ₃ ⁹⁸	3:1	250	5.0	17.3	51.6	176
Cu-Zn-Ga ⁹⁹	3:1	270	3.0	15.9	29.7	136
Cu/ZrO ₂ /CNT ¹⁰⁰	3:1	260	3.0	16.3	43.5	84
Cu-Ba/γ-Al ₂ O ₃ ¹⁰²	3.8:1	280	10.0	25.2	9.3	71
Cu-ZnO/TiO ₂ -ZrO ₂ ¹⁰¹	3:1	240	3.0	17.4	43.8	53
Cu-ZnO/ZrO ₂ ¹⁰¹	3:1	240	3.0	17.0	41.5	49
Cu-K/γ-Al ₂ O ₃ ¹⁰²	3.8:1	280	36.0	28.6	2.1	18
CoMoS ¹⁰³	3:1	310	10.4	28.0	31.0	N/A

1.4.2 Hydrogen as a new efficient and environmental friendly fuel

Hydrogen is considered an inexhaustible source and environmental friendly gas and it has been proposed as a substitute of gas-oil fuels and biodiesel vehicles fuels.¹⁰⁴ Despite of being one of the most abundant elements in the Earth, it is not in gas phase (H₂) but in water and organic molecules like hydrocarbons or proteins. The main application of H₂ are based into making ammonia,¹⁰⁵ a major component of fertilizers

Introduction

and a familiar ingredient in household cleaners. Refineries use the second largest amount of hydrogen for chemical processes such as removing sulfur from gasoline and converting heavy hydrocarbons into gasoline or diesel fuels. Food producers use a small percentage of hydrogen to add to some edible oils through a catalytic hydrogenation process.¹⁰⁶ Moreover, one must consider that the demand for hydrogen both for traditional uses, but also for new fuel cells will increase in the next decades.

Industry generates some 48 million metric tons of hydrogen globally each year from fossil fuels. Also, H₂ can be produced from different sources such as dry biomass¹⁰⁷ or biomass-derived liquid fuels (MeOH, EtOH,^{108,109} biodiesel...), as well as from water. Another exhaustively studied reaction to produce H₂ from experimental and theoretical sides due to its relevant role in the chemical industry is the WGS reaction.¹¹⁰⁻¹¹⁹ This reaction was described firstly by Felice Fontana in 1780, but was in the beginning of the 20th century with the development of the Haber-Bosh process for ammonia production, when started to be in a real practical use.¹²⁰ From this moment the WGS has gained importance due to its crucial role in the pure hydrogen production for fuel cell applications,¹²¹⁻¹²³ and has become an inseparable part of various industrial processes.

1.5 Motivation and outline of the thesis

As is outlined in the preceding sections, the search of cost-effective catalysts able to convert harmful substances for the environment into efficient and environmental friendly fuels is a challenge for heterogeneous catalysis in particular and for the science in general. The CO₂ hydrogenation towards MeOH ($\text{CO}_2 + 3\text{H}_2 \rightarrow \text{CH}_3\text{OH} + \text{H}_2\text{O}$) and the Water Gas Shift reaction ($\text{CO} + \text{H}_2\text{O} \rightarrow \text{CO}_2 + \text{H}_2$) are two clear examples of how to generate energetic resources from disposable and hazardous substances. In this sense, transition metal carbides are very interesting materials due to its low cost and the capability to increase the catalytic activity being a support of small metallic particles. Nevertheless, despite the great contributions from studies using Au and Cu clusters supported on titanium carbide, the difficulty to support small metal particles on TiC (001) involves the research of other TMCs. As is mentioned before, molybdenum carbides are very interesting catalysts.

The work presented here involves the computational part of a combination of experimental and theoretical work about two-key reaction in the field of environmental catalysis using different phases of molybdenum carbides (orthorhombic and cubic) as catalysts or as support of small metal nanoparticles. The aim is to contribute to the knowledge-driven of CO₂ activation and conversion in first instance and subsequently, to carry out an extensive study of both selected reactions, proposing the suitable and efficient catalyst for each one. The computational work has been focused on the reaction mechanisms and to assess the role of the catalyst structure and morphology, in order to determine the key points of the substrate-catalysts interactions and justifying the experimental results qualitatively, evaluating typical catalysts descriptors such as activity, selectivity, and stability.

This thesis is structured as follows:

- Chapter 2 contains a description of the methodology used to perform the computational study of this research, including tools and techniques related with heterogeneous catalysis.
- Chapter 3 talks about the computational models to describe the molybdenum carbide systems.
- Chapter 4 describes the promising experimental results of CO₂ hydrogenation on bare molybdenum carbide surfaces. From a computational point of view, this chapter encompasses the systematic and exhaustive study about CO₂, CO, and H₂ adsorption, activation, and dissociation. Furthermore, CH₄ adsorption study is included due to it is a main product on MeOH synthesis.
- Chapter 5 is focused on MeOH synthesis on bare and Cu supported orthorhombic (001) surface, with a metal/carbon ratio of two. This chapter encompasses the reaction mechanism of CO₂ hydrogenation on both surface terminations (Mo and C atoms).
- Chapter 6 contains the results of MeOH synthesis on clean and Cu supported δ -MoC (001) with a metal/carbon ratio of one, describing the experiments and reaction mechanism.
- Chapter 7 is based on the study of WGS reaction on pristine and Au supported δ -MoC (001), describing the reaction mechanism of supported and unsupported systems.

1.5. Motivation and outline of the thesis

- Chapter 8 summarizes the general conclusions of this thesis. At the end of the thesis, the list of publications is included.
- Finally, a thesis summary in Catalan and the list of publications are included.

1.6 References

- [1] J. Berzelius, *Annales chimie physiques*, **1836**, 61, 146.
- [2] W. Ostwald, Nobel Lecture: On Catalysis, **1909**.
- [3] J. Erisman, M. Sutton, J. Galloway, Z. Klimont and W. Winiwarter, *Nat. Geosci.*, **2008**, 1, 636.
- [4] M. Fernández-García and J. A. Anderson, *Supported Metals in Catalysis*, Catalytic Sciences Series, Vol. 5, Imperial College Press, London, **2005**; A. Wieckowski, E. Savinova, and C. G. Vayenas, *Catalysis and Electrocatalysis at Nanoparticle Surfaces*, Marcel Dekker, New York, **2003**.
- [5] P. Ball, *Nature*, **2006**, 442, 500.
- [6] J. K. Norskov, T. Bligaard, J. Rossmeisl and C. H. Christensen, *Nature Chem.*, **2009**, 1, 37.
- [7] L. E. Toth, *Transition Metal Carbides and Nitrides*; Academic Press: New York, **1971**.
- [8] S. T. Oyama, *Catal. Today*, **1992**, 15, 179.
- [9] S. T. Oyama, *The Chemistry of Transition Metal Carbides and Nitrides*; Blackie Academic and Professional: Glasgow, **1996**.
- [10] J. Chipman, *Metallurgical Transactions*, **1975**, 3, 1972.
- [11] J. M. Thomas and W. J. Thomas, *Principles and Practice of Heterogeneous Catalysis*, Wiley-VCH, New York, **1996**.
- [12] R. B. Levy and M. Boudart, *Science*, **1973**, 181, 547.
- [13] H. C. Woo, K. Y. Park, Y. G. Kim, I. S. Nam, J. S. Chung and J. S. Lee, *Appl. Catal.*, **1991**, 75, 267
- [14] B. Dhandapani, T. St Clair and S. T. Oyama, *Appl. Catal. A*, **1998**, 168, 219.
- [15] J. R. Kitchin, J. K. Nørskov, M. A. Barteau and J. G. Chen, *Catal. Today* **2005**, 105, 66
- [16] N. Ji, T. Zhang, M. Zheng, A. Wang, H. Wang, X. Wang and J. G. Chen, *Angew. Chem., Int. Ed.*, **2008**, 47, 8510.
- [17] D. Ham and J. Lee, *Energies*, **2009**, 2, 873.
- [18] E. C. Weigert, M. B. Zellner, A. L. Stottlemeyer and J. G. Chen, *Top. Catal.*, **2007**, 46, 349.
- [19] A. Serov and C. Kwak, *Appl. Catal., B*, **2009**, 90, 313.
- [20] J. A. Rodriguez, P. Liu, F. Viñes, F. Illas, Y. Takahashi and K. Nakamura, *Angew. Chem., Int. Ed.*, **2008**, 47, 6685.
- [21] J. A. Rodriguez, P. Liu, Y. Takahashi, K. Nakamura, F. Viñes and F. Illas, *J. Am. Chem. Soc.*, **2009**, 131, 8595.
- [22] J. A. Rodriguez, P. Liu, Y. Takahashi, K. Nakamura, F. Viñes and F. Illas, *Top. Catal.*, **2010**, 53, 393.
- [23] G. Rothenberg, *Catalysis: Concepts and Green Applications*. Wiley-VCH, (2008).
- [24] H. H. Hwu and J. G. Chen, *Chem. Rev.*, **2005**, 105, 185.
- [25] M. Dixit, X. Peng, M. D. Porosoff, H. D. Willauer and G. Mpourmpakis, *Catal. Sci. Technol.*, **2017**, 7, 5521.
- [26] F. Viñes, C. Sousa, F. Illas, P. Liu and J. A. Rodriguez, *J. Phys. Chem. C*, **2007**, 111, 16982.
- [27] Y. F. Zhang, F. Viñes, Y. J. Xu, Y. Li, J. Q. Li and F. Illas, *J. Phys. Chem. B*, **2006**, 110, 15454.
- [28] A. L. Stottlemeyer, T. G. Kelly, Q. Meng and J. G. Chen, *Surf. Sci. Rep.*, **2012**, 67, 201.
- [29] J. A. Rodriguez, P. Liu, J. Gomes, K. Nakamura, F. Viñes, C. Sousa and F. Illas, *Phys. Rev. B: Condens. Matter Mater. Phys.*, **2005**, 72, 075427.

1.6 References

- [30] F. Viñes, C. Sousa, F. Illas, P. Liu and J. A. Rodriguez, *J. Phys. Chem. C*, **2007**, *111*, 1307.
- [31] J. A. Rodriguez F. Viñes, F. Illas P. Liu, Y. Takahashi and K. Nakamura, *J. Chem. Phys.*, **2007**, *127*, 211102.
- [32] L. K. Ono and B. Roldán-Cuenya, *Catal. Lett.*, **2007**, *113*, 8.
- [33] J. A. Rodriguez, P. Liu, F. Viñes, F. Illas, Y. Takahashi and K. Nakamura, *Angew. Chem., Int. Ed.*, **2008**, *47*, 6685.
- [34] J. A. Rodriguez, P. Liu, Y. Takahashi, K. Nakamura, F. Viñes and F. Illas, *J. Am. Chem.Soc.*, **2009**, *131*, 8595.
- [35] L. Feria, J. A. Rodriguez, T. Jirsak and F. Illas, *J. Catal.*, **2011**, *279*, 352.
- [36] J. A. Rodriguez, P. Liu, Y. Takahashi, K. Nakamura, F. Viñes and F. Illas, *Top. Catal.*, **2010**, *53*, 393.
- [37] J. A. Rodriguez, P. Liu, Y. Takahashi, F. Viñes, L. Feria, E. Florez, K. Nakamura and F. Illas, *Catal. Today*, **2011**, *166*, 2.
- [38] J. A. Rodriguez, L. Feria, T. Jirsak, Y. Takahashi, K. Nakamura and F. Illas, *J. Am. Chem.Soc.*, **2010**, *132*, 3177.
- [39] E. Florez, T. Gomez, P. Liu, J. A. Rodriguez and F. Illas, *ChemCatChem*, **2010**, *2*, 1219
- [40] T. Wang, Y.W. Li, J. Wang, M. Beller, and H. Jiao, *J. Phys. Chem. C*, **2014**, *118*, 3162.
- [41] F. Viñes, J. A. Rodriguez, P. Liu and F. Illas, *J. Catal.*, **2008**, *260*, 103.
- [42] P. Liu and J. A. Rodriguez, *J. Phys. Chem. B*, **2006**, *110*, 19418.
- [43] N. M. Schweitzer, J. A. Schaidle, O. K. Ezekoye, X. Pan, S. Linic and L. T. Thompson, *J. Am. Chem. Soc.*, **2011**, *133*, 2378.
- [44] J. Ren, C.-F. Huo, J. Wang, Z. Cao, Y.-W. Li and H. Jiao, *Surf. Sci.*, **2006**, *600*, 2329.
- [45] H. Tominaga and M. Nagai, *Appl. Catal., A*, **2007**, *328*, 35.
- [46] A. J. Medford, A. Vojvodic, F. Studt, F. Abild-Pedersen and J. K. Nørskov, *J. Catal.*, **2012**, *290*, 108.
- [47] F. Viñes, C. Sousa, F. Illas, P. Liu and J. A. Rodriguez, *J. Phys. Chem. C*, **2007**, *111*, 16982.
- [48] W. Zheng, T. P. Cotter, P. Kaghazchi, T. Jacob, B. Frank, K. Schlichte, W. Zhang, D. S. Su, F. Schüth and R. Schlögl, *J. Am. Chem. Soc.*, **2013**, *135*, 3458.
- [49] H. Tominaga, Y. Aoki and M. Nagai, *Appl. Catal., A*, **2012**, *423–424*, 192.
- [50] C. Pistonesi, M. E. Pronsato, L. Bugyi and A. Juan, *J. Phys.Chem. C*, **2012**, *116*, 24573.
- [51] J. W. Han, L. Li and D. S. Scholl, *J. Phys. Chem. C*, **2011**, *115*, 6870.
- [52] G. Centi, P. Ciambelli, S. Perathoner and P. Russo, *Catal. Today*, **2002**, *75*,3.
- [53] R. J. Farrauto and R. M. Heck, *Catal. Today*, **2000**, *55*, 179.
- [54] X. Lim, *Nature*, **2015**, *526*, 628.
- [55] Intergovernmental Panel on Climate Change, *Climate Change 2013 – The Physical Science Basis.*, Cambridge University Press, 1st edn., **2014**.
- [56] M. Aresta, Ed. *Carbon Dioxide as Chemical Feedstock*. Wiley-VCH: New York, **2010**.
- [57] U.E.I. Administration, *International Energy Outlook 2013*, Washington DC, **2013**;
<http://www.eia.gov/forecasts/ieo/pdf/0484%282013%29.pdf>.
- [58] M. Z. Jacobson, *Energy Environ. Sci.*, **2009**, *2*, 148.
- [59] D. M. D'Alessandro, B. Smit and J. R. Long, *Angew. Chem. Int. Ed.* **2010**, *49*, 6058.
- [60] IPCC, *IPCC Special Report on Carbon Dioxide Capture and Storage*, Cambridge University Press, Cambridge, **2005**.

- [61] J. D. Figueroa, T. Fout, S. Plasynski, H. McIlvried and R.D. Srivastava, *Journal of Greenhouse Gas Control*, **2008**, 2,9.
- [62] S. Cavenati, C. A. Grande and A. E. Rodrigues, *J. Chem. Eng. Data*, **2004**, 49, 1095.
- [63] Y. Cheng-Hsiu, H. Chih-Hung and C. S. Tan, *Air Qual. Res.*, **2012**, 12, 745.
- [64] A. Alonso, J. Moral-Vico, A. A. Markeb, M. Busquets-Fité, F. Komilis, V. Puentes, A. Sánchez and X. Font, *Science of the Total Environment*, **2017**, 595, 51.
- [65] A. K. Mishra and S. Ramaprabhu, *J. Appl. Phys.*, **2014**, 116, 064306.
- [66] A. R. Millward and O. M. Yaghi, *J. Am. Chem. Soc.*, **2005**, 127, 17998.
- [67] D. Preti, C. Resta, S. Squarzialupi and G. Fachinetti, *Angew. Chem. Int. Ed.* **2011**, 50, 12551.
- [68] W. Wang, S. Wang, X. Ma and J. Gong, *Chem. Soc. Rev.*, **2011**, 40, 3703.
- [69] G. Centi and S. Perathoner, *Catal. Today*, **2009**, 148, 191.
- [70] S. Perathoner and G. Centi, *ChemSusChem*, **2014**, 7, 1274.
- [71] C. Song, *Catal. Today*, **2006**, 115, 2.
- [72] M. D. Porosoff, X. Yang and J. G. Chen, *Energy Environ. Sci.*, **2016**, 9, 62.
- [73] S. Wang, G. Q. Lu and G. J. Millar, *Energ. Fuels*, **1996**, 10, 896.
- [74] A. Caballero and P. J. Perez, *Chem. Soc. Rev.*, **2013**, 42, 8809.
- [75] X. M. Liu, G. Q. Lu, Z. F. Yan and J. Beltramini, *Ind. Eng. Chem. Res.*, **2003**, 42, 6518.
- [76] X. Xiaoding and J. A. Moulijn, *Energ. Fuels*, **1996**, 10, 305.
- [77] G. A. Olah, A. Goepfert and G. K. S. Prakash, *Beyond Oil and Gas: The Methanol Economy*, Wiley-VCH Verlag GmbH & Co. KGaA: Weinheim, **2006**.
- [78] H. A. Gasteiger, S. S. Kocha, B. Sompalli and F. T. Wagner, *Appl. Catal. B*, **2005**, 56, 9.
- [79] Green Carbon Dioxide: Advances in CO₂ Utilization, ed. G. Centi and S. Perathoner, John Wiley & Sons, Hoboken, NJ, **2014**.
- [80] B. W. Lu and K. Kawamoto, *Mater. Res. Bull.*, **2014**, 53, 70.
- [81] C. S. Chen, W. H. Cheng and S. S. Lin, *Catal. Lett.*, **2000**, 68, 45.
- [82] Y. Liu and D. Liu, *Int. J. Hydrogen Energy*, **1999**, 24, 351.
- [83] A. G. Kharaji, A. Shariati and M. A. Takassi, *Chin. J. Chem. Eng.*, **2013**, 21, 1007.
- [84] A. G. Kharaji, A. Shariati and M. Ostadi, *J. Nanosci. Nanotechnol.*, **2014**, 14, 6841.
- [85] S. S. Kim, H. H. Lee and S. C. Hong, *Appl. Catal., A*, **2012**, 423–424, 100.
- [86] W. Xu, P. Ramírez, D. Stacchiola, J. Brito and J. Rodriguez, *Catal. Lett.*, **2015**, 41, 1.
- [87] M. Behrens, F. Studt, I. Kasatkin, S. Kuhl, M. Hävecker, F. Abild-Pedersen, S. Zander, F. Girgsdies, P. Kurr, B.-L. Kniep, M. Tovar, R. W. Fischer, J. K. Nørskov and R. Schlögl, *Science*, **2012**, 336, 893.
- [88] O. Martin and J. Perez-Ramirez, *Catal. Sci. Technol.*, **2013**, 3, 3343.
- [89] A. Bansode and A. Urakawa, *J. Catal.*, **2014**, 309, 66.
- [90] R. Ladera, F. J. Perez-Alonso, J. M. Gonzalez-Carballo, M. Ojeda, S. Rojas and J. L. G. Fierro, *Appl. Catal. B*, **2013**, 142, 241.
- [91] H. Lei, R. Nie, G. Wu and Z. Hou, *Fuel*, **2015**, 154, 161.
- [92] P. Gao, F. Li, N. Zhao, F. Xiao, W. Wei, L. Zhong and Y. Sun, *Appl. Catal. A*, **2013**, 468, 442.
- [93] H. Kong, H.-Y. Li, G.-D. Lin and H.-B. Zhang, *Catal. Lett.*, **2011**, 141, 886.
- [94] X.-L. Liang, J.-R. Xie and Z.-M. Liu, *Catal. Lett.*, **2015**, 145, 1138.

1.6 References

- [95] L. Angelo, K. Kobl, L. M. M. Tejada, Y. Zimmermann, K. Parkhomenko and A. C. Roger, *C. R. Chim.*, **2015**, *18*, 250.
- [96] G. Bonura, M. Cordaro, C. Cannilla, F. Arena and F. Frusteri, *Appl. Catal. B*, **2014**, *152–153*, 152.
- [97] J. Sloczynski, R. Grabowski, A. Kozłowska, P. Olszewski, J. Stoch, J. Skrzypek and M. Lachowska, *Appl. Catal. A*, **2004**, *278*, 11.
- [98] J. Qu, X. Zhou, F. Xu, X.-Q. Gong and S. C. E. Tsang, *J. Phys. Chem. C*, **2014**, *118*, 24452.
- [99] W. J. Cai, P. R. de la Piscina, J. Toyir and N. Homs, *Catal. Today*, **2015**, *242*, 193.
- [100] G. Wang, L. Chen, Y. Sun, J. Wu, M. Fu and D. Ye, *RSC Adv.*, **2015**, *5*, 45320.
- [101] J. Xiao, D. Mao, X. Guo and J. Yu, *Appl. Surf. Sci.*, **2015**, *338*, 146.
- [102] A. Bansode, B. Tidona, P. R. von Rohr and A. Urakawa, *Catal. Sci. Technol.*, **2013**, *3*, 767.
- [103] D. L. S. Nieskens, D. Ferrari, Y. Liu and R. Kolonko Jr, *Catal. Commun.*, **2011**, *14*, 111.
- [104] R.D. Cortright, R.R. Davda and J.A. Dumesic, *Nature*, **2002**, *418*, 964.
- [105] M. Halmann and A. Steinfeld, *Energy*, **2006**, *31*, 3171.
- [106] M. B. Fernandez, G. M. Tonetto, G. H. Crapiste and D. E. Damiani, *J. Food Eng.*, **2007**, *82*, 199.
- [107] D. B. Levin, L. Pitt, and M. Love, *Int. J. Hydrogen Energy*, **2004**, *29*, 173.
- [108] A. N. Fatsikostas and X. E. Verykios, *J. Catal.*, **2004**, *225*, 439
- [109] J. Llorca, P. R. de la Piscina, J. Sales and N. Homs, *Chem. Commun.*, **2001**, *0*, 641
- [110] C. V. Ovesen, B. S. Clausen, J. Schiøtz, P. Stolze, H. Topsøe and J. K. Nørskov, *J. Catal.* **1997**, *168*, 133.
- [111] N. Akiya and P. E. Savage, *Chem. Rev.*, **2002**, *102*, 2725.
- [112] J. Nakamura, J. M. Campbell and C. T. Campbell, *J. Chem. Soc. Faraday Trans.*, **1990**, *86*, 2725.
- [113] J. A. Rodriguez, P. Liu, J. Hrbek, J. Evans and M. Perez, *Angew. Chem. Int. Ed.*, **2007**, *46*, 1329.
- [114] P. Liu and J. A. Rodriguez, *J. Chem. Phys.*, **2007**, *126*, 164705.
- [115] A. A. Gokhale, J. A. Dumesic and M. Mavrikakis, *J. Am. Chem. Soc.*, **2008**, *130*, 1402.
- [116] R. M. Navarro, M. A. Peña and J. L. G. Fierro, *Chem. Rev.*, **2007**, *107*, 3952.
- [117] L. C. Grabow, A. A. Gokhale, S. T. Evans, J. A. Dumesic and M. Mavrikakis, *J. Phys. Chem. C*, **2008**, *112*, 4608.
- [118] J. A. Rodriguez, P. J. Ramírez, G. G. Asara, F. Viñes, J. Evans, P. Liu, J. M. Ricart and F. Illas, *Angew. Chem. Int. Ed.*, **2014**, *53*, 11270.
- [119] C. H. Lin, C. L. Chen and J. H. Wang, *J. Phys. Chem. C*, **2011**, *115*, 18582.
- [120] C. Ratnasamy and J. P. Wagner, *Catal. Rev.*, **2009**, *51*, 325.
- [121] Q. Fu, W. Deng, H. Saltsburg and M. Flytzani-Stephanopoulos, *Appl. Catal. B*, **2005**, *56*, 57.
- [122] G. Jacobs, E. Chenu, P.M. Patterson, L. Williams, D. Sparks, G. Thomas and B.H. Davis, *Appl. Catal. A*, **2004**, *258*, 203.
- [123] D. Andreeva, V. Idakiev, T. Tabakova, L. Ilieva, P. Falaras, A. Bourlinos and A. Travlos, *Catal. Today*, **2002**, *72*, 51.

Introduction

CHAPTER TWO

Theoretical Background

2.1 The Schrödinger equation

Ab initio wave function-based methods rest on solving the time-independent Schrödinger equation for the nuclei and electrons that form the system:

$$\hat{H}\Psi(r_1, R_1 \dots r_n, R_N) = E\Psi(r_1 \dots r_n, R_1 \dots R_N) \quad (2.1)$$

where \hat{H} is the full time-independent Hamiltonian operator, E is the total energy of the studied system, and Ψ is the wave function, which contains the position and spin nuclear and electronic coordinates of the system (R for the nuclei and r for the electrons). The Hamiltonian is the sum of kinetic (\hat{T}) and potential (\hat{V}) energy operators (Equation 2.2),

$$\hat{H} = \hat{T} + \hat{V} = (\hat{T}_{el} + \hat{T}_{nuc}) + (\hat{V}_{ne} + \hat{V}_{ee} + \hat{V}_{nn}) \quad (2.2)$$

where \hat{T}_{el} and \hat{T}_{nuc} is the kinetic of electron and nuclei respectively, \hat{V}_{ne} is the coulombic interaction between electrons and nuclei, and \hat{V}_{ee} and \hat{V}_{nn} are the coulombic repulsion between electrons and between nuclei respectively. The Schrödinger equation is extremely difficult to solve since it depends on the position of each nucleus, on the position of each electron, and their derivatives. The first approximation concern treating nuclear and electronic motion separately, this is the so-called Born-Oppenheimer approximation and can be rigorously derived. A simplified derivation invokes the difference mass between nuclei and electrons to justify treating nuclear and electronic motion as independent. This is justified since the velocity of nuclei in comparison with electrons is very slow, and therefore, the nuclei kinetic term on equation 2.2 (\hat{T}_{nuc}) can be neglected for calculating an electronic wave function, considering the nuclei in fixed positions so that and the nucleus-nucleus repulsion (\hat{V}_{nn}) become constant. In general terms, one can rewrite the expression for the wave function separated by the product of electronic and nuclear wave function:

Theoretical background

$$\Psi_{tot}(R, r) = \Psi_{el}(R, r) \Psi_{nuc}(R) \quad (2.3)$$

Clearly, the electronic wave function ($\Psi_{el}(R, r)$) depends on the nuclear coordinates and, hence, different nuclei configurations have different electronic wave functions. Despite this approximation makes the electronic Schrödinger equation easier to solve, its exact solution remains very difficult even for small polyelectronic systems, insomuch as the potential interaction between electrons (\hat{V}_{ee}) is difficult to be evaluated, and consequently, other approximations are required. In order to obtain an approximate solution of Schrödinger equation, several methods have been developed.

2.2 The density functional theory (DFT)

Hartree-Fock (HF) is one of the classical *ab initio* methods which calculate the ground state of electronic Hamiltonian approximating Ψ by a single Slater determinant of the particle orbitals. It can be proven that this is equivalent to considering each electron independent respect to the other electrons of the system. Nevertheless, this choice guarantees the anti-symmetry of the wave function and considers the exchange energy. However, it does not consider correlation effects which are not negligible. Since it is a variational method, the energy provided by Hartree-Fock is above the exact ground state energy (E_0) and the difference between them is the electronic correlation. In order to improve the HF, several advanced wave function methods have been developed, although with a very significant increase on the computational cost.

Density Functional Theory (DFT) offers an alternative way of facing the electronic Schrödinger equation and becomes useful to evaluate the energy and other properties of a polyelectronic system. DFT method propose to use the electron density $\rho(r)$ to include the electron correlation into the electronic energy. The function $\rho(r)$ is drastically simpler since, for a system with N electrons, the Ψ depends on $3N$ spatial coordinates plus N spin ones, whilst $\rho(r)$ depends only on three spatial coordinates. The electron density, $\rho(r)$, measures the probability density of finding any of the N electrons at r -with an arbitrary spin-, where the $\rho(r)$ at infinite values of r is 0 and the integral of ρ for all the space results in the number of electrons, N .

$$\rho(r) = N \int \cdots \int \Psi(r_1, r_2, \dots, r_n) \Psi^*(r_1, r_2, \dots, r_n) dr_1 dr_2 \cdots dr_n \quad (2.4)$$

The first step to obtain $\rho(r)$ without making explicit use of the electronic wave function as in Eq. (2.4), was established by Thomas and Fermi^{1,2} in 1927, which expressed the properties of the ground state of a homogeneous electron gas. This model

was improved by Dirac (Thomas-Fermi-Dirac) one year later, including an exchange functional, although the kinetic energy was not properly represented. In 1964, Hohenberg and Kohn³ showed that the ground (non-degenerated) state electronic energy is a density functional, *i.e.*, $E = E[\rho(r)]$. They proved two theorems: 1) "*The external potential $V(r)$ (the \hat{V}_{ne} term in equation 2.2) of a non-degenerate electronic state is (to within a constant) a functional of the exact ground state ρ'* ". The theorem is proven *ad absurdum*, this is by assuming that if there existed two different external potentials giving the same ground state density, then, the variational principle leads to a contradicting result, since both external (and different) potentials cannot define the same $\rho(r)$. The main outcome to this first theorem is that all ground state properties, for example the energy, are defined by means of its electronic density. Thus, the ground state energy is a functional of $\rho(r)$ and it can be expressed, including the Born-Oppenheimer approximation, as

$$E(\rho) = T(\rho) + V_{ee}(\rho) + V_{ne}(\rho) = F_{HK}[\rho] + \int \rho(r) V_{ne}(\rho) dr \quad (2.5)$$

where $F_{HK}[\rho]$ is a universal functional, which is defined by the kinetic energy and the electron-electron repulsion potential, \hat{V}_{ee} . Therefore, according to the equation 2.5, the electronic energy can be obtained exactly if the $F_{HK}[\rho]$ is known. Unfortunately, the exact form of $F_{HK}[\rho]$ is unknown, which uncover the weakest point of DFT method giving rise to the research about finding the most accurate mathematical expressions of $F_{HK}[\rho]$.

Once formulated the first theorem, is known that $\rho(r)$ on the ground state is enough to define the ground state energy and extrapolating quite a lot "the observables of the system". Nevertheless, we do not know if a certain $\rho(r)$ is the ground state electron density. In this sense, the second Hohenberg-Kohn theorem determines that

2.2 The density functional theory (DFT)

"the energy of the system, $E(\rho)$, reaches a minimum value of the ground state energy, E_0 , for the exact density ρ_0 ".

In 1965 Kohn and Sham developed an electronic state calculation method (known as the Kohn-Sham method) based on the Thomas-Fermi and Thomas-Fermi-Dirac methods, which are focused to obtain an approximate expression of $F_{HK}[\rho]$ improving the point where both methods fail, the description of the kinetic of the N-electron system, as is commented before. The Kohn-Sham method suggests the calculation of the exact kinetic energy of a fictional system composed by N non-interacting electrons. This means that this fictional system can be represented by a Slater's determinant whose elements are the orbitals, Φ , which represents each electron of this system, being the total kinetic energy the sum of the kinetic energy of each electron:

$$T_s[\rho] = \sum_i^N \langle \Phi_i | -\frac{1}{2} \nabla^2 | \Phi_i \rangle \quad (2.6)$$

Based on this, Kohn and Sham rewrote the universal functional, $F_{HK}[\rho]$, as

$$F_{HK}[\rho] = T_s[\rho] + J[\rho] + E_{xc}[\rho] \quad (2.7)$$

$$J[\rho] = \frac{1}{2} \iint \frac{\rho(\mathbf{r}_1)\rho(\mathbf{r}_2)}{|\mathbf{r}_1 - \mathbf{r}_2|} d\mathbf{r}_1 d\mathbf{r}_2 \quad (2.8)$$

where they include the additional term $J[\rho]$, the classic Coulomb repulsion between two electrons, and $E_{xc}[\rho]$, the so-called exchange-correlation energy functional, which is defined as:

$$E_{xc}[\rho] = T[\rho] - T_s[\rho] - J[\rho] + V_{ee}[\rho] \quad (2.9)$$

Theoretical background

The Kohn-Sham orbitals satisfy the Kohn-Sham equations:

$$\left(-\frac{1}{2} \nabla^2 + V_s(r_1)\right) \Phi_i(r) = \varepsilon_i \Phi_i(r) \quad (2.10)$$

$$V_s(r_1) = \int \frac{\rho(r_2)}{r_{12}} dr_2 + V_{XC} - V_{ne}(r_1) \quad (2.11)$$

where $V_s(r)$ contains the exchange-correlation interaction effects between electrons, V_{XC} , where is the only unknown term in the equation due to the exchange-correlation energy. To summarize, the Kohn-Sham method solve the problem with N interacting electrons confined in a external potential $V_{ne}(r)$, using a fictional system with non-interacting particles but influenced by a effective potential, V_s , which is able to model the real interaction of these N electrons in the non interacting system, *i.e.*, both system must be the electronic density.

2.3 Exchange-correlation functionals

The predictive ability of Kohn-Sham method is directly related with the accuracy of the employed exchange-correlation functional. If the exchange correlation energy and exchange-correlation potential were known, the Kohn-Sham method provides the exact energy. Unfortunately, the exact functional is unknown, and many approximations must be performed. These approximations conform the rungs of the so-called Jacobs ladder, designed by Perdew, which connects the two ends of accuracy, functionals without exchange or correlation energy and functionals with an excellent accuracy in comparison with experiments.

2.3.1 Local Density Approximation (LDA)

LDA was the first (and the easiest) way to evaluate the exchange-correlation energy. LDA assumes that the exchange-correlation energy in a random point depends exclusively on the density in this point.

$$E_{XC}[\rho] = f(\rho) \quad (2.12)$$

LDA has an exchange component given by the Dirac Formula

$$E_x[\rho] = -\frac{3}{4} \left(\frac{3}{\pi} \right)^{1/3} \rho^{1/3} \quad (2.13)$$

although there is not analytical expression for the correlation part, and consequently, a variety of functionals were derived from accurate Monte-Carlo simulations for a homogeneous electron gas.

2.3.2 Generalized Gradient Approximation (GGA)

To account for spatial variations of the electron density, the dependency of the exchange-correlation energy with the gradient of electron density must be considered in order to evaluate how it changes on the near points:

$$E_{XC}[\rho] = \int f_{XC}(\rho(r), |\nabla\rho(r)|) \rho(r) dr \quad (2.14)$$

Several approximations on the gradient have been implemented, and all of them provide better results than LDA in terms of geometry, charge densities, and vibrational frequencies. The main reason for using GGA is the increase of the quality of binding energies. There are many GGA functionals, where foreground Perdew-Wang 91 (PW91) built by means of the LDA data. Perdew-Burke-Ernzerhof (PBE) and Revised Perdew-Burke-Ernzerhof (RPBE) correct the PW91 to improve the results.

In this thesis, all the calculations have been performed using PBE functional with and without the dispersion correction (Section 2.3.4). Previous studies used PW91 as functional, because of it describes well the TMCs features,⁴ although PBE and revised PBE (RPBE) are suited for the description of bulk and surfaces of all the studied TMCs,⁵ and transition metals in general.⁶ Furthermore, new dispersion corrections (for example, D3) are only implemented on PBE, not on PW91, thus, PBE was selected due to the good description of TMCs properties in order to take the chance of reproduce the calculations including new possible dispersion models in a future.

2.3.3 Hybrid Functionals

In GGA functionals, some chemical features are still not well described, as the band gap for semiconductors, for example. GGA functionals underestimate the gap

2.3 Exchange-correlation functionals

whereas HF method overestimates them. These results lead to the idea of mixing both methods to describe better the unknown V_{xc} . The exchange part of this functional includes the exact exchange of HF method whilst the correlation part comes from the DFT treatment. The construction of hybrid functionals is based on the adiabatic connection. The most popular hybrid functional is the B3LYP functional (80% LDA and 20% HF)⁷ although it describes bad metal compounds⁸ due to the correlation part of the functional is incorrect in the limit of homogeneous electron gas.

2.3.4 Dispersion Correction

DFT is the most widely used theoretical approach to molecular structure. For short intermolecular distances this method consistently includes exchange-correlation effects in an approximate way. Nevertheless, there are still difficulties for describing medium-range, and long-range (non-covalent) interactions such as the van der Waals ones. One of the well-established method to describe properly these interactions is proposed by Stefan Grimme.⁹ This methodology is based on the usual energy obtained by means of whatever DFT functional plus an empirical dispersion given by:

$$E_{disp} = -S_6 \sum_{i=1}^{N-1} \sum_{j=i+1}^N \frac{C_6^{ij}}{R_{ij}^6} f_{dmp}(R_{ij}) \quad (2.15)$$

$$f_{dmp}(R) = \frac{1}{1 + e^{-\alpha(R/R_0-1)}} \quad (2.16)$$

where N is the number of atoms in the system, C_6^{ij} is the dispersion coefficient per ij atom pair, S_6 is a global scaling factor which depends only of the used functional, R_{ij} is the interatomic distances, and f_{dmp} is a damping function, which smoothly increases from 0 to 1 as its argument changes of 0 to ∞ (Figure 2.1). This function is necessary

because the vdW corrections are required only to properly describe the long-range interaction between atoms.

Some variants to the original formulation were also introduced by Grimme et al. In the DFT-D2 variant,¹⁰ dispersion coefficients, C_6^{ij} obtained from the geometric mean of tabulated elemental values, are summed over interatomic distances, R_{ij} , modulated by a damping function, that gradually activates the dispersion correction (at a rate characterized by α) over a distance characterized by the sum of the two atomic vdW radii, R_0 , while an overall scaling term, S_6 , is optimized to be unique to each exchange-correlation functional. Grimme also presented a refined method, DFT-D3,¹¹ which incorporates an additional R^{-8} term in the dispersion series and adjusts the C_6^{ij} combination formula and damping function.

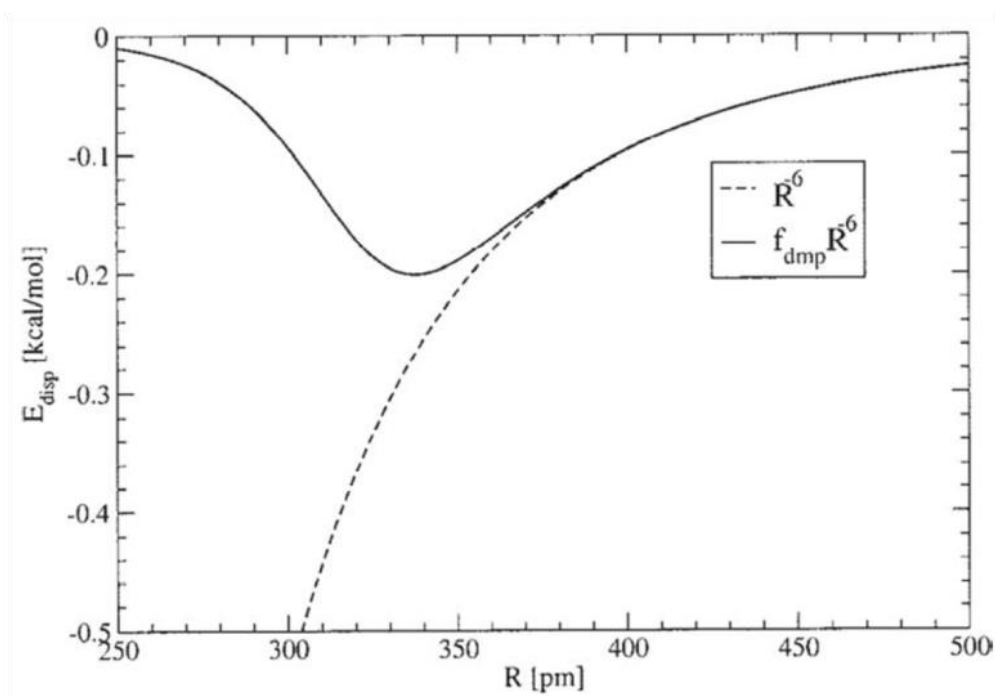


Figure 2.1: Dispersion contribution to the interaction potentials for two carbon atoms separated by a distance R . The dashed lines show the non-damped potential. This figure has been extracted from Ref. 9.

2.4 Plane waves and pseudopotentials

Orbitals or bands (one-electron wave functions) are usually introduced as a basis to expand the electron density. For computational purposes, a linear combination of basis functions is used to allow improved performance of calculations. On non-periodic calculations, the most widely basis sets are made of approximated representations of atomic orbitals and they have a localized character. Atomic orbitals are centered at the nuclei are in turn are represented by a linear combination of a given type of basis functions. In this way, a combination of nuclei-centered functions describes each atomic orbital. Two broadly used families of basis functions exist, Gaussian or Slater functions. Atomic basis sets describe well the atoms, even with few functions although the weak point is the basis set superposition error when limited basis sets are used.

In the description of periodic systems, it is common to use plane wave functions as basis sets, which are expressed as:

$$PW_{basis} = e^{ikr} \quad (2.17)$$

where k represents the crystal plane wave vector. The main advantage respect to local basis set is the periodicity, leading to some increased computational efficiency. However, a weak point is the large number of wave function needed to reach an acceptable accuracy for describing the core electrons. In this sense, there is a method which can be solved this problem, reducing the number of wave function without a significant lost of accuracy: The Effective Core Potentials or Pseudopotentials.

The use of Pseudopotentials is related with the large number of basis sets needed to describe the core atoms and is also encountered when using atomic orbital basis sets. Since core electrons do not play a key role on the reactivity of each atom and do not

intervene in chemical bonds, these electrons are not necessary to be explicitly described. One can assume that these core electrons are frozen, and they can be calculated in a reference configuration, remaining invariable during the calculation. Then, the effect of these core electrons in the valence electron density is considered by a potential, usually referred to as pseudopotentials, since it is an artificially introduced one modeling the core electrons and their interactions with nuclei and other electrons. The aim of this method is decrease the computational cost of these calculations, focusing the major part of the cost in the wave function which describe the valence electrons, responsible to the chemical reactivity.

Several kinds of pseudopotentials are available. Here, we mention those usually employed in periodic calculations with plane waves. These are the ultrasoft pseudopotentials,¹² norm-conserving pseudopotentials,¹³ or projected augmented wave pseudopotentials (PAW), the later are the ones used in the present thesis. The PAW method was introduced by Blöch in 1994¹⁴ and it is built on projector functions that allow the complicated wave functions to be mapped onto a pseudo-wave function, which is obtained neglecting the core electrons. This method models the core electrons taking the difference between the exact wave function and the pseudo-wave function. On DFT method, we solve the Schrödinger equation to determine the pseudo-wave function and projectors then enable us to obtain the exact density, as long as the basis set expansion is complete. Therefore, PAW is a frozen-core method but introduced the advantages of all electron calculations.

2.5 Solid State

This section talks about the computational description and calculation of solid materials. First of all, the discussion is focused on the selection of the periodic model to carry out the calculations of this thesis. The two well known models (the periodic and cluster one) to represent the condensed matter phase are presented, describing their advantages and disadvantages in order to justify our election. The rest of sub-sections talk about different theorems and tools to implement the DFT theory to model the solid-state systems.

2.5.1 Models for Solids

A perfect solid is a macroscopic system formed by a large number of atoms which form a regular structure in the three-dimensional space. Due to the impossibility of solving the electronic Schrödinger equation for the complete system, the study of the electronic structure of solids is based on a simplified model called periodic system. Models under periodic boundary conditions are constructed considering a piece of the solid (unit cell) surrounded by exact replicas in all space directions, with the goal to simulate an infinite solid (Figure 2.2).

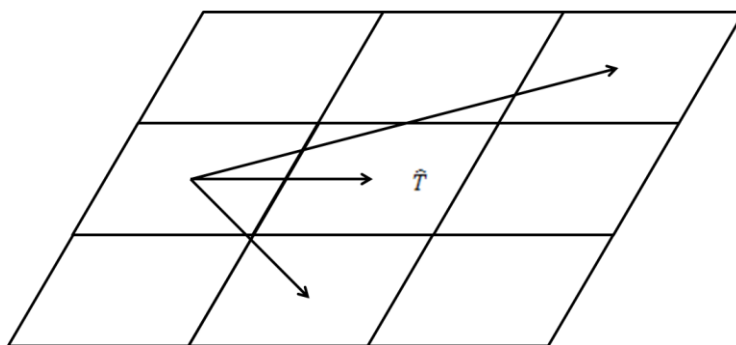


Figure 2.2: Schematic representation about the translation an arbitrary point in a supercell on the supercell replicas.

Theoretical background

The infinite array of discrete atoms in three dimensional space generated by a set of discrete translation operations described in equation 2.18 is known as Bravais lattice (Figure 2.3).

$$\hat{T} = n_1a + n_2b + n_3c \quad (2.18)$$

where n_i are integer numbers and a , b , and c are the cell vectors. Therefore, working with periodic conditions let to generate an infinite solid model storing only the information of the unit cell, since the other ones are exact reproductions of it, owing to the space translations defined by the lattice Bravais vectors. Thus, the replicas contain the same atoms as the unit cell and during the calculation, they suffer the same modifications as the unit cell.

However, the selection of the unit cell is not a trivial step. There are no rules to select the suitable size of the cell, although one can consider that the ideal size is obtained if increasing the unit cell size, the chemical and physical properties remain significantly unchanged.

2.5 Solid state

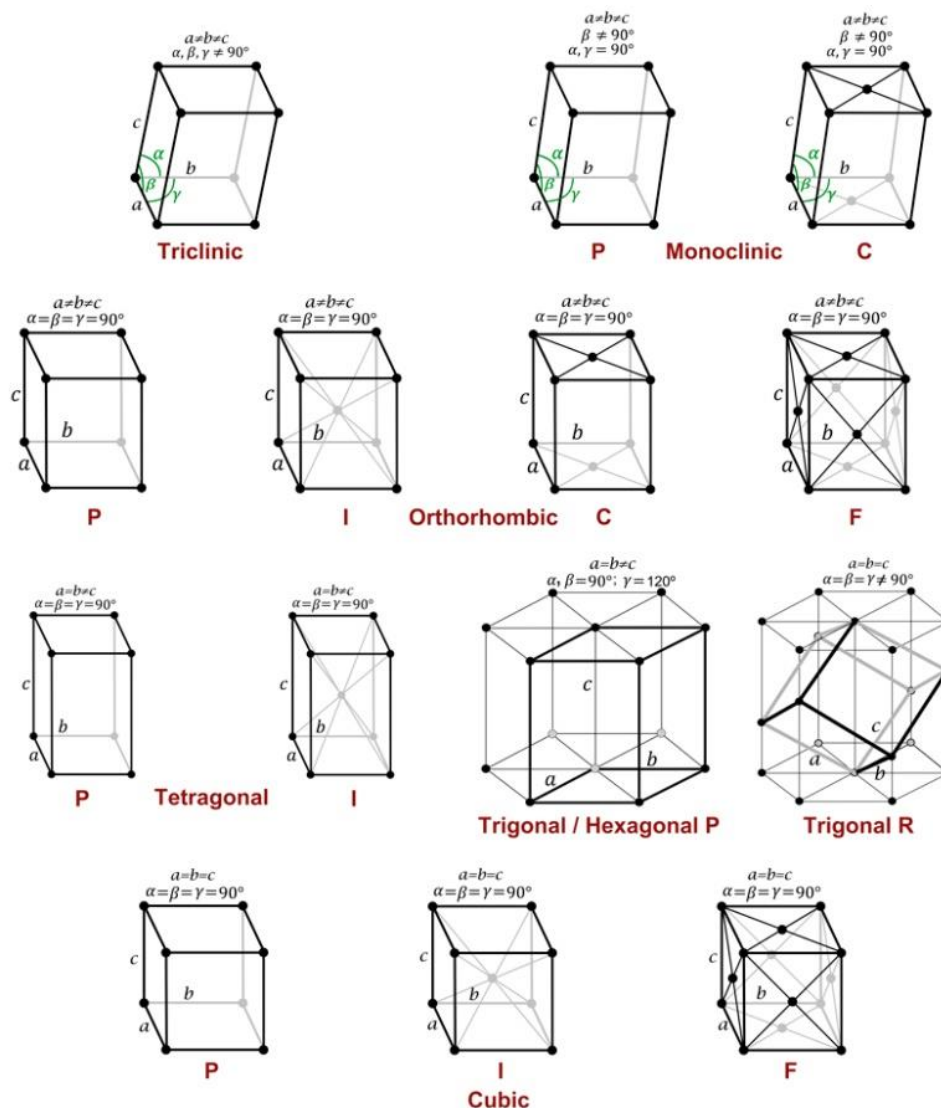


Figure 2.3: Representation of Bravais lattices.

The periodic model is not the only approach to describe the solid properties. The cluster model method is much simpler. In this model, only a small and finite number of aggregate atoms of the solid are studied with the goal to simulate a certain region of an extended solid. The use of the cluster model reduces the computational cost, encouraging the use of more accurate methods than DFT, although the periodic approach has some advantages in comparison to the cluster model. Even if the cluster model is suitable to describe local properties such as point defects, it misses the

macroscopic properties arising from the extended nature of the solid. For example, for metallic systems, infinite solids are suitable to simulate the electronic delocalization, which is not well described on the cluster model with a small number of atoms. Moreover, the number of atoms on the cluster is directly related with its electronic structure. Also, the use of the periodic model is suitable for studying the influence of the adsorbates' coverage.

2.5.2 The reciprocal lattice

The use of reciprocal space is appropriate to carry out the calculations of periodic systems. This is a mathematical construction which defines the reciprocal space associated to the crystalline lattice, defined in the physical space, called real space. The lattice on the real space $\{a, b, c\}$ has its corresponding reciprocal lattice $\{a^*, b^*, c^*\}$ which are defined:

$$a^* = 2\pi \frac{b \times c}{a \cdot (b \times c)}; \quad b^* = 2\pi \frac{a \times c}{b \cdot (a \times c)}; \quad c^* = 2\pi \frac{a \times b}{c \cdot (a \times b)} \quad (2.19)$$

The reciprocal lattice has a very unique set of properties and special points, directly related with the periodicity and translational symmetry of the Bravais cells lattice in real space. The entire reciprocal lattice is itself a Bravais's cell. Thus, any vector belonging to the reciprocal lattice is:

$$G = k_1 a^* + k_2 b^* + k_3 c^* \quad (2.20)$$

where k_i are integer numbers, in analogy with the one that passes through the direct cell. Besides, the reciprocal cell corresponds to the parallelepiped formed by the three reciprocal vectors, where the volume is:

$$V_{rec} = \frac{(2\pi)^3}{V_d} \quad (2.21)$$

where V_d is the volume of the direct cell. Therefore, large real unit cell implies small reciprocal cells and the opposite, small real unit cells evolve large reciprocal cell.

From the analytical point of view, the reciprocal lattice is defined as

$$e^{iK(r+R)} = e^{iKr} \quad (2.22)$$

where e^{iKr} is a plane wave with the same periodicity as Bravais lattice and R are different points of Bravais lattice which could be defined by means of the reciprocal space and the periodic conditions using plane waves, as is indicated by the Bloch's theorem.

2.5.3 Bloch's Theorem

Bloch's theorem¹⁵ uses the translational symmetry to reduce the infinite number of one-electron wave function (orbitals or bands) computing the number of electrons in the unit cell. For this, a wave function able to describe the primary unit cell and the periodic conditions of the supercell is necessary, in such a way the potential (V) in a random point of the unit cell is not modified when it is transfer to an equivalent point in the replicated cell:

$$V(r+R) = V(r) \quad (2.23)$$

Then the wave function for describing the electrons of a solid or crystal orbitals can be expressed as the product of a periodic part and plane wave like part.

$$\Psi_i(r) = e^{ikr} V_i(r) \quad (2.24)$$

where Ψ is the Bloch's wave function and V is a periodic function which can be expanded as a linear combination of plane waves:

$$\Psi_i(r) = \sum_G C_{i,k+G} e^{i(k+G)r} \quad (2.25)$$

$$G = 2\pi m \quad (2.26)$$

where G is the reciprocal vector shown on equation 2.20. Thus, the infinite number of electrons is now mapped onto the problem of expressing the wave function in terms of an infinite number of reciprocal space vectors within the first Brillouin zone, \vec{k} . Even if the plane waves basis set is finite, there is an infinite number of possible k -points, although it is assumed that the values of close K vectors in the space are practically equal and the wave function is calculated for only a grid of points that describe accurately the system. Therefore, one can solve this problem by sampling the Brillouin zone at special set of k -points.

The plane wave on the real system is expanded as a plane wave combination on the reciprocal space. Each plane wave is characterized by a kinetic energy $|k + G|^2 \hbar^2 / 2m$ leading to the fact that one could increase (or decrease) the plane wave basis set defining the kinetic energy, which enables to select the suitable number of plane waves to describe accurately the observables of the system.

2.5.4 Miller Indices

The Miller indices (hkl) form a notation system in crystallography for planes in Bravais lattices. They are defined as the reciprocal intersections between the plane and

2.5 Solid state

the coordinate axis. The Miller indices are related with the inverse of the intersection and then, the indices are multiplied by the least common multiple:

$$h = \frac{1}{a}; k = \frac{1}{b}; l = \frac{1}{c} \quad (2.27)$$

For example, if the intersection between the plane and axis is $3a$, $2b$, and $2c$, the inverse values are $1/3$, $1/2$, and $1/2$. Multiplying by the least common multiple, the Miller indices are (233) . There are some special cases:

- When the plane has not intersection with an axis, the Miller index is 0.
- If the intersection is located on the negative zone of the axis, the Miller index is negative, and it will be expressed as with the symbol on top of the number ($1\bar{1}0$).
- The notation of Miller indices will be bracketed if the set of planes are equivalent to (hkl) by the symmetry of the lattice.

2.5.5 Periodic Models

2.5.5.1 Surface Models (slab)

In case of surfaces, the repetition of the unit cell only in two directions of the space is desired (axis x and y) but not on z axis, where a large region of *vacuum* is added in order to avoid the repetition (see Figure 2.4). According to the system, the interactions may be greater or lesser, although in general terms, a *vacuum* between 10-12 Å is reasonable. Then, the unit cell is repeated infinitely in two directions. As it is explained before, the unit cell may not be the primitive cell due to the accuracy of the calculation and it is denoted as $(n \times m)$, where n and m are the number of times that the primitive cell is replicated in x and y directions respectively. The slab model contains a serie of atomic layers in order to represent an appropriate description of the surface and

bulk properties. Hence, the model thickness, *i.e.*, the number of atomic layers, is one of the keys to model the surfaces. In this sense, one can construct the slab model in two different ways: on the one hand, both ends of the slab model are relaxed, whereas the internal layers are fixed, simulating the bulk. On the other hand, the usual model to build the slab is based on the relaxation of one of the sides whilst the other is fixed, modeling the bulk. This option implies less atomic layers, which reduces the computational cost.

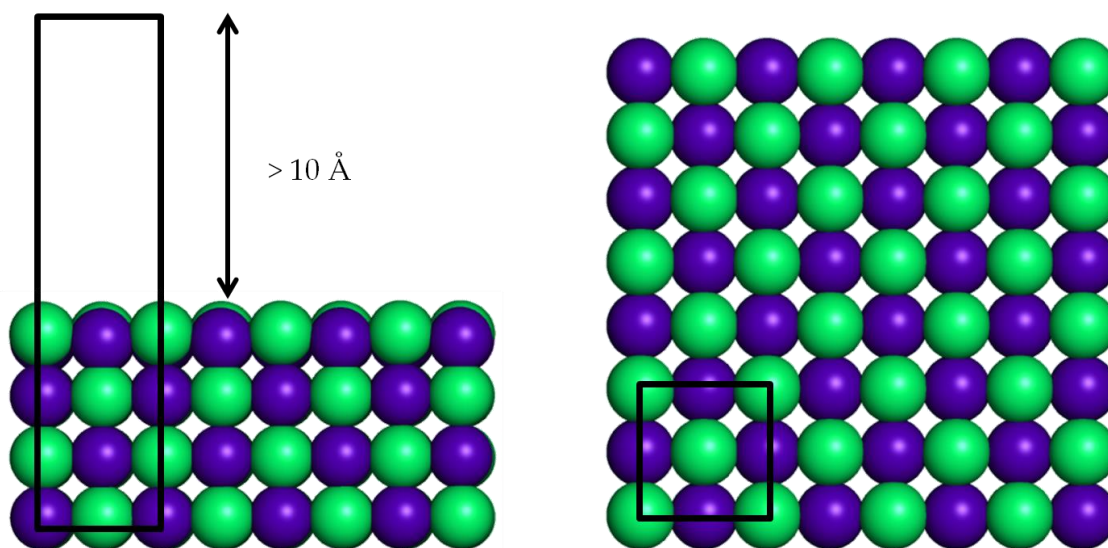


Figure 2.4: Side (left) and top (right) views of a 4 layers slab model of δ -MoC (001) surface. Black lines show the unit cell where a vacuum superior to 10 \AA have been added.

One of the disadvantages is the difficulty to simulate the particle dispersion on a surface, since to avoid possible lateral interactions between the dispersed particles, the use of big supercells is mandatory. The simulation and model of these kind of systems is a challenge in the field of heterogeneous catalysis, where the agreement between the size of the supercell (and dispersed nanoparticles) and the computational cost is probably the most important factor. On the other hand, slab model gives a correct

description of extended surfaces and small cells could be enough to simulate the surface effects due to the periodicity. Moreover, this model allows the study of non-local properties such as Fermi level, coverage effects, and adsorption energies.

2.5.5.2 Nanoparticle Models

As it is commented on previous sections (2.4.1), isolated particles may be modeled as normal clusters, although it is also possible to study these kinds of systems using periodic conditions, adding *vacuum* ($\sim 10 \text{ \AA}$) on all cell directions to avoid interactions with the repeated clusters. The periodic aggregate model is suitable to study covalent, ionic, and metallic systems. A weak point, in comparison with cluster models on non-periodic conditions, is that periodic models are limited to DFT due to periodic boundary conditions, whereas it is possible to use more accurate methods to model the non-periodic cluster model.

2.6 Energy and free energy diagrams

The goal of this section is to show how to construct the simplest potential energy diagrams, those that describe the elementary step of adsorption of a single atom or molecule on a surface. The elementary surface reaction steps are displayed on Figure 2.5. Molecules on a surface must be adsorbed (chemisorption or physisorption), and then, they can dissociate, diffuse, and recombine to generate new molecules for later to be desorbed as the reaction products.

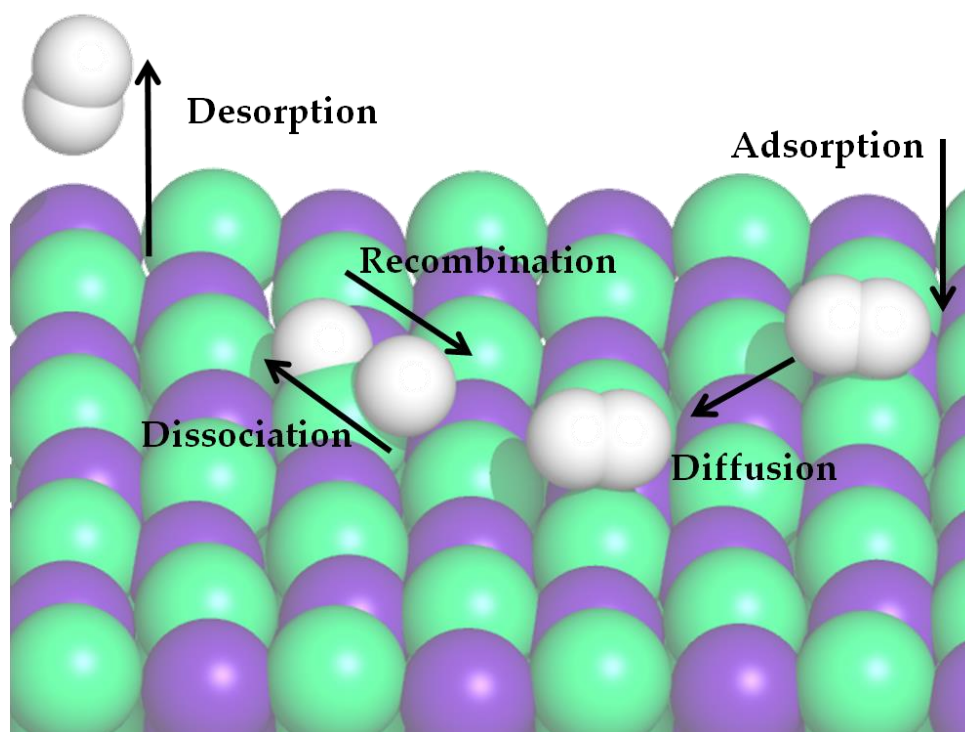


Figure 2.5: Sketches of elementary steps on heterogeneous catalysis.

2.6.1 Optimization of reactants, intermediates, and products.

To obtain the reaction mechanism of any process, the global minimization of energy is needed. It implies a first minimization to find the electronic ground state and

2.6 Energy and free energy diagrams

a second one to find the nuclei arrangement which minimizes the energy. In heterogeneous catalysis, the minimum energy structure is obtained by means of the systematic and exhaustive adsorption of the reactants, products, and reaction intermediates on all the surface sites, where the structure with the lowest energy is considered (after some verifications commented in the next sections) as the most favorable structure. When an atom or a molecule (the adsorbate) approaches a surface, it will start to interact with the electronic states of the solid. At long distances, weak bonding, called physisorption, dominates. This is due to van der Waals forces, which are purely quantum mechanical in nature and which are relatively long ranged. Closer to the surface, when the electron clouds of the adsorbate and solid atoms begin overlapping, chemical bonds can be formed. This stronger form of adsorption is called chemisorption. The strength of the interaction is measured by the change in potential energy of the system at short and long distances:

$$\Delta E = E_{short} - E_{long} \quad (2.28)$$

where E_{short} is the energy of the system when the adsorbate is close to the surface, and E_{long} is the energy at infinite distance between surface and adsorbate. This ΔE is also known as the adsorption energy of the adsorbate:

$$E_{ads} = E_{X/surf} - (E_{surf} + E_X) \quad (2.29)$$

where $E_{X/surf}$ is the energy of the adsorbate either on the corresponding surface, E_{surf} is the energy of that surface, and E_X is the energy of the isolated adsorbate in asymmetric boxes of $9 \times 10 \times 11$ or $12 \times 13 \times 14$ Å dimensions, depending on the number of atoms in the particle or molecule. Note that for the adsorption of molecules on carbide-supported metal clusters, E_{Slab} refers to the relaxed surface with the attached cluster. Within this notation, the more negative the E_{ads} value is, the stronger the interaction becomes. If E_{ads} is negative, the interaction is favorable whereas positive values indicate

a repulsion between surface and the adsorbate specie. Large negative energy values imply a strong surface-reactant interaction, which is not appropriate according to the Sabatier's principle. Notwithstanding, small negative values mean weak interactions, which probably will lead the desorption of the reactant. Even if the VASP calculations are carried out at 0 K, the desorption energies could be related with an experimental measurement, the desorption temperatures, which can be calculated using the Redhead equation:¹⁶

$$\frac{E_b}{R \cdot T_d^2} = A \exp\left(\frac{E_b}{R \cdot T_d}\right) \quad (2.30)$$

where R is the ideal gases constant, T_d is the desorption temperature, A is the preexponential factor, and E_b is the desorption activation energy.

2.6.2 Diffusion

Diffusion is another step in heterogeneous catalysis. This process is based on the displacement of the adsorbate from the most stable surface site towards another reactive site. This new site could be symmetrically equivalent to the most favorable one, *i.e.*, the adsorption energy is the same, or it could be a different site with different environment, where the E_{ads} is slightly less favorable. This second case, thermodynamically unfavorable, normally occurs as a preliminary step of the recombination process, where the adsorbate firstly diffuses to a close site of the other adsorbate, and secondly, the recombination is produced.

Generally, the diffusion barriers for simple adsorbates on metal surfaces are not much higher than 0.5 eV.¹⁷ Furthermore, the diffusion is produced very fast at temperatures above 300 K where most industrial catalytic processes take place. However, the diffusion process depends on the surface coverage, since if there are no free sites available to diffuse into the surface, the energy barriers could change. It has

2.6 Energy and free energy diagrams

been found experimentally and by DFT calculations that for adsorption on metal surfaces, activation barriers for diffusion are typically of the order of 10–15% of their adsorption energy.¹⁷ It can be understood considering that during the diffusion process, the surface–adsorbate bond is not completely broken, and hence, only a small fraction of the maximum adsorption energy is lost when moving along the diffusion path. Inasmuch as, in general terms, the dissociation/recombination energy barriers are clearly superior to diffusion barriers, the last ones are not usually included on the energy diagram.

2.6.3 Transition state search

To complete the energetic pathway, it is necessary to know the higher energy state that links two minima along a path. This state is named transition state (TS) and it is a maximum in the direction which connects the reactant and product minima. At the same time, the TS must be a minimum in all the rest of directions, *i.e.*, the second derivative of the energy respect to the reaction coordinate is negative, but in all the other directions the second derivative is positive. The difference between the energy of the TS structure and the energy of the reactants structure is called as energy barrier (E_b), the energy cost to convert the reactants into products. Two different algorithms are implemented in VASP to search the TS structures; the Nudged Elastic Band (NEB) and the Dimer methods.¹⁸⁻²⁰

2.6.3.1 The nudged elastic band method

The nudged elastic band (NEB) method is based on the connection of several intermediate states (images) of the system. To carry out the search of the TS structure, the first step is the optimization of the reactants and products geometries (initial and final state of the path). Secondly, a set of images ($I_0, I_1, I_2, I_3 \dots I_N$), must be generated by

linear interpolation between the initial and final state. This is the most important step in the method, since the initial guess has to be good enough to converge to a realistic minimum energy path. Each image maintains equal spacing to neighboring images during the optimization, *i.e.*, the structure does not evolve towards a minimum because the optimization is constrained by the chain which connects the images. This constrained optimization is done by adding spring forces along the band between images and by projecting out the component of the force due to the potential perpendicular to the band. Once the optimization is performed, the largest energy image is selected as a TS candidate. Nevertheless, the global optimization of the highest energy image does not ensure that one to be the TS structure. Moreover, the generation of a set of images implies the hypothesis that the reaction mechanism follows this path, which may not be the lowest energy path, and consequently, different reaction ways must be studied. Furthermore, the calculation of the several images requires a large computational cost.[1]

2.6.3.2 The dimer method

The dimer method allows to start from any initial configuration and search for a nearby saddle point. This method can also be used to start from a minimum basin and search in random directions for saddle points. The dimer method is designed to search saddle points corresponding to unknown reaction mechanisms. In some simple systems, reaction endpoints can be guessed, and NEB can be used although some reactions often take place *via* unexpected mechanisms, which implies the calculations of many reaction paths, increasing the computational cost. In opposite to NEB method, Dimer works with two images (replicas) of the target system. These two replicas have

[1] *To optimize the NEB calculation, one should use the same number of cores per image than to optimize the reactants or products geometries. So, a NEB calculation with four images multiplies per four the number of cores respect to the optimization process.*

2.6 Energy and free energy diagrams

almost the same $3n$ coordinates but are displaced a small distance from a common midpoint. The saddle point search algorithm involves moving the dimer (rotation and translation) uphill on the potential energy surface. Each time the dimer is translated it has to be rotated in order to find the lowest curvature mode.

A tutorial including many options to provide the two images to search the TS structure is presented:

Option A) Starting from previous NEB run

The first step is running a NEB calculation using the optimized structures of reactants and products. However, the convergence of the NEB calculation is not necessary, since only a few steps are needed in order to obtain a geometry that could be close to the TS. From such a NEB calculation, just the highest energy image and the preceded one are needed. Later, we need to provide the direction of the first displacement of the dimer. The displacement can be carried out using the "*vtstscripts package*",²¹ where the direction of the displacement is from the preceding image to the highest energy image. In this manner, the preceding image is considered as the initial geometry of the calculation. However, this option presents some weak points. On one hand, the necessity to use the NEB method increases slightly the computational cost. On the other hand, as is commented before, NEB method does not ensure that selected pathway is the lowest in energy, thus, the selected images may not be close to the real TS structure.

Option B) Starting from reactants to products

In this case, a previous NEB calculation is not needed. Here, the structure of reactants and the products geometries could be used as images. By means of these two structures, the dimer displacement could be generated. The weak point of this option is

related with the fact that reactants and products are further away (*a priori*) from the TS structure than the intermediate replicas generated using NEB (for example), which could increase the computational time.

Option C) Starting from intermediate images between reactants and products

This option tries to improve the weak point of the B option. The first step is the optimization of reactants and products structures in order to know the evolution of the reaction. The next step is to modify the reactants structure considering the approximate bond distance of the supposed TS structure. To carry out this step, it would be very appropriate to consult in the literature the bond distances of TS structures, in order to generate a more similar geometry to the possible TS. The third and final step is to create the displacement. Considering the supposed TS structure generated on the last step, the displacement could be introduced generating a new structure, increasing, or decreasing the approximate TS bond distance in 0.05-0.10 Å. With these two structures, the displacement can be created using the "*vtstscripts package*". This option reduces the computational cost of the dimer calculation, avoiding the use of NEB method using a structure closer (*a priori*) to the real TS structure.

2.6.4 Vibrational frequencies

Vibrational spectroscopy is a common tool used to in heterogeneous catalysis, essential to determine and simulate the adsorption modes of the adsorbed molecules on a surface due to the comparison between experimental and calculated vibrations.²² From a computational point of view, the vibrational frequencies are indispensable to ensure that the optimized stationary point is a minimum (or a transition state) on the potential energy surface, to calculate the zero point energy correction and partition functions, and basic to obtain macroscopic properties such as enthalpy, entropy, Gibbs free energy and kinetic constants.

2.6 Energy and free energy diagrams

It is necessary to remark that vibrational calculations only have sense on the optimized geometries, where the forces of first derivatives of the potential energy are zero. Vibrational frequencies are related directly with the force constant (the second derivatives of the potential), and the mathematical analysis ensures that stationary point is minima if the derivatives are real, and a transition state if one of them is imaginary. Two different mathematical methodologies can be used to calculate the second derivatives of the potential. The analytical one calculates explicitly the second derivative of the potential, although VASP package uses the numerical one, where the Hessian matrix²³ is built with the finite differences of Cartesian coordinates and then, evaluates the second derivatives from the energy gradients variation in these displacements. The calculation of the vibrational frequencies is usually done under the harmonic approximation, obtaining the matrix of force constant for later diagonalization, where the eigenvalues are the vibrational frequencies and the eigenvectors are the vibrational normal modes.²⁴ Calculations have been performed neglecting the coupling between surface phonons and adsorbate vibrations. Thus, during the frequencies calculations, the surface atoms are frozen and only the vibrations modes of the adsorbates are computed.

$$\begin{pmatrix} \frac{d^2f}{dx_1^2} & \dots & \frac{d^2f}{dx_1 dx_n} \\ \vdots & \ddots & \vdots \\ \frac{d^2f}{dx_n dx_1} & \dots & \frac{d^2f}{dx_n^2} \end{pmatrix} \quad (2.31)$$

2.6.5 Zero-point energy correction (ZPE)

The idea of zero-point energy (ZPE) arises from the Heisenberg uncertainty principle, the fact that each particle has a wave associated with it imposes constraints on the ability to determine its position and momentum at the same time. For this reason, if the particle does not move, its moment and its position would be known simultaneously, violating the principle of uncertainty and therefore, there must be some kind of movement. This movement is related with the molecule nuclei vibration around their equilibrium position since the geometry optimization lead to an estimation of the electronic energy of the system without consider the zero-point vibrational energy. The total energy, including the energy of the zero point can be calculated as follows:

$$E_{ZPE} = E + \sum_i^{NMV} \frac{1}{2} h \nu_i \quad (2.32)$$

where E is the energy obtained by DFT, h is the Planck's constant and ν_i are the frequencies of the adsorbate. Importantly, frequencies that are significantly smaller than 1000 cm^{-1} contribute only little to ZPE, while frequencies larger than 1000 cm^{-1} can contribute to the DFT energy (Figure 2.6).

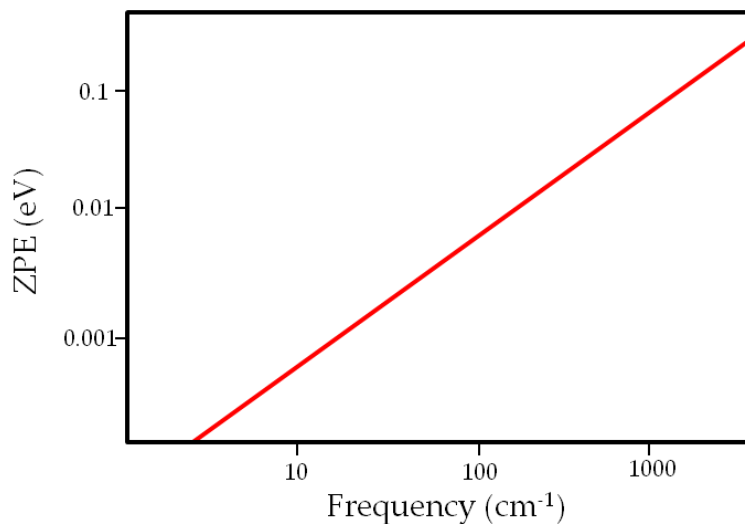


Figure 2.6: ZPE plotted as a function of vibrational frequency. The plot has been extracted from Ref. 17.

2.6.6 Gibbs free energy diagrams

The energy profiles built by means of the DFT energy (corrected by the ZPE) provides information about the reaction mechanism at 0 K of temperature. In order to provide better comparison with experiments, reaction mechanism including the Gibbs free energy (ΔG) can be performed considering the temperature and pressure effects. The Gibbs free energy has been calculated following the approximate procedure proposed by Nørskov et al.¹⁷ summarized in Eq. 2.33 below

$$\Delta G_A = \Delta H_A - T(S_A - S_R) \quad (2.33)$$

where the ΔG_A is the free energy of a step A, ΔH_A is the enthalpy change associated to the step A starting from the reactants R and, in absence of mechanical work, approximated by the corresponding change in total DFT energy, T is the absolute temperature, and S_A and S_R are the entropy of the products and reactants for step A. In practice, the entropy of gas phase and adsorbed species is computed by considering all contributions to the partition function with the assumption of rigid rotor and harmonic frequencies. For the reactants, intermediates, and products species, the entropy (S_{v_i}) contributions can be calculated as in Eq. 2.34,

$$S_{v_i} = -k_B \ln(1 - e^{\frac{-hv_i}{k_B T}}) \quad (2.34)$$

where v_i corresponds to the harmonic vibrational frequency of the i^{th} vibrational degree of freedom, and k_B and h are the Boltzmann and Planck constants, respectively. Large frequencies will only give small values of S_{v_i} , while small frequencies lead to larger values of S_{v_i} . To give an estimate of the magnitude of S_{v_i} , Figure 2.7 shows how ΔG for a single vibrational mode varies as a function of the frequency due to the vibrational entropy (ignoring the ZPE contribution). It can be seen that only frequencies that are around 50 cm^{-1} or lower give significant contributions to ΔG .

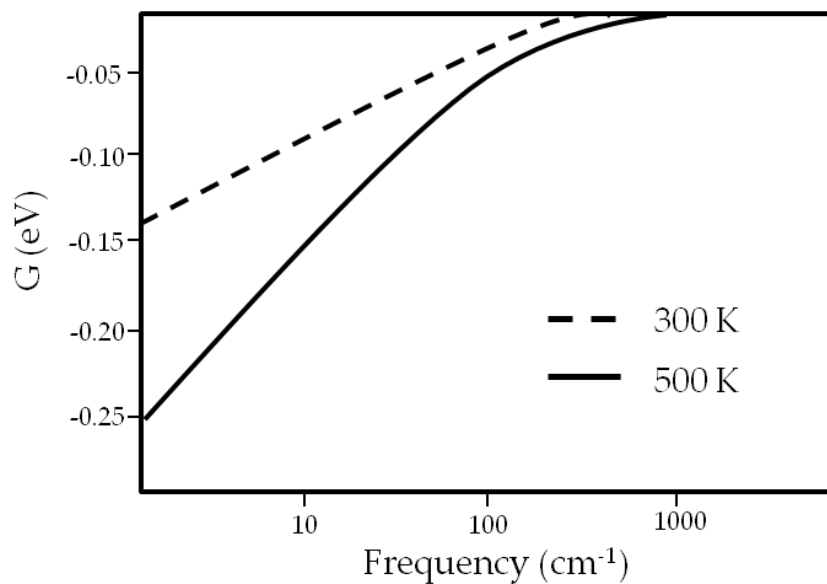


Figure 2.7: Gibbs free energy plotted as a function of vibrational frequency (ignoring the ZPE contribution) at 300 and 500 K of temperature.

Moreover, in the Nørskov's formalism, is customary to neglect the entropy of adsorbed species:

$$\Delta S_{ads}^{\circ} = S_{ads}^{\circ} - S_{gas-phase}^{\circ} \approx -S_{gas-phase}^{\circ} \quad (2.35)$$

which implies the main changes in going from the total energy to Gibbs free energy profiles involves adsorption and desorption steps. On Chapters 6 and 7, the effect of pressure and temperature is exhibited for the CO₂ hydrogenation towards methanol and WGS reactions.

2.7 Minima analysis

2.7.1 Density of states

Density of states (DOS) is the representation of the number of states occupied in a specified energy. The problem is the use of plane waves, that are delocalized functions, and consequently we know the states although we do not know whom they belong to. This can be solved projecting DOS into the spherical harmonics, which belong to each atom. These spherical harmonics orbitals have a specific radius, called Wigner-Seitz radius. Wigner-Seitz radius depends on the element and the chemical embedding of every atom.

On systems with a large number of atoms, such as a solid, the bands are continuous, where normally one can differentiate two, the valence band, where the orbitals are occupied below to Fermi level (E_F) and the conduction band, where the states are not occupied. The DOS is a useful tool to understand the electronic structure of a solid and to study the variation on the electronic structure after the adsorption of adsorbates, specially from the qualitative point of view.

2.7.2 Electronic localization function (ELF)

The electron localization function (ELF) is a model to study the position of the electrons in a system by means of their kinetic energy, based on the principle proposed by Becke,²⁵ where electrons with high kinetic energy are more delocalized whilst electrons with low kinetic energy are more localized. The ELF plots are very useful to determine the chemical bonds between the solid atoms and solid-adsorbate atoms. The scale of values is between 0 and 1, where values close to 0 means the electronic

delocalization and values close to 1 are related with electrons with low kinetic energy. Metallic bonds are identified through 0 values around the metallic atom and a high delocalization between them as one can be observed on the metallic clusters deposited on TiC (001) (Figure 2.8). The covalent bond is identified through the electron localization on the atoms and on the bond insomuch as the covalent bond is based on the electrons sharing (see TiC on Figure 2.8), in opposite to ionic bonds, where the values around the atoms are close to 1, although the 0 values is observed between the bonded atoms, since the electrons are localized on the atoms.

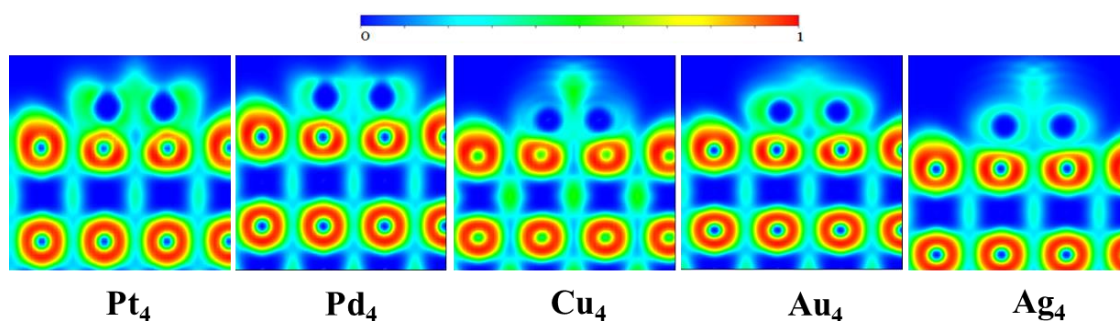


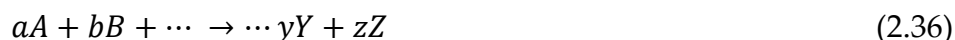
Figure 2.8: ELF plots of different metal clusters supported on TiC (001) surfaces. This picture has been extracted from Ref. 26.

2.7.3 Bader charges

Richard Bader developed an intuitive way of dividing molecules into atoms (Atoms in Molecules).²⁷ His definition of an atom is based purely on the electronic charge density. Bader uses what are called zero flux surfaces to divide atoms. Typically, in molecular systems, the charge density reaches a minimum between atoms and this is a natural place to separate atoms from each other. Besides, being an intuitive scheme for visualizing atoms in molecules, Bader's definition is often useful for charge analysis, which is useful to know the chemical properties of atoms in different environments. The atom charge is calculated by the difference between the electronic charge assigned to the system atoms and the number of valence electrons of the same atom when it is isolated, and of course, neutral.

2.8 Kinetic study

Chemical reactions kinetics deals with the rates of chemical processes. Any chemical process may be broken down into a sequence of one or more single-step processes. A study into the kinetics of a chemical reaction is usually carried out with one or both of two main goals: on the one hand, the analysis of the sequence of elementary steps giving rise to the overall reaction. *i.e.*, the reaction mechanism, and on the other hand, the determination of the reaction rate constant of every single-step.[2] The energy and free energy diagrams are excellent tools to determine the lowest energy pathway although the profiles does not provide information about the reaction rate. Chemical kinetics deals with the rate of chemical reactions and with how the rate depends on factors like temperature or products/reactants concentration. A chemical reaction could be expressed as:



where capital letters are referred to reactants and products, and lowercase letters are the stoichiometric coefficients. The velocity rate of the reaction is defined as the products formation rate or the products consume rate:

$$v_r = \frac{1}{a} \frac{d[A]}{dt} = \dots = \frac{1}{y} \frac{d[Y]}{dt} \quad (2.37)$$

where the values between square brackets are the concentration of reactants/products. The rate of an elemental reaction could be expressed as:

$$v_r = k[A]^a \quad (2.38)$$

where k is the rate coefficient and a is the reaction order. The empirical Arrhenius equation (2.39) correlates the coefficient k with the activation energy (E_a):

[2] The rate is defined as the number of times that the process occurs per site and time unit.

Theoretical background

$$k = A \exp\left(\frac{E_a}{k_B T}\right) \quad (2.39)$$

where A is the pre-exponential factor, k_B denotes the Boltzmann constant and T is the temperature. The rate of a surface elementary process can be calculated by using either the transition state theory (TST) or the collision theory (CT). Usually, TST values from DFT results constitute a better choice.²⁸

Transition state theory (TST) was developed simultaneously by H. Eyring^{29,30} and Evans and Polanyi.³¹ The TST theory describes the reaction *via* an activated complex located at the top of the energy barrier between reactants and products, i.e, the TS structure, and involves the knowledge of the activation energies and of the partition functions. The rate of a surface elementary process (r_i) can be calculated by the transition state theory (TST) and using values from DFT calculations. These rates can be calculated as Eq 2.40

$$r_i = \frac{k_B T}{h} \frac{Q_{TS}}{Q_r} e^{\frac{-\Delta G_i}{k_B T}} \quad (2.40)$$

where k_B denotes the Boltzmann constant, h the Planck constant, T is the temperature, Q_{TS} and Q_r are the harmonic partition function of transition state and reactants of the process i ,¹⁷ and ΔG_i is the Gibbs free energy barrier (including the ZPE correction) of process i . In practical terms, the equation of the rate constants is:

$$r_i = \frac{k_B T}{h} \frac{\prod_{i=1}^{i=3N-1} \left(1 - e^{-\frac{h\nu_i^{TS}}{k_B T}}\right)}{\prod_{i=1}^{i=3N} \left(1 - e^{-\frac{h\nu_i^R}{k_B T}}\right)} e^{\frac{-\Delta G_i}{k_B T}} \quad (2.41)$$

2.8 Kinetic study

where ν_i^{TS} are the vibrational frequencies of the TS structure and ν_i^R are the vibrational frequencies of reactants.[3]

[3] Note that to calculate the reverse rate constants, the vibrational frequencies are from the products. Products are the reagents of the reverse reaction.

2.9 Ab Initio Thermodynamics

Ab initio thermodynamics (AITD) has become standard tool in research on model catalysts. If we consider several structures for our system, AITD let to obtain the preferred one as function of pressure and temperature due to the calculation of free energies, *i.e.*, we can obtain macroscopic measures by means of DFT calculations (microscopic measures). As an illustrative example, Figure 2.9 gives the corresponding temperature-pressure (T,p) diagram, showing which Pd phase would be most stable in the whole range of experimentally accessible conditions from UHV to ambient pressure and on the basis of DFT data, if the surface were in full thermodynamic equilibrium with the surrounding oxygen gas phase.³² Note that although state of the art, some approximations during the DFT calculations like the present treatment of vibrational contributions to the free energies, as well as the uncertainty introduced by the finite basis set and the employed exchange-correlation functional, may well allow for errors in the phase boundaries of the order of ± 100 K and (depending on temperature) of up to several magnitude orders in pressures as is observed on Figure 2.9.

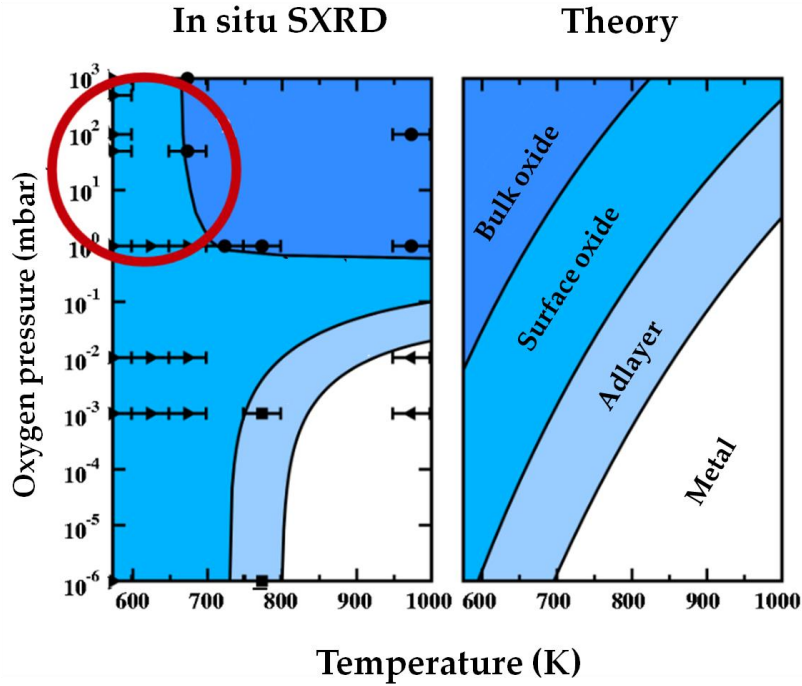


Figure 2.9: Adapted plot from reference 32 about the comparison of an experimental (left) and DFT (right) AITD for PdO. Plots are delimited by different colors, representing different phases of Pd and PdO; white zone represents bare Pd (100) surface, light blue and normal blue exhibit the O/Pd (100) adlayers with 0.25 and 0.5 ML of oxygen coverage respectively and dark blue zone depict the PdO bulk.

Using the AITD formalism proposed by Reuter and Scheffler^{33,34} one can estimate the surface free energy after the adsorption of whatever gas phase substrate (γ^{cover})—Gibbs adsorption energy per surface area— at different substrate coverages (N) and as a function of pressure (p) and temperature (T). The γ^{cover} can be calculated as the sum of the surface free energy of the clean surface (γ^{clean}) plus the Gibbs free energy related with the adsorption of the substrate atoms or molecules (γ^{ads}), both of them normalized per surface area, following Eq. 2.42:

$$\gamma^{\text{cover}}(T, p, N) = \gamma^{\text{clean}}(T, p) + \gamma^{\text{ads}}(T, p, N) \quad (2.42)$$

Theoretical background

Following Reuter and Scheffler, the surface free energy of a clean surface as function of p and T can be obtained using Eq. 2.43:

$$\gamma^{\text{clean}}(T, p) = \frac{1}{A} [G^{\text{clean}}(T, p) - \sum_i N_i \mu_i(T, p)] \quad (2.43)$$

where G^{clean} is the Gibbs free energy of the surface, $\mu_i(T, p)$ is the chemical potential of the i species which form the solid surface, N_i is the number of atoms of element i , and A is the total surface area. If we extend the formalism to study Mo_xC carbides surfaces, one can adapt Eq. 2.43 as shown on Eq. 2.44:

$$\gamma^{\text{clean}}(T, p) = \frac{1}{A} [G_{\text{Mo}_x\text{C}}^{\text{slab}} - N_{\text{C}} \mu_{\text{C}}(T, p) - N_{\text{Mo}} \mu_{\text{Mo}}(T, p)] \quad (2.44)$$

where $G_{\text{Mo}_x\text{C}}^{\text{slab}}$ is the Gibbs free energy of δ - MoC or β - Mo_2C surfaces and μ_{C} and μ_{Mo} are the chemical potentials of C and Mo atoms, normally obtained using graphite and Mo bulk references, respectively.^{35,36} The N_{C} and N_{Mo} terms are the number of C and Mo atoms on the surfaces. Here, is very important to remark that γ^{clean} value depends on the slab models used. The number of layers of the slab and, whether they are relaxed or not must remain equal during all the process since the relaxation criteria is directly related with the energy (or Gibbs free energy) value.

Aside, the adsorption Gibbs free energy [$\gamma^{\text{ads}}(T, p, N)$] can be estimated as in Eq. 2.45:

$$\gamma^{\text{ads}}(T, p, N_{\text{ADS}}) = \frac{1}{A} [G^{\text{cover}}(T, p, N_{\text{H}}) - G_{\text{Mo}_x\text{C}}^{\text{slab}}(T, p) - G^{\text{ADS}}(T, p)] \quad (2.45)$$

where $G^{\text{cover}}(T, p, N_{\text{ADS}})$ is the Gibbs energy of the covered surface at T , p , and containing N_{ADS} atoms of the adsorbate (ADS), and $G^{\text{ADS}}(T, p)$ the Gibbs energy of the

2.9 Ab initio thermodynamics

adsorbate molecule also at T and p . In addition, the $G^{cover}(T, p, N_{ADS})$ and $G_{Mo_xC}^{slab}(T, p)$ terms can be obtained from the DFT energy of the covered and clean slabs since

$$G^{cover}(T, p, N_H) = (E^{cover} - TS^{cover} + pV) \quad (2.46)$$

$$G_{Mo_xC}^{slab}(T, p) = (E_{Mo_xC}^{slab} - TS_{Mo_xC}^{slab} + pV) \quad (2.47)$$

where E^{cover} and $E_{Mo_xC}^{slab}$ are the total energy of the systems (covered and clean) obtained from the corresponding DFT based calculations (E^{total}) plus the zero point vibrational energy (E^0), S^{cover} and $S_{Mo_xC}^{slab}$ are the corresponding entropy values, and pV is the pressure-volume term. Both entropy and pV terms are usually neglected. Note, in fact, that for a cell dimension of $10 \times 10 \times 10 \text{ \AA}$ and an external pressure of at 10^5 Pa , the contribution of pV term is 1 meV, and a similar argument applies to the entropy term.^{33,34} Therefore, Gibbs free energy of clean and H covered surfaces are represented by the total energy of clean (E^{clean}) and covered (E^{cover}) surfaces obtained by DFT calculations, whereas the Gibbs energy for the gas considers all thermodynamic contributions. With these approximations one can estimate the adsorption surface free energy (γ^{ads}) as in Eq. 2.48:

$$\gamma^{ads}(p, T, N_{ADS}) \frac{1}{A} \left[E^{cover} - E_{Mo_xC}^{slab} - N_{ADS} \left(\frac{E_{ADS}}{2} + \frac{E_{ADS}^{ZPE}}{2} + \Delta\mu_{0_{ADS}} + k_B T \ln \frac{p}{p_0} \right) \right] \quad (2.48)$$

where E_{ADS} is the DFT total energy of adsorbate molecule in vacuum, E_{ADS}^{ZPE} is its zero point energy correction, k_B is the Boltzmann constant, p is the working pressure and $\Delta\mu_{0_{ADS}}$ is the chemical potential of the adsorbate calculated as in Eq. 2.49:

$$\Delta\mu_{0_{ADS}} = -\frac{1}{2} k_B T \ln Q_{Total} \quad (2.49)$$

where Q_{Total} is the sum of the electronic, rotational, translational, and vibrational partition functions of the gas phase adsorbate molecule. The definition in Eq. 2.49

Theoretical background

implicitly contains a dependence on p and T . In this point, note that to obtain the chemical potential of whatever gas phase adsorbate specie, is needed to perform excessive large number of calculations to cover the entire range of temperatures and pressures, which become this process as unapproachable since computational point of view. Nevertheless, to calculate this term, experimental values from thermodynamic tables could be used.³⁷

2.10 Computational Details

In the previous sections we established the method used to carry out all the calculations in this thesis. To obtain generally uniform results, certain parameters must be controlled: the ideal cut-off on the plane wave expansion, the number of \mathbf{k} -points needed to converge the energy, and the electronic and ionic relaxation convergence criterion. The valence electron density is expanded in a plane-wave basis set with a cut-off of 415 eV for the kinetic energy and the effect caused by the core electrons on the valence region is described by the projector augmented wave method of Blöchl,¹⁴ as implemented by Kresse and Joubert.³⁸ The threshold for electronic relaxation was less than 10^{-5} eV and relaxation of the atomic positions was allowed until forces acting on the atoms are always smaller than $0.01 \text{ eV } \text{\AA}^{-1}$. Integration in the reciprocal space was carried out by means of a $3 \times 3 \times 1$ Monkhorst-Pack³⁹ scheme for cubic δ -MoC (001) nonpolar surfaces and a $5 \times 5 \times 1$ grid for polar β -Mo₂C (001)-Mo and β -Mo₂C (001)-C surfaces in the case of (2×2) supercells. The use of (3×3) supercells involves an increase in the number of atoms and cell dimensions and, consequently, the number of \mathbf{k} -points was reduced to Γ -point for cubic and orthorhombic surfaces. Final adsorption minima and TS structures have been characterized *via* frequency analysis. This is carried out by construction and diagonalization of the relevant block of the Hessian matrix whose elements are calculated by finite difference of analytical gradients using individual displacements of 0.03 \AA in each cell direction including only elements of the Hessian matrix involving the displacement of atoms in adsorbates are considered.

Adsorption of metal adatoms, metal clusters, reactants, products, and reaction intermediate molecules, was studied on the relaxed slab surface. The adsorption energy (E_{ads}) of a moiety has been calculated according to equation 2.29.

The cohesion energy (E_{coh}) of the gas phase M_n particles is defined as in Eq. (2.51)

Theoretical background

$$E_{\text{coh}} = \frac{E_{M_n} - n E_M}{n} \quad (2.51)$$

where E_{M_n} is the energy of a M_n isolated metal particle.

Starting from E_{ads} value, one can define the adhesion energy (E_{adh}) of the M_n clusters on the Mo_xC surfaces as in Eq. 3

$$E_{\text{adh}} = E_{\text{ads}} - E_{\text{def}}^{\text{surf}} - E_{\text{def}}^{M_n} \quad (2.52)$$

where $E_{\text{def}}^{\text{surf}}$ is the difference between the energy of the isolated surface at the relaxed equilibrium geometry and at the geometry adopted upon M_n adsorption, and $E_{\text{def}}^{M_n}$ is the energy difference for the isolated M_n particle at the optimum geometry at the surface and the one corresponding to the gas phase structure.

2.11 Experimental details

As mentioned, all the experiments in this thesis were performed in the research group of Dr. José Rodríguez at the Brookhaven National Laboratory, in New York. In this section, I want to describe the experimental methods and preparation of molybdenum carbide surfaces.

Experiments were carried out on polycrystalline MoC and on a Mo and C terminated Mo₂C(001) surface.⁴⁰ Ion bombardment and subsequent annealing at 1000 K were used to clean and prepare the Mo₂C (001) surface.⁴¹ Images of scanning tunneling microscopy indicate that under these conditions this surface has the expected bulk-terminated (1×1) orthorhombic periodicity,⁴¹ with two or three rotationally misaligned orthorhombic domains. The surface of MoC examined in this study is best described as polycrystalline.⁴⁰ Surface impurities were removed by Ar⁺ sputtering, and a C/Mo ratio close to 1 was restored by exposing this surface to C₂H₂ or C₂H₄ at 800-900 K.⁴⁰ Several attempts were made to prepare well-defined surfaces of δ-MoC oriented along the (001) plane of this carbide. However, it was not possible to prepare an ideal δ-MoC (001) surface. The preparation of this particular surface is very difficult due to the complex phase diagram of MoC.⁴² The experimental data were collected in a set-up that combined an ultra-high vacuum (*UHV*) chamber for surface characterization and a micro-reactor for catalytic tests.⁴³ In the studies of CO₂ hydrogenation, the sample was transferred to the reactor at ~300 K, then the reactant gases, 0.049 MPa (0.5 atm) of CO₂ and 0.441 MPa (4.5 atm) of H₂, were introduced and the sample was rapidly heated to the reaction temperature (500, 525, 550, 575, and 600 K). Product yields were analyzed by a gas chromatograph.^{44,45} This set of pressure and temperature conditions is identical to those used in previous studies for CO₂ hydrogenation on Cu/ZnO (000 $\bar{1}$),⁴⁵ a model of commercial catalysts for methanol production, and ZnO/Cu (111).⁴⁶ The data was

Theoretical background

collected at intervals of 15 min up to a total reaction time of 270 min. The number of molecules produced in the catalytic tests was normalized by the active area exposed by the sample and the total reaction time. The number of molecules produced was normalized by the active area exposed by the sample.⁴⁷ In our reactor a steady-state regime for the production of H₂ and CO₂ was reached after 2-3 minutes of reaction time. The kinetic measurements were done at the limit of low conversion (< 5%). The CO gas was cleaned of any metal carbonyl impurity by passing it through purification traps.⁴⁷ For the WGS reaction, the sample was transferred to the batch reactor at ~ 300 K, then the reactant gases were introduced (20 Torr of CO and 10 Torr of H₂O) and the sample was rapidly heated to the reaction temperatures investigated (410, 425, 435, 450, and 465 K).

Metallic copper and gold were vapor-deposited on the MoC (001) and Mo₂C (001) surfaces at 300 K. The Cu or Au dose consisted of a resistively heated W basket with a drop of ultrapure Cu or Au inside.⁴⁸ Initially, the flux of each doser was calibrated by taking thermal desorption spectra for the desorption of Cu or Au from a Mo (100) substrate.⁴⁹

1.6 References

-
- [1] L. H. Thomas, *Proc. Cambridge Phil. Soc.*, **1927**, 23, 542.
- [2] E. Fermi, *Zeitschrift für Phys.*, **1928**, 48, 73.
- [3] P. C. Hohenberg and W. Kohn, *Phys. Rev.*, **1964**, 136, 864.
- [4] F. Viñes, *PhD Thesis*, 2008.
- [5] J. R. d. S. Politi, F. Viñes, J. A. Rodriguez, F. Illas, *Phys. Chem. Chem. Phys.*, **2013**, 15, 12617.
- [6] P. Janthon, S. M. Kozlov, F. Viñes, J. Limtrakul, F. Illas, *J. Chem. Theo. Comput.*, **2013**, 9, 1631.
- [7] P. J. Stephens, F. J. Devlin and M. J. Frisch, *J. Phys. Chem.*, **1994**, 98, 11623.
- [8] J. Paier, M. Marsman and G. Kresse, *J. Chem. Phys.*, **2007**, 12, 024103.
- [9] S. Grimme, *J. Comput. Chem.* **2004**, 25, 1463.
- [10] S. Grimme, *J. Comput. Chem.*, 2006, **27**, 1787.
- [11] S. Grimme, J. Antony, S. Ehrlich and H. Krieg, *J. Chem. Phys.*, **2010**, 132, 154104.
- [12] D. Vanderbilt, *Phys. Rev. B*, **1990**, 41, 7892.
- [13] D. R. Hamman, M. Schlüter and C. Chiang, *Phys. Rev. Lett.*, **2007**, 99, 235502.
- [14] P. E. Blöchl, *Phys. Rev. B*, **1994**, 50, 17953.
- [15] F. Bloch, *Z. Phys.*, **1929**, 57, 545.
- [16] P. A. Redhead, *Vacuum* 1962, **12**, 203.
- [17] Nørskov, J. K.; Studt, F.; Abild-Pedersen, F.; Bligaard, T. *Fundamental Concepts in Heterogeneous Catalysis* Wiley, New Jersey, 2014.
- [18] G. Henkelman and H. Jónsson, *J. Chem. Phys.*, **2000**, 113, 9978.
- [19] G. Henkelman, B. P. Uberuaga, and H. Jónsson, *J. Chem. Phys.*, **2000**, 113, 9901.
- [20] G. Henkelman and H. Jónsson, *J. Chem. Phys.*, **1999**, 111, 7010.
- [21] <http://theory.cm.utexas.edu/vtsttools/scripts.html>
- [22] P. Hollins, J. Pritchard, *Prog. Surf. Sci.*, **1985**, 19, 275.
- [23] J. Marsden and A. Tromba, *Cálculo vectorial*, Madrid, 5 edition, 2004.
- [24] P. Atkins, *Química Física*, Panamericana, Madrid, 8 edition, 2008.
- [25] A. D. Becke, K. E. Edgecombe, *J. Chem. Phys.*, **1990**, 92, 5397.
- [26] S. Posada-Pérez, F. Viñes, J. A. Rodriguez and F. Illas, *Top. Catal.*, **2015**, 58, 159.
- [27] R. Bader, *Atoms in Molecules: A quantum Theory*, Oxford University Press, 1994.
- [28] A.P.J. Jansen, *An introduction to kinetic Monte Carlo simulations of surface reactions*, *Lecture Notes in Physics*, Springer-Verlag, Heidelberg, Germany, 2012
- [29] H. Eyring, *J. Chem. Phys.*, **1935**, 3, 107.
- [30] H. Eyring, *Trans. Faraday Soc.*, **1938**, 34, 41.
- [31] M. G. Evans and M. Polanyi, *Trans. Faraday Soc.*, **1935**, 31, 875.
- [32] E. Lundgren, J. Gustafson, A. Mikkelsen, J. N. Andersen, A. Stierle, H. Dosch, M. Todorova, J. Rogal, K. Reuter and M. Scheffler, *Phys. Rev. Lett.*, **2004**, 92, 046101.
- [33] K. Reuter and M. Scheffler, *Phys. Rev. B*, **2002**, 65, 035406.
- [34] K. Reuter and M. Scheffler, *Phys. Rev. Lett.*, **2003**, 90, 046103.
- [35] T. Wang, X. Tian, Y. Yang, Y.W. Li, J. Wang, M. Beller and H. Jiao, *Surf. Sci.*, **2016**, 651, 195.

Theoretical background

- [36] T. Wang, X. Liu, S. Wang, C. Huo, Y.W. Li, J. Wang and H. Jiao, *J. Phys. Chem. C* **2011**,115, 22360.
- [37] D. R. Stull, a. H. P., *JANAF thermochemical Tables, 2nd Ed.* U. S. National Bureau of Standards: U.S. EPO, Washington D. C: 1971.
- [38] G. Kresse and D. Joubert, *Phys. Rev. B*, **1999**, 59, 1758.
- [39] H. J. Monkhorst and J. D. Pack, *Phys. Rev. B: Solid State*, **1976**, 13, 5188.
- [40] P. Liu, J.A. Rodriguez, T. Asakura, J. Gomes and K. Nakamura, *J. Phys. Chem. B*, **2005**, 109, 4575.
- [41] T.P. Saint Clair, S.T. Oyama, D.F. Cox, S. Otani, Y. Ishizawa, R.L. Low, K. Fukui, Y. Iwasawa, *Surf. Sci.* **1999**, 426, 187.
- [42] J.G. Chen, *Chem. Rev.* **1996**, 96, 1447.
- [43] A. B. Vidal, L. Feria, J. Evans, Y. Takahashi , P. Liu, K. Nakamura, F. Illas, J. A. Rodriguez, *J. Phys. Chem. Lett.* **2012**, 3, 2275.
- [44] J. Yoshihara and C.T. Campbell, *J. Catal.* **1996**, 161, 776.
- [45] Y. Yang, J. Evans, J.A. Rodriguez, M.G. White and P. Liu, *Phys. Chem. Chem. Phys.* **2010**, 12, 9909.
- [46] S. Senanayake, P.J. Ramirez, I. Waluyo, S. Kundu, K. Mudiyansele, Z.-Y. Liu, Z. Liu, S. Axnanda, D.J. Stacchiola, J. Evans and J.A. Rodriguez, *J. Phys. Chem. C*, **2016**, 120,
- [47] J. A. Rodriguez, P. Liu, J. Hrbek, J. Evans and M. Perez, *Angew. Chem. Int. Ed.*, **2007**, 46, 1329.
- [48] J. A. Rodriguez, P. Liu, T. Jirsak, F. Illas, *J. Catal.*, **2013**, 307, 162.
- [49] J. A. Rodriguez and M. Kuhn, *Surf. Sci.*, **1995**, 330,1657.

CHAPTER THREE

Computational Models for Molybdenum Carbide based systems

3.1 Introduction

In the field of computational catalysis, most of studies are carried out using the slab approach, which is able to simulate the experimental catalytic tests performed on surfaces. By means of the slab approach, is possible to detail the reaction mechanism and each elementary step of the reaction. Furthermore, is possible to investigate how catalytic activity changes with the exposed surface and the surface coverage.

The main aim of this thesis is to investigate from a computational point of view (supported by experiments), green chemistry reactions catalyzed by different molybdenum carbide (001) surfaces, to provide explanations about the catalyst activity, selectivity, and stability. To be able to perform this study, the modeling of catalyst surfaces is an essential step. In this chapter, we want to describe in detail the slab models of molybdenum carbides surfaces used in this thesis. For this, the results of previous works accomplished before the beginning of this thesis will be summarized to shy a little light in the model's choice.

Furthermore, transition metal carbides enhance the catalytic properties of supported metal particles, being excellent supports for the dispersion of metals.¹⁻³ In a set of pioneer studies, Roldan-Cuenya and co-workers investigated the interaction of Au nanoparticles with TiC films.¹ The Au nanoparticles did not wet well the carbide surface, displaying the tendency to form three-dimensional (3D) aggregates at medium and large coverages.¹ These systems were able to catalyze the low-temperature oxidation of CO. This motivated a detailed study of the interaction of Au with TiC (001),⁴ where STM and XPS studies revealed the formation of 2D and 3D Au particles over the carbide surface.^{4,5} Experimental data for the Au/TiC (001) systems indicated that the maximum chemical activity is found for very small coverages ($\theta < 0.2$ monolayer) of the admetal,⁵ as is displayed in Figure 3.1, where the importance of the metal nanoparticles size and coverage respect to the amount of

products obtained for the CO₂ hydrogenation reaction is reported. Figure 3.1a reveals that the major amount of products are obtained when the metal coverage is low, and Figure 3.1b displays that the size concentration of small particles is superior than the big ones at low coverage. From an experimental point of view, the synthesis of small metal nanoparticles on TiC (001) is very difficult, whereas to support big nanoparticles or metal monolayers is significantly easier, although these kinds of systems do not have interest owing to their low catalytic power.

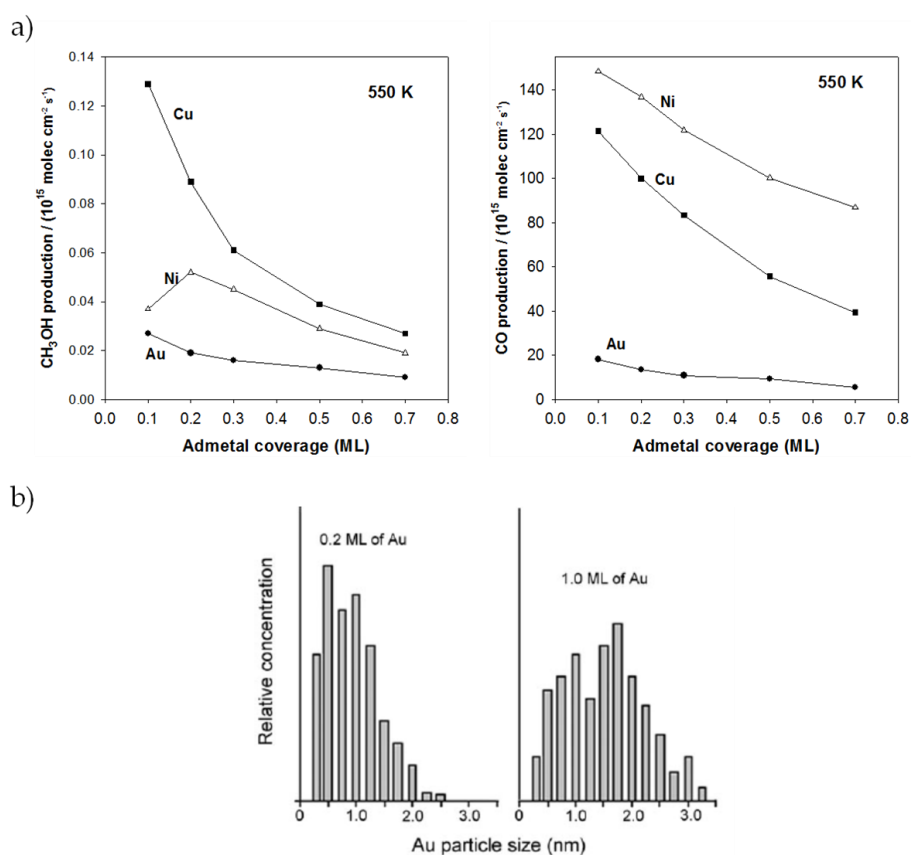


Figure 3.1: a) Experimental Methanol (left) and CO (right) production depending of metal nanoparticles coverage on TiC (001) surface at 550 K and b) STM plot of Au nanoparticle size supported on TiC (001) depending of two different coverages.

Nevertheless, the experimentalists have not found these difficulties using molybdenum carbides, since they do not require special conditions for their synthesis. Thus, a systematic and extensive computational study about small metal clusters (Cu and Au) deposition on molybdenum carbide surfaces must be

3.1 Introduction

accomplished in order to model the metal/support systems, in order to get proper models to describe the experimental results, considering the agreement between accuracy and computational cost.

Next Chapters of this thesis discuss the experimental and theoretical results associated to CO₂ hydrogenation and water gas shift reactions. It should be borne in mind that from a computational point of view, we only have modeled the most promising catalysts proposed by experimentalists for each reaction. The Cu supported clusters on cubic and orthorhombic phases of molybdenum carbides were modeled to investigate exhaustively the reaction mechanisms for CO₂ hydrogenation towards methanol, in order to study the catalyst's activity and the effect of the surface termination in the case of orthorhombic Mo₂C (001). On the other hand, the complete and exhaustive study performed to investigate the CO₂ hydrogenation reaction on cubic and orthorhombic molybdenum carbide (001) surfaces was essential to discover some catalyst's features related with the stoichiometry and morphology, which has a critical role on the catalyst performance. The reached conclusions on CO₂ hydrogenation study promoted the use of molybdenum carbides with metal/carbon ratio of one (cubic δ -MoC (001)). Thereby, to investigate the reaction mechanism of WGS, only cubic δ -MoC (001) surfaces were used. The experiments revealed that the deposition of small Au particles increased drastically the quantity of products, and consequently, the Au/ δ -MoC (001) system was model from a computational point of view.

3.2 Modeling concepts

The key parameters entering the construction of a slab model are the slab thickness (the number of layers), the lateral repeat dimension (which determines the minimum separation, or coverage, of adsorbates), and the vacuum spacing. Optimal choices depend on the problem of interest.

To determine the positions of atoms in the slab, the bulk lattice constant and atomic positions must be optimized using computational parameters consistent with those to be used later for the surface. The bulk structure is then truncated at the desired surface termination. To compensate for the finite thickness of the slab, the coordinates of some number of layers on one side of the slab are often fixed to their bulk positions, thus mimicking the constraints of a semi-infinite surface. It costs energy to create a surface, and the surface atoms will generally relax in some directions to minimize this energy. Using DFT, it is possible to quantify this relaxation in at least two ways. On the one hand, relaxed bond lengths can be compared with the ideal bulk bond lengths. On the other hand, the surface energy, γ , can be calculated for the system with atoms fixed in the bulk positions ($E_{slab}^{unrelaxed}$) and again, with the relaxed surface (E_{slab}), and these energies can be compared. The surface energy can be calculated for a symmetric slab (both sides of the slab either fixed or relaxed, but not one of each) according to equation 3.1:

$$\gamma = \frac{E_{slab} - nE_{bulk}}{A} - \frac{E_{slab}^{unrelaxed} - nE_{bulk}}{2A} \quad \text{Eq. (3.1)}$$

where E_{slab} is the energy of the relaxed slab, with half layers relaxed and the other held fixed, E_{bulk} is the energy of optimized bulk, n represent the number of bulk structural units, $E_{slab}^{unrelaxed}$ is the energy of the bulk-terminated slab, and A is the exposed surface area per unit cell. Note, however, some surface terminations are polar, and so, the calculation of the surface energy of differently terminated surfaces

3.2 Modeling concepts

is, *a priori*, unfeasible.⁶ To supply this difficulty, the computed of cleavage energies proposed by Moreira *et al.*⁷ is a good method to obtain the surface energy.

The thickness of the slab and the number of layers fixed or relaxed will also influence the surface energy. Thus, surface energy is one method for determining an appropriate slab setup by calculating the surface energy for several different slab thickness or number of relaxed layers and finding the slab where the surface energy converges and reaches some limiting value.

On the other hand, the supercell size is also an important aspect to select, in order to avoid possible lateral interactions between adsorbates and/or supported clusters. The cluster/adsorbate size determines the lateral repeat dimension of the supercell, to avoid possible cluster-cluster and/or adsorbate-adsorbate interactions. Therefore, as is explained in next sections, all these key parameters were considered with the aim to obtain suitable models to describe the experimental observations. To properly investigate the interaction of metal clusters with molybdenum carbide surfaces, equations 2.29, 2.51, and 2.52 were used. The logic for the energy decomposition of the metal-support interaction is sketched on Figure 3.2.

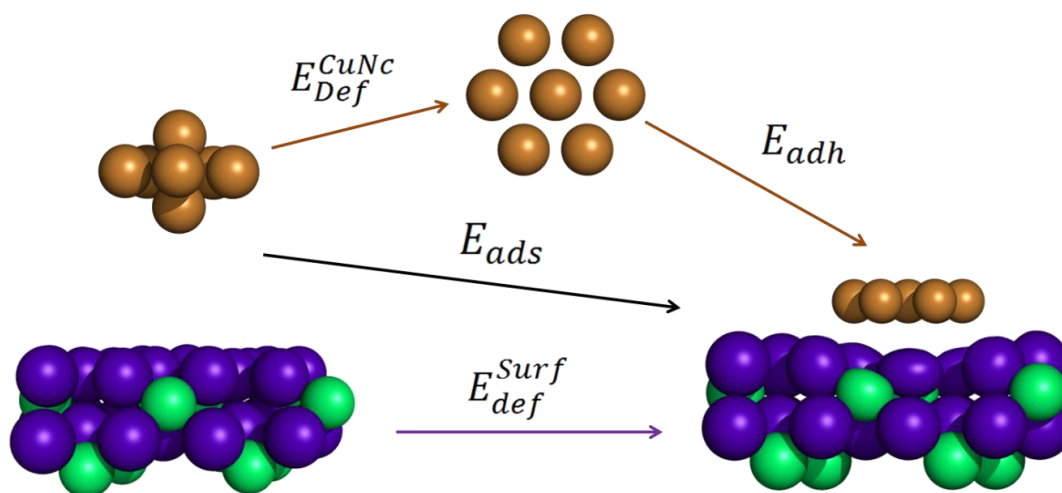


Figure 3.2: Visual representation of adhesion, adsorption, and deformation energies.

3.3 Modeling bare molybdenum carbide surfaces

3.3.1 Previous works

The experimental phase diagrams of molybdenum carbides showed that stoichiometries with metal/carbon ratio of one and two are the most stable ones.^{8,9} Experimental and theoretical studies¹⁰⁻¹² exhibited that orthorhombic β -Mo₂C phase is more stable than hexagonal α -Mo₂C. It is worth pointing out that here we follow the notation convention defined by the Joint Committee on Powder Diffraction Standards (JCPDS) data files,¹³ in which hexagonal and orthorhombic Mo₂C are denoted α -Mo₂C and β -Mo₂C, respectively. Note, however, that some authors in the literature refer to orthorhombic Mo₂C as α -Mo₂C,¹⁴⁻¹⁶ following an early definition by Christensen.¹⁷ The metal atoms in β -Mo₂C are in slightly distorted hexagonal close-package arrangement, with carbon atoms occupying ordered positions in lattice octahedral voids. The bulk coordination of Mo is three and the bulk coordination of carbon is six.¹⁸ With respect to the MoC, hexagonal α -MoC and face centered cubic δ -MoC phase can be synthesized. Several studies at different DFT levels have been performed to study the bulk phases.¹⁹⁻²⁴ As long as surfaces study were concerned, the number of systematic works was scarce, and moreover, at different DFT level than the bulk studies.²⁵⁻²⁷ Fortunately, the work of Politi *et al.*,²⁸ contributed to the modeling of different phases and stoichiometries of molybdenum carbides using the same level of theory (PBE).

The work of Politi *et al.*, optimized the k-points mesh for different supercells and the number of layers, concluding that surface properties can be described properly using four layers models, with the two outmost layers were fully relaxed (2+2 approximation). In the case of β -Mo₂C, our experimental partners synthesize single crystal orthorhombic Mo₂C (001) surfaces although the computational calculations predicted that the nonpolar (011) surface is the most stable one. Concerning to molybdenum carbides with metal/carbon ratio of one, the (001)

3.3 Modeling bare molybdenum carbide surfaces

surface of δ -MoC was reported as the most stable surface. This result acquires a great importance on the computational simulations given that from an experimental point of view, δ -MoC is polycrystalline. The DFT calculations revealed that (001) is the most exposed surface termination. In relation to the supercell size, the (1 \times 1) was considered too small, since only contains four atoms *per* layer on δ -MoC (001) (two C and two Mo atoms) and β -Mo₂C contains four Mo atoms on Molybdenum layers and two C atoms on the C layers. Thus, (2 \times 2) and (3 \times 3) supercells were considered. The (2 \times 2) supercells for orthorhombic β -Mo₂C contain 32 atoms of molybdenum and 16 atoms of carbon. The cell dimensions are 12.12 \times 10.46 \times 20.75 Å, as is displayed on Figure 3.3. Otherwise, Figure 3.4 exhibits the (3 \times 3) supercells, which contain 72 atoms of molybdenum and 36 atoms of carbon and the supercell dimensions are 18.18 \times 15.69 \times 20.75 Å. Cubic δ -MoC (001) (2 \times 2) supercell, see Figure 3.5a, contains 32 carbon and 32 molybdenum atoms. The cell dimensions are 8.75 \times 8.75 \times 18.75 Å. On the other hand, the (3 \times 3) supercell contain 64 carbon and 64 molybdenum atoms, and the cell dimensions are 13.11 \times 13.11 \times 18.75 Å, see Figure 3.5b.

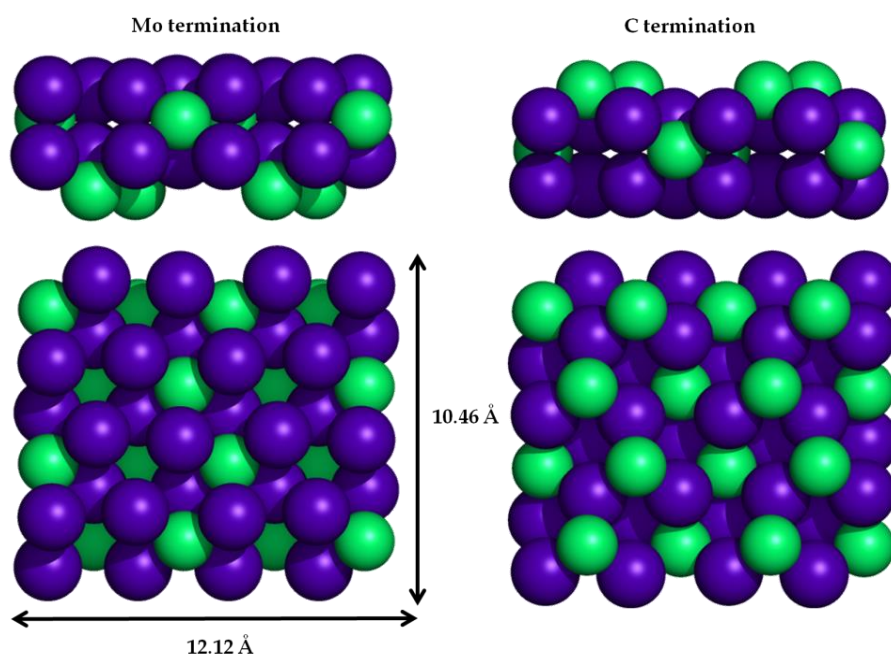


Figure 3.3: Sketches of (2 \times 2) supercells of β -Mo₂C (001) surfaces with the two possible terminations. Showing side views (top) and top views (bottom). Green and violet balls represent carbon and molybdenum atoms respectively.

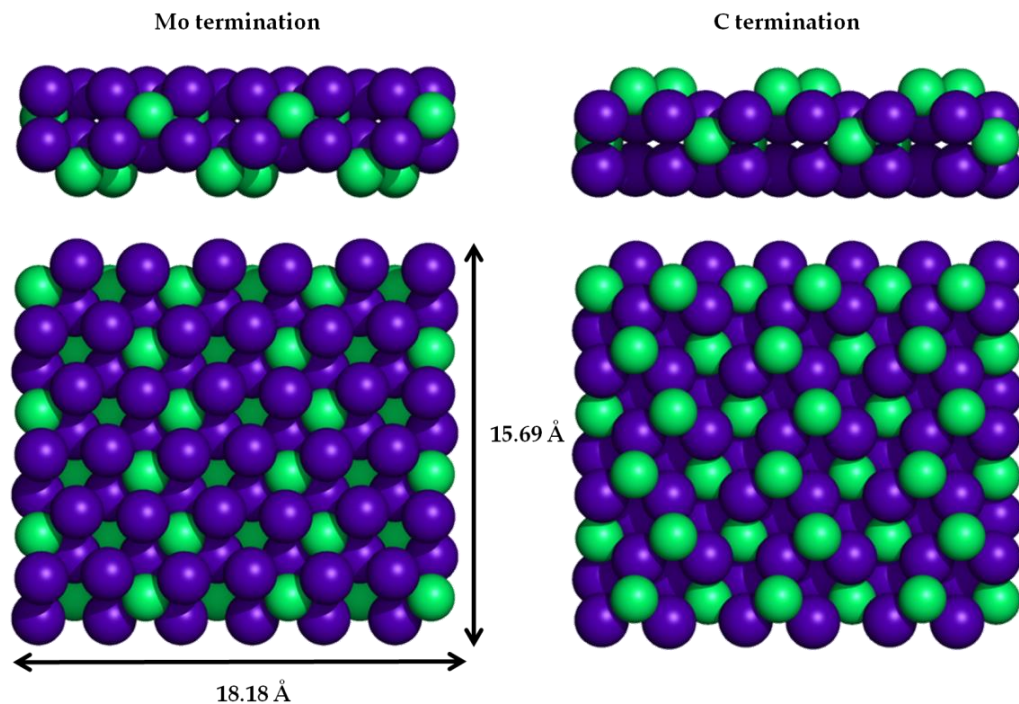


Figure 3.4: Sketches of (3×3) supercells of β -Mo₂C (001) surfaces with the two possible terminations. Showing side views (top) and top views (bottom).

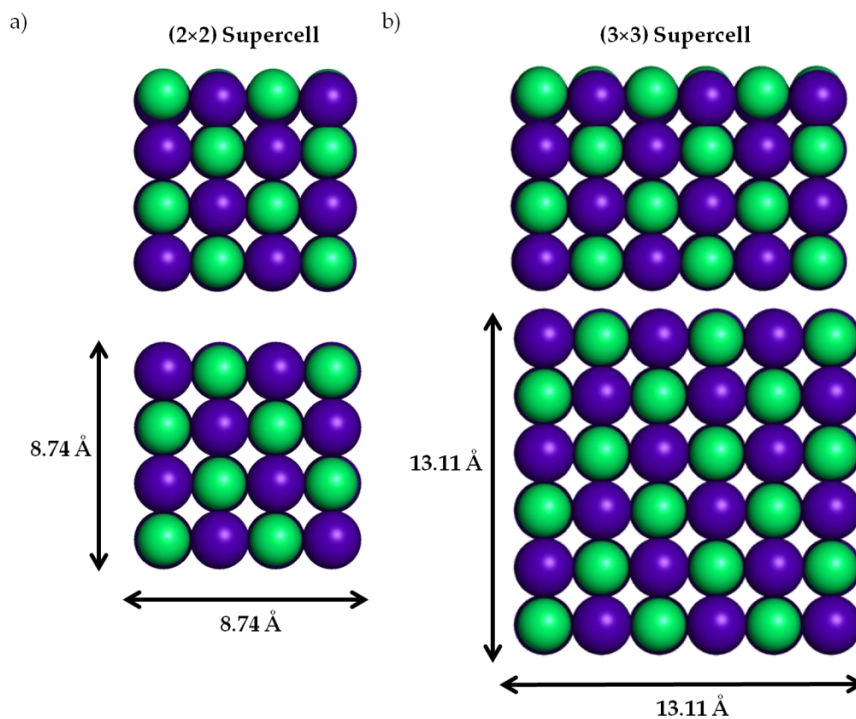


Figure 3.5: Sketches of a) (2×2) and b) (3×3) supercells of δ -MoC (001). Showing side views (top) and top views (bottom).

3.3.2 Adsorption sites on Mo_nC (001) surfaces

With the purpose of a detailed assessment of the adsorption capability of these surfaces, we explored different sites for reactants, intermediates, and products adsorption, which are presented on Figure 3.6.

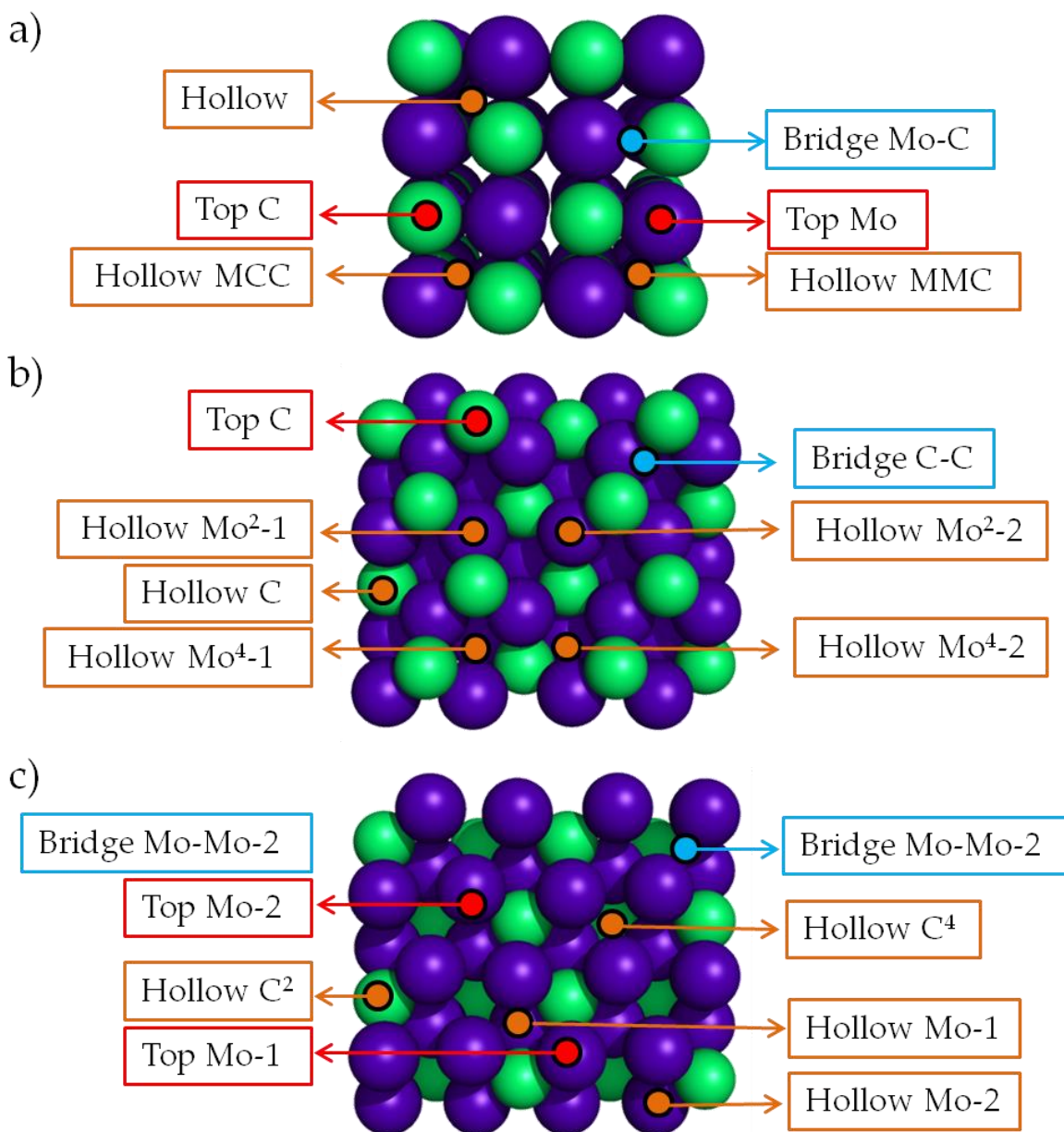


Figure 3.6: Sketches of the different adsorption sites tested for the three studied surfaces. Images show top views of a) $\delta\text{-MoC}$, b) $\beta\text{-C}$, and c) $\beta\text{-Mo}$ (001) surfaces. Red, orange, and blue marks denote Top, Hollow, and Bridge adsorption sites, respectively.

We defined top sites where the adsorbate sits on-top of a surface atom. This site is present in all the studied surfaces; for instance, Top C is found on δ -MoC (001) and β -Mo₂C (001)-C surfaces (hereafter referred as β -C) and Top Mo in δ -MoC (001) and β -Mo₂C (001)-Mo surfaces (hereafter referred as β -Mo). Bridge sites are considered when the contact is above the bond between two surface atoms and can involve either Mo-C, C-C, or Mo-Mo bonds; on Hollow, the adsorbate is binding simultaneously to many surface atoms. Particularly, on β -Mo₂C (001), there are different hollow sites depending whether the molecule is aiming to carbon or molybdenum atoms of the inner layers. For these reason, a number after the name of the site is added to differentiate topologically distinct sites in the same layer, whereas a super index is added to indicate the layer of the hollow site, the second (2) or the fourth (4).

3.3.3 Adsorption tests on Mo_nC (001) surfaces

Following the modeling concepts discussed on section 3.2, several tests were performed to investigate the proper supercell size of cubic δ -MoC and orthorhombic β -Mo₂C (001) surfaces. Different test molecules as CO₂, CO, and H₂, were used to compare the adsorption energies on (2×2) and (3×3) supercells. Note that Table 3.1 reveals that supercell size does not play significant role on the adsorption energy value, *i.e.*, a (2×2) supercell is a properly model to describe the adsorbate-catalysts interaction.

Table 3.1: Adsorption energies (eV) of different molecules on (2×2) and (3×3) supercells of studied molybdenum carbide (001) surfaces. Values of (3×3) supercell are in parenthesis.

	$E_{\text{ads CO}_2}$ /eV	$E_{\text{ads CO}}$ /eV	$E_{\text{ads H}_2}$ /eV
β -Mo	-1.39 (-1.36)	-2.26 (-2.30)	-0.67 (-0.69)
β -C	-0.06 (-0.06)	-1.93 (-1.94)	-0.02 (-0.10)
δ -MoC	-0.85 (-0.85)	-1.91 (-1.97)	-0.46 (-0.49)

3.4 Modeling metal clusters on molybdenum carbide surfaces

The previous works discussed above strongly suggests that small metal nanoclusters supported on transition metal carbides can exhibit enhanced reactivity towards many reactions. As a first mandatory step to investigate the chemical reactivity of these model catalysts, either from theory or experiments, information regarding the nature of the metal-support interaction and the structure of supported metal clusters was required. This section aims at providing this information through a systematic computational study of Cu and Au nanoclusters (hereafter referred to as Cu_n and Au_n) deposited on $\beta\text{-Mo}_2\text{C}$ (001) molybdenum and carbon termination and $\delta\text{-MoC}$ (001) surfaces.

3.4.1 Cu nanoclusters supported on Mo_nC (001) surfaces

This section deals with the geometric and electronic structure of different Cu_n nanoclusters encompassing the two and three-dimensional structures proposed by Jug *et al.*,²⁹ Jaque *et al.*,³⁰ as well as other possible structures dictated by the morphology of the underlying substrate. This is followed by the results for the Cu_n particles supported on the different surfaces.



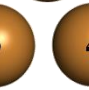



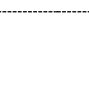
























3.4.1.1 Isolated Cu nanoclusters

In this subsection, the study of isolated Cu nanoclusters is reported with emphasis on previous Cu_n structures proposed in the literature.³¹⁻³⁴ Several other candidate structures were also considered on the basis of the analysis of different possible surface adsorption sites on each particular studied surface, of previous studies about Cu atoms supported on cubic $\delta\text{-MoC}$ (001),³⁵ and also of Cu

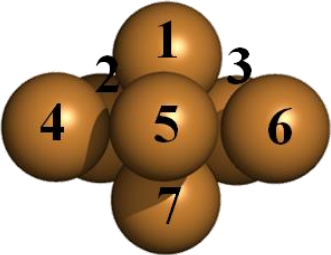
nanoclusters supported on TiC (001).² The complete set of selected clusters considered is reported in Table 3.2. The number of 2D clusters is quite large despite of the fact that for $n > 7$, the 3D structures are more stable.³¹ The reasons for this choice come from previous experimental works which indicates that, at small coverages, transition metal clusters supported on TMC tend to acquire planar structures.⁵ This behavior results from the fact that metal-surface interactions are larger than metal-metal ones, favoring 2D supported clusters even if their gas phase counterparts are higher in energy than the 3D ones.³⁶

Following these premises, different sizes and geometries of Cu_n clusters were investigated with $n = 4, 6, 7$, and 10. The Cu-Cu distances are reported on Table 3.2 and, logically, these are smaller than the nearest-neighbor Cu-Cu distances in bulk Cu —of 2.567 Å as predicted by the PBE functional³⁷— simply because of larger number of coordinately unsaturated atoms.

Table 3.2: Selected Cu clusters of different sizes, including the Cu-Cu distances (Å).

		Cu 1	Cu 2	Cu 3	Cu 4	Cu 5	Cu 6	Cu 7	Cu 8	Cu 9
Cu ₄ Rhombus	Cu 1									
	Cu 2	2.37								
	Cu 3	2.38	4.17							
	Cu 4	2.26	2.38	2.37						
Cu ₄ Tetrahedron	Cu 1									
	Cu 2	2.41								
	Cu 3	2.41	2.41							
	Cu 4	2.37	2.37	2.37						
Cu ₄ Square	Cu 1									
	Cu 2	2.32								
	Cu 3	2.31	3.28							
	Cu 4	3.28	2.31	2.32						
Cu ₆ 3D	Cu 1									
	Cu 2	2.34								
	Cu 3	2.34	2.41							
	Cu 4	4.67	2.34	4.09						
	Cu 5	4.09	2.41	2.41	2.34					

3.4 Modeling metal clusters on molybdenum carbide surfaces

	Cu 6	4.67 4.09 2.34 4.67 2.34	
Cu ₇ 3D	Cu 1		
	Cu 2	2.42	
	Cu 3	2.42 2.42	
	Cu 4	2.43 2.42 3.92	
	Cu 5	2.42 3.92 3.91 2.42	
	Cu 6	2.42 3.92 2.42 3.92 2.42	
	Cu 7	2.55 2.43 2.42 2.42 2.43 2.42	
	Cu ₇ Close-packed 2D	Cu 1	
Cu 2		2.38	
Cu 3		2.39 4.13	
Cu 4		2.38 2.38 2.39	
Cu 5		4.14 2.39 4.79 2.39	
Cu 6		4.13 4.77 2.39 2.38 4.14	
Cu 7		4.77 4.13 4.14 2.38 2.39 2.38	
Cu ₇ Close-packed 3D		Cu 1	
	Cu 2	2.36	
	Cu 3	2.42 4.12	
	Cu 4	2.44 2.44 2.35	
	Cu 5	4.11 2.42 4.70 2.35	
	Cu 6	2.45 3.40 2.42 2.43 4.12	
	Cu 7	3.40 2.45 4.12 2.43 2.42 2.36	
	Cu ₁₀ 3D	Cu 1	
Cu 2		2.49	
Cu 3		2.49 2.37	
Cu 4		2.49 3.35 2.37	
Cu 5		2.49 2.37 3.36 2.37	
Cu 6		4.28 2.46 3.74 3.73 2.46	
Cu 7		4.28 2.45 2.46 3.74 3.74 2.37	
Cu 8		4.28 3.73 2.46 2.45 3.74 3.35 2.37	
Cu 9		4.28 3.74 3.74 2.45 2.46 2.37 3.35 2.37	
Cu 10		5.78 4.28 4.28 4.28 4.28 2.49 2.49 2.49 2.49	
Cu ₁₀ Close-packed 2D		Cu 1	
	Cu 2	2.40	
	Cu 3	4.81 2.40	
	Cu 4	2.39 4.16 6.36	

	Cu 5	2.37	2.41	4.18	2.37				
	Cu 6	4.18	2.40	2.37	4.84	2.47			
	Cu 7	6.35	4.15	2.39	7.21	4.84	2.37		
	Cu 8	4.13	4.78	6.34	2.39	3.37	4.18	6.35	
	Cu 9	4.77	4.13	4.78	4.15	2.40	2.41	4.16	2.40
	Cu 10	6.33	4.77	4.12	6.35	4.18	2.37	2.39	4.81
Cu ₁₀ Close-packed 3D	Cu 1								
	Cu 2	2.40							
	Cu 3	2.46	4.22						
	Cu 4	2.43	2.43	2.45					
	Cu 5	4.22	2.46	4.89	2.45				
	Cu 6	4.20	4.85	2.42	2.43	4.22			
	Cu 7	4.86	4.21	4.22	2.43	2.42	2.45		
	Cu 8	2.43	3.42	2.42	2.50	4.21	3.41	4.20	
	Cu 9	3.42	2.43	4.21	2.50	2.42	4.20	3.42	2.42
	Cu 10	4.20	4.20	3.44	2.51	3.43	2.42	2.42	2.42

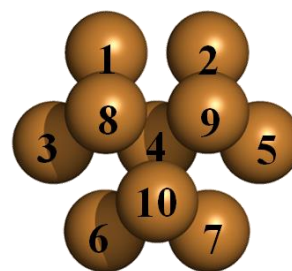


Table 3.3 shows that the rhombus structure is the most stable Cu₄ cluster, followed by square and tetrahedron structures and these results agreed with previous calculations by Calaminici *et al.*³¹ obtained at PW86x-P86c level. Next, the Cu₆ cluster was considered since previous studies^{29,30} showed that this is the largest cluster where the most stable isomer is still planar. The results were in full agreement with previous studies, although some Cu-Cu distances are slightly different, probably attributed to the use of different functionals and basis sets. Also, 3D structures for Cu₆ clusters were optimized although all of them were found to exhibit higher energy (> 0.8 eV) than 2D clusters. Furthermore, 3D clusters did not show similarities with the molybdenum carbide surface morphology, and consequently, they were not considered as adsorption candidates. Regarding Cu₇ and Cu₁₀, the 3D geometries proposed by Jug *et al.*²⁹ were considered. Nevertheless, one needs to realize that, once adsorbed, the number of Cu-surface interactions is larger for other 3D or even 2D possible structures. For this reason, close-packed Cu₇ and Cu₁₀ hexagonal nanoclusters were included in the study even though these

3.4 Modeling metal clusters on molybdenum carbide surfaces

isomers were higher in energy (~ 1 eV) than those reported by Jug *et al.*²⁹ (Table 3.2). The structure of the close-packed clusters was in agreement with the results of Balbuena *et al.*³⁸ Finally, to model very large flat supported Cu nanoparticles, a full monolayer with 16 Cu atoms in a close-packed arrangement above the appropriate supercell (2×2) was considered. Logically, the geometry of close-packed Cu₁₆ overlayer was modified depending on the surface to, in each case, accommodate the cell parameters.

Table 3.3: Relative (E_{rel}) and cohesive (E_{coh}) energy (eV) of gas phase Cu_n nanoparticles of increasing size; structures are as in Table 3.1.

n	Structure	E_{rel} /eV	E_{coh} /eV
4	Rhombus	0.00	-1.57
	Square	0.94	-1.37
	Tetrahedron	1.16	-1.28
6	2D	0.00	-2.15
7	3D	0.00	-2.05
	2D Close-packed	1.01	-1.91
	3D Close-packed	1.12	-1.89
10	3D	0.00	-2.21
	2D Close-packed	0.84	-2.13
	3D Close packed	1.26	-2.09

3.4.1.2 Supported Cu nanoclusters on β -Mo₂C (001) surfaces

After the optimization of isolated Cu clusters in *vacuum*, the structural and energetic stability of Cu nanoclusters supported molybdenum carbides surfaces were accomplished. The study of the structure and electronic properties of Cu₄ supported on β -Mo₂C were carried out using the (2×2) supercell model. This supercell was also used to investigate the case of a full Cu monolayer (ML) composed by 16 Cu atoms which provides a model for very large flat supported clusters. To avoid possible Cu-Cu interactions in the periodically repeated images, a (3×3) supercell was used to model the deposition of Cu₇ and Cu₁₀. On β -Mo surface,

the most stable Cu_4 geometry corresponds to a rhombus structure (see Figure 3.7a) with the Cu atoms above the Mo hollow sites. The large stability of this isomer was consistent with the fact that most of initial structures of Cu_4 clusters converge to a rhombus geometry, and the next available stable structure was 1.2 eV higher in energy. It is worth pointing out that the different types of hollow Mo sites behave all in a similar way, the adsorption energy of the Cu_4 rhombus at these sites differ at most by 0.04 eV. Respect to Cu_7 , the initial 3D cluster becomes 2D upon interaction with the surface and the adsorption energy is nearly the same as for the final structure corresponding to the initial close-packed 2D isomer. Hence, there is a clear trend to stabilize 2D structures as is evidently seen in Figure 3.7, which is a well-known fact since metal clusters tend to be planar, simulating a metal layer, in order to compensate the surface polarity.^{39,40} A similar behavior was observed for the Cu_{10} clusters, where the 3D cluster proposed in the literature evolved to a 2D geometry (Figures 3.6d, 3.6e) and rearranged to a hexagonal structure. Moreover, the 3D hexagonal close-packed supported cluster was higher in energy, as happened for isolated Cu_7 . In the case of Cu ML deposited on β -Mo, it maintained a well-defined 2D geometry, thus following the trend observed for the smaller clusters.

Table 3.4: Relative energies (in eV), adsorption energy and adhesion energy *per atom*, and charge on the cluster (in a.u.) for the optimized structure of Cu_n supported on β -Mo.

n	Structure	E_{rel} /eV	$E_{\text{ads/atom}}$ /eV	$E_{\text{adh/atom}}$ /eV	ΔQ /a.u.
4	Rhombus	—	-1.99	-2.24	-1.82
7	3D	0.00	-1.55	-1.97	-2.19
	3D close-packed	1.42	-1.35	-1.76	-1.79
10	2D close-packed	0.00	-1.41	-1.81	-3.98
	3D	0.39	-1.37	-1.76	-2.92
	3D close-packed	1.41	-1.27	-1.51	-2.03
∞	ML	—	-1.67	-1.73	-5.28

3.4 Modeling metal clusters on molybdenum carbide surfaces

From the obtained results one can conclude that Cu_4 , Cu_7 , or Cu_{10} nanoclusters supported on $\beta\text{-Mo}$ follow the same pattern. This was in line with the analysis of the DOS plots in Figure 3.8 where the differences between supported clusters are almost indistinguishable. The Bader charge analysis exhibited that the charge transfer is from the surface to the Cu nanoparticles.

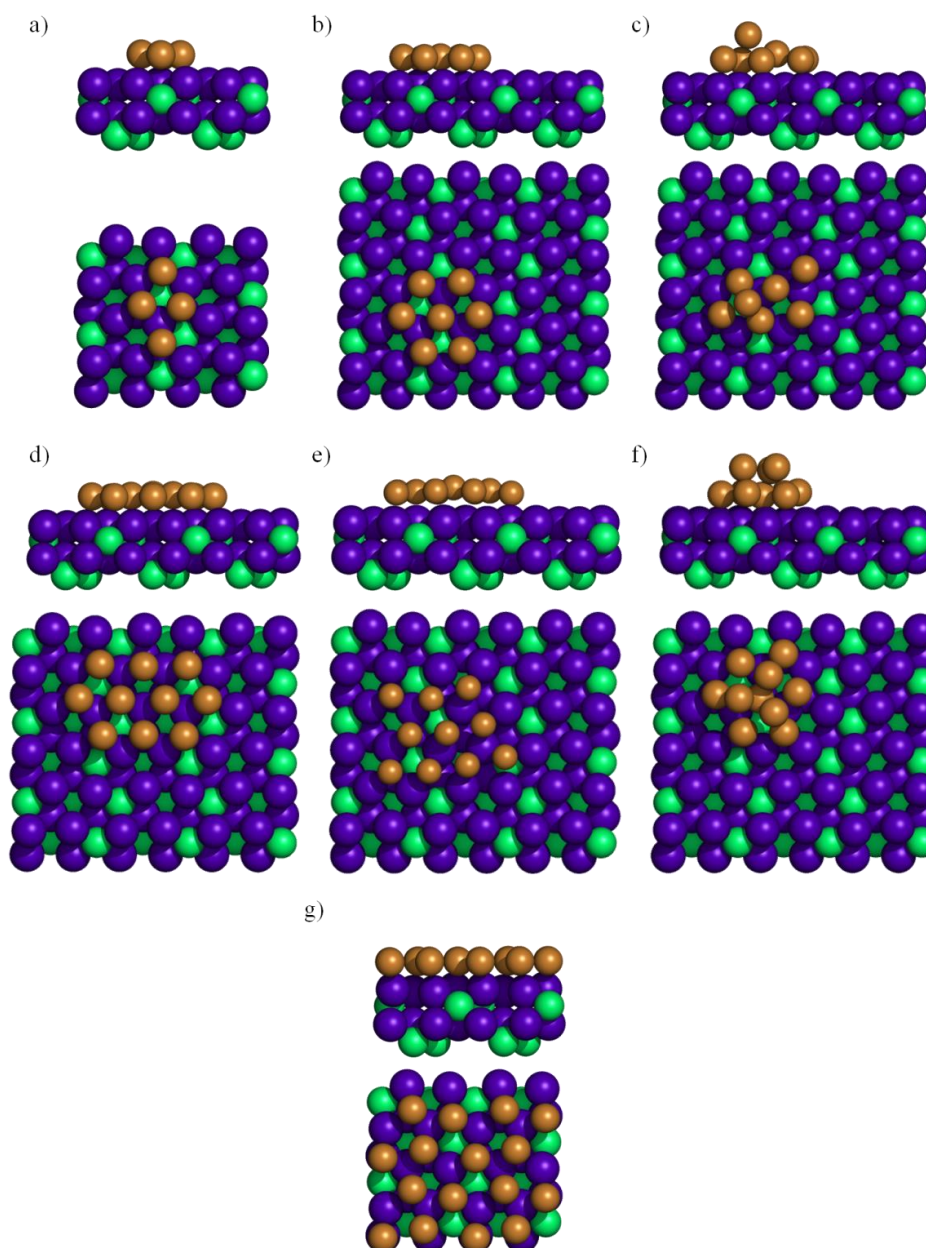


Figure 3.7: Structure of the Cu_n nanoparticles supported on the $\beta\text{-Mo}$ surface: Cu_4 rhombus structure (a), Cu_7 2D close packed (b), Cu_7 3D close packed (c), Cu_{10} 2D close packed (d), Cu_{10} 3D become on 2D (e), Cu_{10} 3D close packed (f), and Cu ML (g). Side (top) and top views (bottom) are displayed.

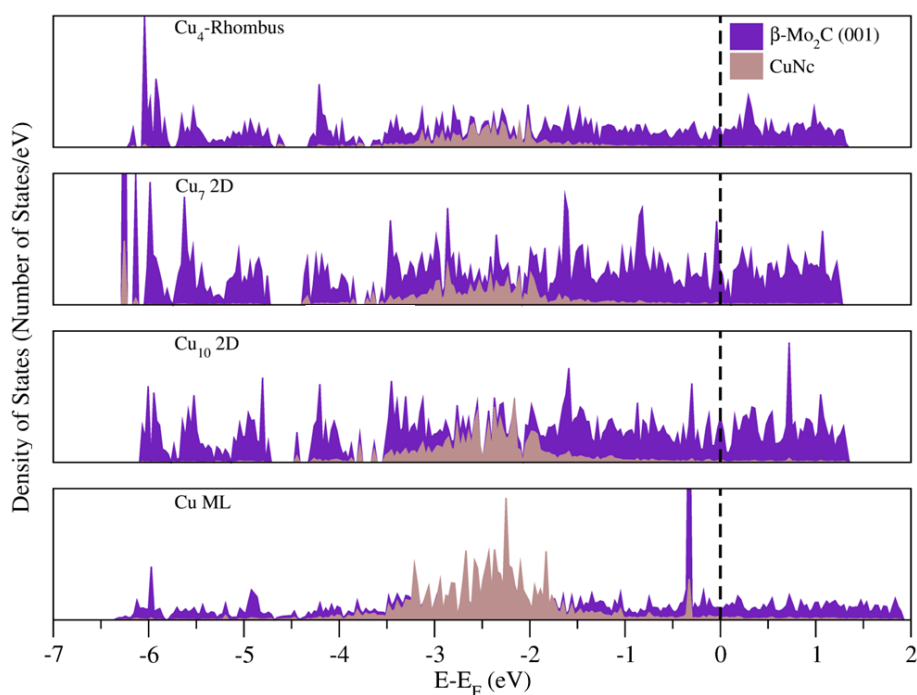


Figure 3.8: Total DOS of studied Cu nanoclusters adsorbed on β -Mo. The y axis are not the same in the different graphs in order to facilitate the visualization.

To complete the study, we also investigated the effect of the surface termination by considering the β -C terminated surface. Table 3.5 reports that optimized geometries for the supported Cu_4 , Cu_7 , and Cu_{10} clusters correspond to a rhombus and to 2D close-packed structures, respectively (Figure 3.8). Moreover, in all cases, the Cu atoms occupy hollow Mo^4 sites as in the case of the Mo terminated surface. The adsorption energy and adhesion energy values also followed the trend discussed for the Mo terminated surface. The tendency to stabilize 2D structures was confirmed when realizing that, starting from the 3D Cu_{10} cluster proposed by Jug *et al.*,²⁹ different stable 3D geometries were found for the supported particle but always more than 1 eV higher in energy than the 2D supported isomer. In this sense, both Mo and C terminations of polar β - Mo_2C (001), favors 2D supported clusters.

On the other hand, Table 3.5 displays that on β -C terminated the Cu particle tends to get oxidized whereas on the β -Mo the particle gets reduce. This similarity

3.4 Modeling metal clusters on molybdenum carbide surfaces

points for a key role played by surface available C atom and polarity in the Cu_n oxidation process; when $\beta\text{-Mo}_2\text{C}$ (001) is Mo terminated, the electron transfer is from Mo to C atoms, *i.e.* on the negative z axis direction, so Mo give electronic density to C atoms. Consequently, the dipole moment is along the positive z axis direction. The Cu_n deposition on Mo termination surface implies electron density charge transfer from Mo to Cu atoms, therefore, the charge transfer is on z axis direction, compensating the surface dipole. The opposite occurs on $\beta\text{-C}$, but on the inverse direction. This opens an interesting way to tune the reactivity of the supported particles by support engineering. The DOS analysis (Figure 3.9) also follows the trend discussed for the systems presented above with remarkable electron delocalization showing up for the larger supported clusters.

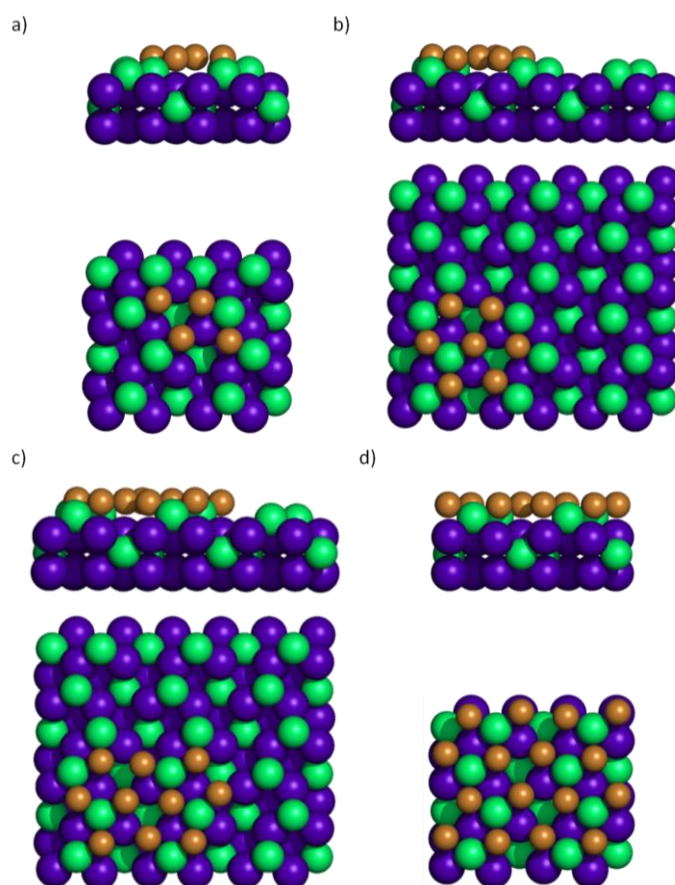


Figure 3.8: Sketches of the Cu_4 rhombus structure (a), Cu_7 (b), Cu_{10} (c), and Cu ML (d) deposited on $\beta\text{-C}$. Side (top) and top views (bottom) are displayed.

Table 3.5: Relative energies (in eV), adsorption energy and adhesion energy *per atom*, and charge transfer (in a.u.) for the optimized structure of Cu_n supported on $\beta\text{-C}$ (001).

n	Structure	$E_{\text{ads/atom}}$ /eV	$E_{\text{adh/atom}}$ /eV	ΔQ /a.u.
4	Rhombus	-2.28	-2.71	+0.56
7	3D close-packed	-1.71	-2.52	+1.19
10	2D close-packed	-1.48	-2.42	+1.90
∞	ML	-1.66	-2.00	+1.99

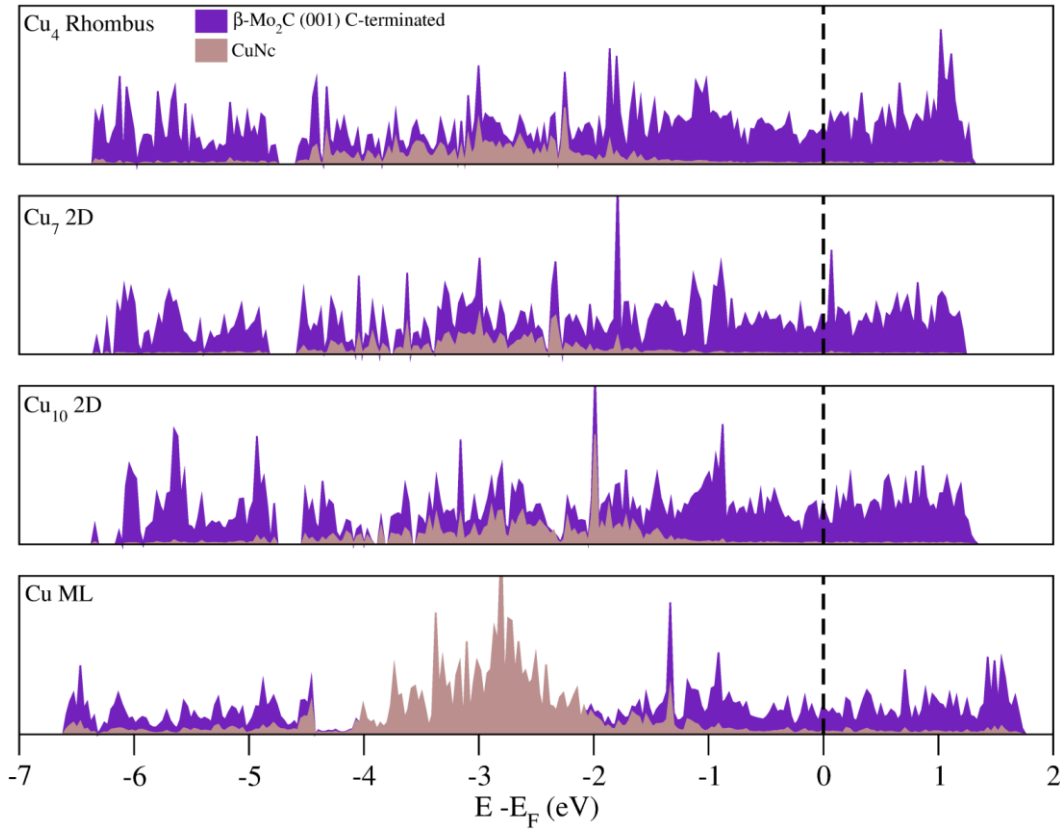


Figure 3.9: Total DOS of studied Cu nanoclusters adsorbed on $\beta\text{-C}$ terminated. The y axis are not the same in the different graphs in order to facilitate the visualization.

3.4.1.3 Supported Cu nanoclusters on $\delta\text{-MoC}$ (001) surfaces

The study of the structure and electronic properties of Cu_n supported on $\delta\text{-MoC}$ (001) were carried out following the scheme used on $\beta\text{-Mo}_2\text{C}$ (001) surface. The

3.4 Modeling metal clusters on molybdenum carbide surfaces

(2×2) supercell model was used to investigate the case of Cu₄ and Cu ML, whilst Cu₆ and Cu₇ were deposited on (3×3) supercell.

In the case of the supported Cu₄ cluster, the optimization procedure led to two degenerate structures (Table 3.6). These were the tetrahedron and distorted rhombus displayed in Figures 3.10a and 3.10b. Upon interaction with the surface, the Cu₄ square nanocluster did not maintain its structure and evolved to distorted rhombus. Even though tetrahedron and rhombus structure were degenerate, the adsorption energy *per* atom was larger in the case of the tetrahedron because the isolated cluster was higher in energy. In the Cu₄/δ-MoC (001) system, the adhesion energy did not significantly differ from the adsorption energy implying that the surface and cluster deformation were not dominant. In the case of supported Cu₆, two degenerate structures were found as in the case of Cu₄ supported clusters; one of these corresponds to a 2D cluster which has a hexagon like shape (Figure 3.10c) whilst the other isomer corresponded to a 3D structure with a distorted rhombus in the first atomic layer, which was reminiscent of the structure of the supported Cu₄ cluster, and two Cu atoms above these ones as seen in Figure 3.10d. Finally, regarding the structure of the supported Cu₇ cluster, a 3D structure was obtained, but significantly different from the isolated Cu₇ geometry predicted by our DFT calculations and also by Jug *et al.*²⁹ In fact, the structure of the supported cluster involved five Cu atoms adsorbed located not always above high symmetry adsorption sites, and two atoms forming the second layer (Figure 3.10e).

The optimization of the supported Cu monolayer placed the metal atoms on top of surface atoms as one can observe in Figure 3f, this was at variance of the case of single atoms tending to occupy MMC sites.³⁵ Interestingly, the structure of the supported monolayer exhibited a considerable rumpling essentially with eight Cu atoms on each layer. This followed from the different atomic radii of C and Mo with concomitant C-Cu distances (~1.97 Å) shorter than Cu-Mo (~3.30 Å). With the aim of further investigating the possibility of existence of a stable planar monolayer,

additional studies were performed using a Cu_8 planar cluster model formed by eight Cu single atoms placed above all possible high symmetry sites. In all cases, a 3D structure is obtained, which was in agreement with the trends discussed for supported Cu_6 and Cu_7 clusters, where planarity was not maintained. Considering the results mentioned above, one can argue that, except for very small clusters containing three or four atoms, the structure of supported Cu nanoparticles will tend to be 3D. This tendency is not in agreement with $\beta\text{-Mo}_2\text{C}$ (001) surface, since independently of the termination, the most favorable Cu_n structures are planar.

Table 3.6: Relative energies (in eV), adsorption energy and adhesion energy *per atom* of Cu_n ($n=4, 6, 7, \infty$) supported on $\delta\text{-MoC}(001)$, the case with ∞ atoms is modeled by full monolayer. Charge transfer from the Bader analysis is reported as ΔQ , a positive charge implies that the supported cluster is oxidized.

n	Structure	E_{rel} /eV	$E_{\text{ads/atom}}$ /eV	$E_{\text{adh/atom}}$ /eV	ΔQ /a.u.
4	Tetrahedron	0.00	-1.35	-1.72	+0.42
	Rhombus	0.03	-1.35	-1.34	+0.47
6	2D	0.00	-2.16	-2.47	+0.44
	3D	0.08	-2.15	-2.42	+0.56
7	3D	—	-1.91	-2.19	+0.79
∞	ML	—	-0.50	-0.51	+0.75

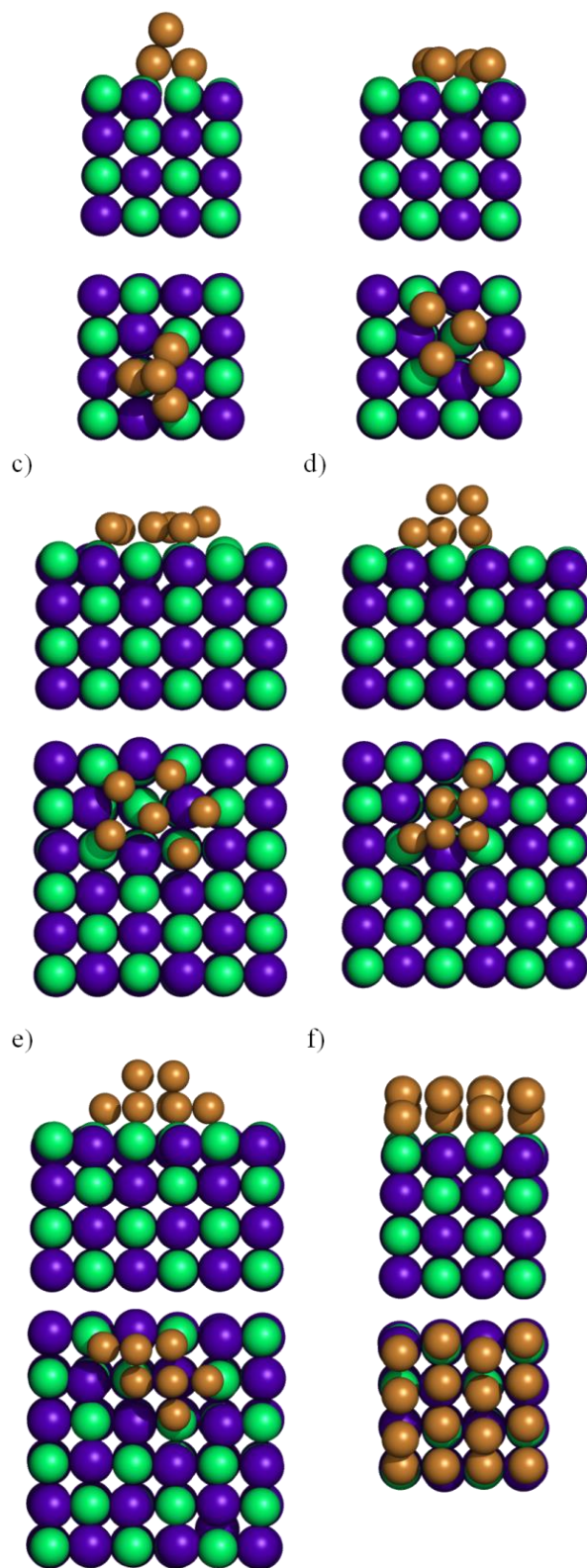


Figure 3.10: Top (upper panel) and side (bottom panel) views of the optimized structures of Cu_n supported on $\delta\text{-MoC}$ (001): Cu_4 tetrahedron (a), Cu_4 rhombus (b), Cu_6 2D (c), Cu_6 3D (d), Cu_7 3D (e), and Cu ML (f).

In the case of Cu_4/MoC (001), the DOS plots (Figure 3.11) for the supported tetrahedron and rhombus structures did not exhibit significant variations and the same behavior was found for the Cu_6 and Cu_7 supported particles. Apparently, the Cu d and s orbitals mix with the valence and conduction bands of the underlying carbide. The Bader analysis revealed a charge transfer from the metal cluster to the carbide surface as indicated by the ΔQ values in Table 3.6. The Bader analysis exhibited that, in all obtained structures, there was charge transfer from the cluster to the carbide surface indicating that binding to the support tends to oxidize the metallic particle. This fact agrees with $\beta\text{-C}$ surface and in opposite with $\beta\text{-Mo}$. This difference strongly suggest that Cu-C interaction play a key role determining the structure and oxidation state of the supported particles, and in consequence, this fact could play a key role on the catalytic activity.

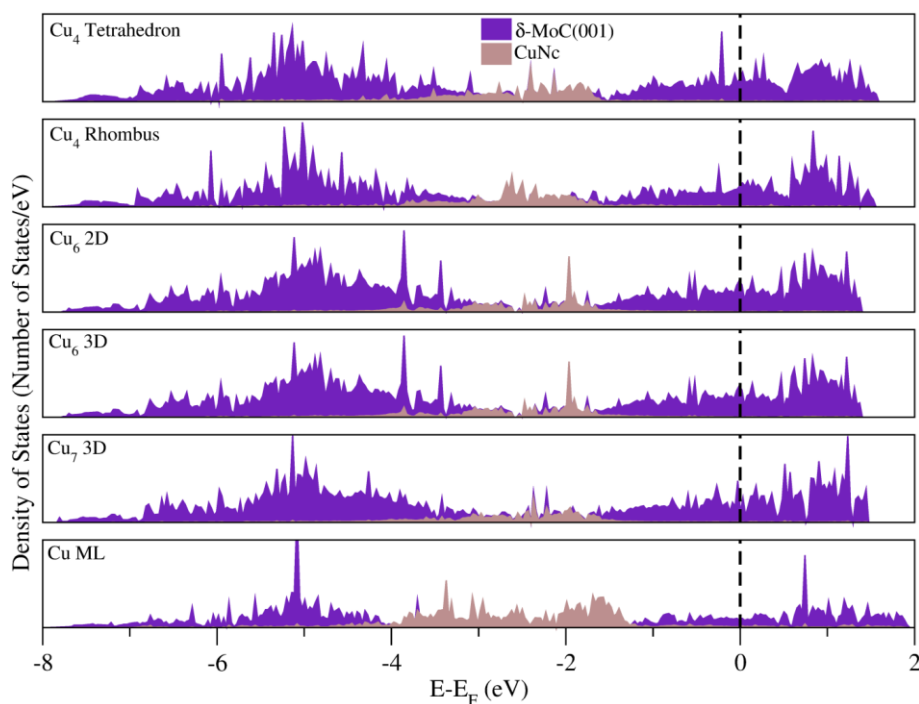


Figure 3.11: Total DOS of studied Cu nanoclusters adsorbed on $\delta\text{-MoC}(001)$. The y axis are not the same in the different graphs in order to facilitate the visualization.

3.4.2 Au nanoclusters supported on δ -MoC (001) surface

3.4.2.1 Isolated Au nanoclusters

The Au_n adsorption study were accomplished considering the results obtained of Cu_n clusters deposited on δ -MoC (001) and previous works in the literature. Regarding to Au_4 clusters, four different geometries were tested, square, rhombus, pyramid, and half-pyramid. Table 3.7 reports the main data of the calculations such as the relative and cohesion energies. Note that the isolated half-pyramid is not included on Table 3.7 because this cluster became to rhombus structure after the optimization process, as was observed with Cu_4 clusters. As in the case of Cu_4 clusters, the rhombus geometry is more stable than planar and pyramid clusters. The Au-Au neighborhood distances are lower than results obtained on Au bulk using PBE as functional (2.95 Å).⁴¹

On the other hand, different 2D Au_9 clusters (Table 3.7) were modeled based on previous works in the literature.⁴² The initial selected geometries where the square structure, with three Au atoms in three different rows (3×3×3), the (4×3×2) planar pyramid, where the name was associated to the number of Au atoms per row, and the alternate square, with the second row displaced to the hollow sites between rows one and three. Except to square structure, the other ones maintained the initial structure after the optimization process, whereas square evolves towards rhombus structure, being the most stable one. Note that the major difference was only 0.16 eV, so these Au_9 structures could be consider as degenerated.

Regarding to Au_{13} models, the selected structure is a 3D cluster with nine Au atoms on the first floor and four atoms on the second one, deposited on Hollow Au sites of the first nine Au atoms. This cluster model was used on previous works using TiC (001).⁴³ The sketches of all tested Au_n clusters are in Figure 3.12.

Table 3.7: Relative (E_{rel}) and cohesive (E_{coh}) energies (eV) of gas phase Au_n nanoparticles of increasing size; structures are as in Figure 3.11.

n	Structure	E_{rel} /eV	E_{coh} /eV
4	Rhombus (a)	0.00	-1.56
	Square (b)	0.85	-1.40
	Tetrahedron (c)	1.42	-1.05
9	Rhombus (d)	0.00	-2.00
	Planar 4×3×2 (e)	0.11	-1.98
	3×3×3 Alternate (f)	0.16	-1.97
13	Pyramid (g)	-	-2.35

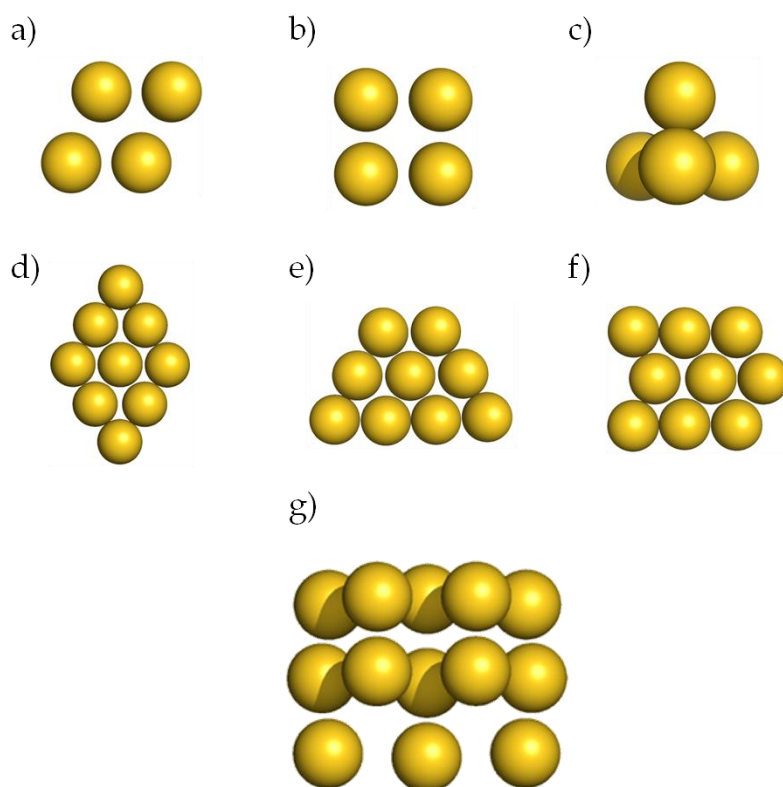


Figure 3.12: Structure of the isolated Au_n nanoparticles. Au_4 rhombus structure (a), Au_4 square (b), Au_4 3D pyramidal (c), Au_9 rhombus (d), Au_9 2D pyramid 4×3×2 (e), Au_9 2D 3×3×3 (f), and Au_{13} cluster (g).

3.4.2.2 Supported Cu nanoclusters on δ -MoC (001) surfaces

As is discussed on the introduction (section 3.1), the Au clusters were deposited only on δ -MoC (001) surface. Different adsorption sites were checked to obtain the most relevant systems of Au₄ deposition on (2×2) supercell of δ -MoC (001), reported on Table 3.8. The most favorable systems corresponded to a degenerate 3D geometry with its three based atoms deposited on MMC sites (see Figures 3.13a and 3.13b). As is observed on top view sketches, the top Au atom is in hollow site respect the three Au based atoms, leading to a trigonal pyramid structure on figure 3.13a, whereas on figure 3.13b, the structure is similar to half-pyramid. Otherwise, the half pyramid reported with a relative energy of 0.25 eV, contains one Au atom in contact with molybdenum surface atoms and the probable metal-metal repulsion between them lead to the cluster tilt (Figure 3.13c). The last two structures could be described as 2D (Figures 3.13d and 3.13e) despite of the fact that the Au atoms nearby and/or in contact with Mo surface atoms are located slightly above than atoms in contact with C surface atoms. The relative and adsorption energies of these 2D clusters were clearly superior to the 3D structures. This fact was not in agreement with previous results on TiC (001), where the most stable system was a square Au₄ clusters deposited on top of C surface atoms.³⁵ Moreover, the same square structure was observed after the deposition of Pt₄, Pd₄, Cu₄, and Ag₄ clusters on TiC (001), although these results were obtained using PW91 functional. Furthermore, our results about the Cu₄ deposition revealed that 2D and 3D clusters were degenerate in energy, as is discussed in previous sections. Therefore, this disagreement was investigated by means of two different ways. On the one hand, four Au atoms were deposited on top of neighbor C surface atoms, despite that the C-C distance on δ -MoC (001) is slightly superior that Au-Au distance of isolated square Au₄ cluster. Nevertheless, this structure turned into pyramid structure, as the most favorable system reported on Table 3.8. On the other hand, it was considered that (2×2) supercell could be small, leading to lateral Au-Au interactions between clusters, despite of the cluster-cluster

distance was larger than 6 Å. For this reason, the same procedure followed using the (2×2) supercell were repeated using (3×3) supercell. However, the final results on (3×3) supercell of δ -MoC (001), presented the same results obtained using the (2×2) supercell, with no significant changes on relative and adsorption energies. Even the four Au atoms deposited on top of neighbor C surface atoms, generating a square planar structure, evolved towards the same 3D geometry obtained on (2×2) supercell. Thus, one could conclude that the disagreement was due to the use of different GGA functional.

Respect to Au₉/ δ -MoC (001) structures, Table 3.8 reports the top-five lowest in energy ordered by the relative energy value. Note that there are clearly three degenerate structures, with different location of Au atoms. Whereas the first and third models (Figure 3.13f and Figure 3.13h), present two or three Au atoms in a second-floor cluster, the Au atoms on second structure maintained its planar structure (Figure 3.13g), with only slightly displacements of Au atoms to the second floor. Note also that second structure acquires a nano-row structure, since both ends were connected due to the surface periodicity (see Figures 3.13f-3.13h). The other two structures, (Figure 3.13i and Figure 3.13j), exhibited similar structure than the most stable one (Figure 3.13f).

Regarding to the deposition of Au₁₃ cluster, a (4×4) supercell of δ -MoC (001) was used due to the size of Au₁₃ nanoparticle. Different adsorption sites were tested, obtaining two different minima structures, as is reported on Table 3.8. On the most stable one, the Au are adsorbed on top of C surface atoms (Figure 3.13k), in agreement with our results using Cu and Au clusters of different sites. Furthermore, note that the adsorbed Au₁₃ structure did not change significantly respect to the isolated clusters. On the other hand, the second geometry is adsorbed on MCC sites and the geometry is slightly distorted (Figure 3.13l).

3.4 Modeling metal clusters on molybdenum carbide surfaces

Table 3.8: Relative (E_{rel}), adsorption (E_{ads}), and adhesion (E_{adh}) energies (eV) of Au_n nanoparticles supported on δ -MoC (001) surface. Structures are in Figure 3.13.

n	Structure	E_{rel} /eV	$E_{ads/atom}$ /eV	$E_{adh/atom}$ /eV	ΔQ /a.u.
4	a	0.00	-1.40	-1.79	-0.37
	B	0.02	-1.39	-1.71	-0.34
	C	0.25	-1.34	-1.68	-0.33
	D	0.45	-1.14	-1.40	-0.34
	e	0.52	-0.92	-1.01	-0.34
9	f	0.00	-1.37	-1.41	-0.69
	g	0.01	-1.39	-1.43	-1.11
	H	0.05	-1.37	-1.40	-0.64
	I	0.35	-1.34	-1.25	-0.66
	J	0.38	-1.35	-1.24	-0.65
13	K	0.00	-0.61	-0.76	-1.00
	L	0.22	-0.39	-0.60	-0.90

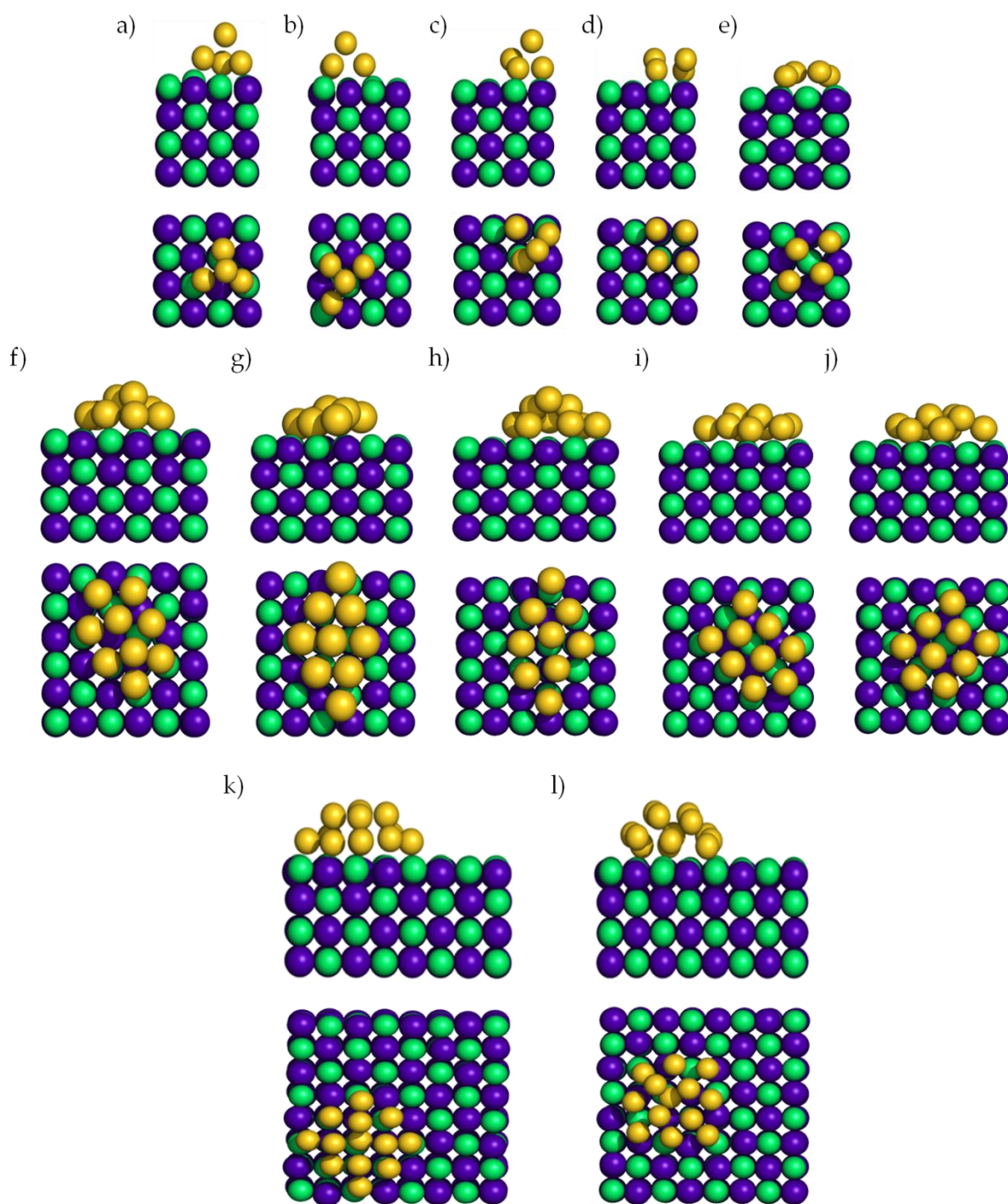


Figure 3.13: Top (upper panel) and side (bottom panel) views of the optimized structures of Au_n supported on δ -MoC(001). Sketches from a to e represent Au₄ clusters, from f to j denote Au₉ clusters and k and l Au₁₃ structures.

3.5 Conclusions

In this chapter, the slab models of molybdenum carbides (001) surfaces with and without small metal nanoparticles supported on thereon were reported. These models were exhaustively selected in order to represent properly the experimental catalysts.

With respect to bare molybdenum carbide (001) surfaces, this chapter has summarized the number of atoms, layers, and cell dimension of different supercells. Furthermore, test calculations revealed that a (2×2) supercell is enough to avoid the lateral interactions between adsorbates after the adsorption of different test molecules, and consequently, it will be the model used to study the adsorption, activation, and reactivity of different reactants and intermediates.

For the polar β -Mo₂C (001)-Mo and -C (001) surfaces, the results showed that, despite the different termination, the supported particles tended to become 2D, despite of the fact that isolated Cu_n with n>7, are 3D. The charge transfer direction was different for the two terminations in order to compensate the surface polarity. On the Mo terminated surface the supported particles tended to be reduced whereas on the C terminated surface the supported particle tends to become oxidized. This difference may result in a different reactivity and suggests that it is possible to control the donor or acceptor character of the supported metallic particle by engineering the carbide support. For the δ -MoC (001) surface, small Cu_n clusters (n= 4, 6, and 7) and a Cu ML were considered. The trends indicated that larger supported particles are likely to adopt a 3D structure and to become noticeable oxidized. This was confirmed by the Cu ML model featuring a rumpling bilayer structure being originated by Cu atoms located on top of surface C or Mo atoms.

Respect to Au_n clusters, the systematic deposition was only carried out on δ -MoC (001), since the investigations discussed in next chapters reveal that is the suitable catalyst for WGS reaction. The deposition of small Au_n clusters (n= 4, 9 and

13) showed that the supported particles tended to become 3D. This was in opposite to previous works using M_4 clusters on TiC (001), where they were planar. Our calculations conclude that this disagreement is due to the use of different GGA functionals, since calculations increasing the supercell size displayed the same results, discarding thus, possible cluster-cluster interactions on the repeated cells.

3.6 References

- [1] L. K. Ono and B. Roldán-Cuenya, *Catal. Lett.*, **2007**, *113*, 8.
- [2] T. Gomez, E. Florez, J. A. Rodriguez and F. Illas, *J. Phys.Chem. C*, **2011**, *115*, 11666.
- [3] N. M. Schweitzer, J. A. Schaidle, O. K. Ezekoye, X. Pan, S. Linic and L. T. Thompson, *J. Am. Chem. Soc.*, **2011**, *133*, 2378.
- [4] J. A. Rodriguez F. Viñes, F. Illas P. Liu, Y. Takahashi and K. Nakamura, *J. Chem. Phys.*, **2007**, *127*, 211102.
- [5] J. A. Rodriguez, P. Liu, Y. Takahashi, K. Nakamura, F. Viñes and F. Illas, *J. Am. Chem. Soc.*, **2009**, *131*, 8595.
- [6] J. Goniakowski, F. Finocchi and C. Noguera, *Rep. Prog. Phys.*, **2008**, *71*, 016501.
- [7] N. H. Moreira, G. Dolgonos, B. Aradi, A. L. da Rosa and T. Frauenheim, *J. Chem. Theory Comput.*, **2009**, *5*, 605.
- [8] T. B. Massalski, *Binary Alloy Phase Diagrams*, ASM Intern.,1990.
- [9] E. Rudy, S. Windisch, A. J. Stosick and J. R. Hoffmann, *Trans. Metall. Soc. AIME*, **1967**, *239*, 1247.
- [10] K. Page, J. Li, R. Savinelli, H. N. Szumila, J. Zhang, J. K. Stalick, T. Proffen, S. L. Scott and R. Seshadri, *Surf. Sci.*, **2008**, *10*, 1499.
- [11] J. Haines, J. M. Léger, C. Château and J. E. Lowther, *J. Phys.: Condens. Matter*, **2001**, *13*, 2447.
- [12] H. W. Hugosson, U. Jansson, B. Johansson and O. Eriksson, *Chem. Phys. Lett.*, **2001**, *333*, 444.
- [13] *Powder Diffraction File*; JCPDS International Center for Diffraction Data: Pennsylvania, 2004.
- [14] J. Ren, C.-F. Huo, J. Wang, Z. Cao, Y.-W. Li, and H. Jiao, *Surf.Sci.*, **2006**, *600*, 2329.
- [15] H. Tominaga, Y. Aoki and M. Nagai, *Appl. Catal., A*, **2012**, *423*, 192.
- [16] H. Tominaga and M. Nagai, *J. Phys. Chem. B*, **2005**, *109*, 20415.
- [17] A. N. Christensen, *Acta Chem. Scand., Ser. A*, **1977**, *31*, 509.
- [18] T. St Clair, S. T. Oyama, D. F. Cox, S. Otani, Y. Ishizawa, R. L. Lo, K. Fukui and Y. Iwasawa, *Surf. Sci.*, **1999**, *426*, 187.
- [19] A. Fernández-Guillermot, J. Häglund and G. Grimvall, *Phys. Rev. B: Condens. Matter Mater. Phys.*, **1992**, *45*, 11557.
- [20] H. W. Hugosson, L. Nordström, U. Jansson, B. Johansson and O. Eriksson, *Phys. Rev. B: Condens. Matter Mater. Phys.*, **1999**, *60*, 15123.
- [21] P. Janthon, S. M. Kozlov, F. Viñes, J. Limtrakul and F. Illas, *J. Chem. Theory Comput.*, **2013**, *9*, 1631.
- [22] J. P. Perdew and Y. Wang, *Phys. Rev. B: Condens. Matter Mater. Phys.*, **1992**, *45*, 13244.
- [23] J. P. Perdew, K. Burke and M. Ernzerhof, *Phys. Rev. Lett.*, **1996**, *77*, 3865.
- [24] X. R. Wang, M. F. Yan and H. T. Chen, *J. Mater. Sci. Technol.*, **2009**, *25*, 419.
- [25] X.-R. Shi, S.-G. Wang, H. Wang, C.-M. Deng, Z. Qin and J. Wang, *Surf. Sci.*, **2009**, *603*, 852.
- [26] J. W. Han, L. Li and D. S. Sholl, *J. Phys. Chem. C*, **2011**, *115*, 6870.
- [27] B. Hammer, L. B. Hansen and J. K. Nørskov, *Phys. Rev. B: Condens. Matter Mater. Phys.*, **1999**, *59*, 7413.
- [28] J. R. d. S. Politi, F. Viñes, J. A. Rodriguez and F. Illas, *Phys. Chem. Chem. Phys.*, **2013**, *15*, 12617.
- [29] K. Jug, B. Zimmermann, P. Calaminici, and A. M. Köster, *J. Phys.Chem.*, **2002**, *116*, 4497.
- [30] P. Jaque and A. Toro-Labbé, *J. Chem. Phys.*, **2002**, *17*, 3208.
- [31] P. Calaminici, A. M. Köster, N. Russo and D. R. Salahub, *J. Phys. Chem.*, **1996**, *105*, 9546.

- [32] P. Calaminici, M. Pérez-Romero, J. M. Vásquez-Pérez and A. M. Köster, *Comp. Theor. Chem.*, **2013**, 1021, 41.
- [33] E. Florez, W. Tiznado, F. Mondragón, and P. Fuentealba, *J. Phys. Chem A*, **2005**, 109, 7815.
- [34] I. A. Hijazi and Y. H. Park, *Eur. Phys. J. D.*, **2010**, 59, 215.
- [35] G. G. Asara, F. Viñes, J. M. Ricart, J. A. Rodriguez, and F. Illas, *Surf. Sci.*, **2014**, 624, 32.
- [36] J. A. Rodriguez and F. Illas, *Phys. Chem. Chem. Phys.*, **2012**, 14, 427.
- [37] P. Janthon, S. M. Kozlov, F. Viñes, J. Limtrakul and F. Illas, *J. Chem. Theory Comput.*, **2013**, 9, 1631.
- [38] P. B. Balbuena, P. A. Derosa and J. M. Seminario, *J. Phys. Chem. B*, **1999**, 103, 2830.
- [39] O. Dulub, M. Batzill and U. Diebold, *Top. Catal.*, **2005**, 36, 65.
- [40] A. Asthagiri, C. Niederberger, A. J. Francis, L. M. Porter, P. A. Salvador and D. S. Sholl, *Surf. Sci.*, **2003**, 537, 134.
- [41] P. Janthon, S. J. Luo, S. M. Kozlov, F. Viñes, J. Limtrakul, D. G. Trulhar and F. Illas, *J. Chem. Theory Comput.*, **2014**, 10, 3832.
- [42] L. Xiao, B. Tollberg, X. Hu and L. Wang, *J. Chem. Phys.*, **2006**, 124, 114309.
- [43] J.A. Rodriguez, P.J. Ramírez, G.G. Asara, F. Viñes, J. Evans, P. Liu, J.M. Ricart, F. Illas, *Angew. Chem., Int. Ed.*, **2014**, 53, 11270.

CHAPTER FOUR

Interaction of Greenhouse Related Compounds with Molybdenum Carbide Surfaces

4.1 Introduction

CO₂ hydrogenation to CO, MeOH, and to other alcohols constitutes an appealing route to recycle the large amount of CO₂ accumulated in the atmosphere through fossil-derived fuels burning. However, CO₂ high chemical stability makes the overall process difficult for these reactions to occur. The chemical activation of CO₂ molecule is a necessary and oftentimes crucial step, which typically implies a charge transfer from the catalyst and the molecular bending.¹ The other side of the coin in CO₂ conversion implies the H₂ usage and, hence, adsorption and dissociation themselves become key processes to control the reaction. The hydrogen molecule is also quite stable because of the strong covalent single bond and is chemically useful only when the two hydrogen atoms can be split apart in a controlled way.²⁻⁴

The objective here was to explore and examine from an experimental and computational point of views the interaction and activation of CO₂ and H₂ molecules on the pristine (001) surfaces of δ -MoC and β -Mo₂C and see if an activation of CO₂ and dissociation of H₂ occurs, as a first, preliminary, and necessary steps for using molybdenum carbides as catalysts in CO₂ conversion. One must unveil how the activity towards CO₂ and H₂ activation changes with the carbon/metal ratio in the carbide, the importance of ensemble effects, *i.e.*, whether surface carbon atoms do play a role or are mere spectators and the effect of covalent bonding with the carbide substrate in CO₂ adsorption, in order to improve the Mo carbide catalytic performance. Moreover, final states for H₂ and CO₂ splitting were also studied.

The results of combined experimental and theoretical methods about the interaction of reactants and catalysts allowed to predict the suitable performance of Mo Carbide surface to convert CO₂. This chapter contributes to determine the effect of metal/carbon ratio on Mo carbides, as key (or not) fact to select the appropriate catalyst and study the effect of the carbide stoichiometry on the reaction. Furthermore, the

Interaction of greenhouse related compounds with molybdenum carbide surfaces

calculations were carried out using DFT and DFT-D2 methodologies, which was not execute on previous works.

To finalize this chapter, the CH₄ interaction on bare δ -MoC and β -Mo₂C (001) surfaces was also studied insomuch as the experiments presented in the next section revealed that CH₄ is the most abundant product on the CO₂ hydrogenation reaction on β -Mo₂C (001). Furthermore, this study provided a preliminary key data about the possible use of Mo carbides for green chemistry reactions such as methane dry reforming ($\text{CH}_4 + \text{CO}_2 \rightarrow 2\text{CO} + 2\text{H}_2$) and methane steam reforming ($\text{CH}_4 + \text{H}_2\text{O} \rightarrow \text{CO} + 3\text{H}_2$).

4.2 Experimental results

The O 1s region in XPS was used by experimentalist to investigate the adsorption of CO₂ on polycrystalline δ -MoC and on a β -Mo₂C (001) surface at 300 K. The interaction of CO₂ with polycrystalline δ -MoC was weak and a very small and broad peak was seen by XPS at O 1s binding energies between 531-533 eV.⁵ This binding energy could be attributed to the presence of CO or CO₂ species on the surface⁶ and considering that the experimentalists did not found signal where surface atomic O is expected (528-530 eV),⁵ the weak features seen at 531-533 eV correspond to adsorbed CO₂. For the CO₂ adsorption on the β -Mo₂C (001) surface, XPS showed two separate features in the O 1s region. The first one, peaked at 529.8-530.2, could be attributed to atomic oxygen. The second one exhibited its maximum intensity at 531.2-531.5 eV and corresponds to adsorbed CO.⁵ Thus, the CO₂ \rightarrow CO + O reaction occurred on β -Mo₂C (001) but the experiments were not able to determine which surface termination (or both) was the cause of this strong interaction. Figure 4.1 was used to compare the growth of the O 1s signal on MoC and β -Mo₂C (001) after several doses of CO₂. The data seemed to show a rapid CO₂ dissociation on β -Mo₂C (001) whereas this dissociation was not detected on MoC.

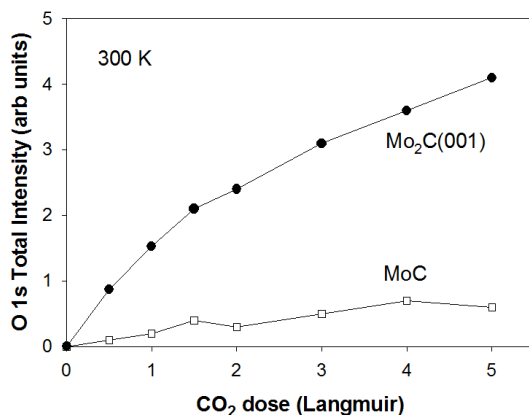


Figure 4.1: Variation of the total O 1s signal after dosing CO₂ to polycrystalline MoC and a β -Mo₂C (001) surface.

In addition, Figure 4.2 displayed that the amount of O present on the β -Mo₂C (001) surface was always larger than that of CO, a clear guide that part of the CO product dissociates towards atomic C and O. Thus, the two decomposition reactions are taking place on the β -Mo₂C (001) surface: $\text{CO}_2 \rightarrow \text{CO} + \text{O}$; $\text{CO} \rightarrow \text{C} + \text{O}$. This is particularly the case at low coverages when the concentration of O is more than doubles the concentration of CO. Once the adsorbate coverage increases on the surface, the full decomposition of CO₂ becomes more difficult and the ratio of surface O/CO decreases.

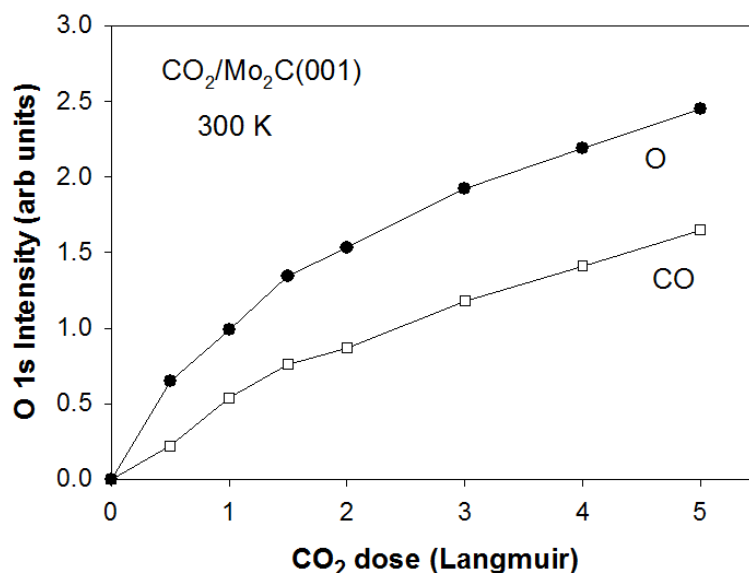


Figure 4.2. Uptake of O and CO after several doses of CO₂ to β -Mo₂C (001) at 300 K.

Respect to the CO₂ hydrogenation on both Mo carbides studied surfaces, Figure 4.3 revealed that the major products on β -Mo₂C (001) are CO and CH₄, whilst the amount of MeOH is clearly lower and also traces of C₂H₆, CH₃OCH₃, and C₂H₅OH were found by experimentalists. On the other hand, Figure 4.3 showed that on polycrystalline δ -MoC, the hydrogenation of CO₂ produced only CO and MeOH.

4.2 Experimental results

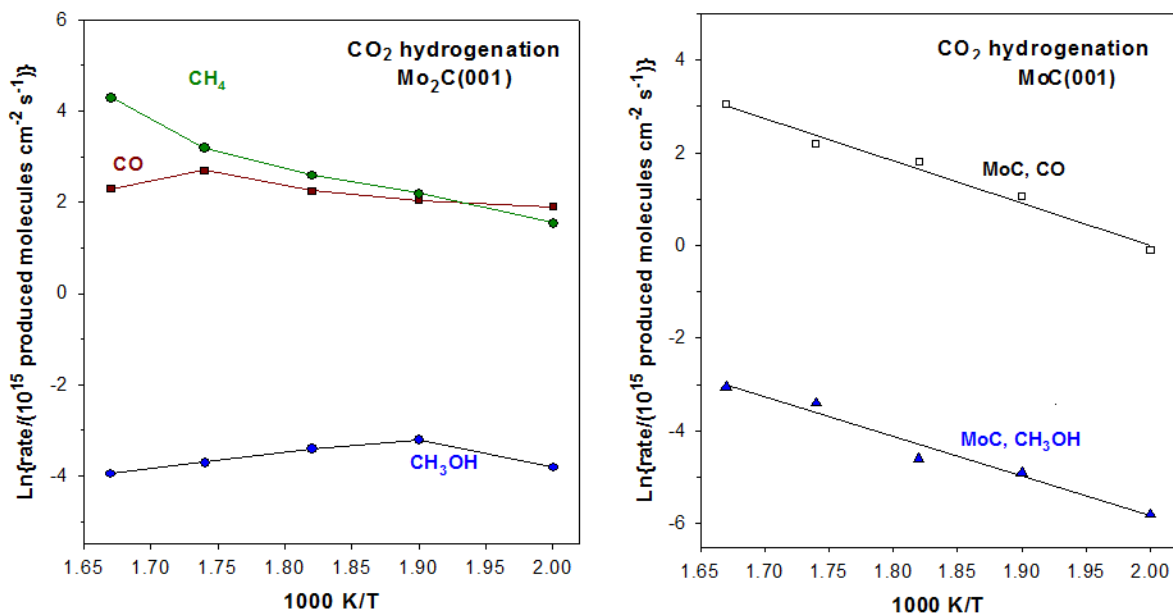


Figure 4.3: Arrhenius plot for the production of CO, methane and methanol on $\beta\text{-Mo}_2\text{C}(001)$ (left) and $\text{MoC}(001)$ (right). In a batch reactor, the metal carbide catalyst was exposed to 0.049 MPa (0.5 atm) of CO_2 and 0.441 MPa (4.5 atm) of H_2 at temperatures of 600, 575, 550, 525, and 500 K.

4.3 CO₂ study on (001) Mo carbide surfaces

4.3.1 CO₂ adsorption and activation

The first step was to determine the CO₂ molecule orientation upon adsorption. In the perpendicular to surface orientation, only one oxygen interacts with the studied surfaces whilst in the parallel to surface orientation all CO₂ atoms are in contact with the surface. The calculations indicated that the parallel adsorption of CO₂ was much more favorable than the perpendicular orientation. Indeed, the CO₂ molecule was chemisorbed if the initial orientation was parallel to the surface whereas the adsorption energy was lower than -0.3 eV, *i.e.*, CO₂ was physisorbed, when only one oxygen is in contact with catalysts. Consequently, on the following, only the results for parallel adsorption will be presented because these distributions are the main candidates to carry out the CO₂ activation and conversion.

DFT calculations acquire a great importance to study the CO₂ adsorption on β -Mo₂C (001) surface. From an experimental point of view, the two terminations (Mo and C atoms) of β -Mo₂C (001) polar surface are exposed with a proportion of ~50% each. Unfortunately, the experimental techniques are not able to distinguish the role of each termination on CO₂ activation and conversion. This is where the computational calculations could be able to elucidate the behavior of Mo and C terminations with the CO₂.

All adsorption sites were tested in order to study the interaction of CO₂ with the two terminations (Mo and C atoms) of β -Mo₂C (001) polar surface. Respect to C termination surface, the DFT calculations showed that the adsorption energy is -0.61 eV (Table 4.1). Initially, the CO₂ was placed on top of a carbon surface atom, but during the optimization process a displacement of the surface carbon atom bonded to the CO₂ molecule (1.47 Å) was observed (Figure 4.4a). The C=O bond lengths are 1.21 and 1.42

4.3 CO₂ study on (001) Mo carbide surfaces

Å, where clearly the preferential activation of a single C=O bond was observed. This fact can lead to an easier C=O bond cleavage and, therefore, the dissociation of the adsorbed molecule (CO₂ → CO + O). The CO₂ was activated, displaying an angle of 122°, because the β-C terminated ceded ~0.75 electrons, irrespective of including or not the vdW dispersion terms. In this surface, the vdW correction did not significantly change the geometry of the adsorbed CO₂ molecule on β-C surface, yet the adsorption energies slightly increase.

Table 4.1: Adsorption structural data and energy values for CO₂ molecule adsorbed on β-Mo₂C(001) surfaces.

Surface	Functional	Site	E _{ads} /eV	d(C-C) /Å	d(C=O) /Å	α(OCO) /°	ΔQ (CO ₂) /a.u.
β-C	PBE	Top C	-0.59	1.47	1.21/1.42	122	-0.76
	PBE-D2	Top C	-1.02	1.47	1.21/1.42	122	-0.75
β-Mo	PBE	Top Mo	-3.27	—	1.22 ^a	—	-0.91 ^b /-1.95 ^c
	PBE-D2	Top Mo	-3.69	—	1.26 ^a	—	-0.91 ^b /-1.97 ^c
	PBE	Bridge Mo	-1.39	—	1.27	133	-1.26
	PBE-D2	Bridge Mo	-1.76	—	1.27	133	-1.27

^a This distance belongs to the CO molecule adsorbed on β-Mo surface.

^b This ΔQ is for CO moiety.

^c This ΔQ is for O moiety.

As far as the β-Mo termination was concerned, interestingly, when the initial position was not on Top Mo, the CO₂ molecule got activated solely, whereas the CO₂ adsorption was produced on a Top Mo site, the surface evolves towards an easy C=O bond cleavage (CO + O) with larger adsorption energies (-3.27 eV at best). The E_{ads} of the non-dissociated CO₂ structure situation is -1.38 eV, and the molecule displays a C=O bond lengthening, reaching final values are 1.27 Å, in opposite with C termination surfaces, where one of the C=O atoms are larger than the other (Figure 4.4b). Again, the CO₂ molecule received charge density from the molybdenum carbide substrate of 1.26 electrons, and the molecule adopted a bended conformation with a molecular angle of 133°. As happened in β-C surface, the inclusion of vdW dispersion terms did not alter

the final structure. Respect to the dissociated structure, note that the E_{ads} of -3.27 eV is very large because it is gained considering the CO₂ molecule in vacuum as the energy reference; this is, the value adds the adsorption energy of a CO and O moieties on the surface. The CO and O moieties are preferred adsorbed on Hollow C² site.

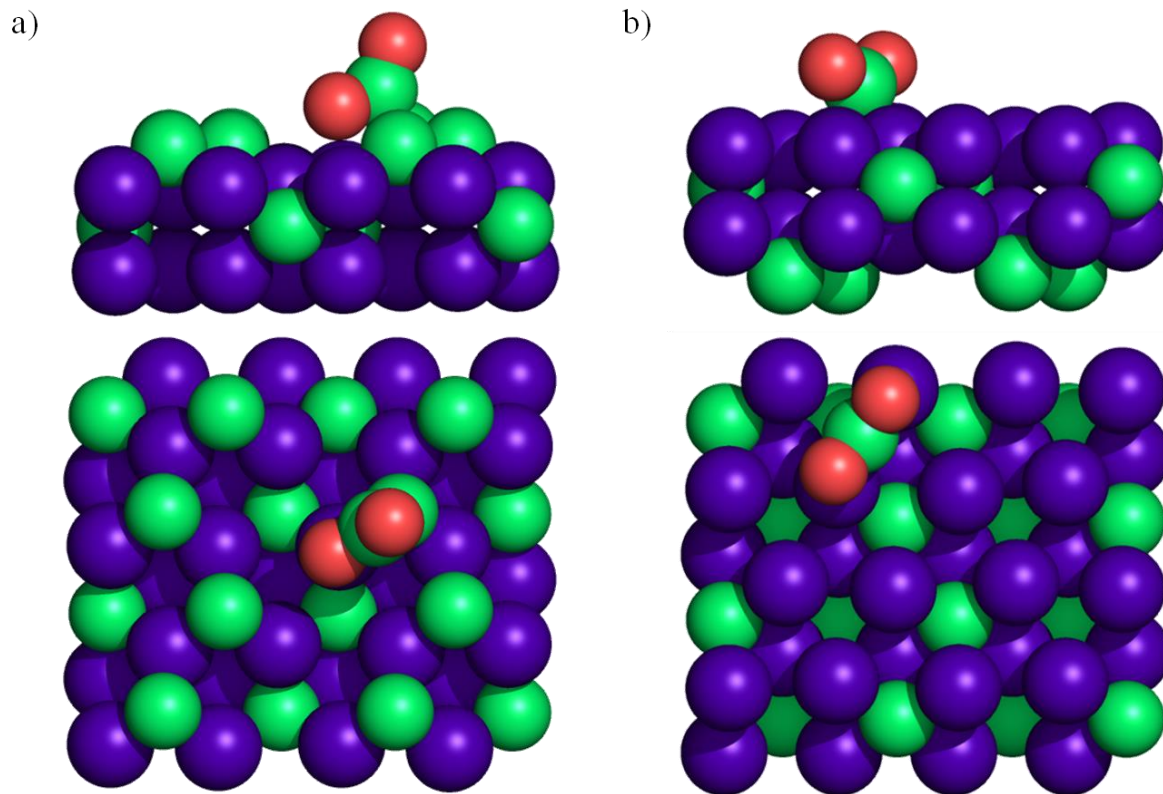


Figure 4.4: Sketches of activated CO₂ adsorption on a) β -C, b) β -Mo (001) surfaces. Showing side view (top) and top view (bottom).

The same procedure followed on β -Mo₂C (001) were carried out to investigate the CO₂ adsorption on δ -MoC (001) surface, and the main results are summarized in Table 4.2. The CO₂ molecule is adsorbed in two competitive sites (see Figure 4.5). In the first one, the C atom is above a MMC site and O atoms are on top of Mo surface atoms resulting in an adsorption energy value of -0.82 eV; in addition, upon adsorption, the molecule forms one regular C-C bond (1.46 Å) with the surface C atom. In the second

4.3 CO₂ study on (001) Mo carbide surfaces

case, the C atom is on-top of a surface C atom and the corresponding E_{ads} is -0.74 eV and the adsorbed molecule also forms a regular C-C bond (1.47 Å) with the surface C atom. Note that the C-C bond length lies between a single and a double bond. In both cases, the chemisorption of CO₂ leads to an elongation of the C=O bonds from 1.17 Å as in vacuum calculations to 1.29 Å in the adsorbed molecule accompanied by a bending of molecular angle reaching values in the 120-130° range, highlighting the molecular activation. The bending of the CO₂ molecule was found to be indicative of a net carbide→CO₂ charge transfer⁷ of ~1 electron, which transform the CO₂ molecule towards CO₂^{δ-}, with the consequent changes on the adsorbate structure. In comparison with the vdW calculations, the values listed in Table 4.2 exhibited that only adsorption strengths are increased whereas the geometries of these systems did not vary, revealing that dispersive forces do not play a role in CO₂ activation. Although the preferential site for PBE and PBE-D2 is different, the adsorption energy value difference is lower than 0.1 eV, which assure that the CO₂ adsorption on δ-MoC (001) presents two competitive adsorption sites. These results agreed with experimental evidences, since the CO₂ activation is a mandatory step to promote the CO₂ conversion towards CO and methanol.

Table 4.2: Adsorption structural data and energy values for CO₂ molecule adsorbed on δ-MoC (001) surface.

Functional	Site	E_{ads} /eV	$d(\text{C-C})$ /Å	$d(\text{C=O})$ /Å	$\alpha(\text{OCO})$ /°	$\Delta Q(\text{CO}_2)$ /a.u.
PBE	MMC	-0.82	1.46	1.30	122	-0.93
PBE-D2	MMC	-1.33	1.46	1.30	121	-1.02
PBE	Top C	-0.74	1.47	1.29	129	-0.76
PBE-D2	Top C	-1.35	1.47	1.29	129	-0.93

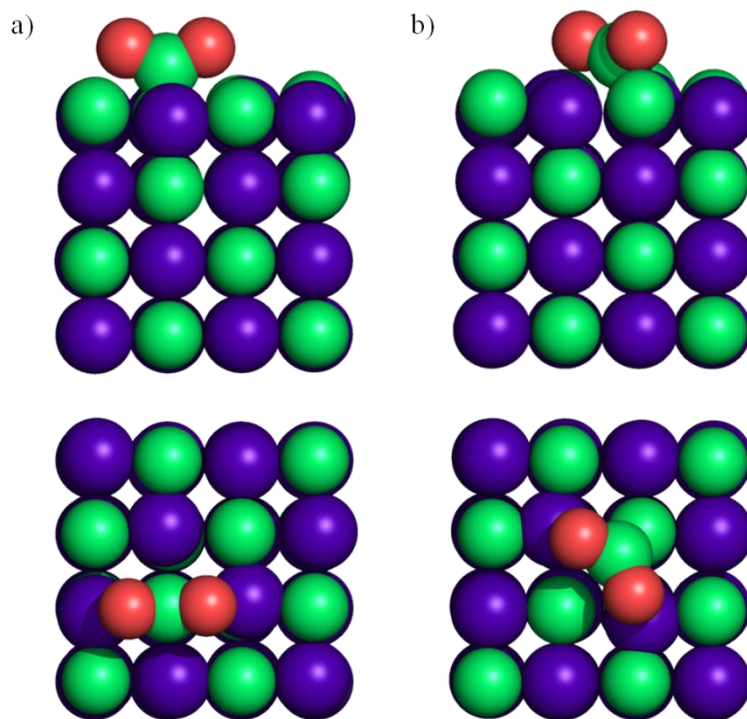


Figure 4.5: Sketches of activated CO₂ adsorption on δ -MoC (001) on a) Top C and b) MMC adsorption sites. Showing side view (top) and top view (bottom).

Table 4.3 displays the comparison of the adsorption energy values and structures of CO₂ adsorbed on the favorable sites of other (001) cubic surfaces of TMCs (TM= Ti, Nb, Zr, Hf, and Ta) with metal-carbon ratio 1:1.⁸ In general terms, the CO₂ adsorption follows the same tendency exhibited on δ -MoC (001), since the most favorable adsorption sites are Top C and MMC, which implies the C-C bond formation. The CO₂ molecules are bent with a molecular angle reaching values in the 120-129° range. Titanium and Niobium carbides display lower adsorption energies than δ -MoC. Considering that TiC (001) surface was proposed from experimental and theoretical points of view as catalyst of CO₂ conversion to methanol and the differences in the strength of the CO₂-carbide binding when going from TiC to δ -MoC, δ -MoC surfaces emerge as promising catalysts for CO₂ hydrogenation. On the other hand, HfC (001)

4.3 CO₂ study on (001) Mo carbide surfaces

and ZrC (001) surfaces exhibit adsorption energy values even larger than β -Mo surface, with a metal/carbon ratio of two. These results seem to propose a change in the reaction mechanism on these cubic transition metal carbides, where CO₂ could be dissociated directly to CO and O as in the case of β -Mo₂C (001) surfaces. Respect to TaC (001) surface, the adsorption energy values of CO₂ molecule are similar to our results on δ -MoC (001).

To summarize, the DFT results agreed with experimental evidences. The CO₂ molecule is activated on δ -MoC (001) and β -Mo₂C (001), on the two possible terminations on C and Mo atoms. Furthermore, calculations revealed that the CO₂ interaction with β -Mo₂C (001) was stronger than the CO₂ interplay on δ -MoC (001).

Table 4.3: Adsorption structural data and energy values for CO₂ molecule adsorbed on different (001) surface of metal carbides with metal/carbon ratio of one. These results come from Ref. 8.

Surface	Functional	Site	E _{ads} /eV	d(C-C) /Å	d(C=O) /Å	$\alpha(\text{OCO})$ /°
TiC (001)	PBE	Top C	-0.57	1.49	1.29	127.4
	PBE-D3	Top C	-0.83	1.48	1.29	127.5
NbC (001)	PBE	MMC	-0.59	1.47	1.31	121.3
	PBE-D3	MMC	-0.87	1.47	1.31	121.4
HfC (001)	PBE	Top C	-1.42	1.47	1.30	124.7
	PBE-D3	Top C	-1.65	1.47	1.30	124.8
ZrC (001)	PBE	Top C	-1.39	1.47	1.30	124.1
	PBE-D3	Top C	-1.60	1.47	1.30	124.2
TaC (001)	PBE	MMC	-0.95	1.45	1.30	119.9
	PBE-D3	MMC	-1.21	1.46	1.30	120.1

4.3.2 CO₂ dissociation

After the promising results about CO₂ activation on Mo carbides, the next step was focused on the direct CO₂ dissociation. As in the case of the adsorptions, the transition state geometries were calculated including or not the dispersion terms (DFT-

D2). Results depicted on Figure 4.6 and reported on Table 4.4, showed that the effect of vdW dispersion terms does not play any role on the energy barriers and TS structures. The presented DFT and DFT-D2 calculations agreed with experimental XPS plots (Figures 4.1 and 4.2). On the one hand, for β -Mo surface, the reaction profile showed that CO_2 dissociates spontaneously (0.21 eV) towards CO and atomic O. On β -C, the energy barrier is slightly superior (0.48 eV) although is easily approachable. These results are in agreement with recent results about CO_2 dissociation on α - Mo_2C (001), where the energy barrier is 0.27 eV,⁹ exhibiting the high catalytic power of Mo carbides with metal/carbon ratio of 2 for direct CO_2 dissociation. On the other hand, CO_2 is not directly dissociated on δ - MoC (001) due to the huge energy barrier (1.20 and 1.41 eV including or not the dispersion terms), in agreement with the low intensity of XPS plot of 1s O signal on Figure 4.1, which shows that CO_2 is (predominantly) not dissociated. The CO_2 sketches are displayed on Figure 4.7.

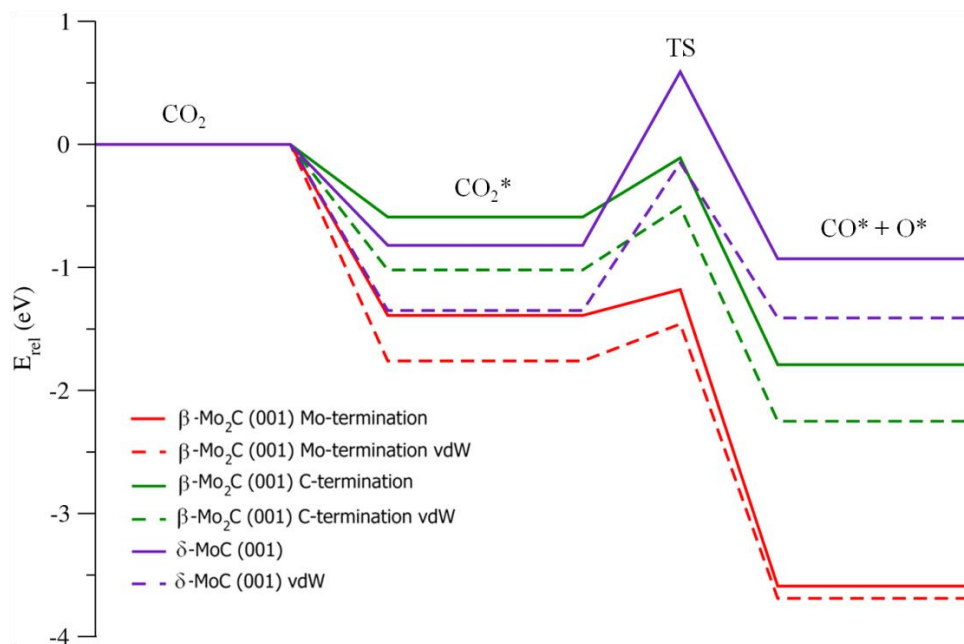


Figure 4.6: ZPE plot of CO_2 dissociation on δ - MoC and β - Mo_2C (001) surfaces. Solid and dashed lines represent the reaction mechanism without and with dispersion terms respectively.

4.3 CO₂ study on (001) Mo carbide surfaces

Table 4.4: CO₂ adsorption energy ($E_{\text{ads}}(\text{CO}_2)$), dissociation energy (ΔE), dissociation energy barrier (E_b) and H₂ formation energy barrier (E_{rb}) including vdW dispersion or not on β -Mo, β -C and δ -MoC (001) surfaces. All energies are given in eV.

	No vdW				vdW			
	$E_{\text{ads}}(\text{CO}_2)$ /eV	ΔE /eV	E_b /eV	E_{rb} /eV	$E_{\text{ads}}(\text{CO}_2)$ /eV	ΔE /eV	E_b /eV	E_{rb} /eV
β -Mo (001)	-1.39	-2.20	0.21	2.41	-1.76	-1.93	0.29	2.22
β -C (001)	-0.59	-1.20	0.48	1.68	-1.02	-1.24	0.51	1.75
δ -MoC (001)	-0.82	-0.11	1.41	1.52	-1.35	-0.06	1.20	1.26

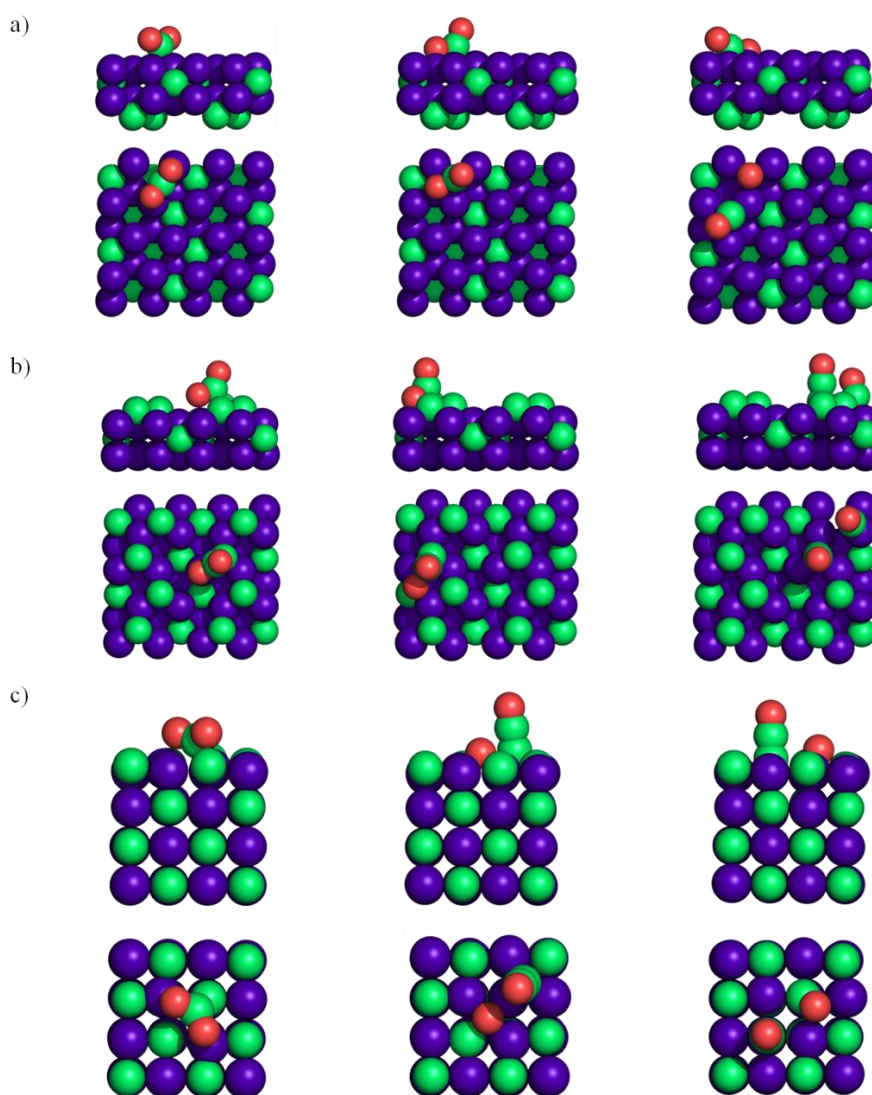


Figure 4.7: Sketches of activated CO₂ adsorption (left), TS (middle) and dissociated CO₂ (right) on a) β -Mo, b) β -C, and c) δ -MoC (001) surfaces.

4.4 CO adsorption and dissociation

The CO is one of the key moieties on the CO₂ hydrogenation towards methanol. Indeed, is the main product (joined to CH₄) using orthorhombic β -Mo₂C and cubic δ -MoC (001) surfaces. Moreover, many reactions paths for the CO₂ conversion to methanol implies the CO formation, either from direct CO₂ dissociation (CO₂ → CO + O) or CO₂ hydrogenation towards carboxylate intermediate and its subsequent dissociation to CO.

Firstly, the CO adsorption study was carried out on β -Mo₂C and δ -MoC (001) surfaces including or not the dispersion terms. Results reported on Table 4.5 exhibited that vdW dispersion did not play relevant role on CO adsorption, because its effect was only detected on the adsorption energy value. The adsorption on β -Mo surface presented various adsorption sites degenerate in energy. In all of them, CO is clearly activated due to the C=O bond elongation (1.27 Å respect to 1.12 Å in the *vacuum*). In opposite, β -C and δ -MoC surfaces have only a unique favorable adsorption site and the CO elongation is minor respect to β -Mo. Note also that on β -C and δ -MoC the C-C bond distance between C atom of CO and C surface atom is lower than the same C-C distance with CO₂ molecule (see Table 4.2).

4.4 CO adsorption and dissociation

Table 4.5: Adsorption structural data and energy values for CO molecule adsorbed on β -Mo₂C and δ -MoC(001) surface.

Surface	Functional	Site	E _{ads} /eV	d(C-C) /Å	d(C=O) /Å
β -Mo	PBE	Hollow Mo	-2.26	—	1.27
	PBE-D2	Hollow Mo	-2.55	—	1.27
	PBE	Hollow C ²	-2.25	—	1.27
	PBE-D2	Hollow C ²	-2.52	—	1.27
	PBE	Top C	-2.24	—	1.27
	PBE-D2	Top C	-2.52	—	1.27
β -C	PBE	Top C	-1.93	1.32	1.18
	PBE-D2	Top C	-2.14	1.33	1.18
	PBE	Hollow Mo ¹	-1.35	—	1.16
	PBE-D2	Hollow Mo ¹	-1.54	—	1.16
δ -MoC	PBE	Top C	-1.91	1.32	1.19
	PBE-D2	Top C	-2.21	1.33	1.18
	PBE	Top Mo	-1.18	—	1.16
	PBE-D2	Top Mo	-1.41	—	1.16

As in the case of CO₂ study, CO dissociation was performed on β -Mo₂C and δ -MoC (001) surfaces including or not the dispersion terms despite of they not play any remarkable role on CO adsorption. Figure 4.8 and Table 4.6 report the most remarkable results, which show that CO could be dissociate on β -Mo with an energy barrier of 0.86 eV. The sketches of the most stable CO, TS and CO dissociated geometries are displayed on Figure 4.9. On the other two surfaces, the CO dissociation could be discarded due to the large energy barriers, superior to 1.4 and 1.8 eV on β -C and δ -MoC surfaces respectively. These results agreed with XPS experiments reported on Figures 4.1 and 4.2, where the amount of atomic O on β -Mo₂C (001) surface is superior to the amount of CO, a clearly descriptor that part of CO is dissociated on β -Mo₂C (001) surfaces. Our DFT calculations suggested that this dissociation is produced exclusively on Mo termination. This fact could be related with the CH₄ production on β -Mo₂C surface, since the atomic C atom could be hydrogenated towards methane. Furthermore, the impossibility to dissociate CO on δ -MoC joined to the fact that the experiments do not

detect methane, remark the importance of CO dissociation to produce CH₄. This discussion will be completed in chapters 5 and 6, where the reaction mechanism of CO₂ hydrogenation will be reported. On the other hand, the CO dissociation profile agrees with the Brønsted-Evans-Polanyi (BEP) relationships connecting the reaction step energy barriers with the degree of exothermicity,¹⁰ since the larger barriers implies less exothermicity (even endothermicity in the case of δ -MoC). In general terms, the dispersion correction terms do not play remarkable role, although their effect on δ -MoC (001) is superior, increasing the energy barrier in 0.34 eV, whereas on both terminations of β -Mo₂C, this increment is between 0.10-0.17 eV.

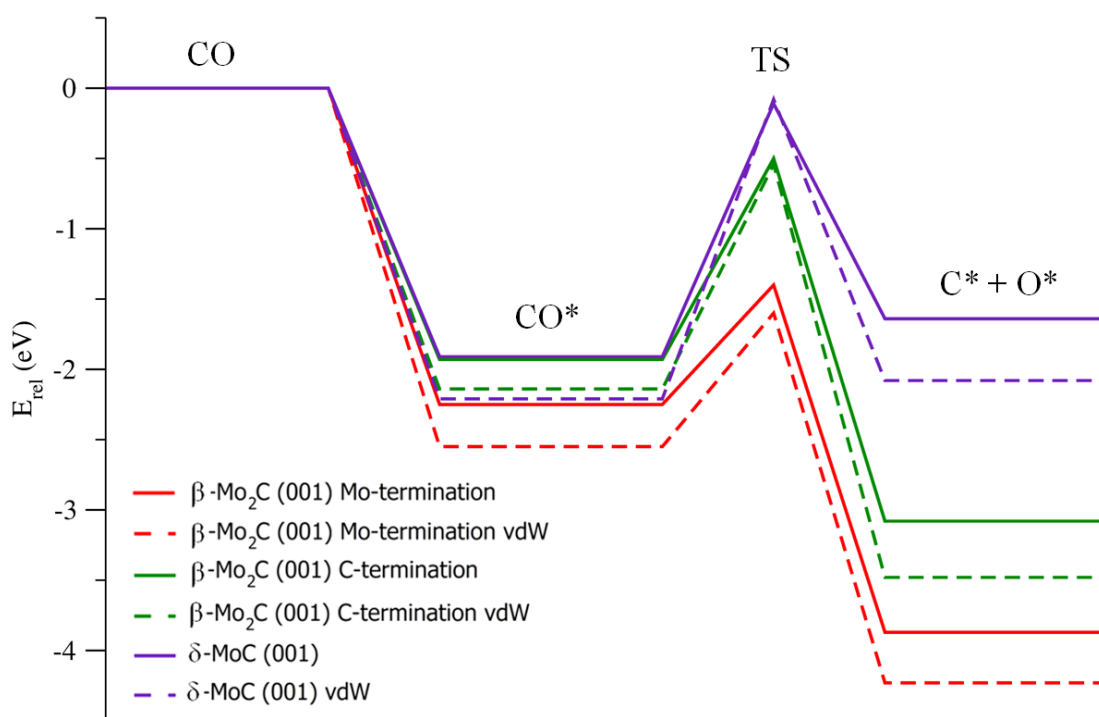


Figure 4.8: ZPE plot of CO dissociation on δ -MoC and β -Mo₂C (001) surfaces. Solid and dashed lines represent the reaction mechanism without and with dispersion terms respectively.

4.4 CO adsorption and dissociation

Table 4.6: CO adsorption energy ($E_{\text{ads}}(\text{CO})$), dissociation energy (ΔE), dissociation energy barrier (E_b) and H_2 formation energy barrier (E_{rb}) including vdW dispersion or not on $\beta\text{-Mo}$, $\beta\text{-C}$ and $\delta\text{-MoC}$ (001) surfaces. All energies are given in eV.

	No vdW				vdW			
	$E_{\text{ads}}(\text{CO})$ /eV	ΔE /eV	E_b /eV	E_{rb} /eV	$E_{\text{ads}}(\text{CO})$ /eV	ΔE /eV	E_b /eV	E_{rb} /eV
$\beta\text{-Mo}$ (001)	-2.26	-1.62	0.86	2.47	-2.55	-1.68	0.95	2.63
$\beta\text{-C}$ (001)	-1.93	-1.15	1.43	2.58	-2.14	-1.34	1.60	2.94
$\delta\text{-MoC}$ (001)	-1.91	0.27	1.79	1.53	-2.21	0.13	2.13	2.00

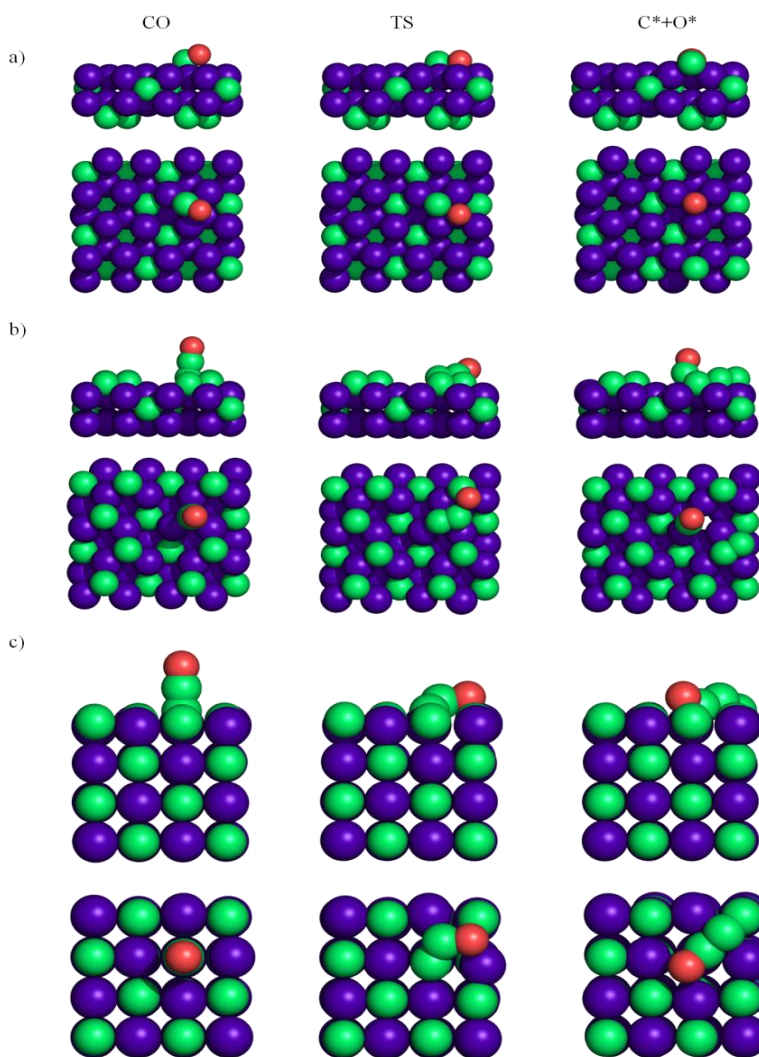


Figure 4.9: Sketches of activated CO adsorption (left), TS (middle) and dissociated CO (right) on a) $\beta\text{-Mo}$, b) $\beta\text{-C}$ and c) $\delta\text{-MoC}$ (001) surfaces.

4.5 H₂ study on (001) Mo carbide surfaces

The CO₂ conversion to alcohols and many green chemical reactions involve hydrogenation and/or dehydrogenation steps. Hence, the relative stability of the different phases of the Mo carbides in absence/presence of H₂ is also an important issue to evaluate their possible use in hydrogenation reactions. Likewise, the study of the H₂ adsorption/desorption and H₂ dissociation/formation elementary steps is important since these are common and determinant ones and, therefore, understanding the molecular mechanisms involved in these pathways is essential to reach a complete picture of the underlying chemistry. Therefore, the study of the interaction of H₂ with β -Mo₂C and δ -MoC (001) surfaces is a mandatory step.

4.5.1 H₂ adsorption and dissociation

Figure 4.10 displays the ZPE energy profile for H₂ dissociation including or not the vdW correction. Table 4.7 summarizes the reaction energy values (ΔE), the H₂ dissociation energy barriers (E_b) and the H₂ formation energy barriers (E_{br}). The sketches exhibited on Figure 11, represent the H₂, the transition states (TS) and 2H adsorptions corresponding to the calculations including the vdW dispersion, since as is explained below, except in the case of the β -Mo surface results including vdW interactions are slightly different from those neglecting them.

Table 4.7: H₂ adsorption energy ($E_{\text{ads}}(\text{H}_2)$), dissociation energy (ΔE), dissociation energy barrier (E_b) and H₂ formation energy barrier (E_{rb}) including vdW dispersion or not on β -Mo, β -C and δ -MoC (001) surfaces. All energies are given in eV.

	No vdW				vdW			
	$E_{\text{ads}}(\text{H}_2)$ /eV	ΔE /eV	E_b /eV	E_{rb} /eV	$E_{\text{ads}}(\text{H}_2)$ /eV	ΔE /eV	E_b /eV	E_{rb} /eV
β -Mo (001)	-0.67	-1.20	~0	1.20	-0.82	-1.20	~0	1.20
β -C (001)	-0.02	-2.31	0.32	2.63	-0.30	-2.26	~0	2.27
δ -MoC (001)	-0.46	-0.11	0.64	0.75	-0.70	-0.35	0.60	0.96

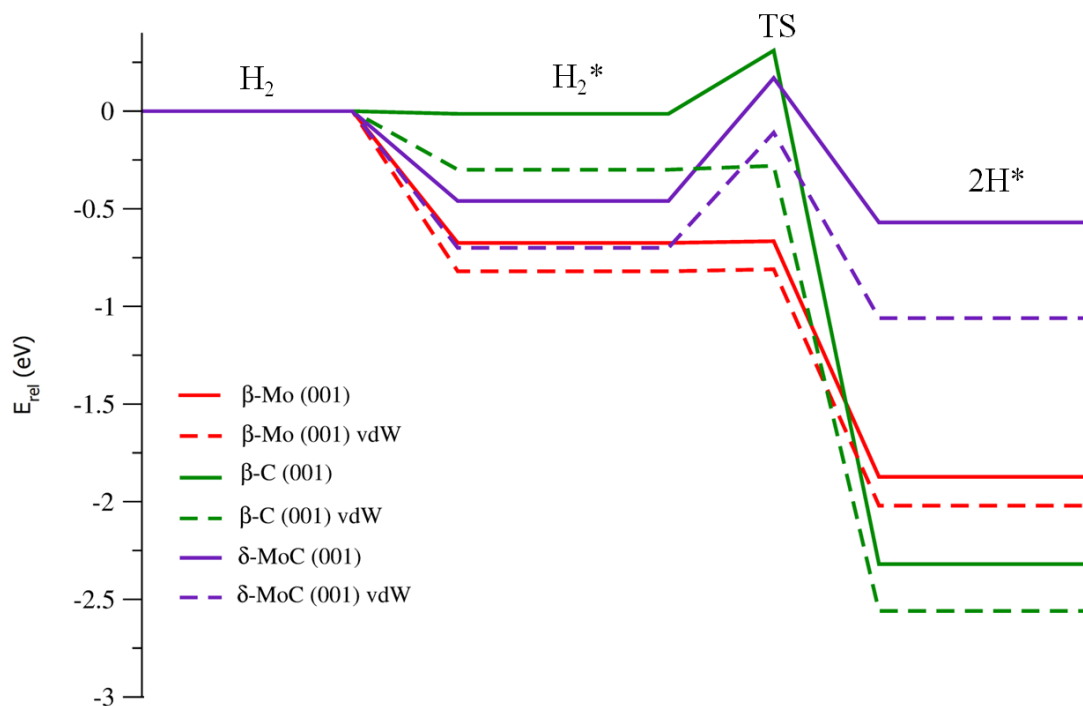


Figure 4.10: ZPE plot of H₂ dissociation on δ -MoC and β -Mo₂C (001) surfaces. Solid and dashed lines represent the reaction mechanism without and with dispersion terms respectively.

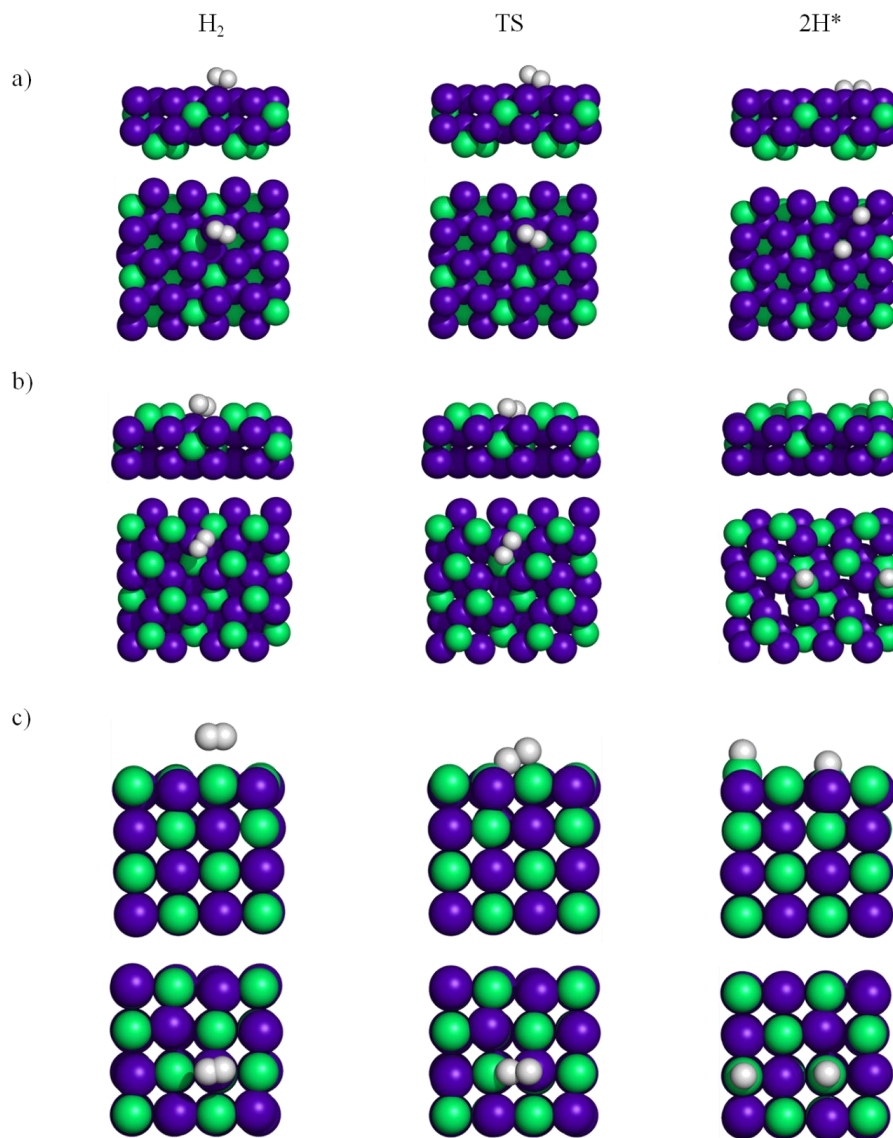


Figure 4.11: Sketches of activated H_2 adsorption (left), TS (middle) and dissociated H_2 (right) on a) β -Mo, b) β -C and c) δ -MoC (001) surfaces. These structures are calculated including the dispersion terms.

In the case of the β -Mo surface, both approaches described the H_2 dissociation as an essentially spontaneous process. The H_2 adsorption energy presents a difference of 0.15 eV between calculations with or without vdW dispersion, and the same difference was found for the two adsorbed hydrogen atoms. Thus, the calculated energy barrier

for the H₂ formation including or not dispersion is the same (1.20 eV). Therefore, these results indicated that vdW dispersion does not play a crucial role on the H₂ energy profile on β -Mo, probably because the electronic interaction between β -Mo and H₂ molecule is already strong (-0.67 eV), and vdW dispersion is usually used for describing very weak interactions. Note that, as is reported in Table 4.8, the H₂ adsorption geometry including or not the dispersion terms do not vary significantly, only 0.02 Å on the H-H bond distance.

Table 4.8: Adsorption structural data and energy values for H₂ molecule adsorbed on β -Mo and surface.

No vdW				vdW			
Initial site	Final Site	E _{ads} /eV	d(H-H) /Å	Initial site	Final site	E _{ads} /eV	d(H-H) /Å
TopMo ¹	TopMo ¹	-0.67	0.91	TopMo ¹	TopMo ¹	-0.82	0.93
TopMo ²	TopMo ²	-0.67	0.91	-	-	-	-
Bridge	Dissociated	-	-	Bridge	Dissociated	-	-
Hollow Mo	Dissociated	-	-	Hollow Mo	Dissociated	-	-
Hollow C ¹	Dissociated	-	-	Hollow C ¹	Dissociated	-	-
Hollow C ²	Dissociated	-	-	Hollow C ²	Dissociated	-	-

The H₂ adsorption on β -C surface, showed a very weak interaction between H₂ and β -C surface (-0.02 eV) and the dissociation process has an energy barrier of 0.33 eV without vdW dispersion. Therefore, H₂ desorption is favored with respect to dissociation, and, consequently, these results would seem to indicate that the H₂ dissociation does not occur on C termination of orthorhombic Mo₂C (001) surface. However, calculations explicitly including the vdW dispersion terms predicted a physisorption state with an adsorption energy of -0.30 eV with an essentially zero barrier for dissociation. It is mandatory remark that the H-H bond distance differ slightly (from 0.74 to 0.89 Å) on the majority of tested sites if the dispersion terms are included, displaying the H₂ activation as is reported on Table 4.9. The H₂ dissociation exhibited a large exothermicity due to the CH moiety formation, which also provokes a surface reconstruction as is shown on Figure 4.11b, where the CH moiety at low

coverage, is displaced from the initial position to the vicinal Hollow Mo² sites. This C redistribution, which was observed in previous section with CO₂ as adsorbate, stabilize the surface energy increasing the exothermicity of the H adsorption process. Thus, calculations suggested that H₂ dissociation is likely to occur on both surface terminations. Since in the case of the β -C surface the interaction with H₂ is very weak, the inclusion of vdW terms becomes unavoidable. In comparison to H₂ adsorption on hexagonal α -Mo₂C phase,¹¹ the H₂ dissociation was also very exothermic and involved a very low energy barrier (less than 0.30 eV) reinforcing the idea that Mo carbides with metal/carbon ratio of two are very reactive.

Table 4.9: Adsorption structural data and energy values for H₂ molecule adsorbed on β -C and surface.

No vdW				vdW			
Initial site	Final Site	E _{ads} /eV	d(H-H) /Å	Initial site	Final site	E _{ads} /eV	d(H-H) /Å
TopC	TopC	-0.01	0.74	TopC	TopC	-0.06	0.75
Hollow C	Hollow C	-0.02	0.75	Hollow C	Bridge C Hollow	-0.30	0.89
Hollow Mo ¹	Hollow Mo ¹	-0.02	0.74	Hollow Mo ¹	Bridge C Hollow	-0.30	0.89
Hollow Mo ³	Hollow Mo ³	-0.02	0.74	Hollow Mo ³	Bridge C Hollow	-0.30	0.89
Bridge	Bridge	-0.02	0.74	Bridge	Bridge C Hollow	-0.30	0.89

Calculations concerning the δ -MoC (001) show that the energy barrier for H₂ dissociation is not affected by dispersion; 0.60 and 0.64 eV, without and with dispersion, respectively. Table 4.10 show that the H-H bond activation is not produce neither including nor neglecting the dispersion terms. Respect to the exothermicity of the reaction, the δ -MoC (001) surface is unsurprisingly similar to those on C termination given that both surfaces contain C atoms in the first layer leading to the C-H bond (~1.10 Å) formation, leading to the C displacement in z axis direction, as was reported previously¹² on a set of metal carbides with metal/carbon ratio of one.

Table 4.10: Adsorption structural data and energy values for H₂ molecule adsorbed on β -C and surface.

No vdW				vdW			
Initial site	Final Site	E _{ads} /eV	d(H-H) /Å	Initial site	Final site	E _{ads} /eV	d(H-H) /Å
TopC	TopC	-0.45	0.75	TopC	TopC	-0.67	0.75
TopMo	TopMo	-0.46	0.75	TopMo	TopMo	-0.68	0.77
4-Hollow	TopMo	-0.46	0.75	4-Hollow	4-Hollow	-0.68	0.75
Bridge C	Bridge C	-0.45	0.75	Bridge C	TopMo	-0.70	0.76
Bridge Mo	Bridge C-Mo	-0.45	0.75	Bridge Mo	4-Hollow	-0.50	0.75
Bridge C-Mo	TopMo	-0.15	0.76	Bridge C-Mo	TopMo	-0.42	0.79

Table 4.11 encompasses the thermodynamic and kinetic results on different carbides with metal/carbon ratio 1:1 using PW91 functional without including the dispersion correction terms. The next discussion comparing the H₂ adsorption on various carbides with metal/carbon ratio of one must be taken with caution, since the computational level is different (PW91 or PBE) and the dispersive forces effects does not include in these previous studies, which could give rise that the transition state would lie below the desorbed H₂ energy level, and, therefore, dissociation would be more favorable than desorption.

The H₂ adsorption on TiC (001) and ZrC (001) leads to similar adsorption energy values and, in both cases, dissociation is exothermic although slightly more for the latter carbide. This is in line with similar chemical activity of group IV carbides towards O₂ dissociation.^{13,14} The H₂ adsorption on TiC (001) performed using a large (3×3) supercell revealed that the molecule prefers to bind on top of a surface C atom with the H₂ aligned towards vicinal surface C atoms and with a strong interaction leading to a calculated value of -0.48 eV for the adsorption energy.¹⁵ In the final state (dissociated molecule), there is strong interaction between the adsorbed H atoms and the underlying TMC surface, which is evidenced by H adatom displacement perpendicular to the surface (C-H stretching) as is reported in this thesis for δ -MoC (001) surface. Thus, the different computational levels used exhibited the same behavior of these metal carbides.

Despite the similitude in adsorption and reaction energy, the H₂ dissociation energy barrier on ZrC (0.80 eV) is noticeable larger than on TiC (0.52 eV). The energy barrier for H₂ dissociation on the δ -MoC (001) surface is of the order of the value reported on TiC (001)¹⁵⁻¹⁷ and ZrC (001)¹⁸ which have also an face centered cubic structure, although the functional used is different.

Nevertheless, the situation for H₂ on VC (001) and δ -MoC (001) surfaces is quite different since calculations with the PW91 functional predict a positive adsorption energy, in disagreement with the calculations carried out in this thesis, where the H₂ adsorption on δ -MoC (001) at PBE level showed adsorption energies around -0.46 and -0.70 eV depending if the dispersion terms were included or not. Moreover, previous works also showed that on these two surfaces, H₂ dissociation was unlikely. However, a strong deformation of the surface which eventually leads to the extraction of surface C atoms and the formation of CH entities was detected, as in the case of other metal carbides tested on previous studies. The discrepancy between results predicted by the PW91 and PBE functionals is cumbersome to explain since these functionals usually exhibit quite similar trends¹⁹ and since the PBE reaction exothermicity remains similar to the one predicted by PW91. It is worth to point that discrepancy may well arise from slightly smaller lattice parameter (0.02 Å) as calculated at PBE level compared to PW91 values.

Table 4.11: Data of previous works about the H₂ adsorption and dissociation on different TMCs.

System	Xc	$E_{H_2}^{ads}$ /eV	E_{2H}^{ads} /eV	E_{act} /eV	E_{react} /eV
TiC (001)	PW91 ¹⁵	-0.48	-0.91	0.52	-0.43
	PW91 ¹⁷	-0.05	-0.35	0.60	-0.30
ZrC (001)	PW91 ¹⁸	-0.66	-1.10	0.80	-0.44
VC (001)	PW91 ¹⁸	0.04	0.28	—	0.24
δ -MoC (001)	PW91 ¹⁸	0.04	-0.46	—	-0.50

^a Ref. 15, ^b Ref. 17, ^c Ref. 18

4.5.2 Full coverage surface hydrogenation

From an experimental point of view, the amount of H₂ used is usually in excess in order to carry out hydrogenation reactions.^{20,21} Therefore, the catalyst surface is likely to be completely covered by H atoms and this situation needs to be considered as well. To this end, different coverages containing of one, two, eight, and sixteen H adsorbed atoms on the (2×2) supercells were tested. A similar study was performed by Wang *et al.*²² on the same (2×2) supercells, although this is slightly different from the situation studied up to 20 and 24 adsorbed H atoms were considered depending on the surface termination. Our study considered that a maximum coverage is reached by 16 adsorbed H atoms since the sequential H₂ dissociation steps necessarily need available surface-active sites, and probably, higher energy barriers would be obtained for subsequent hydrogenation due to the fact that active sites would be already occupied by H atoms. The adsorption energy values *per atom*, listed on Table 4.12, indicate that the full coverage surface hydrogenation is favorable and shows that the adsorption energy *per atom* is practically the same whether the adsorption process includes eight or sixteen H atoms above the supercell. The most noticeable variations are detected on δ -MoC (001) surface.

Table 4.12: Adsorption energies *per atom* (eV) for different H coverage on β -Mo₂C and δ -MoC (001) surfaces.

	No vdW			vdW		
	2H	8H	16H	2H	8H	16H
β -Mo	-3.23	-3.07	-3.09	-3.31	-3.14	-3.17
β -C	-3.53	-3.01	-2.91	-3.65	-3.11	-2.98
δ -MoC	-2.67	-2.55	-2.10	-2.90	-2.68	-2.78

The full coverage adsorption on β -Mo surface, reveals that the H atoms occupy hollow Mo sites despite of the fact that on the co-adsorption of two and eight H atoms,

the most favorable site is the C^2 hollow, in agreement with Wang *et al.*²² Probably this variation is due to the distribution of sites in the supercell surface model; β -Mo surface contains eight hollow C^2 and sixteen hollow Mo sites. If the first eight H atoms are adsorbed on hollow C^2 , the rest of eight H atoms should be adsorbed on hollow Mo and/or hollow C^1 , increasing the H-H interaction owing to the H-H proximity. Nevertheless, the sixteen H adsorption on Hollow Mo sites reduces these H-H interactions. Regarding to the hydrogen adsorption on the β -C surface, the reconstruction detected at low coverages is also observed at 50% coverage (eight H atoms). This is because after the H adsorption, the surface energy of the reconstructed β -C is ~ 0.7 eV more stable than non-reconstructed surface, where the C displaced atoms are located on Hollow Mo^2 sites (see Figure 4.12).

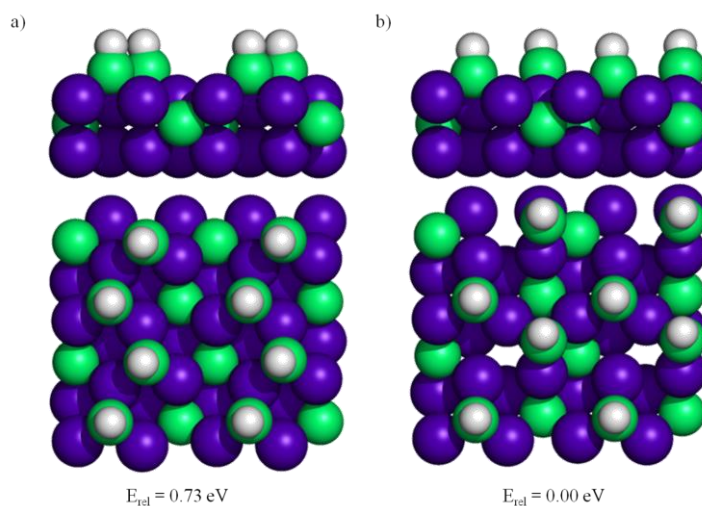


Figure 4.12: Sketches of side views (top) and top views (bottom) of non-reconstructed (a) and reconstructed (b) β -C (001) surface at 50% of coverage of H atoms.

Nevertheless, tests at full coverage—see Figure 4.13— reveal that the most stable β -C surface is a non-reconstructed structure. The full coverage hydrogenation on β -C surface leads to two degenerate structures even though both involve top C sites. The difference in these two different structures is on the distribution of CH, CH₂, and CH₃

groups; Note also that structure A contains the three kinds of possible moieties whereas on B, only CH and CH₃ are present. Structure A is slightly more stable (~ 0.12 eV) than B although the adsorption energy *per* H atom is practically the same. In comparison to the study of Wang *et al.*,²² the stepwise adsorption of H atoms used by these authors lead to a situation where the sixteen H atoms are located on top of C atoms, leading to the formation of CH₂ moieties. In the present work, this structure (D) is ~ 0.3 eV less stable than the A structure. Geometries where only CH moieties are formed, and the rest of H atoms are located on Hollow C and Mo sites, are ~ 2 eV higher in energy (E and F).

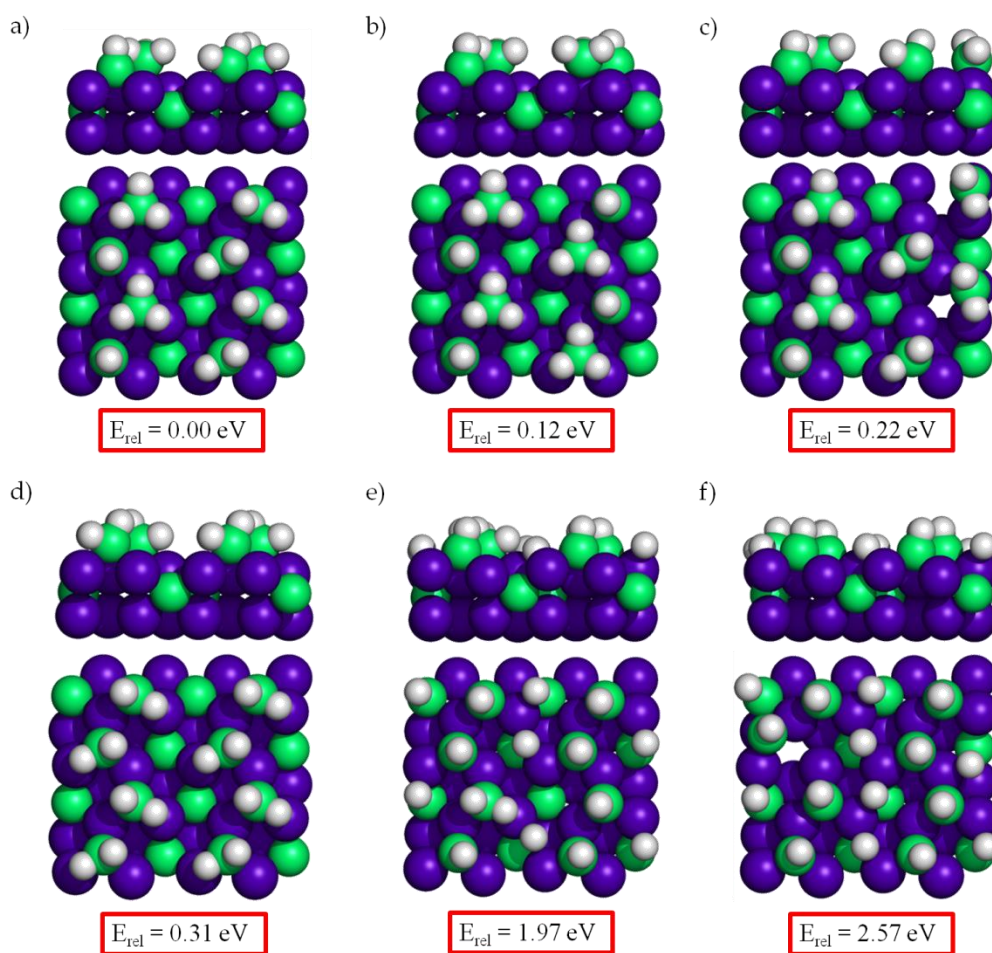


Figure 4.13: Sketches of side views (top) and top views (bottom) of β -C (001) surfaces after the full coverage H adsorption.

On δ -MoC (001) surface, H atoms occupy top-C and top-Mo sites at full coverage, where from the eight C-H bonds thus formed, only four involve a significant (~ 1 Å) displacement of the C atoms along the *vacuum* direction. The reason behind this surface rumpling is simply to decrease the vicinal H-H repulsion. To proof that this is the case, calculations were carried out hampering these C displacements. In this artificial structure, the total energy was 2 eV higher. On the other hand, in the half coverage situation, H adsorption occurs only on top of C surface atoms, where the C surface rumpling is not as pronounced as compared to full coverage situation.

4.5.3 Relative stability of H-covered Mo_nC (001) surfaces

The largely exothermic adsorption energy values reported on Table 4.12 show that the presence of H atoms stabilize these surfaces. In the case of δ -MoC (001), the strong interaction implies a considerable surface rumpling. Nevertheless, considering only the adsorption energy values is not possible to establish the relative stability of surfaces with different H coverage situations. To estimate the relative stability of H-covered of β -C, β -Mo, and δ -MoC (001) surfaces we rely on the calculated surface free energy of H covered (γ^{cover}) following the *ab initio* atomistic thermodynamics formalism described in section 2.9 and using values of hydrogen chemical potential ($\Delta\mu_{0\text{H}_2}$) at different working temperatures and pressures, and the pertinent surface free energy values.

It is very important to remark that for the special case of Mo_2C carbides surfaces, the slab and relaxation model used in the present work (four layers, two of them fixed and the two-outermost relaxed) leads to different energy values depending on the surface termination. For this reason, in order to calculate the Gibbs free energy of clean surface (γ^{clean}), we approximate γ^{clean} as the surface energy predicted in previous works.²³ In the case of Mo- and C-terminated β - Mo_2C surfaces we used instead the cleavage energies computed as proposed by Moreira and coworkers.²⁴ This is because to

estimate the surface energy of slabs with two differently terminated surfaces is cumbersome.²⁵ Note that, using these surface energy values, the chemical potential of C and Mo atoms does not need to be taken into account. Instead, the calculated values are referred to MoC and Mo₂C bulk materials.

The main goal is to predict the phase diagram representing the temperature *vs.* pressure. However, to obtain these diagrams requires the use of experimental data. As is reported on Eq. 2.48, the adsorption Gibbs free energy depends of the chemical potential of the adsorbed specie (H₂ in our case), which depends directly of the partition function. Thus, the partition function must be calculated at all pressures and temperatures, which becomes the process as unapproachable due to the high number of calculations required. In this subsection, we want to study the Gibbs free energy surface stability with and without the use of experimental data.²⁶

Figure 4.14 reports the calculated adsorption free energy of the three studied surfaces respect to the H coverage at different temperatures setting the external pressure to 5 atm. The partition function was calculated at 5 atm, varying the temperature between 300 and 600 K. From Figure 4.14, one can first observe that increasing the temperature slightly destabilizes the surfaces. Note that for β -Mo₂C, independently of the surface termination, the surface stability increases with increasing H coverage at working conditions. From the preceding discussion this fact is not so unexpected since H atoms adsorption on this surface result in the formation of strong C-H bonds in the case of β -C surface, and, in the case of β -Mo, the charge transfer from Mo to H atoms stabilizes the system. A slightly different situation is found for the δ -MoC (001) surface where it is stabilized up to half coverage, whereas further increasing of hydrogen coverage up to full coverage destabilizes the surface. This is simply because situation with H coverage higher than 50% involve H atoms at Mo sites; recall that H atoms are preferably bonded to C surface sites Furthermore, the surface area is

lower than on β -Mo₂C, which probably implies a superior H-H repulsion at higher coverages.

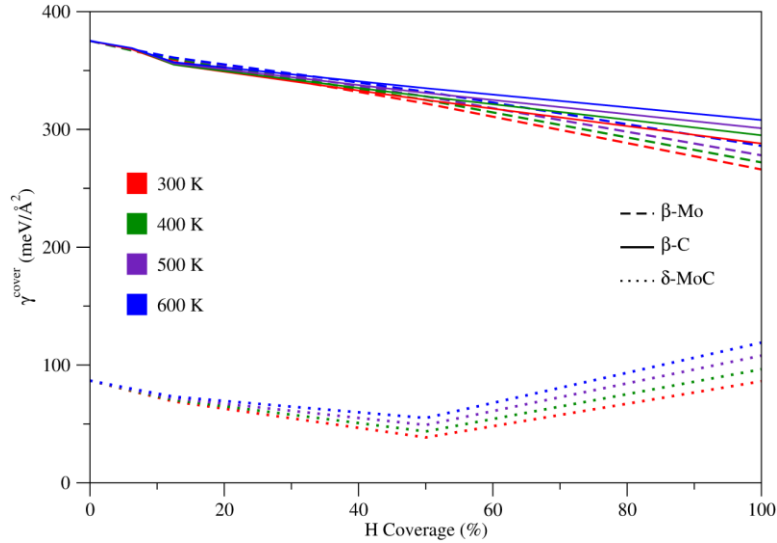


Figure 4.14: Plots of surface free energy at H coverage (γ^{cover}) depending of the temperature at different H coverage at 5 atm of pressure.

On the other hand, the use of experimental data let to obtain a scanning at different temperatures and pressures. The Eq. 2.49 could be modified as follows:

$$\gamma^{\text{ads}}(p, T, N_{\text{ADS}}) \frac{1}{A} \left[E^{\text{cover}} - E_{\text{Mo}_x\text{C}}^{\text{slab}} - N_{\text{ADS}} \left(\frac{E_{\text{ADS}}}{2} + \frac{E_{\text{ADS}}^{\text{ZPE}}}{2} \right) - N_{\text{ADS}} \Delta\mu_{0_{\text{ADS}}} - N_{\text{ADS}} k_B T \ln \frac{p}{p_0} \right] \quad \text{Eq. (4.1)}$$

where the $\Delta\mu_{0_{\text{ADS}}}$ is the experimental chemical potential at different temperatures (T). Thus, since a theoretical point of view we only need the energy of the covered surface (E^{cover}), the energy of clean surface ($E_{\text{Mo}_x\text{C}}^{\text{slab}}$) and the energy of the adsorbate in *vacuum* including the ZPE correction. So, the $\gamma^{\text{ads}}(p, T, N_{\text{ADS}})$ can be calculated oscillating the $\ln \frac{p}{p_0}$ value from ultra high *vacuum* to ambient pressures in front of temperature. Figure 4.15 provides the T vs. p diagrams for the tested surfaces. For all surfaces, note that the adsorption of 2H atoms is favorable respect the adsorption of 1H atom. On the other hand, on β -Mo and β -C (4.15a and b) the full coverage is favorable at low temperatures

whereas on δ -MoC (4.15c), the 50% of coverage is favorable respect to full coverage in agreement with theoretical predictions at 5 atm exhibited on Figure 4.14.

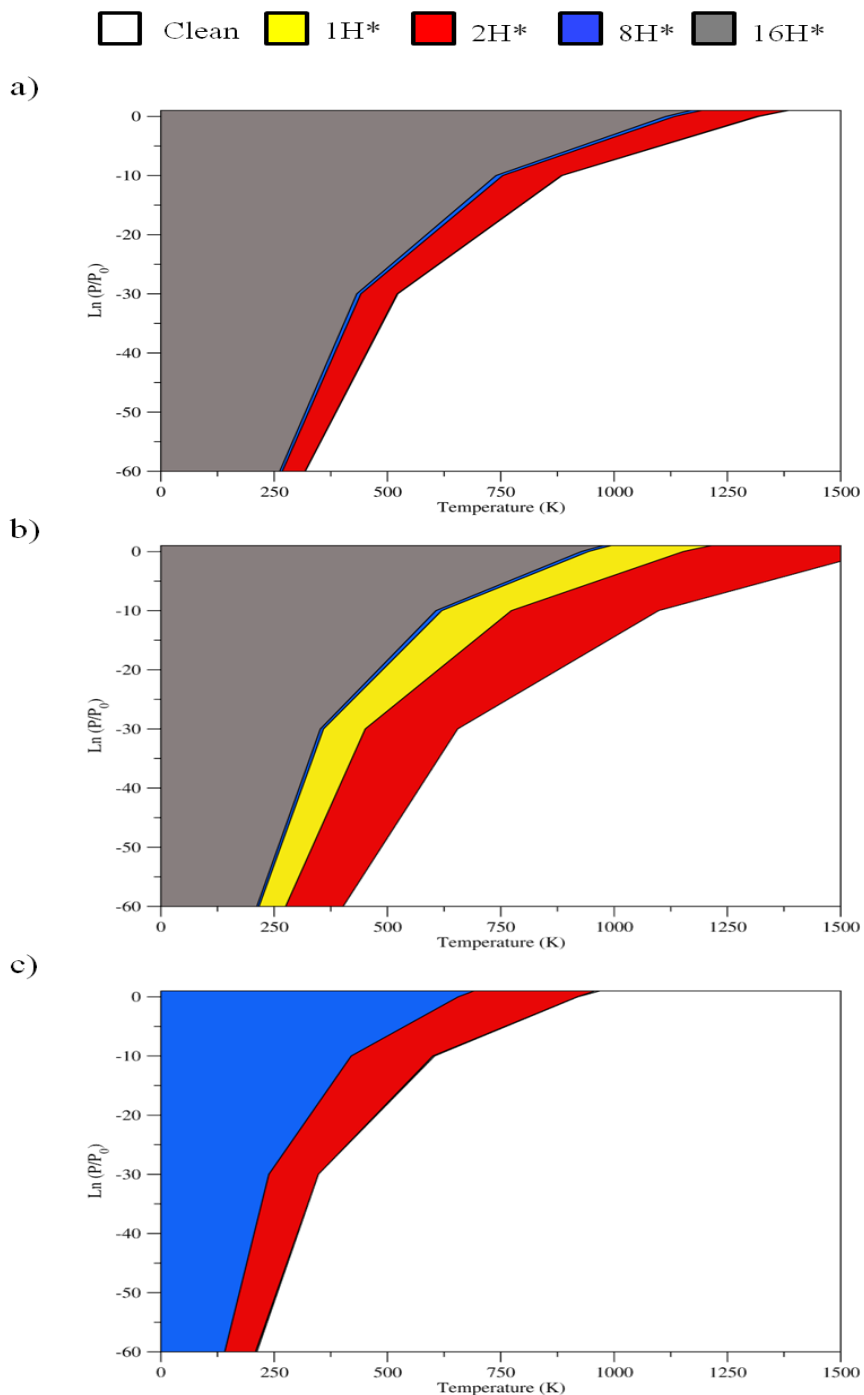


Figure 4.15: Phase diagram of a) β -Mo, b) β -C, and c) δ -MoC (001) at different H coverage as function of pressure and temperature

4.6 CH₄ study on (001) Mo carbide surfaces

Methane emerged as the main product on the CO₂ hydrogenation using β -Mo₂C (001) as catalyst whereas on δ -MoC (001) methane is not produced. Consequently, a computational study about the CH₄ adsorption on these (001) Mo carbide surfaces were accomplished since it was considered an essential step to understand the reaction mechanism of CO₂ hydrogenation. Besides, in the field of industry and green chemistry, one of the most important research goals during the last years has been the study of a large-scale chemical conversion of CH₄ into environmentally friendly chemical compounds. Despite of the fact the methane emissions are five times lower²⁷ than CO₂ (the most abundant has in the Earth's atmosphere after water), CH₄ can retain 23 times more heat than CO₂, and consequently it has a key role on the greenhouse effect. Therefore, and given that the promising results for CO₂ activation, it was intended to analyze the possible use of these Mo carbide catalysts for CH₄ activation, since it is the most stable alkane molecule, and, thus its activation is very difficult. The CH₄ activation has been extensively studied using catalysts based on transition metals,^{28,29} nickel being the most common metal among them,³⁰ even though it has been determined in theoretical³² and experimental studies³³ on single crystal surfaces that platinum could reduce the energy barrier of the rate-limiting reaction step which corresponds to the first C-H bond scission. Once CH₄ is activated, it can be used in a variety of reactions, such as methane partial oxidation ($\text{CH}_4 + 1/2\text{O}_2 \rightarrow \text{CO} + 2\text{H}_2$),³⁴⁻³⁶ steam reforming ($\text{CH}_4 + \text{H}_2\text{O} \rightarrow \text{CO} + 3\text{H}_2$),^{33,37} or methane dry reforming ($\text{CH}_4 + \text{CO}_2 \rightarrow 2\text{CO} + 2\text{H}_2$).³⁸⁻⁴¹

For each of the sites described in Figure 3.6, three possible adsorption CH₄ orientations have been tested; with one, two, or three hydrogen atoms aiming to the surface as seen in Figure 4.16. Considering the tested surfaces sites and the molecular orientations, more than 80 different adsorption structures were explored for methane

adsorption. For the sake of simplicity, the adsorbed conformations shall be labelled hereafter only by the methane configuration (H₁, H₂, and H₃), the adsorption surface (δ for δ -MoC(001), β (C) and β (Mo)) and the site of adsorption. The adsorption sites are labelled as follow: h for hollow, tC for Top C, tMo for Top Mo and b for Bridge. For β -Mo₂C (001) the labels of hC and hMo have been added to distinguish the different hollow sites. To clarify any doubt, consider the adsorption of methane with one Hydrogen directed to δ -MoC (001) surface on top Mo site; its label would be δ -H₁(tMo).

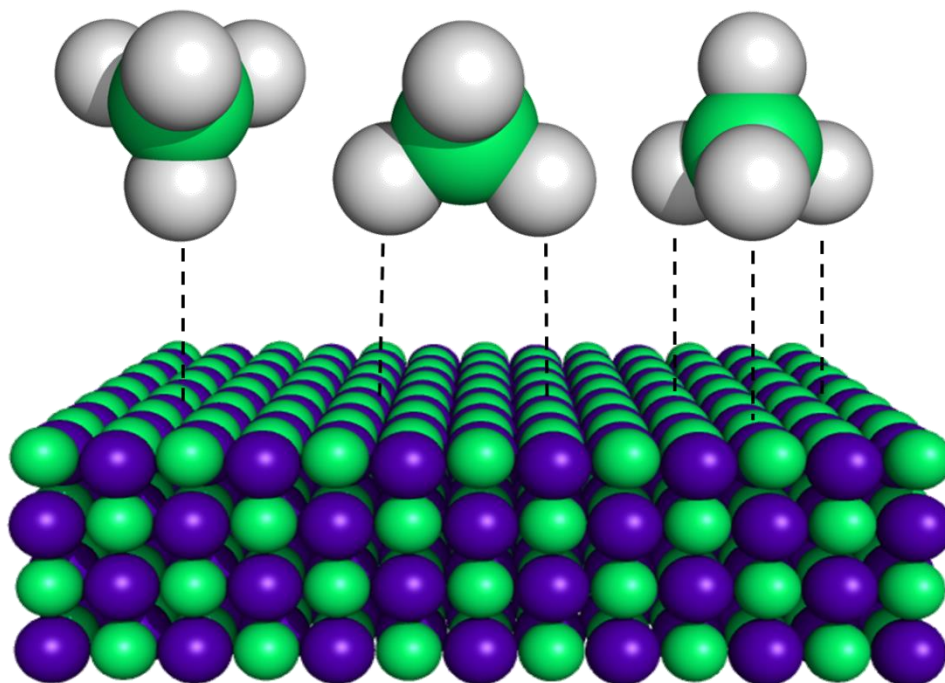


Figure 4.16: Sketches of the three different tested methane orientations. The images show methane molecules with one Hydrogen (left), two Hydrogen (middle), or three Hydrogen (right) atoms, pointing to the surface.

The results about the CH₄ adsorption on β -Mo₂C (001) are listed in Table 4.13, which encompasses both the site preferences and the adsorption energy values including vdW or not. Furthermore, the increase of the C-H bond distances respect to the isolated molecule in gas phase (1.095 Å), the Bader charges and the desorption temperature calculated by means of the Redhead equation (2.31) were also reported.

Note in passing by that E_{ads} is slightly higher on Mo-termination compared to C-termination. Both surfaces display slightly higher adsorption energies of CH_4 compared to various Ni surfaces. Results obtained including a vdW description are -0.19 eV for Ni (110) and Ni (100) surfaces, -0.24 eV for Ni (533), and -0.31 for Ni (577).⁴² On $\beta\text{-Mo}_2\text{C}$ (001) the adsorbed molecule structure is almost indistinguishable from the one in gas phase which is similar to results for CH_4 on Ni surfaces. Consistent with the rather low adsorption energy values, the estimated desorption temperatures are also low, much lower than room temperature. Moreover, the increase of C-H bond distances with respect to the isolated methane molecule are negligible in all the tested cases, less than 0.02 Å. Notwithstanding, the C-H bond distances slightly increase when the hydrogen atoms are pointing towards the surface. Clearly, in all these cases, CH_4 is physisorbed. Most favorable adsorption geometries are represented in Figure 4.17. In the case of C termination, there exist two geometries degenerated in energy, with two or three Hydrogen atoms pointing to the surface (Figure 4.17a and 4.17b), respectively. On the other hand, in the case of Mo termination (Figure 4.17c), a distinct situation was observed; when vdW correction was not included in the calculations, only a quarter of the tested geometries reached the most stable physisorbed state. The rest tend to reach other minima with adsorption energies of -0.03 eV at best and likely to be artifacts rather than physically meaningful structures. Nevertheless, when vdW correction is included, the majority of the tested geometries reach the most favorable adsorption geometry. This issue was not featured on C termination, yet another effect was noticeable; once vdW dispersion is turned on, the CH_4 -surface distance can be reduced by ~ 1 Å in selected cases. Despite of this proximity to the surface, the molecular structure was not varied, *i.e.*, the approach is carried out in a rigid fashion. Because of all these reasons, a proper vdW correction is necessary to study the methane adsorption on these surfaces, both from the structural and the energetic aspects. Curiously these results differ slightly respect to the trend encountered for CO_2 adsorption on these

4.6 CH₄ study on (001) Mo carbide surfaces

molybdenum carbide surfaces where the effect of Grimme correction on the calculations only affects the energy adsorption value, without modification of the adsorbate structure. Here, and also in the case of some H₂ adsorption geometries, the use of vdW dispersion modify slightly the adsorption geometry, either elongating the bond distance (on H₂ adsorption) or altering the adsorption site and surface-adsorbate distances (on CH₄ adsorption).

Table 4.13: Adsorption structural data and energy values for methane molecule adsorbed on β -Mo₂C (001) surfaces

Initial State	Final State	E _{ads} /eV	E _{ads} ^{vdW} /eV	Δ C-H _s /Å	Δ C-H _t /Å	Δ Q (C) /e	Δ Q(H _s) /e	Δ Q(H) /e	T _a /K	
β (C)-H ₃ (hC)	H ₃ (hC)	-0.05	-0.29	0.006	0.005	-0.06	0.00	0.00	95	
				0.006			0.005			0.09
				0.005						
β (C)-H ₁ (hC)	H ₁ (hC)	-0.04	-0.24	0.014	0.002	-0.04	0.07	-0.01	80	
				0.003	0.002		0.00			
				0.002						
β (C)-H ₂ (hC)	H ₂ (hC)	-0.05	-0.29	0.002	0.002	-0.27	0.06	0.06	95	
				0.002	0.002		0.08	0.08		
β (Mo)-H ₂ (hC ²)	H ₂ (tMo)	-0.11	-0.39	0.027	0.002	-0.10	0.09	-0.01	134	
				0.029	0.001		0.05	0.04		
β (Mo)-H ₃ (tMo)	H ₂ (tMo) ^a	-0.03	-0.39	0.027	0.002	-0.10	0.09	-0.01	134	
				0.029	0.001		0.05	0.04		
β (Mo)-H ₁ (hMo)	H ₂ (tMo) ^a	-0.03	-0.39	0.027	0.002	-0.10	0.08	-0.01	134	
				0.029	0.001		0.05	0.03		

^aThese geometries are obtained only when vdW correction is included.

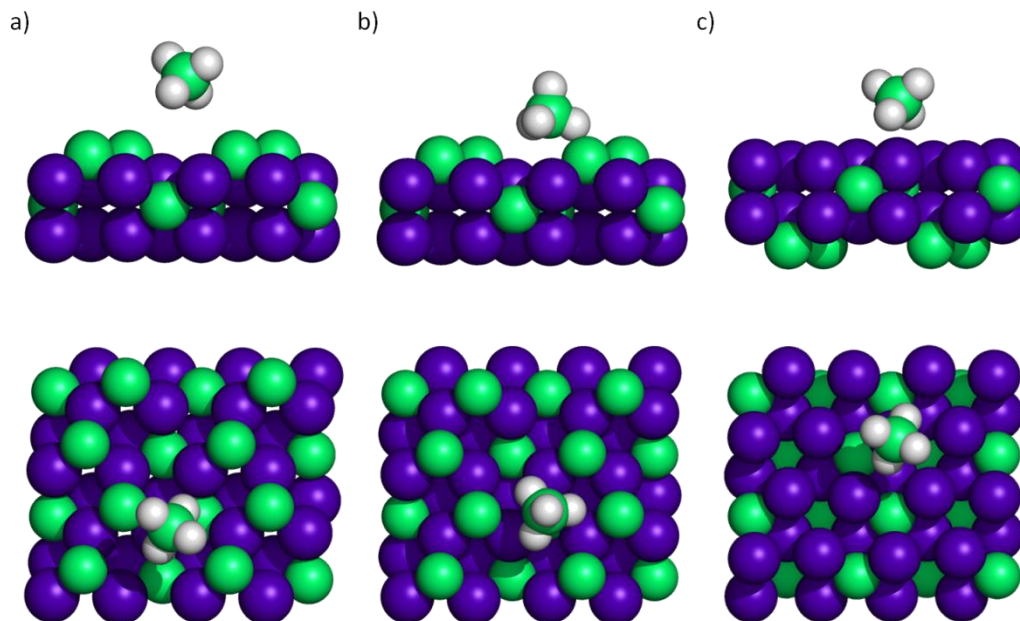


Figure 4.17: Most stable CH₄ adsorption geometries on β -C surface with a) two or b) three Hydrogen atoms aiming to the surface, and c) most stable structure on β -Mo. Side (top) and top views (bottom) are displayed.

The Bader charges analysis indicate that the charge transfer when the molecule is adsorbed is essentially negligible, with values below 0.1 electrons, thus, within the method accuracy limit. ELF images (Figure 4.18) show only a slight polarization of the electron density within the methane molecule, and neither metallic nor covalent bonding with the surface is observed. In order to check differences between isolated and adsorbed methane molecule, the vibrational frequencies were calculated and are shown in Table 4.14. Most of vibrational frequencies decrease, probably due to a slightly weakening of C-H bonds. This is especially interesting in the case of $\beta(\text{Mo})\text{-H}_2(\text{tMo})$ for the two highest energy vibration modes (T_2 and A_1), whose frequency values shift considerably, by more than 250 cm^{-1} . In general, when the H atoms are pointing to the surface, the C-H bond distance increases very slightly in comparison of the rest C-H bonds, but in the case of $\beta(\text{Mo})\text{-H}_2(\text{tMo})$ these differences are one order of magnitude

larger with respect the other studied systems, which could be assigned with the decrease of vibrational frequency values.

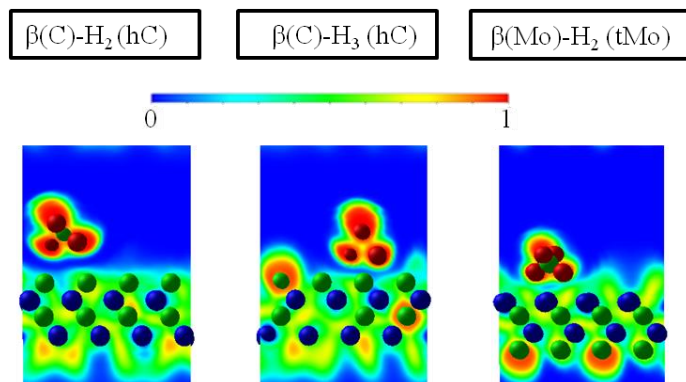


Figure 4.18: ELF of most stable configurations of methane adsorbed on β -Mo₂C (001) surfaces. Blue and green balls denote Mo and C atoms, respectively.

Table 4.14: Vibrational frequencies (in cm⁻¹) for adsorbed methane molecule (ν) on β -Mo₂C(001) surfaces and shifts with respect CH₄ in vacuum ($\Delta\nu$).

Gas phase ν /cm ⁻¹	$\nu[\beta(\text{C})\text{-H}_3(\text{hC})]$ /cm ⁻¹	$\Delta\nu$ /cm ⁻¹	$\nu[\beta(\text{C})\text{-H}_2(\text{hC})]$ /cm ⁻¹	$\Delta\nu$ /cm ⁻¹	$\nu[\beta(\text{Mo})\text{-H}_2(\text{tMo})]$ /cm ⁻¹	$\Delta\nu$ /cm ⁻¹
3083	3061	-22	3095	12	3106	23
3082	3047	-35	3090	8	3033	-49
3065	3033	-33	3086	21	2778	-288
2952	2929	-23	2974	22	2700	-252
1510	1486	-24	1505	-5	1516	6
1495	1483	-12	1503	8	1423	-72
1286	1280	-6	1283	-3	1308	22
1286	1275	-11	1280	-6	1302	16
1273	1251	-22	1276	3	1145	-128

Overall, this computational study could help to understand the experiments about the CO₂ hydrogenation, where CH₄ is the main product. Inasmuch as the weak interaction between CH₄ and β -Mo₂C (001) surface, the desorption process is very auspicious, avoiding possible lateral reactions, *i.e.*, whatever CH₄ molecule produced

will desorb spontaneously being detected by means of mass spectrometry. Furthermore, these results discard *a priori* the use of any termination of β -Mo₂C (001) surface as a catalyst for methane conversion, due to the difficulty of these surfaces to activate the C-H bond of CH₄.

In comparison with previous works on Mo carbides with metal/carbon ratio of two, the results presented here differ clearly respect to the work of Tominaga *et al.*, where they have predicted theoretically⁴³ that CH₄ is dissociated on hexagonal α -Mo₂C, which bulk space group is *P3m1*,⁴⁴ but the authors define (incorrectly) this surface as β as the same case that experimental studies carried out by Oshikawa *et al.*⁴⁵ In fact, the CH₄ adsorption energy on α -Mo₂C is around -3 eV, *i.e.*, a huge difference between our calculations. This incongruity is not in agreement with calculations about H₂ and CO₂, where hexagonal and orthorhombic Mo₂C (001) present similar results as is compared in last sections. However, the main reason of the large adsorption energy of CH₄ on α -Mo₂C (001) is probably the simplicity of the slab model, which only contains 3 layers (Mo/C/Mo) with 18 atoms (12 Mo and 6 C), what could cause the large exothermicity on the CH₄ adsorption.

On δ -MoC (001) surface the procedure and analysis have been carried out as for the β -Mo₂C (001) surfaces and the results are summarized in Table 4.15. The calculated energy values show that on the δ -MoC (001) surface the adsorption is significantly stronger than on β -Mo₂C (001). Despite of this, the C-H bond distance increments are similar to the β -Mo₂C (001) surfaces, *i.e.*, CH₄ is not activated. Table 4.15 exhibits four degenerated adsorption geometries with two (Figure 4.19a) or three (Figure 4.19b) H atoms pointing towards the surface.

The results in Table 4.15 imply that CH₄ becomes physisorbed on δ -MoC(001); the adsorption energy value is, without vdW and for all the tested geometries, \sim -0.54 eV. In agreement with the no activation of methane molecule, Bader analysis reveals no clear

charge transfer in between the molecule and the surface. When vdW correction is included in the calculations, the E_{ads} value obviously increases in all the tested systems. However, the CH₄ structure did not vary in comparison to the calculations without vdW dispersion and despite of the fact that an adsorption energy value ~ -1 eV could be consider as a chemisorption process, the CH₄ molecule is physisorbed. The increment in adsorption energy value is only due to the inclusion of vdW correction and no new interactions emerge.

Table 4.15: Adsorption data and energy values for methane adsorption on δ -MoC(001) surfaces.

Initial State	Final State	E_{ads} /eV	$E_{\text{ads+vdW}}$ /eV	$\Delta\text{C-H}_s$ / \AA	$\Delta\text{C-H}_f$ / \AA	$\Delta\text{Q (C)}$ /e	$\Delta\text{Q (H}_s)$ /e	$\Delta\text{Q (H)}$ /e	T_d /K	
δ -H ₃ (h)	δ -H ₃ (h)	-0.54	-0.92	0.006	0.003	0.004	-0.03	0.01	-0.02	317
				0.003				0.03		
δ -H ₃ (tC)	δ -H ₃ (tC)	-0.54	-0.90	0.004	0.004	-0.02	0.00	0.01	0.01	310
				0.004				0.03		
δ -H ₂ (tMo)	δ -H ₂ (tMo)	-0.54	-0.96	0.007	0.003	0.01	-0.05	-0.01	-0.01	331
				0.005				0.02		
δ -H ₃ (tMo)	δ -H ₃ (tMo)	-0.55	-0.95	0.004	0.005	0.004	-0.02	0.01	-0.03	330
				0.004				0.05		

The estimated desorption temperature values indicate that δ -MoC (001) is able to capture methane at room temperature, which would suggest that δ -MoC could be considered as a CH₄ sequestration material. In order to corroborate these results, the adsorption energy values were compared with experimental and theoretical studies,^{46,47} which used MOFs as a methane sequestration material. The adsorption energy value for these systems are -0.32 eV at best case. Therefore, δ -MoC (001) surface seems to be a much better material for methane sequestration.

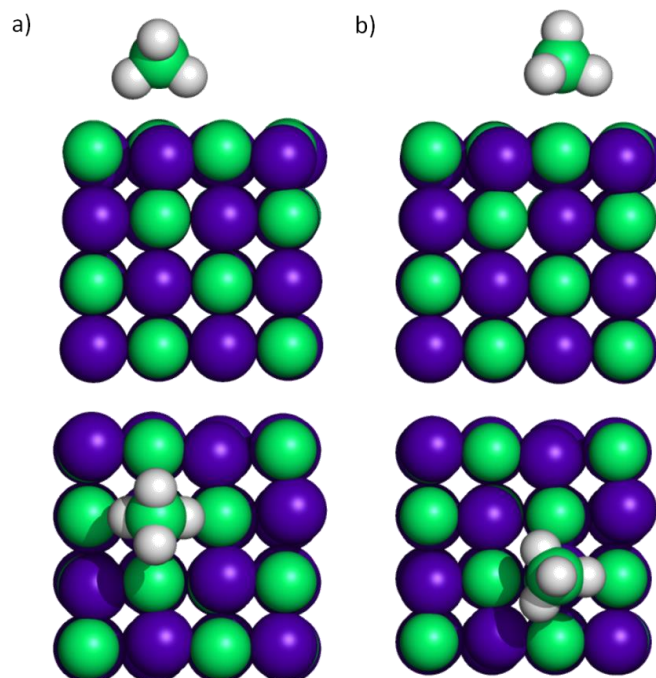


Figure 4.19: Most stable CH_4 adsorption geometries on δ -MoC (001) surface with a) two (δ -H₂(tMo)) or b) three (δ -H₃(tMo)) Hydrogen atoms aiming to the surface. Side (top) and top views (bottom) are displayed.

To complete this study the vibrational frequencies (Table 4.16) were performed using the same methodology as in β -Mo₂C (001) surfaces. Moreover, the ELF sketches (Figure 4.20) do not show any indication of bonding with the surface but still a slight electron density polarization. One can expect that charge transfer results would vary with the support, since the adsorption energy differences and the capacity of capture CH_4 between δ -MoC (001) and β -Mo₂C (001) surfaces is notable. The vibrational frequencies are reported in Table 4.16. Almost all frequencies present a red shift when the molecule is adsorbed, *i.e.*, the vibrational modes lower their frequency energy after the adsorption. Despite the adsorption energy values on δ -MoC (001) are higher than on β -Mo₂C (001) surfaces, the C-H bond distance increment is higher in the second case, and, as a result, the vibrational frequency values are lower when CH_4 is adsorbed on β -Mo₂C (001) surfaces. This is somewhat unpredictable, since in general one could think that C-H bonds should be weaker when the adsorption is stronger, as happens when is

4.6 CH₄ study on (001) Mo carbide surfaces

adsorbed on δ -MoC (001). The reason behind this behaviour is the subtle interplay between Pauli repulsion, generally increasing vibrational frequency, and charge transfer to the adsorbate which has the opposite effect.^{48,49}

Table 4.16: Vibrational frequencies (ν) for adsorbed methane molecule on δ -MoC(001) surface, in cm^{-1} , and variation with respect CH₄ molecule in vacuum ($\Delta\nu$).

Gas phase ν / cm^{-1}	$\nu[\delta\text{-H}_3(\text{h})]$ / cm^{-1}	$\Delta\nu$ / cm^{-1}	$\nu[\delta\text{-H}_3(\text{tC})]$ / cm^{-1}	$\Delta\nu$ / cm^{-1}	$\nu[\delta\text{-H}_2(\text{tMo})]$ / cm^{-1}	$\Delta\nu$ / cm^{-1}	$\nu[\delta\text{-H}_3(\text{tMo})]$ / cm^{-1}	$\Delta\nu$ / cm^{-1}
3083	3085	2	3083	0	3084	1	3075	-8
3082	3081	-1	3073	-9	3067	-15	3073	-9
3065	3054	-11	3072	6	3044	-21	3070	5
2952	2953	1	2959	7	2943	-9	2955	3
1510	1507	-3	1502	-8	1509	0	1506	-4
1495	1497	2	1501	6	1505	11	1505	11
1286	1290	4	1285	-1	1293	7	1288	2
1286	1283	-3	1284	-2	1288	2	1285	-1
1273	1277	4	1281	7	1267	-7	1280	6

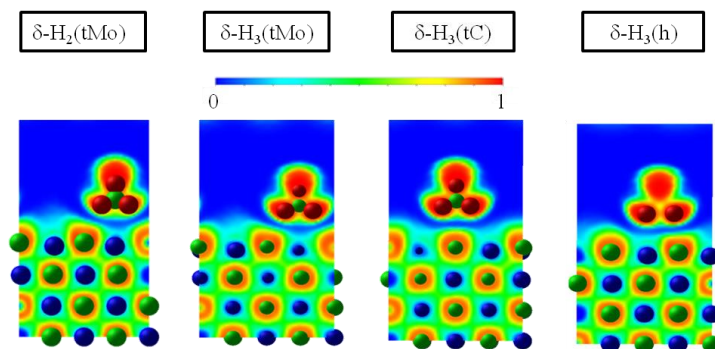


Figure 4.20: ELF of most stable configurations of methane adsorbed on δ -MoC (001) surfaces. Blue and green balls denote Mo and C atoms, respectively.

4.7 Conclusions

In this chapter an extensive theoretical study of the adsorption of CO₂, H₂, and CH₄ on cubic δ -MoC and orthorhombic β -Mo₂C (001) surfaces — the last one with C and Mo terminations— are presented in based on experimental studies about CO₂ hydrogenation on the cited Mo Carbide surfaces.

With respect to CO₂ adsorption and dissociation, DFT and DFT-D2 calculations are in clear agreement with the experiments. We can conclude that CO₂ dissociates easily towards CO without the H₂ assistance on orthorhombic Mo₂C (001) surface, independently of the surface termination, foster β -Mo₂C as promising catalyst for CO₂ reduction. Calculations also reveal that Mo termination is able to dissociate CO towards atomic C and O moieties. Indeed, it is in agreement with experimental XPS results, which shows that the amount of atomic O on β -Mo₂C is superior than the amount of CO, which is only explicable if CO dissociates. Notwithstanding the energy profile of CO₂ hydrogenation on β -Mo₂C (001) will be detailed in Chapter 5, the CO dissociation opens a new way to justify the CH₄ formation (as a main product) on CO₂ hydrogenation since the atomic C that comes from CO dissociation could hydrogenate to CH₄.

On the other hand, calculations on δ -MoC (001) surface are also in agreement with experimental results. The direct CO₂ reduction towards CO implies a huge energy barrier, whereby the XPS signal of atomic O should not be detected, as it is provided by experimentalist. Despite of this step will not happen, CO is produced following alternative reaction mechanisms, since it is the main product of the synthesis. Therefore, the CO dissociation has been also studied, discarding its dissociation. This fact could be related with the non-methane formation in this surface, which reinforces the hypothesis that CH₄ detected on β -Mo₂C is produced by C moieties.

Regarding to H₂ study, calculations reveal that the dissociation of H₂ is spontaneous on β -Mo₂C whereas it implies an energy barrier of 0.64 eV on δ -MoC (001). This dissociation is very exothermic, specially on surfaces which contain C atoms in contact with the adsorbate due to the formation of C-H bonds. In this Chapter, a study about the surface stability at different H coverages has revealed that full coverage stabilizes β -Mo₂C surface, independently of the surface termination whereas on δ -MoC (001), 50% is the most favorable coverage since the Mo-H bonds formation increases the surface Gibbs free energy.

The CH₄ study has been accomplished given that the experimental results revealed that CH₄ is the main product of CO₂ hydrogenation on β -Mo₂C and to bring knowledge about the possible use of Mo carbides as catalysts of methane dry/steam reforming. The DFT calculations display that none of the studied pristine surfaces can activate the methane C-H bonds. Hence, they do not constitute possible candidates for methane dry reforming catalysts. Respect to the adsorption on β -Mo₂C (001), our calculations suggest that CH₄ desorbs easily due to its low adsorption energy, avoiding probably possible lateral reactions.

To finalize, the calculations in this chapter were performed using DFT and DFT-D2. Except to the case of H₂ adsorption and dissociation on β -C surface, DFT-D2 does not play any role on the adsorption sites or adsorbate structure. The difference between these calculations is only detected on the adsorption energy values.

4.8 References

-
- [1] F. Viñes, A. Borodin, O. Höfft, V. Kempter and F. Illas, *Phys. Chem. Chem. Phys.*, **2005**, *7*, 3866.
- [2] G. J. Kubas, *J. Organomet. Chem.*, **2009** *694*, 2648
- [3] H. Tøpsoe, B. S. Clausen and F. E. Massoth, *Hydrotreating Catalysis: Science and Technology*, Springer, Berlin, **1996**
- [4] G. C. Bond, *Heterogeneous Catalysis: Principles and Applications*, 2nd ed., Oxford University Press: Oxford, **1998**.
- [5] T.P. Saint Clair, S.T. Oyama and D.F. Cox, *Surf. Sci.*, **2000**, *468*, 62.
- [6] L. Bugyi, A. Oszko and F. Solymosi, *Surf. Sci.*, **2000**, *461*, 177.
- [7] S. Y. Wu and J. J. Ho, *J. Phys. Chem. C*, **2012**, *116*, 13202.
- [8] C. Kunkel, F. Viñes and F. Illas, *Energy Environ. Sci.*, **2016**, *9*, 141.
- [9] X. Liu, C. Kunkel, P. Ramírez de la Piscina, N. Homs, F. Viñes and F. Illas, *ACS Catal.*, **2017**, *7*, 4323.
- [10] F. Viñes, A. Vojvodic, F. Abil-Pedersen and F. Illas, *J. Phys. Chem. C*, **2013**, *117*, 4168.
- [11] T. Wang, Y.W. Li, J. Wang, M. Beller and H. Jiao, *J. Phys. Chem. C*, **2014**, *118*, 8079.
- [12] F. Viñes, C. Sousa, P. Liu, J. A. Rodriguez and F. Illas, *J. Chem. Phys.*, **2005**, *122*, 174709.
- [13] F. Viñes, C. Sousa, P. Liu, J. A. Rodriguez and F. Illas, *J. Phys. Chem. C*, **2007**, *111*, 16982
- [14] F. Viñes, C. Sousa, P. Liu, J. A. Rodriguez and F. Illas, *J. Phys. Chem. C*, **2007**, *111*, 1307
- [15] E. Florez, T. Gomez, P. Liu, J. A. Rodriguez and F. Illas, *ChemCatChem*, **2010**, *2*, 1219.
- [16] S. Posada-Pérez, F. Viñes, J.A. Rodriguez and F. Illas, *Top. Catal.*, **2015**, *58*, 159.
- [17] F. Viñes, J.A. Rodriguez, P. Liu and F. Illas, *J. Catal.*, **2008**, *260*, 103.
- [18] E. Florez, T Gomez, J.A. Rodriguez and F. Illas, *Phys. Chem. Chem. Phys.*, **2011**, *13*, 6865.
- [19] P. Janthon, S. M. Kozlov F. Viñes J. Limtrakul and F. Illas, *J. Chem. Theo. Comput.*, **2013** *9*, 1631
- [20] S.D. Senanayake, P.J. Ramírez, I. Waluyo, S. Kundu, K. Musiyanselage, Z. Liu, Z. Liu, S. Axnanda, D.J. Stacchiola, J. Evans and J. A. Rodriguez, *J. Phys. Chem. C*, **2016**, *120*, 1778.
- [21] J. A. Rodriguez, J. Evans, L. Feria, A. B. Vidal, P. Liu, K. Nakamura and F. Illas, *J. Catal.*, **2013**, *307* 162.
- [22] T. Wang, X. Tian, Y. Yang, Y.W. Li, J. Wang, M. Beller, and H. Jiao, *Surf. Sci.*, **2016**, *651*, 195.
- [23] J. R. d. S. Politi, F. Viñes, J. A. Rodriguez and F. Illas, *Phys. Chem. Chem. Phys.*, **2013**, *15*, 12617.
- [24] N.H. Moreira, G. Dolgonos, B. Aradi, A.L. da Rosa and T. Frauenheim, *J. Chem. Theory. Comput.*, **2009**, *5*, 605.
- [25] C.G. Tang, M.J.S. Spencer and A. S. Barnard, *Phys. Chem. Chem. Phys.*, **2014**, *16*, 22139.
- [26] D. R. Stull, a. H. P., *JANAF thermochemical Tables, 2nd Ed.* U. S. National Bureau of Standards: U.S. EPO, Washington D. C: **1971**.
- [27] J. Feichter, U. Schurath and R. Zellner, *Chem. Unserer Zeit*, **2007**, *41*, 138.
- [28] R. D. Beck, P. Maroni, D. C. Papageorgopoulos, T. T. Dang, M. P. Schmid and T. R. Rizzo, *Science*, **2003**, *302*, 98.
- [29] A. C. Luntz, *Science*, **2003**, *302*, 70.
- [30] P. D. F. Vernon, M. L. H. Green, A. K. Cheetham and A. T. Ashcroft, *Catal. Today*, **1992**, *13*, 417.

4.8 References

- [31] R. Bisson, M. Sacchi, T. T. Dang, B. Yoder, P. Maroni and R. D. Beck, *J. Phys. Chem. A*, **2007**, *111*, 12679.
- [32] S. Nave and B. Jackson, *J. Chem. Phys.*, **2009**, *130*, 054701.
- [33] F. Besenbacher, I. Chorkendoff, B. S. Clausen, B. Hammer, A. M. Molenbroek, J. K. Nørskov and I. Stensgaard, *Science*, **1998**, *279*, 1913.
- [34] M. Pettre, C. Eichner and M. Perrin, *J. Chem. Soc. Faraday Trans.*, **1946**, *43*, 335.
- [35] D. A. Hickman and L. D. Schmidt, *Science*, **1993**, *259*, 343.
- [36] V. R. Choudhary, A. M. Rajput and B. Prabhakar, *J. Catal.*, **1993**, *139*, 326.
- [37] J. P. Van Hook, *Catal. Rev. Sci. Eng.*, **1980**, *21*, 1.
- [38] A. T. Ashcroft, A. K. Cheetham, M. L. H. Green and P. D. F. Vernon, *Nature*, **1991**, *352*, 225.
- [39] M. C. Bradford and M. A. Vannice, *Catal. Rev. Sci. Eng.* **1999**, *41*, 1.
- [40] M. C. J. Bradford and M. A. Vannice, *Appl. Catal. A*, **1996**, *142*, 97.
- [41] K. Tomishige and Y.-G. Chen, K. Fujimoto, *J. Catal.*, **1999**, *181*, 91.
- [42] S. González, F. Viñes, J. F. García, Y. Erazo and F. Illas, *Surf. Sci.*, **2014**, *625*, 64.
- [43] H. Tominaga and M. Nagai, *Appl. Catal., A*, **2007**, *328*, 35.
- [44] *Powder Diffraction File*; JCPDS International Center for Diffraction Data: Pennsylvania, 2004
- [45] K. Oshikawa, M. Nagai and S. Omi, *J. Phys. Chem. B*, **2001**, *105*, 9124.
- [46] H. Wu, J. M. Simmons, Y. Liu, C. M. Brown, X. S. Wang, S. Ma, V. K. Peterson, P. D. Southon, C. J. Kepert, H. C. Zhou, T. Yildirim, W. Zhou, *Chem Eur. J.*, **2010**, *16*, 5205.
- [47] Y. He, W. Zhou, G. Qian and B. Chen, *Chem. Soc. Rev.*, **2014**, *43*, 5657.
- [48] F. Illas, S. Zurita, J. Rubio and A. M. Marquez, *Phys. Rev. B*, **1995**, *52*, 12372.
- [49] F. Illas, S. Zurita, A. M. Marquez and J. Rubio, *Surf. Sci.*, **1997**, *376*, 279.

CHAPTER FIVE

CO₂ Hydrogenation on Orthorhombic β -Mo₂C and Cu/ β -Mo₂C (001) Surfaces

5.1 Introduction

The promising results of CO₂ activation on molybdenum carbides described in Chapter 4, open a new way of recovering CO₂ for its hydrogenation to CO, alcohols, or other hydrocarbon compounds in order to recycle the released carbon dioxide.

Different reaction mechanisms have been proposed to describe the CO₂ hydrogenation to CO and MeOH. Respect to CO production, CO₂ could be hydrogenated to formate specie (HCOO) with the subsequent C=O bond cleavage,¹ where metal particles supported on oxides are extensively used catalysts owing to the capability of dispersed particles to dissociate H₂ and the spill-over of atomic H from particles to support, with the goal to hydrogenate the CO₂, adsorbed on the oxide.^{2,3} On the other hand, the redox mechanism, normally observed using Cu-based catalysts, occurs when Cu reduces the CO₂ towards CO whereas Cu⁺ oxidizes H₂ to H₂O,⁴ as it is evidenced using Cu/ZnO,⁵ where also HCOO is detected on Cu⁰ nanoparticles.⁶ In regard to the use of TMCs, an experimental work carried out by Porosoff *et al.*, clearly showed that Mo₂C was an active catalyst for the CO₂ reduction (assisted by H₂) to CO, although the CO:CH₄ ratio was not so good, becoming Mo₂C into an unselective catalyst.⁷ Nevertheless, the deposition of Co on Mo₂C improved this ratio, from 15 to 51.⁷

The key step on the CO₂ hydrogenation towards MeOH is the stabilization of the intermediate species such as HCOO, carboxyl (COOH), or formic acid (HCOOH).⁸ Many studies revealed that HCOO is the intermediate over Zn-modified Cu(111)⁹ or on Cu(111), where the HCOO is hydrogenated towards HCOOH,¹⁰ although a DFT study proposed the COOH pathway as the most favorable intermediate, relegating the HCOO specie as a spectator.¹¹ An extensive study combining DFT and UHV experiments on Cu-based model surfaces confirmed that stabilization of COOH combined with facile hydrogenation of HCOO and dioxomethylene (H₂COO) are critical for high MeOH

CO₂ hydrogenation on orthorhombic β -Mo₂C and Cu/ β -Mo₂C (001) surfaces

yield.¹² Thus, there is a clear controversy about the CO₂ hydrogenation mechanism towards MeOH. This reaction was catalyzed also by TiC (001) and Au and Cu supported on TiC (001).¹³ The CO₂ hydrogenation on Cu/TiC and Au/TiC model catalysts systems leads to CO even in larger amounts than methanol. In order to investigate the origin of CO, the CO₂ hydrogenation towards different intermediates and the dissociation of CO₂ into CO and O and was further investigated by means of pertinent theoretical calculations and the results showed that CO came from COOH intermediate which eventually would decompose into OH and CO. Despite of the possible isomerization from COOH to HCOO is exothermic, the calculated energy barrier was superior to the COOH decomposition, discarding the HCOO mechanism. The MeOH synthesis rate on small Cu and Au clusters supported on TiC (001) surface was correlated with the easy H₂ dissociation on the supported metal clusters and spillover to the carbide support, which acts as a H reservoir, but also with the strong adsorption of CO₂ on the supported cluster, which activates the molecule and favors CO formation through RWGS reaction and COOH intermediate formation.

In general, it has become clear that TMCs can be quite useful for the transformation of CO₂ into CO, methanol, methane, and other hydrocarbons.¹⁴⁻²⁰ Furthermore, TMCs could be used as supports for the dispersion of metal particles⁵⁻⁷ insomuch as TMC can enhance the reactivity of a supported metal through strong metal-support interactions, as was observed with Au and Cu supported on TiC (001).^{3,21}

In this sense, our experimental coworkers tested different transition metal particles supported on cubic and orthorhombic phases of molybdenum carbides, to improve the catalytic activity of bare molybdenum carbides catalysts for CO₂ hydrogenation towards methanol. Of all of them, experimentalist observed that Cu particles supported on molybdenum carbides exhibited better results in terms of activity and methanol production. In this chapter and the next one, the mechanism of CO₂ hydrogenation on bare and Cu supported molybdenum carbides is investigated.

5.1 Introduction

On the other hand, Chapter 4 has put in context the strong effect of metal/carbon ratio in a carbide. Experimental results in Chapter 4 displayed that on β -Mo₂C (001), CH₄ and CO were the main products of CO₂ hydrogenation whilst the amount of methanol was lower. Otherwise, the amount of CO and methanol was slightly superior on δ -MoC, although CH₄ was not detected. These differences were justified using theoretical calculations, where carbides with metal/carbon ratio of one adsorb CO₂ without cleaving the C=O bonds,²² besides to discard the CO dissociation. By contrast, a higher reactivity towards CO₂ has been observed in TMCs with a metal/carbon ratio close to two.^{7,25} On a β -Mo surface, the exposed Mo atoms partially dissociate CO₂ at low temperature (< 300 K) and the CO produced also can decompose into C and O adatoms by overcoming a relatively small (~0.86 eV) energy barrier. Therefore, both experimental and computational studies evinced the role of metal/carbon ratio to dictate the reaction mechanism of CO₂ hydrogenation. This is the reason because of an individualized study were accomplished by means of theory and experiments, in order to determine the role of metal/carbon ratio and the reaction mechanism on bare and Cu supported δ -MoC and β -Mo₂C (001) surfaces.

First of all, the experimental and DFT results for β -Mo₂C (001) surface, with metal/carbon ratio of two, are reported in this chapter, encompassing the reaction mechanism of the CO₂ hydrogenation on β -Mo₂C and Cu/ β -Mo₂C (001) surfaces. Theoretical calculations let us determine the role of different terminations of β -Mo₂C (001) in carbon or molybdenum atoms. The addition of Cu to a β -Mo₂C substrate produces drastic changes in the selectivity of the system towards CH₄ and MeOH. The yield of methanol on a Cu/ β -Mo₂C (001) surface is substantially larger than on bare Mo₂C (001), Cu (111) or a Cu/ZnO (000 $\bar{1}$) model for an industrial catalyst.

5.2 CO₂ hydrogenation on bare β -Mo₂C (001)

Experimental results reported in Figure 4.3 of chapter 4 revealed that the major products of the hydrogenation of CO₂ on β -Mo₂C (001) are CO and CH₄, whilst the amount of MeOH is clearly lower and also traces of C₂H₆, CH₃OCH₃, and C₂H₅OH were found.

In order to corroborate the experimental observations and to determine which reaction path is the most probable, the analysis of the adsorption of the different reactants and their hydrogenations and dissociations were carried out by means of periodic DFT based calculations. Figure 5.1 displays the complex underlying reaction network for this hydrogenation process. The many different reaction pathways have been represented using color codes to differentiate the possible products: hydrocarbons –orange–, aldehydes –blue–, alcohols –yellow–, acids –green–, and carbonates –brown–. These different species are interconnected by black and red arrows, which indicate dissociation or hydrogenation process, respectively.

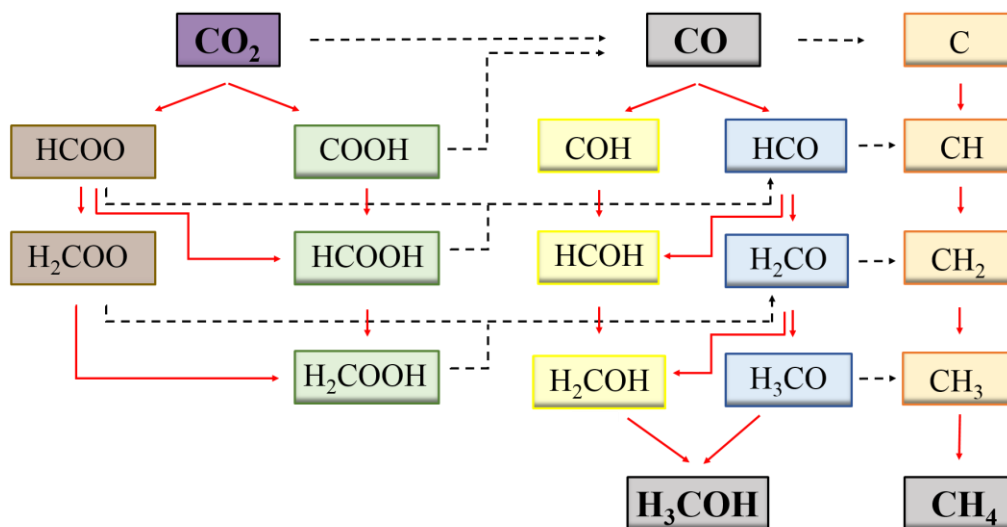


Figure 5.1: Scheme of the reaction network for the heterogeneously catalyzed CO₂ hydrogenation. Possible reaction intermediates are highlighted using color codes to differentiate the hydrocarbons –orange–, aldehydes –blue–, alcohols –yellow–, acids –green–, and carbonates –brown–.

DFT calculations revealed that in the case of the β -Mo surface (molybdenum termination), CO₂ dissociation is favored over hydrogenation since the energy barrier for CO₂ dissociation is only 0.21 eV whereas the first hydrogenation elementary step was endothermic by at least 0.25 eV, implying an even higher energy barrier. Thereupon, the dominant pathway for the majority of CO₂ is the dissociation towards CO –see Figure 5.2–. The reported XPS in chapter 4 for the O 1s binding energy showed that the amount of atomic O on the surface is superior to the amount of CO which strongly suggests that CO dissociation follows the dissociation of CO₂. This interpretation agrees with present theoretical results, where the CO dissociation entails an energy barrier of 0.86 eV and it is one of the possible elementary steps explaining CH₄ formation ($C+2H_2\rightarrow CH_4$) *via* the hydrocarbons pathway (orange) represented on Figure 5.1. Notwithstanding, one needs to keep in mind that the above conclusion regarding CO formation comes from the β -Mo surface and that CO is also predicted to be formed on the β -C one as discussed below. Moreover, the O adatom could form water or could be strongly adsorbed on the surface, poisoning some reactive sites due to the oxycarbide formation.

Part of the produced CO desorbs as is detected by experiments and part of the adsorbed CO could be hydrogenated towards an aldehyde-like intermediate HCO. This moiety is less endothermic than the alcohol-like species, COH, since the enthalpy of CO hydrogenation to HCO is ~ 0.5 eV whereas the COH formation implies an enthalpy around to 1.2 eV. Furthermore, the energy barrier of HCO formation process is 0.99 eV, *i.e.*, the energy barrier is lower than the endothermicity of COH, which discard *a priori* the alcohol-like way represented on Figure 5.1. Nevertheless, HCO formation (0.99 eV) is slightly less favorable than CO dissociation (0.86 eV). This difference enhances methane production with respect to methanol, but it is not enough to fully justify the experimental observations –Figure 4.3, Chapter 4– where the amount of CH₄ is clearly

CO₂ hydrogenation on orthorhombic β -Mo₂C and Cu/ β -Mo₂C (001) surfaces

superior to the amount of methanol. Thus, other reaction paths were investigated in order to further understand the observed CH₄:MeOH ratio production.

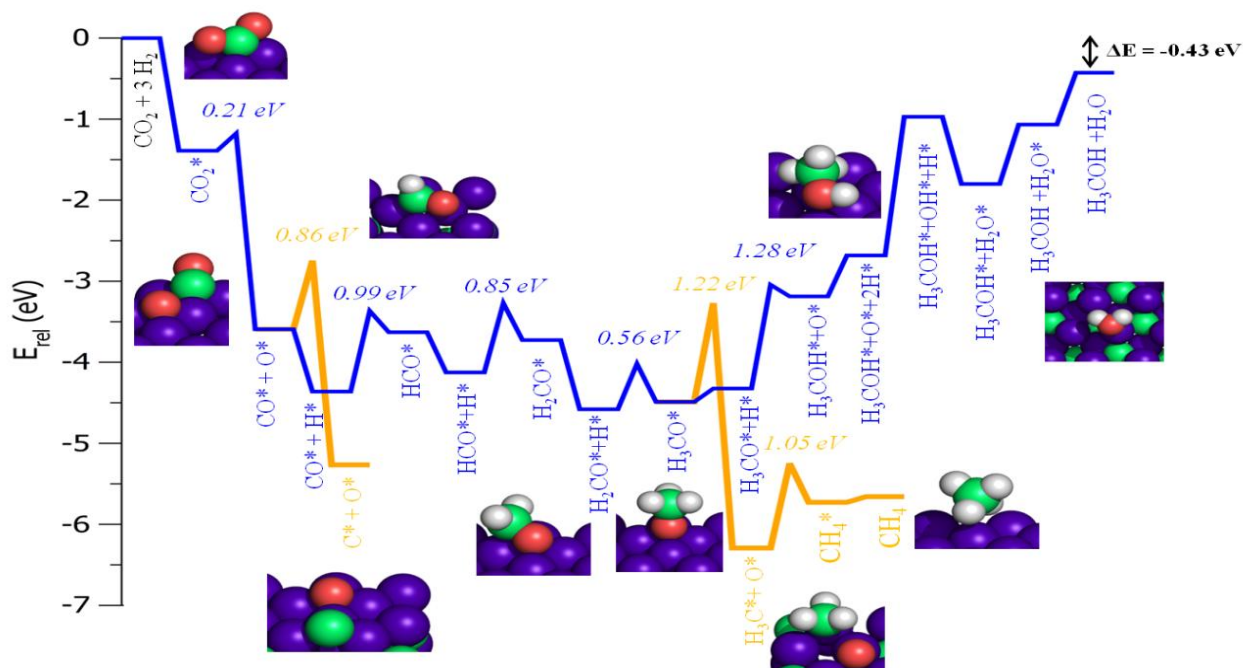


Figure 5.2: Calculated energy profile for CO₂ hydrogenation on the clean β -Mo surface.

From Figure 5.2, it appears that the methoxy intermediate (H₃CO) plays a crucial role. Once the HCO species is formed, it could be easily hydrogenated towards H₃CO (blue pathway). The last hydrogenation to methanol implies an energy barrier of 1.28 eV, overcoming the H₃CO dissociation (CH₃+O) with an energy barrier of 1.22 eV, generating the last intermediate involved in CH₄ production. Eventually, the CH₃ intermediate evolves to methane through a moderate energy barrier (1.05 eV). According to the calculated barriers, the production of methanol and methane are likely comparable, while the desorption energies of both species play an important role in tuning the selectivity towards methane rather than methanol. Methane desorption occurs readily on the β -Mo termination surface as is reported in Chapter 4 whereas

methanol desorption is less favorable than the reverse dehydrogenation to H₃CO, which entails a problematic fact for methanol production, favoring the CH₄ formation in agreement with the experimental results.

Note that methanol or methane synthesis is not the final point during the reaction, but that the oxygen formed during CO formation would hydrogenate together with an extra H₂ molecule to water. The water formation reaction steps are slightly endothermic, and the final H₂O desorption requires 0.65 eV according to our DFT calculations, thus not being a rate limiting step, and so, presence of water is not a reaction inhibitor. Note also by passing by that the reaction enthalpy of -0.43 eV is close to the experimental value of \sim -0.5 eV.^{23,24}

Nevertheless, a problem associated with the use of TMCs as catalysts is their tendency to form oxycarbides when exposed to oxygen-containing molecules.²⁵⁻²⁷ The CO dissociation to atomic C and O and the subsequent O deposition decrease the catalysts activity as is demonstrated by Dixit *et al.*, where ensures that the CO₂ can no longer chemisorb at high oxygen coverage (O-coverage > 0.5 ML).²⁸ Besides, the high O coverages favor the CO desorption, which is a handicap for methanol production. Thus, the strong interaction between CO₂ and CO is not in agreement with Sabatier's principle, since these strong interactions lead to the complete reactants' dissociation and the catalyst deactivation at high O coverages.

Regarding the β -C surface, DFT calculations showed that it is less reactive than the β -Mo one. In fact, CO₂, H₂,¹⁸ and CO adsorptions are less favorable as has been reported in Chapter 4. Figure 5.3 portrays the CO₂ dissociation –left– and hydrogenation –right– pathways displaying that the β -C surface is a CO generator because it can dissociate CO₂ towards CO as in the Mo terminated surface with an energy barrier of 0.48 eV. However, the formed CO is hardly further promoted towards

CO₂ hydrogenation on orthorhombic β -Mo₂C and Cu/ β -Mo₂C (001) surfaces

dissociation or hydrogenation, since the energy barriers are both higher than 1.40 eV. In addition, CO₂ could be hydrogenated towards carboxylate specie (COOH) with an energy barrier of 0.64 eV, although calculations show that this intermediate readily dissociates into CO and OH through a small energy barrier of 0.59 eV. Further hydrogenation towards formic acid (green pathway) is also discarded since it involves a large energy barrier (>2 eV). On the other hand, the atomic oxygen released in the CO₂ dissociation step is strongly adsorbed on both β -Mo and β -C surfaces. In this sense it is important to point out that O adsorption on the β -C surface could entail CO formation through bonding to C surface atoms as predicted by Liu and Rodriguez.²⁷ This possibility could imply a new way for CO production and the generation of new Mo terminated surfaces, which catalyze the methanol and methane synthesis as we explain above.

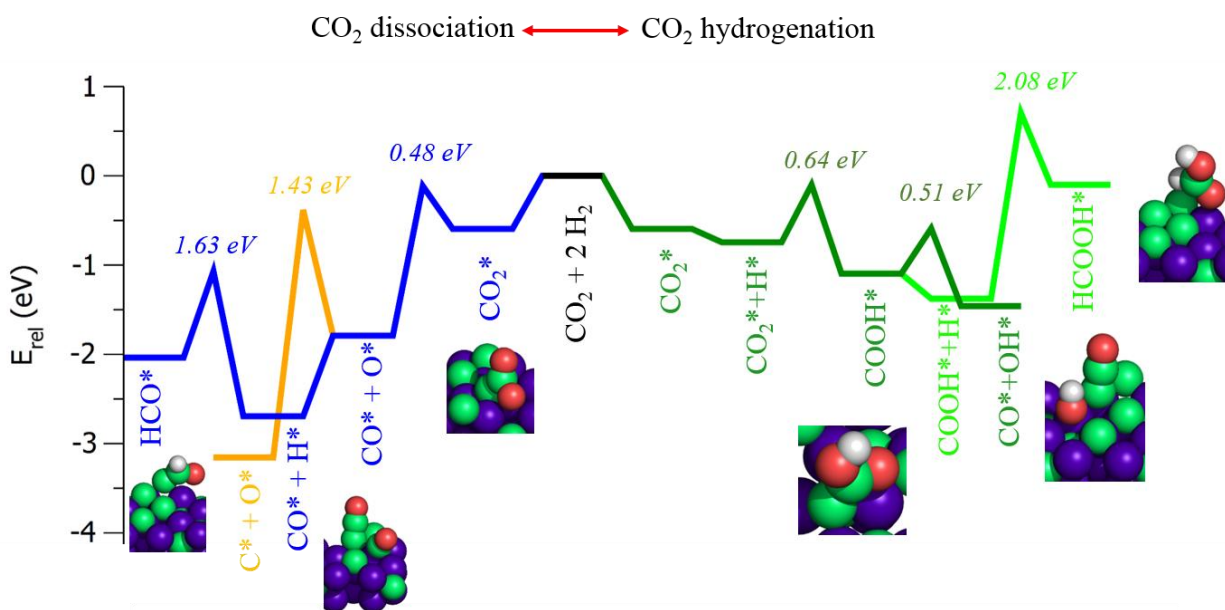


Figure 5.3: Energy profile of CO₂ dissociation (left) and hydrogenation (right) on clean β -Mo₂C (001)-C surface.

In summary, methanol is produced *via* CO hydrogenation on bare β -Mo surface, although during the synthesis, this route competes at least against two different

5.2 CO₂ hydrogenation on bare β -Mo₂C (001)

methane production paths, CO and H₃CO dissociations, which are slightly favorable processes. These results, added to the handicap of the methanol desorption energy and the oxycarbide formation, explain the limited capability of the β -Mo surface to produce methanol since, at the same time, it becomes a CH₄ generator. Note that at high temperatures this is the main product, even above the production of CO, which is formed on both terminations of the β -Mo₂C (001) surface.

5.3 CO₂ hydrogenation on Cu/ β -Mo₂C (001)

5.3.1 Experimental results

5.3.1.1 Interaction of CO₂ with Cu/Mo₂C (001) surfaces

The XPS studies reported in Chapter 4, shown that CO₂ dissociates on β -Mo₂C (001) at room temperature to produce CO (531.2-531.5 eV binding energy in the O 1s region) and atomic O (529.8-530.2 eV). Nevertheless, in general, the deposition of Cu on β -Mo₂C (001) led to a decrease in the rate of CO₂ dissociation. Figure 5.4 displays the variation in the O 1s signal for CO after dosing CO₂ to β -Mo₂C (001) and surfaces pre-covered with 0.4 or 0.8 ML of Cu. The conclusion is clear: the larger the coverage of copper present on the carbide surface, the smaller the amount of CO generated by the decomposition of CO₂. Experiments suggested that without H moiety, CO₂ can decompose to produce CO only on sites of β -Mo₂C (001) not covered by copper. The oxygen deposited of the carbide surface by the CO₂ → CO + O reaction can lead to poisoning. In order to prevent this, the hydrogenation of CO₂ will be carried out under hydrogen rich conditions.

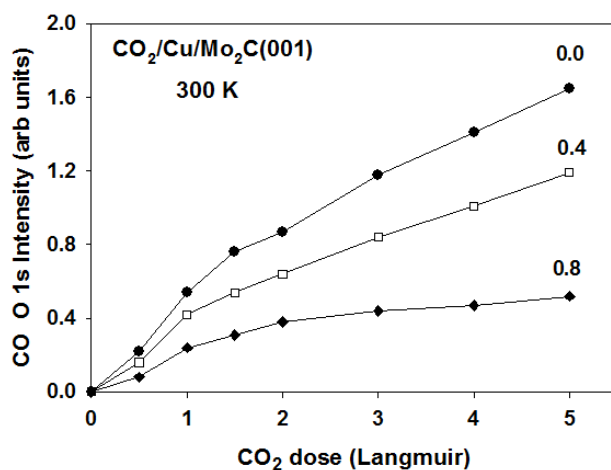


Figure 5.4: Variation of the O 1s signal for adsorbed CO after several doses of CO₂ to pure β -Mo₂C(001) and surfaces pre-covered with 0.4 or 0.8 ML of copper. T= 300 K.

5.3.1.2 Hydrogenation of CO₂ on Cu/Mo₂C (001) surfaces

The first step carried out by the experimentalist was to determine the optimum coverage to reach the larger methanol production. They found that the coverage of copper has a strong influence on the performance of the Cu/Mo₂C (001) catalysts. Figure 5.5 displays the rate for the formation of methanol on a series of Cu/Mo₂C (001) surfaces. At small to medium coverages of Cu there is a constant increase in catalytic activity with a maximum seen around 0.4 ML. At this point we also observed a maximum in the total conversion of CO₂ and the production of MeOH. These trends suggested that the Cu-Mo₂C interface and/or Cu nanoparticle sizes play a key role in the catalytic activity. This interface has special properties not seen for isolated Cu surfaces or Mo₂C.

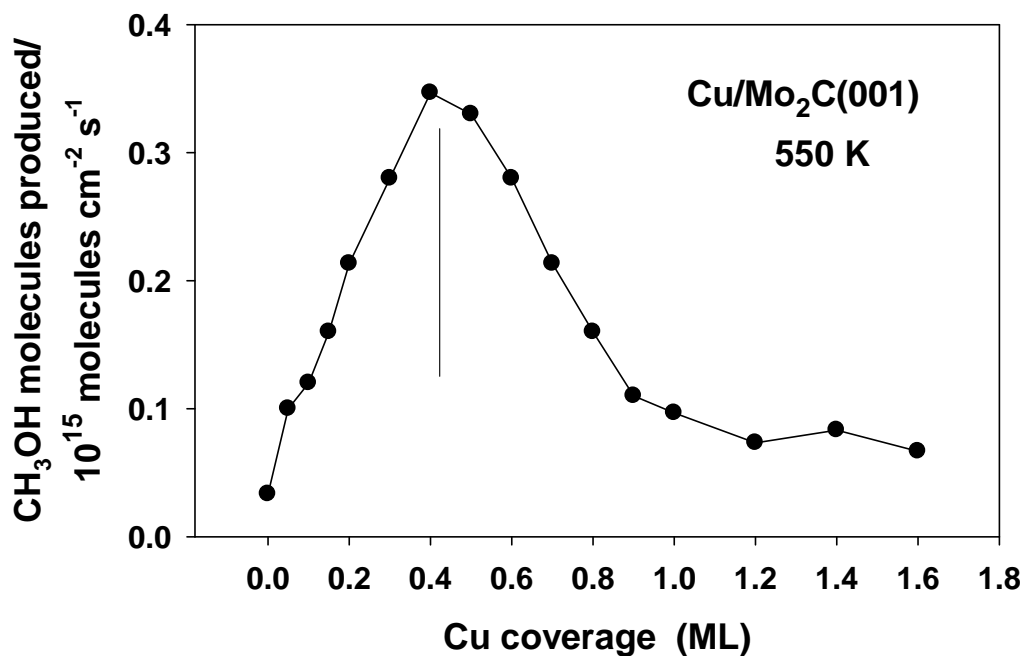


Figure 5.5: Rate for the production of methanol on Cu/Mo₂C (001) surfaces as a function of copper coverage. In a batch reactor, the catalysts were exposed to 0.049 MPa (0.5 atm) of CO₂ and 0.441 MPa (4.5 atm) of H₂ at a temperature of 550 K.

CO₂ hydrogenation on orthorhombic β -Mo₂C and Cu/ β -Mo₂C (001) surfaces

The second step implied the comparison between bare and Cu supported molybdenum carbide surfaces. The main products for the hydrogenation of CO₂ on a bare β -Mo₂C (001) surface are CH₄, CO, and MeOH with traces of C₂H₆, C₂H₅OH and CH₃OCH₃ as it has commented on previous chapters. Figure 5.6 compares the Arrhenius plot for the rates of formation of CH₄, CO, and MeOH on β -Mo₂C (001) (left) and Cu/ β -Mo₂C (001) (right). The deposition of 0.4 ML of Cu on the β -Mo₂C (001) surface enhanced the total conversion of CO₂ by 25-35% and completely altered the selectivity of the CO₂ hydrogenation reaction. The production of methane decreased while the generation of CO and MeOH increased. It is likely that the Cu present on the surface blocked the full decomposition of CO₂ preventing the poisoning of active sites and the final formation of CH₄ since limited amounts of C were available on the surface.

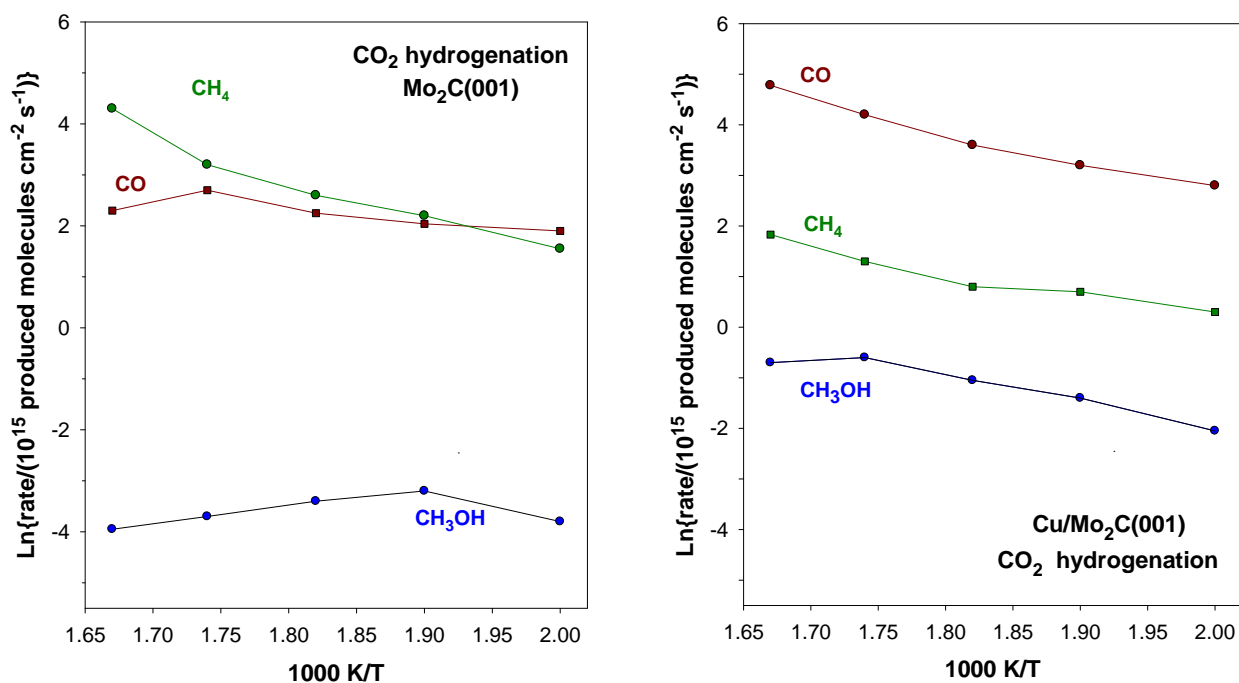


Figure 5.6: Arrhenius plots for the production of CO, methane and methanol on bare β -Mo₂C (001), left-side panel, and a surface pre-covered with 0.4 ML of copper, right-side panel. In a batch reactor, the catalysts were exposed to 0.049 MPa (0.5 atm) of CO₂ and 0.441 MPa (4.5 atm) of H₂ at temperatures of 600, 575, 550, 525 and 500 K.

5.3 CO₂ hydrogenation on Cu/ β -Mo₂C (001)

Figure 5.7 confirmed the experimentalist hypothesis about the negative effect of Cu coverage on the production of methane. The pronounced drop in the rate of methane production supports the idea that Cu is probably blocking the highly active sites that dissociate CO and hydrogenate C to form CH₄. These sites are intrinsically associated with the bare carbide surface. At copper coverages below 0.4 ML, a Cu-Mo₂C interface is generated that still can adsorb well CO₂ and transform it into CO and methanol. When the copper coverage goes above 0.4 ML, the whole reactivity of the catalytic system drops, and the experimentalists found a drastic decrease in the total conversion of CO₂ and in the formation of CO, CH₄ and MeOH.

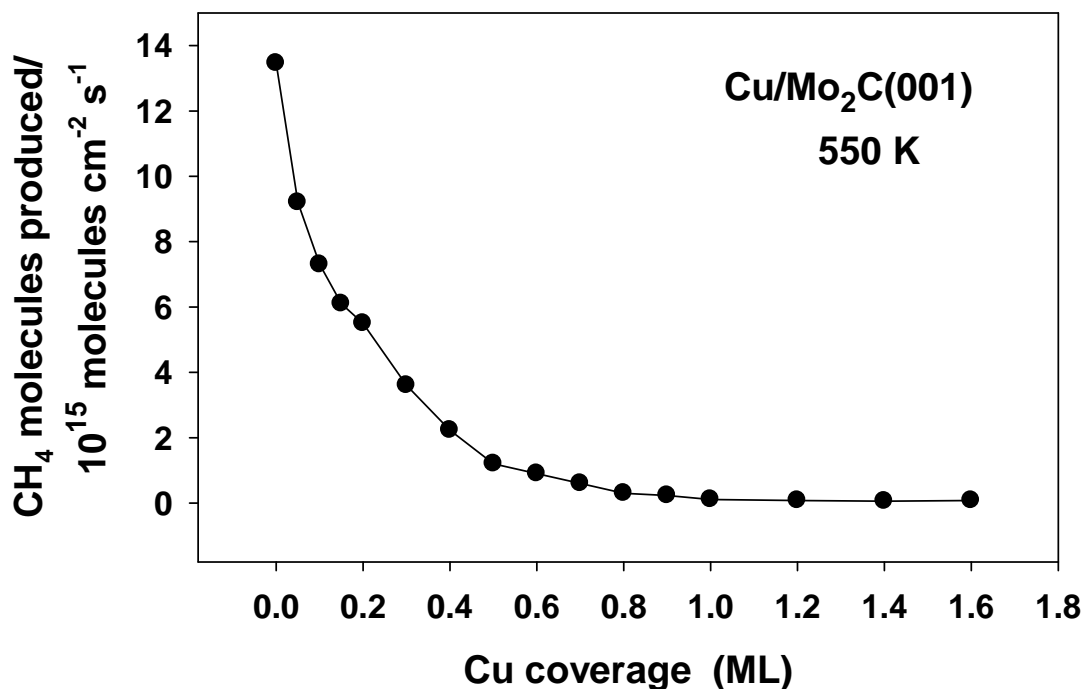


Figure 5.7: Rate for the production of methane on Cu/Mo₂C (001) surfaces as a function of copper coverage. In a batch reactor, the catalysts were exposed to 0.049 MPa (0.5 atm) of CO₂ and 0.441 MPa (4.5 atm) of H₂ at a temperature of 550 K.

CO₂ hydrogenation on orthorhombic β -Mo₂C and Cu/ β -Mo₂C (001) surfaces

After determining the relevant role of Cu clusters on the selectivity of CO₂ hydrogenation, the last step was the comparison of methanol production with typical catalysts used with this purpose. Figure 5.8 compares the rates for the production of methanol at 550 K on Cu (111),¹² bare β -Mo₂C (001), a carbide surface with 0.4 ML of copper, ZnO/Cu (111)²⁹ and a Cu/ZnO (000 $\bar{1}$) system, which is a model for an industrial catalyst for methanol synthesis.¹² In Figure 5.8, an improvement in the catalytic activity is seen when going from pure Cu (111) to Cu/ZnO (000 $\bar{1}$) or ZnO/Cu (111), but by large the best catalyst is Cu/Mo₂C (001). The amounts of Cu on ZnO (000 $\bar{1}$)¹² and β -Mo₂C (001) are similar, but the Cu-ZnO interface seems to be less efficient than the Cu-Mo₂C interface for the CO₂→MeOH conversion. The intrinsic ability of Mo₂C to adsorb and dissociate CO₂ probably facilitates the process.

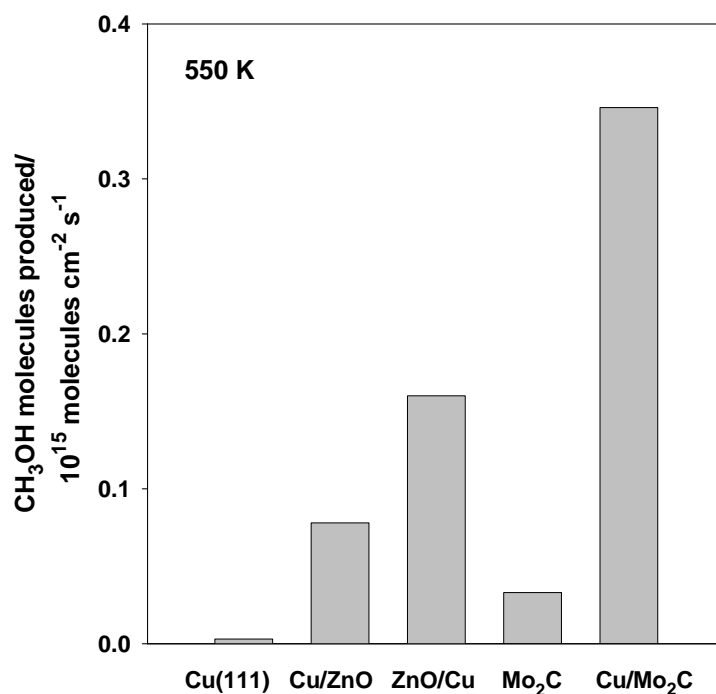


Figure 5.8: Rates for the production of methanol on Cu (111),¹² Cu/ZnO (000 $\bar{1}$),¹² ZnO/Cu (111),²⁹ bare β -Mo₂C (001) and Cu/Mo₂C (001). In a batch reactor, the catalysts were exposed to 0.049 MPa (0.5 atm) of CO₂ and 0.441 MPa (4.5 atm) of H₂ at a temperature of 550 K.

5.3.2 DFT studies for CO₂ hydrogenation on Cu/Mo₂C (001) surfaces

Experiments were able to demonstrate an increase of the catalytic activity towards CO and methanol and the key role of Cu clusters to block molybdenum carbide reactive sites to dissociate CO, avoiding the methane formation. However, experiments cannot evidence the role of Mo and C terminations and the CO₂ conversion mechanism on Cu deposited clusters. Using computational models and DFT calculations, the contribution of each different termination to CO₂ hydrogenation could be clarified.

5.3.2.1 CO₂ adsorption on Cu_n/Mo₂C (001) surfaces

In Chapter 3, theoretical models of Cu supported clusters were reported showing that Cu_n clusters in contact with β -Mo₂C (001) adopt a planar configuration, independently of the surface termination. The study about the reaction mechanism of methanol synthesis was performed using Cu₄ cluster models supported on a (2×2) supercell of β -Mo₂C (001) with Mo or C termination. The justification of this choice was twofold. On the one hand, the use of larger clusters implies a larger supercell and the overall computational resources required are excessive and, on the other hand, as is reported on Table 5.1, the Cu₄, Cu₇, or Cu₁₀ clusters supported on both terminations exhibited similar adsorption energies (results reported on Table 5.1 correspond to the activated/bended CO₂ molecule). Besides, the energy profile of CO₂ dissociation (Figure 5.9) also shows the great similarity between different sizes of Cu clusters. These results clearly exhibit that CO₂ interaction with supported Cu clusters is weak, independently of the Cu_n size. One can properly argue that the Cu₄/ β -Mo₂C (001) surface models provide an oversimplified representation of the real systems, but the main goal was to contribute and to clear up the experimental results, such as the selectivity switch

CO₂ hydrogenation on orthorhombic β -Mo₂C and Cu/ β -Mo₂C (001) surfaces

between CH₄ and MeOH or the enhancement in the reactivity of Cu/ β -Mo₂C (001) systems with respect to the bare surfaces, considering that the number of possible reaction pathways and intermediates is excessively large. We will present compelling evidence that this simplified model explains most of the experimental observations.

Table 5.1: Adsorption energy (eV) of CO₂ and CO adsorbed on different Cu_n/ β -Mo₂C (001) surfaces.

	Cu ₄ / β -Mo /eV	Cu ₄ / β -C /eV	Cu ₇ / β -Mo /eV	Cu ₇ / β -C /eV	Cu ₁₀ / β -Mo /eV	Cu ₁₀ / β -C /eV
CO ₂	-0.14	-0.10	-0.10	-0.11	-0.10	-0.10
CO	-1.13	-1.33	-1.18	-1.35	-1.24	-1.37

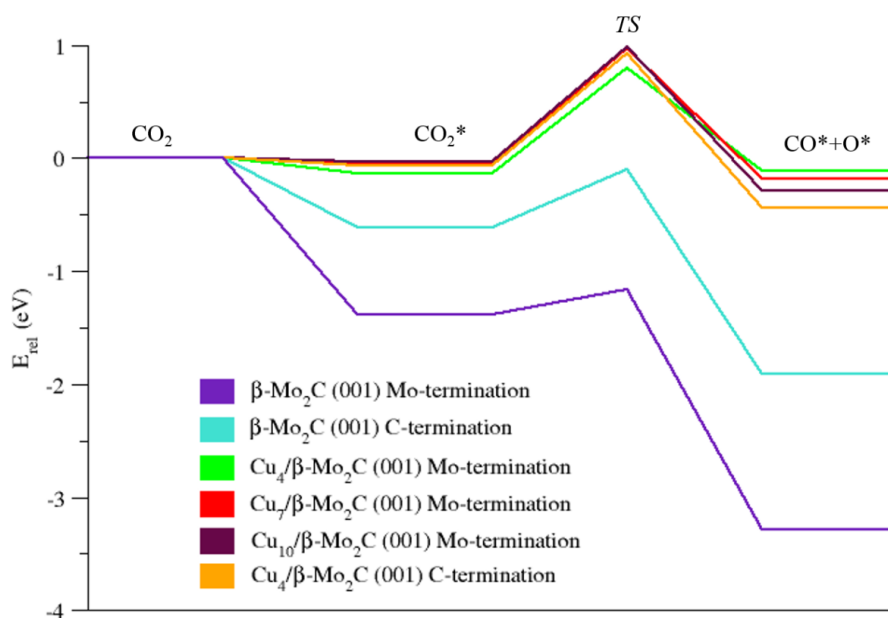


Figure 5.9: Energy profile for CO₂ dissociation on the clean Mo- and C-terminated surfaces of β -Mo₂(001) and on various Cu_n/ β -Mo₂C (001) (n=4,7,10) surfaces models.

Figure 5.9 agrees with the experimental results in Figure 5.4, which shows that the amount of detected CO decreases when the Cu coverage increases. Indeed, CO₂ adsorption energy values are larger for the clean β -Mo and β -C surfaces (-1.38 and -0.61

5.3 CO₂ hydrogenation on Cu/ β -Mo₂C (001)

eV respectively) than on the Cu_n adclusters. It is very important to remark that the majority of tested sites on the Cu-Mo₂C interface and on top of Cu_n are not able to bend (activate) the CO₂ molecule. On Cu₄/ β -Mo, the CO₂ activation is produced on top of Cu cluster, elongating one of the C=O bonds (see Figure 5.10a), although the adsorption energy is too low (-0.14 eV). Nevertheless, CO₂ remains non-activated (linear) in many sites, see Figure 5.10b, with adsorption energies lower than -0.06 eV, even reaching positive values. On the other hand, on Cu₄/ β -C, the activated CO₂ structure (-0.10 eV), Figure 5.10c, is not the most favorable structure, because the non-activated CO₂ structure on top of Cu cluster and on the interface, presented slightly favorable adsorption energy (-0.13 eV), although both structures can be considered equal in energy. These tendencies were also observed on Cu₇ and Cu₁₀ supported clusters, displaying again the same trend of small models. Therefore, these preliminary results seem to indicate that Cu clusters does not favor the CO₂ activation and dissociation, in agreement with experimental results.

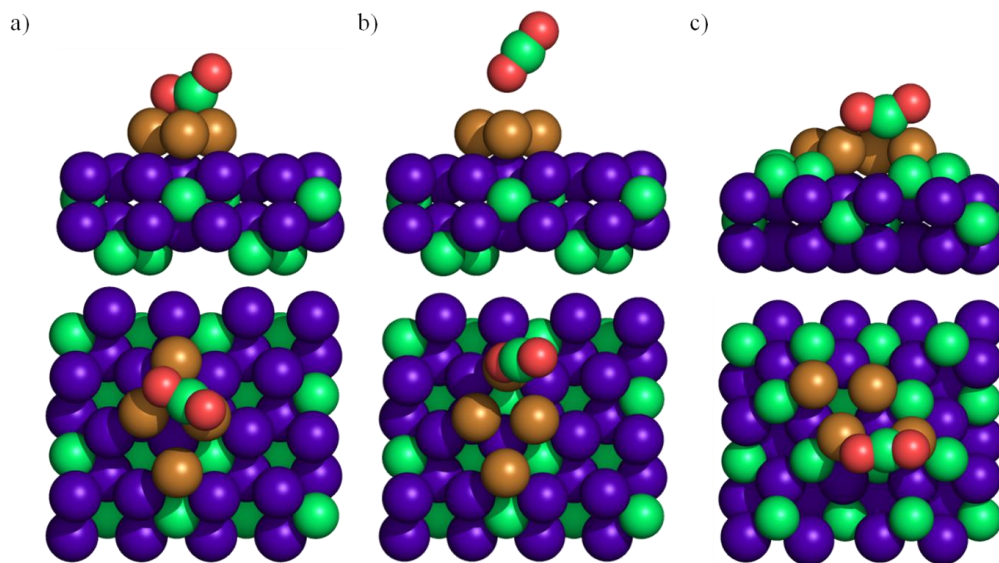


Figure 5.10: a) Activated CO₂ moiety on Cu₄/ β -Mo (001) surface, b) physisorbed CO₂ on Cu₄/ β -Mo (001) surface, and c) Activated CO₂ moiety on Cu₄/ β -C (001) surface. Side (top) and top views (bottom) are displayed.

5.3.2.2 CO₂ hydrogenation mechanism on Cu₄/ β -Mo (001) surfaces

In this section, we describe in detail the results obtained for CO₂ hydrogenation on Cu₄/ β -Mo₂C (001) surfaces. As it has been already commented, direct CO₂ dissociation is not produced on Cu clusters or interface, and thus, the COOH and HCOO pathways (green and brown ways on Figure 5.1) were analyzed.

First of all, the reaction mechanism was carried out on Cu₄/ β -Mo surface model. Figure 5.11 exhibits the reaction pathway through COOH intermediate. Note that the energy barrier to hydrogenate CO₂ towards COOH is 0.36 eV and even easier is its dissociation towards CO (COOH \rightarrow CO + OH). Nevertheless, this produced CO cannot evolve to methanol, by means of its hydrogenation, or to methane, through its dissociation, since both energy barriers are superior to 2 eV on top of Cu supported clusters. Thereupon, CO produced on Cu clusters could desorb, as is indicated on Figure 5.11 or the spill-over of CO from particles to support could occur, generating MeOH or CH₄ on bare carbide region. These results agree with experimental evidences, being that Cu supported clusters avoid the CO dissociation, increasing the amount of CO and decreasing the methane production, which it just happen only on bare regions of molybdenum termination.

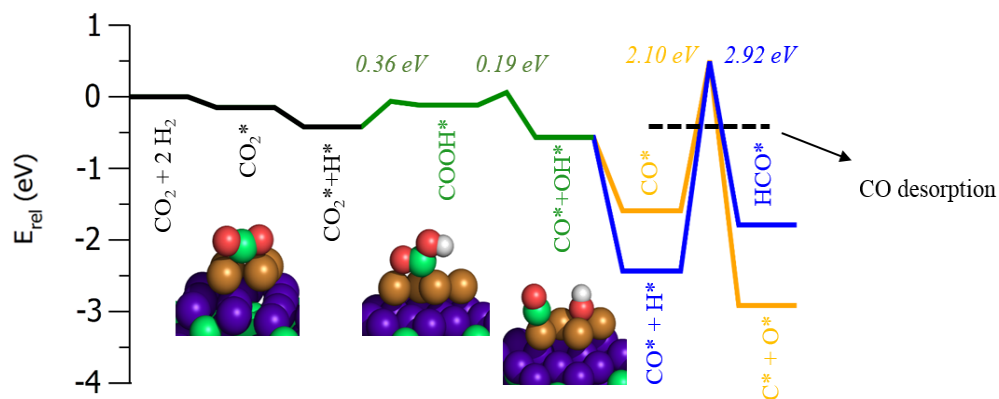


Figure 5.11: Energy profile of CO₂ hydrogenation following the COOH intermediate on Cu₄/ β -Mo surface model.

5.3 CO₂ hydrogenation on Cu/ β -Mo₂C (001)

The DFT calculations suggested that methanol is not produced through CO hydrogenation. Nevertheless, the increase of MeOH detected by experiments must be related with different reaction mechanism. Indeed, the MeOH production on Cu supported clusters and interface entails the generation of HCOO as is displayed on Figure 5.12. Note that, in comparison with COOH, the HCOO-Cu interaction is ~ 1 eV stronger. However, despite being thermodynamically favored, its formation energy barrier is slightly superior (0.46 eV) than COOH. Considering that the HCOO dissociation barrier is larger than 2.5 eV, HCOO hydrogenation towards dioxymethylene (H₂COO) or formic acid (HCOOH) appeared as alternative route where both intermediates evolve to H₂CO, and eventually it hydrogenates to MeOH. Indeed, the present calculations on the Cu₄/ β -Mo model suggest that the route towards MeOH production implies the H₂COO formation in agreement with several works on related Cu surfaces.^{12,30,31} This assertion follows from the DFT calculations showing that the adsorption energy of H₂COO moiety on the Cu-Mo interface is ~ 0.5 eV favorable than HCOOH. Moreover, the HCOO \rightarrow H₂COO process entails an energy barrier of 0.61 eV (see Figure 5.12) whereas the HCOO \rightarrow HCOOH path has an energy barrier of 1.26 eV (see Figure 5.13).

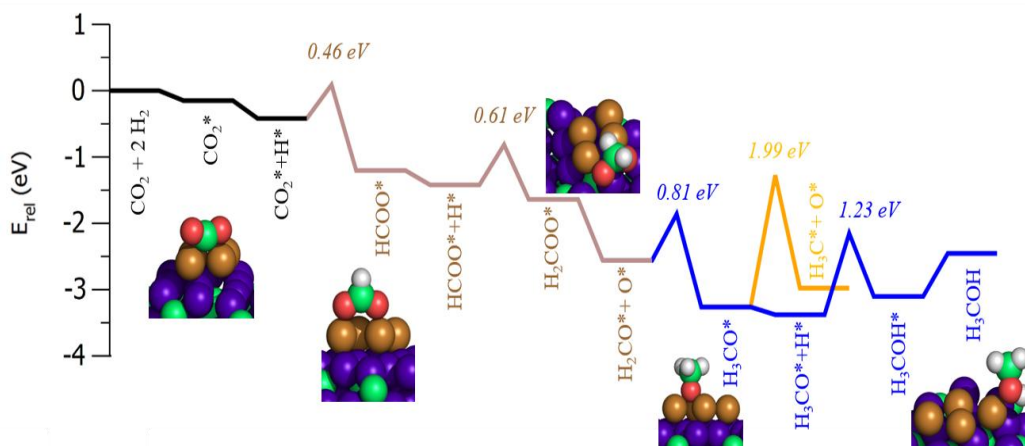


Figure 5.12: Energy profile of CO₂ hydrogenation following the HCOO intermediate on Cu₄/ β -Mo surface model.

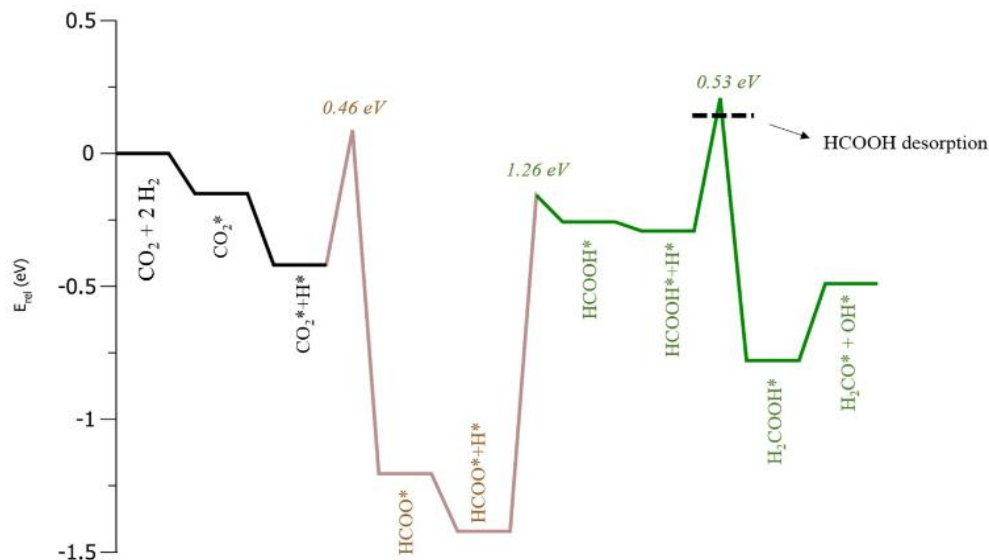


Figure 5.13: Energy profile of CO₂ hydrogenation following the HCOO intermediate and formic acid production on Cu₄/ β -Mo surface model.

Moreover, as is displayed in Figure 5.13, given that HCOOH would be formed, it would rather react back to HCOO than desorb. Indeed, the only exit for HCOO would be to do reverse react towards CO₂ + H₂ through a competitive reaction step energy barrier, as also found in the literature. Note as well that CO₂ + 2H₂ energy level is located below HCOOH, strengthening the thermodynamics of the process. Also, would some HCOOH be formed, it will easily desorb and hence, further hydrogenation towards the H₂COOH intermediate cannot occur. Nevertheless, HCOOH has not been detected in the experiments, not even in trace amounts. Thus, considering the available information it can be safely concluded that HCOOH is not a key path as suggested by Taylor *et al.*³² and that HCOO hydrogenation leads to a H₂COO intermediate as in the pathway schematically shown in Figure 5.12.

The next step towards methanol involves H₃CO formation *via* H₂COO hydrogenation as already proposed in some kinetic models.^{33,34} However Grabow and

5.3 CO₂ hydrogenation on Cu/ β -Mo₂C (001)

Mavrikakis suggested instead that H₂COO dissociates to H₂CO + O and that H₂CO is subsequently hydrogenated to H₃CO.¹⁰ The energy barrier of H₂CO hydrogenation towards H₃CO is slightly favorable on bare region than Cu-Mo interface (0.56 eV *vs.* 0.81 eV). The H₂CO hydrogenation on bare surface regions will follow the reaction pathway discussed above on Figure 5.2, where methane formation is favored with respect to methanol. In this sense, we can speculate that methanol formation is enhanced by migration of part of the formed H₂CO to the supported Cu cluster where further hydrogenation towards a methoxy intermediate would be possible. Above the supported cluster the energy barrier for H₃CO dissociation into CH₃ and O is higher than 2 eV whilst hydrogenation of H₃CO to MeOH is of only 1.23 eV, virtually, the same energy barrier as for H₃CO hydrogenation on a clean β -Mo surface. Hydrogenation of H₃CO towards methanol is favored with respect to dissociation eventually leading to CH₄ which, again, agrees with the experimental observations. Furthermore, the MeOH desorption on Cu₄ clusters is a favorable process, contrary to MeOH desorption on bare regions, where lateral reactions are favorable.

In summary, the supported Cu clusters avoid CO dissociation and the subsequent reaction towards CH₄ (orange way) which adds one justification to the selectivity switch from CH₄ to CO production on Cu/Mo₂C relative to Mo₂C as shown in the experiments. Furthermore, the DFT calculations propose a new path to produce MeOH on the Cu-Mo interface, which imply the HCOO intermediate.

5.3.2.3 CO₂ hydrogenation mechanism on Cu₄/ β -C (001) surfaces

On β -C, CO₂ direct decomposition is not favored and hydrogenation towards a HCOO intermediate seems to be more likely. Nevertheless, contrary to the β -Mo surface, a H₂COO species has not been found in the calculations since all attempts lead

CO₂ hydrogenation on orthorhombic β -Mo₂C and Cu/ β -Mo₂C (001) surfaces

to HCOOH formation with an energy barrier of 1.31 eV and with an adsorption energy slightly stronger than that calculated for the Cu₄/ β -Mo models. Moreover, HCOOH hydrogenation to H₂COOH competes with HCOOH desorption. The low desorption energy of formic acid together to the absence this product in the experiments strongly suggest that this route can be discarded for the Cu₄/ β -C model. Furthermore, the studies carried out on the interface do not show an improvement respect to a clean region surface. On the other hand, the role of the Cu₄/ β -C surface in the catalytic process could be similar to that of a clean region; despite of the Cu deposition, CO formation from the bonding between an O adatom and a C surface atom is not affected. Therefore, the CO produced could desorb, leading to a Mo layer-Cu cluster interaction, which could entail the same reactivity explained above.

5.4 Conclusions

In this Chapter, the CO₂ hydrogenation mechanism towards methanol was studied for orthorhombic phase of Mo₂C, with metal/carbon ratio of two. Furthermore, the effect of small Cu particles deposition on β -Mo₂C (001) to methanol formation was also studied.

Regarding to the reaction mechanism on bare β -Mo₂C (001) surface, DFT calculations concluded that Mo termination carries out the CO₂ conversion towards CO, CH₄ and methanol, whereas on C termination surface only produces CO. The large amount of CO and CH₄ are due to the strong interaction between Mo termination surface and CO₂, since surface can induce the double C=O bond cleavage. Furthermore, the CH₄ interaction with β -Mo is too weak, favoring its desorption, whereas the MeOH desorption entails an energy barrier superior to 0.80 eV. These facts stimulate the CH₄ production and restrict the MeOH formation. This strong interaction is counterproductive for the reaction since atomic O is deposited strongly on β -Mo₂C (001) surface, leading to the oxycarbide formation, which prejudices the CO₂ activation, decreasing the catalytic activity.

For the Cu/Mo₂C systems, the experimental results show that, in comparison to the bare Mo₂C surfaces, CO₂ conversion increases by about 25-35%. Furthermore, experimental observations revealed a selectivity switch between MeOH and CH₄, a decrease of methane and an increase in the amount of methanol. This is interpreted in terms of Cu blocking the most reactive surface sites involved in CH₄ production. Periodic DFT calculations carried out on a Cu₄/ β -Mo₂C (001) model disclosed some of the reasons behind this change of selectivity. DFT calculations predict, firstly, that C termination is an inactive surface despite the deposition of Cu clusters, and only CO is produced, as in the case of bare C termination. Secondly, in opposite to bare surfaces,

CO₂ hydrogenation on orthorhombic β -Mo₂C and Cu/ β -Mo₂C (001) surfaces

calculations revealed that CO₂-Cu clusters interaction is too weak, and its activation is produced through H₂ assistance. Besides, the supported Cu clusters are not able to dissociate CO, which is produced by means of COOH dissociation, explaining the observation that under Cu deposition on Mo₂C, the amount of methane decreases.

To justify the increase on the amount of methanol, our calculations suggested a possible new route for methanol production involving the formation of a HCOO intermediate which is subsequently hydrogenated to H₂COO at the interface formed by Mo carbide and Cu supported cluster and ultimately leading to CH₃O and to MeOH. Besides, on the supported Cu surface model, methoxy dissociation, necessary to produce methane, is not favorable whereas methanol desorption is a favorable process, justifying the selectivity switch observed in the experiments.

Our objectives in this chapter were to determine the reaction mechanism in order to compare the β -Mo₂C (001) activity, selectivity, and stability for CO₂ hydrogenation with cubic δ -MoC (001), which will be reported in Chapter 6, and on the other hand, to determine the role of Cu supported clusters. These are *i*) to block the clean region sites for CH₄ production, *ii*) to generate a new route for MeOH production involving sites at the Cu-Mo₂C interface, increasing selectivity towards methanol *iii*) to hinder CO and H₃CO dissociation thus leading to a decrease of CH₄ and *iv*) to favor the MeOH desorption.

5.5 References

-
- [1] C.-S. Chen, W.-H. Cheng and S.-S. Lin, *Catal. Lett.*, **2000**, 68, 45.
- [2] R. Todorovic and R. J. Meyer, *Catal. Today*, **2011**, 160, 242.
- [3] W. C. Conner and J. L. Falconer, *Chem. Rev.*, **1995**, 95, 759.
- [4] M. Gines, A. J. Marchi and C. R. Apesteguia, *Appl. Catal. A*, **1997**, 154, 155.
- [5] S. Fujita, M. Usui and N. Takezawa, *J. Catal.*, **1992**, 134, 220.
- [6] J. Yoshihara and C. T. Campbell, *J. Catal.*, **1996**, 161, 776.
- [7] M. D. Porosoff, X. Yang, J. A. Boscoboinik and J.G. Chen, *Angew. Chem. Int. Ed.*, **2014**, 53, 6705.
- [8] E. L. Uzunova, N. Seriani and H. Mikosch, *Phys. Chem. Chem. Phys.*, **2015**, 17, 11088.
- [9] T. Fujitani, I. Nakamura, T. Uchijima and J. Nakamura, *Surf. Sci.*, **1997**, 383, 285.
- [10] L. C. Grabow and M. Mavrikakis, *ACS Catal.*, **2011**, 1, 365.
- [11] Y.-F. Zhao, Y. Yang, C. Mims, C. H. F. Peden, J. Li and D. Mei, *J. Catal.*, **2011**, 281, 199.
- [12] Y. Yang, J. Evans, J. A. Rodriguez, M. G. White and P. Liu, *Phys. Chem. Chem. Phys.*, **2010**, 12, 9909.
- [13] A. B. Vidal, L. Feria, J. Evans, Y. Takahashi, P. Liu, K. Nakamura, F. Illas and J. A. Rodriguez, *J. Phys. Chem. Lett.*, **2012**, 3, 2275.
- [14] J. A. Rodriguez, P. Liu, D. J. Stacchiola, S. D. Senanayake, M. White and J. G. Chen, *ACS Catal.*, **2015**, 5, 6696.
- [15] S.T. Oyama, *Chemistry of Transition Metal Carbides and Nitrides*, (editor), Springer, Berlin, **1996**.
- [16] M. D. Porosoff, S. Kattel, W. Li, P. Liu and J. G. Chen, *Chem. Commun.*, **2015**, 51, 6988.
- [17] J.-L. Dubois, K. Sayama and H. Arakawa, *Chemistry Letters*, **1992**, 7, 1115.
- [18] S. Posada-Pérez, F. Viñes, J. A. Rodriguez and F. Illas, *Top. Catal.*, **2015**, 58, 159.
- [19] S. Wannakao, N. Artrith, J. Limtrakul and A. Kolpak, *ChemSusChem.*, **2015**, 8, 2745.
- [20] F. Solymosi, A. Oszkó, T. Bánsági and P. Tolmásov, *J. Phys. Chem. B*, **2002**, 106, 9613.
- [21] J. A. Rodriguez and F. Illas, *Phys. Chem. Chem. Phys.*, **2012**, 14, 427.
- [22] C. Kunkel, F. Viñes and F. Illas, *Energy Environ. Sci.* **2016**, 9, 141.
- [23] J. Krzypek, M. Lachowska, M. Grzesik, J. Sloczynski and P. Nowak *Chem. Eng. J.*, **1995**, 58, 101.
- [24] S. S. Iyer, T. Renganathan, S. Pushpavanam, M. V. Kumar and N. Kaisare, *Journal of CO₂ Utilization*, **2015**, 10, 95.
- [25] X. M. Liu, G. Q. Lu, Z. F. Yan and J. Beltramini, *Ind. Eng. Chem. Res.* **2003**, 42, 6518.
- [26] H. H. Hwu and J. G. Chen, *Chem. Rev.* **2005**, 105, 185.
- [27] P. Liu and J. A. Rodriguez, *J. Phys. Chem. B*, **2006**, 110, 19418.
- [28] M. Dixit, X. Peng, M. D. Porosoff, H. D. Willauer and G. Mpourmpakis, *Catal. Sci. Technol.*, **2017**, 7, 5521.
- [29] S. Senanayake, P.J. Ramirez, I. Waluyo, S. Kundu, K. Mudiyansele, Z.-Y. Liu, Z. Liu, S. Axnanda, D.J. Stacchiola, J. Evans and J.A. Rodriguez, *J. Phys. Chem. C*, **2016**, 120, 1778.
- [30] J. R. B Gomes and J. A. N. F. Gomes, *Surf. Sci.*, **2000**, 446, 283.
- [31] J. R. B Gomes and J. A. N. F. Gomes, *Electrochim. Acta*, **1999**, 45, 653.

- [³²] P. A. Taylor, P. B. Rasmussen and I. Chorkendorff, *J. Chem. Soc. Faraday Trans.*, **1995**, *91*, 1267.
- [³³] J. Nerlov and I. Chorkendorff, *Catal. Lett.*, **1998**, *54*, 171.
- [³⁴] P. B. Rasmussen, P. M. Holmblad, T. Askgaard, C. V. Ovesen, P. Stoltze, P. J. K. Nørskov and I. Chorkendorff, *Catal. Lett.*, **1994**, *26*, 373.

CHAPTER SIX

CO₂ Hydrogenation on Cubic δ -MoC and Cu/ δ -MoC (001) Surfaces

6.1 Introduction

In Chapter 5, the high catalytic activity exhibited by orthorhombic Mo₂C (001) surface (as catalysts or support of small Cu nanoparticles) for CO₂ conversion to CO, CH₄, and MeOH was presented. Nevertheless, a problem associated with the use of β -Mo₂C as catalysts was observed: the tendency to form oxycarbides when β -Mo₂C (001) is exposed to oxygen-containing molecules.¹⁻³ The strong interaction of CO₂ with β -Mo₂C favors its rapid dissociation to CO, although this fact triggers the atomic O deposition which lead the carbide deactivation. Thus, in the search for a viable catalyst for CO₂ conversion, this trend must be minimized and the search of new metal carbides catalysts for CO₂ hydrogenation reaction must be focused on carbides able to activate CO₂ moderately, in order to avoid the O deposition.

In this sense, Chapter 4 reported that δ -MoC (001) surface, with metal/carbon ratio of one, bind CO₂ well and can induce the cleavage of C=O bonds assisted by hydrogen, since the direct dissociation was discarded due to the huge energy barrier. This behavior was also observed using other transition metal carbides with metal/carbon ratio of one.^{2,4,5} Furthermore, δ -MoC (001) surface is not able to dissociate CO, avoiding the generation of atomic O. In this chapter, a theoretical study (supported by experiments) of CO₂ hydrogenation on δ -MoC (001) is reported with the goal to investigate the catalytic activity of this molybdenum carbide surface. In addition, considering the promising results of the deposition of metal particles on transition metal carbides, the CO₂ hydrogenation was also studied on Cu/ δ -MoC (001) and Au/ δ -MoC (001) systems, although only the first one was modeled theoretically. Furthermore, the activity, selectivity, and stability of these systems were compared with Au/Mo₂C and Cu/Mo₂C, to investigate the crucial effect of metal/carbon ratio on the catalyst performance.

6.2 CO₂ hydrogenation on bare δ -MoC (001)

6.2.1 Experimental results

Experimental results on bare transition metal carbides surfaces are summarized on Figure 6.1, which collects data for the hydrogenation of CO₂ on the bare TiC (001),⁵ δ -MoC, and orthorhombic β -Mo₂C (001) surfaces, comparing the activity of carbides with different metal/carbon ratio. The left-side panel in Figure 6.1, exhibits, on the one hand, that TiC and MoC (001) only produce CO and methanol, and on the other hand, that δ -MoC is more active catalyst than TiC (001) surface. In contrast, as was commented in Chapters 4 and 5, on a metal carbide with a metal/carbon ratio of two (right-side panel of Figure 6.1), there was production of a large amount of methane in addition to CO and methanol. In general, a decrease in the metal/carbon ratio in a carbide usually reduces the reactivity of the system because of electronic—a raise in the positive charge on the metal centers—and structural effects—a reduction in the number of metal centers exposed on the carbide surface.

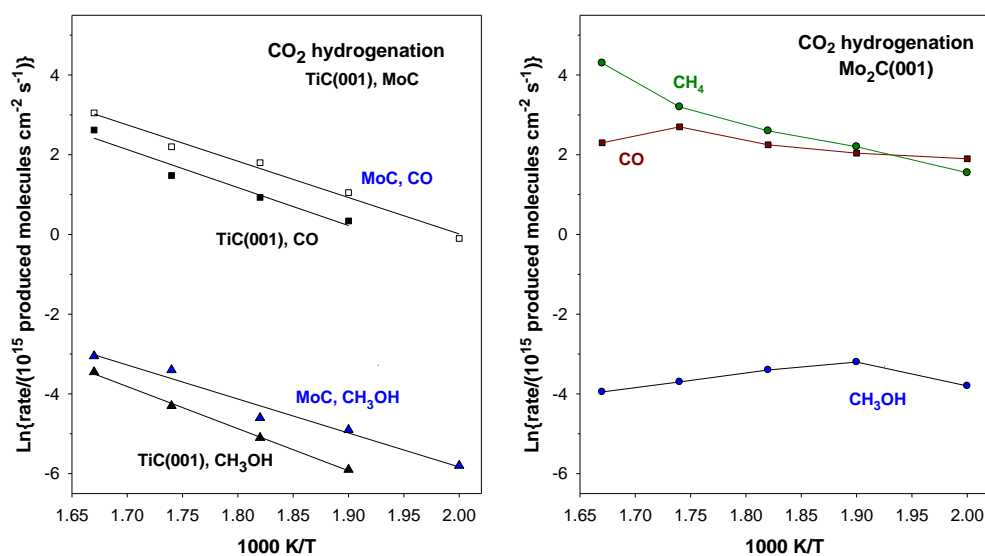


Figure 6.1: Hydrogenation of CO₂ on TiC(001), polycrystalline δ -MoC, and orthorhombic β -Mo₂C(001). Arrhenius plots for the production of CO, methanol, and methane. In a batch reactor, the catalysts were exposed to 0.049 MPa (0.5 atm) of CO₂ and 0.441 MPa (4.5 atm) of H₂ at temperatures of 600, 575, 550, 525, and 500 K.

Despite of the fact that β -Mo₂C (001) is very active towards CO₂ dissociation, the CO and methanol production is very similar than carbides with metal/carbon ratio of one (even lower at 600 K). This fact suggests, in agreement with Sabatier's principle, that strong interactions between reactants and support is a handicap to the catalytic activity, in this case due to the easy dissociation and the consequent oxycarbide formation.

6.2.2 DFT results

To better understand the chemistry involved in the experiments on powder MoC, DFT based calculations were carried out on a series of systems using δ -MoC (001) as appropriate models, since constitutes the most stable phase,⁶ and consequently, it is likely to be the most exposed surface in the experimental polycrystalline catalysts.

In previous chapters, DFT studies showed that the CO₂ direct dissociation is not favored on clean δ -MoC (001) since it involves a large energy barrier of 1.41 eV. A large energy barrier was also found for CO₂ dissociation on a TiC(001) substrate,⁷ clearly exhibiting different tendency respect to transition metal carbides with metal/carbon ratio of two. By means of DFT calculations, various elementary steps of interest for the full reaction map of CO₂ hydrogenation (Figure 5.1) on bare δ -MoC (001) were explored, aims at providing the main trends of the underlying molecular mechanism. Figure 6.2 shows that CO can be generated through the CO₂ hydrogenation to COOH entailing an energy barrier of 0.78 eV only; *i.e.* 0.63 eV lower than direct dissociation. *A priori*, direct hydrogenation of CO₂ to formate (HCOO) is not discarded but involves a much higher energy barrier (1.76 eV) and, hence, this route was not further considered. The COOH species can evolve easily to CO through a barrier of 0.31 eV. Thereby, the CO production implies two steps (hydrogenation to COOH and dissociation towards CO) whereas on β -Mo₂C only one step, with low energy barrier, is required for CO formation.

DFT calculations also displayed that CO hydrogenation towards MeOH is produced *via* HCO since the route of alcohol-like moieties, COH, presented an endothermic character of the elementary step, leading to the COH intermediate exhibiting an enthalpy very similar to the energy barrier for HCO formation. Then, our DFT calculations suggested that the reaction progress evolve through the aldehyde like species like H₂CO, H₃CO, and the final hydrogenation towards methanol. The rate limiting step of methanol synthesis is the H₂CO hydrogenation step, with an energy barrier of 0.85 eV. The absence of CH₄ detected by experiments was also justified considering that the hydrogenation of the methoxy intermediate (CH₃O) towards MeOH entails a low energy barrier, whereas the possible dissociation of methoxy intermediate to CH₃ was superior to 2 eV, dismissing this step. Nevertheless, as was observed on β -Mo (001) surface, the desorption process of methanol plays a negative role, since the desorption barrier is around -0.8 eV, i.e., similar barrier than the rate limiting step of the synthesis.

The experimental apparent energy barriers were consistent with the energy profile of CO₂ hydrogenation on bare δ -MoC (001). The apparent barrier is very similar for CO (0.78 eV) and MeOH production (0.74 eV), suggesting that both products have similar rate limiting step. These experimental values collect all the elementary barriers, where the rate limiting step has a higher statistical weight. Therefore, both experiment and computational models are in qualitative agreement indicating that it proceeds through CO formed in an initial step.

6.2 CO₂ hydrogenation on bare δ -MoC (001)

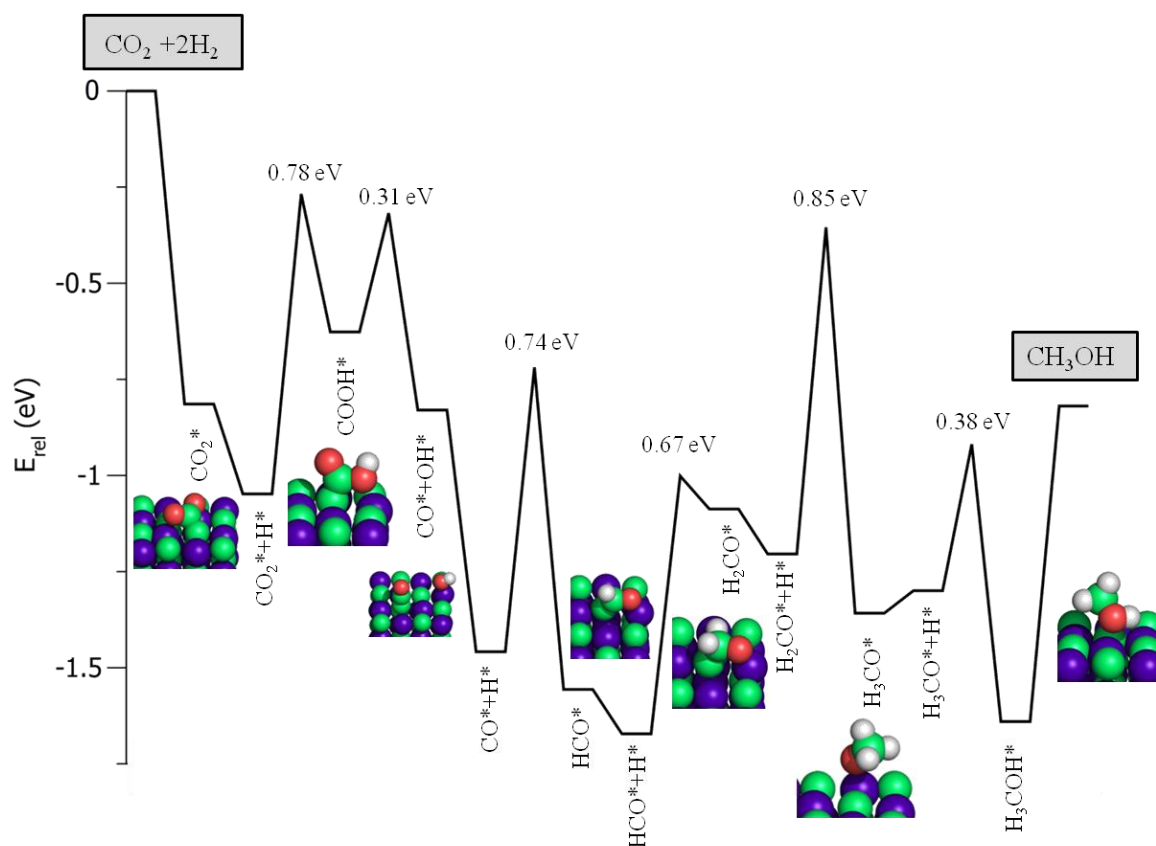


Figure 6.2: Energy profile for the elementary steps involved in CO₂ hydrogenation on δ -MoC as predicted from DFT calculations on a δ -MoC(001) slab model. Sketches represent the adsorption of CO₂ (I), COOH (II), CO + OH (III), HCO (IV), H₂CO (V), H₃CO (VI), and CH₃OH (VII).

The energy profile in Figure 6.2 indicates that, at 0 K, H₂O and MeOH desorption processes are likely to slow down the yield since desorption involves barriers of ~ 0.8 eV. Furthermore, the energy difference between adsorbed reactants (CO₂ + 6H) and the gas phase desorbed products is around 2 eV indicating that, despite of methanol synthesis is exothermic, the overall process is not favored. In order to gather information for the process under more realistic conditions, Figure 6.3 shows the Gibbs free energy profile for CO₂ hydrogenation to methanol on clean δ -MoC (001) at the minimum and maximum temperatures (500 and 600 K) used in the experiments, and also at different pressures (1 and 5 atm). Note that the Gibbs free energy barriers in the profiles drawn by solid lines in Figure 6.3, are identical to those reported in Figure 6.2, at 0 K. This is because calculated Gibbs free energy values neglect the entropic contributions from adsorbed species, as is proposed by

Nørskov *et al.*⁸ Nevertheless, the entropic effect of adsorbed species is computed in profile represented by dashed lines on Figure 6.3, exhibiting that these effects lead to variations on the energy barriers which are less than 0.1 eV, see Table 6.1, justifying the good agreement of the approximation proposed by Nørskov *et al.*⁸ From the results in Figure 6.3, the CO₂ hydrogenation to methanol at 0 K is exergonic whilst at 500 and 600 K the process becomes endergonic. However, the effect of temperature is crucial to favor H₂O and MeOH desorption. On the other hand, pressure effects affect adsorption and desorption thus facilitating methanol and water production.

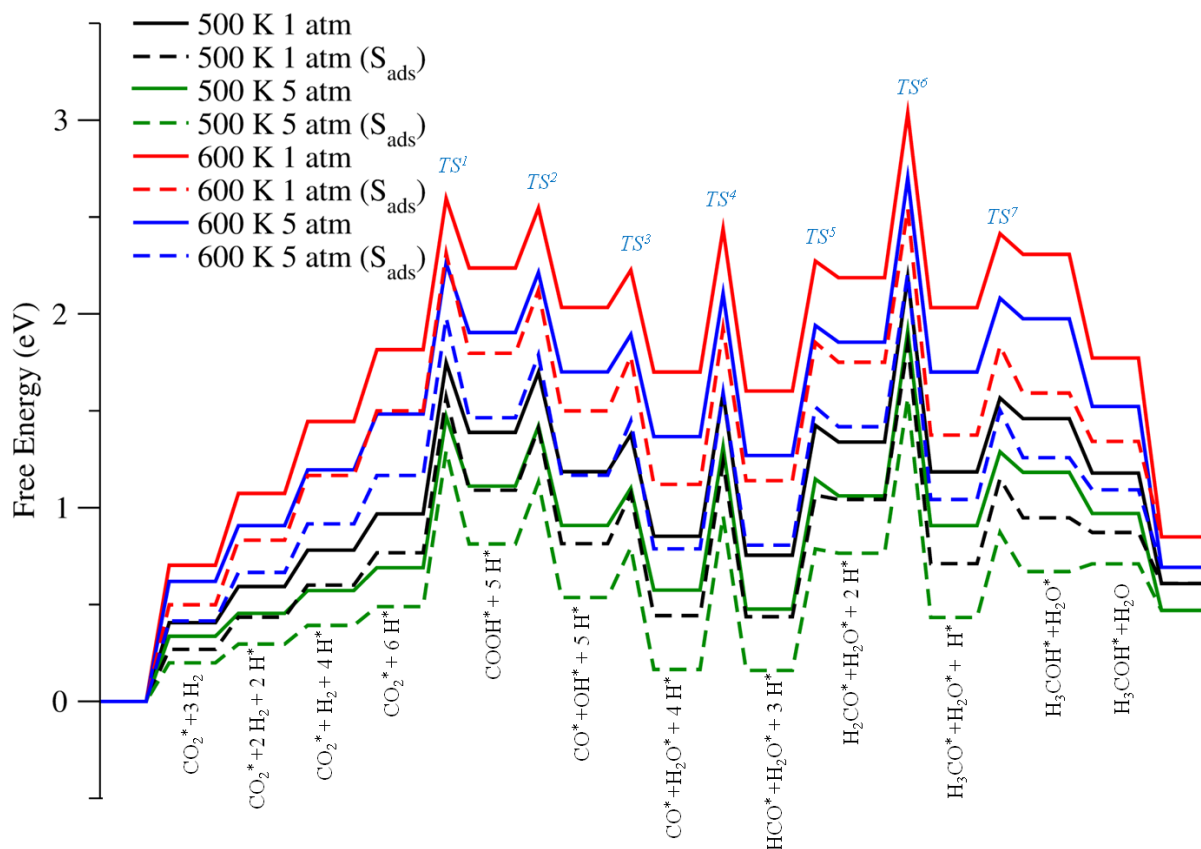


Figure 6.3: Free energy profiles of methanol synthesis at 500 and 600 K at different pressures (1 and 5 atm), including (dashed lines) or not (solid lines) the entropy of adsorbed species.

6.2 CO₂ hydrogenation on bare δ -MoC (001)

Table 6.1: Energy barriers of methanol synthesis (eV) at 0, 500, and 600 K of temperature.

	TS ¹	TS ²	TS ³	TS ⁴	TS ⁵	TS ⁶	TS ⁷
	/eV	/eV	/eV	/eV	/eV	/eV	/eV
0 K	0.78	0.31	0.19	0.74	0.67	0.85	0.38
500 K 1 atm	0.78	0.31	0.19	0.74	0.67	0.85	0.38
500 K 1 atm (S _{ads})	0.80	0.32	0.26	0.79	0.63	0.80	0.44
600 K 1atm	0.78	0.31	0.19	0.74	0.67	0.85	0.38
600 K 1atm (S _{ads})	0.81	0.32	0.28	0.81	0.71	0.79	0.46

To summarize, bare δ -MoC (001) present slightly superior energy barriers than β -Mo₂C (001) although is more selective due to the fact that only two main products were detected. Besides, bare δ -MoC (001) is more active at 600 K, given that part of the CO needed to produce methanol, is dissociated on β -Mo₂C (001) leading to CH₄ production.

6.3 CO₂ hydrogenation on Cu/ δ -MoC (001) and Au/ δ -MoC (001)

6.3.1 Experimental results

Previous studies on other TMCs (001) surfaces⁹ and on β -Mo₂C (001) surface exhibited that Au and Cu adatoms undergo electronic perturbations when in contact with these carbides. Results of scanning tunneling microscopy (STM) indicate that at small coverages ($\theta < 0.2$ ML), Au and Cu grow on TiC (001) forming very small particles, many of them two-dimensional.¹⁰⁻¹² This experimental research has a lot of importance when modeling surfaces and metal particles supported on thereon.

Figure 6.4 displays Arrhenius plots for the rates of CO, MeOH, and CH₄ production on Au/MoC and Au/ β -Mo₂C (001) surfaces with a gold coverage close to 0.2 ML. Small gold aggregates dispersed on the carbide surfaces are active for these chemical reactions. On δ -MoC, the addition of gold enhanced the rates of formation of CO and MeOH by a factor of 3. The enhancement of these rates of formation is large on β -Mo₂C (001) because gold, substantially reduces the formation of methane on this carbide surface (as it was observed in Chapter 5 with using Cu).

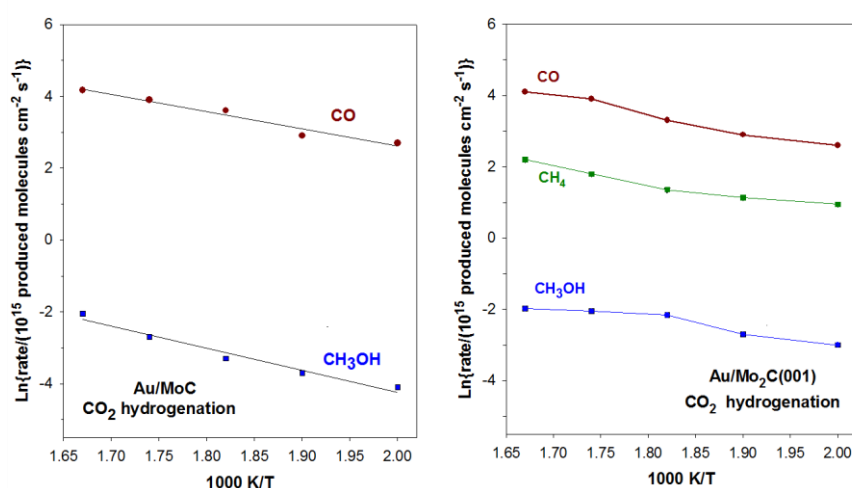


Figure 6.4: Hydrogenation of CO₂ on Au/MoC and Au/ β -Mo₂C (001) surfaces. Arrhenius plots to produce CO, methanol, and methane.

6.3 CO₂ hydrogenation on Cu/ δ -MoC (001)

This increase in selectivity was accompanied by an increase in stability (Figure 6.5). After reaction, XPS showed the presence of a minor amount of oxygen (~ 0.1 ML) on the MoC substrate. This oxygen coverage did not increase with time, and consequently the catalytic activity was not affected. However, the experimentalist found a very different behavior for Au/ β -Mo₂C (001) system. The amount of oxygen detected on this carbide system after reaction was large ($\theta > 0.4$ ML) and increased with time probably due to the formation of an oxycarbide. As result of this, the Au/ β -Mo₂C (001) system exhibited poor stability since the surface activity decreased due to the O poisoning. This fact is proven on Figure 6.5, where combining top and bottom pictures is clearly observed that the amount of produced CO decrease when the amount of deposited atomic O increase. These results displayed that the metal/carbon ratio in the transition metal carbide is critical in terms of good activity, selectivity, and stability for the reduction of CO₂ to CO.

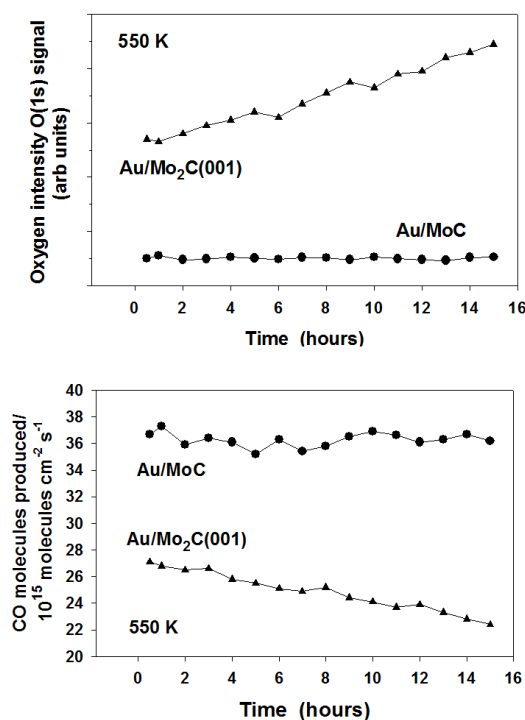


Figure 6.5: Top: Variation of the oxygen intensity in O 1s XPS spectra for Au/MoC and Au/ β -Mo₂C (001) catalysts ($\theta_{\text{Au}} \sim 0.2$ ML) as a function of time. Bottom: Rate of CO production for the Au/MoC and Au/ β -Mo₂C (001) catalysts as a function of time.

Figure 6.6 was key to select the appropriate catalyst to be modeled theoretically. This figure compares the effects of Au and Cu coverage on the activity for CO production of δ -MoC (001) and TiC (001) systems showing that the deposition of Cu generates the best catalysts. A maximum of catalytic activity was seen at admetal coverages of 0.2-0.25 ML. An identical result was obtained after plotting the rate to produce methanol instead of the rate to produce CO. Thus, the computational modeling and theoretical simulations will only carry out on Cu/ δ -MoC systems.

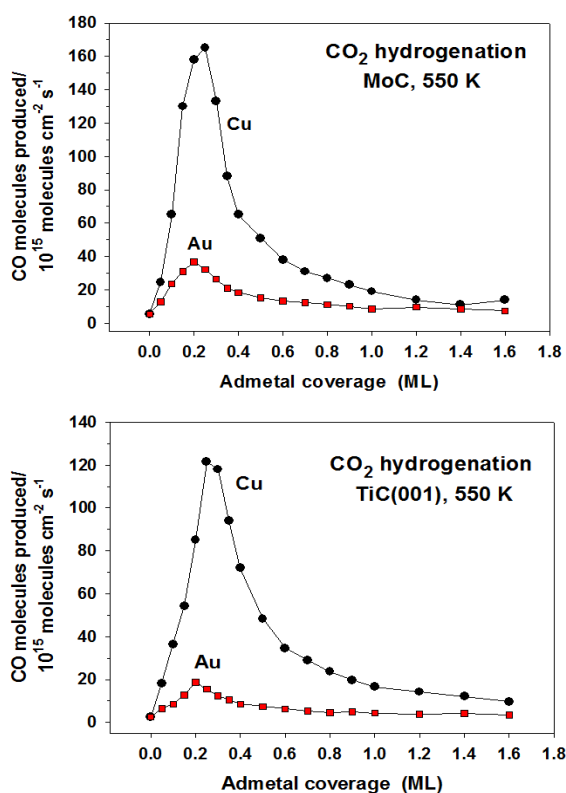


Figure 6.6: Rate of CO production on MoC, top, and TiC (001), bottom, for different coverages of Au and Cu.

The high catalytic activity of Cu/MoC systems towards CO is clearly observed on Figure 6.7. The derived apparent activation energies are listed in Table 6.2. From the slopes of the lines in Figures 6.7 it is clear that the Cu/ δ -MoC system has a lower apparent activation energy, 0.39 eV, than clean δ -MoC, 0.78 eV, or plain Cu(111),¹³ 0.95 eV. From the data in Figure 6.7, one can conclude that the Cu/ δ -MoC system has

6.3 CO₂ hydrogenation on Cu/ δ -MoC (001)

unique properties for the reduction of CO₂ into CO. The bare δ -MoC material presents worst activity than a model of a commercial Cu/ZnO catalysts,¹³ but upon the addition of a small amount of Cu one obtains a remarkable catalyst for the reduction of CO₂. In fact, Au/ δ -MoC also exhibits a better activity than Cu/ZnO, although its performance is not as good as that of Cu/ δ -MoC.

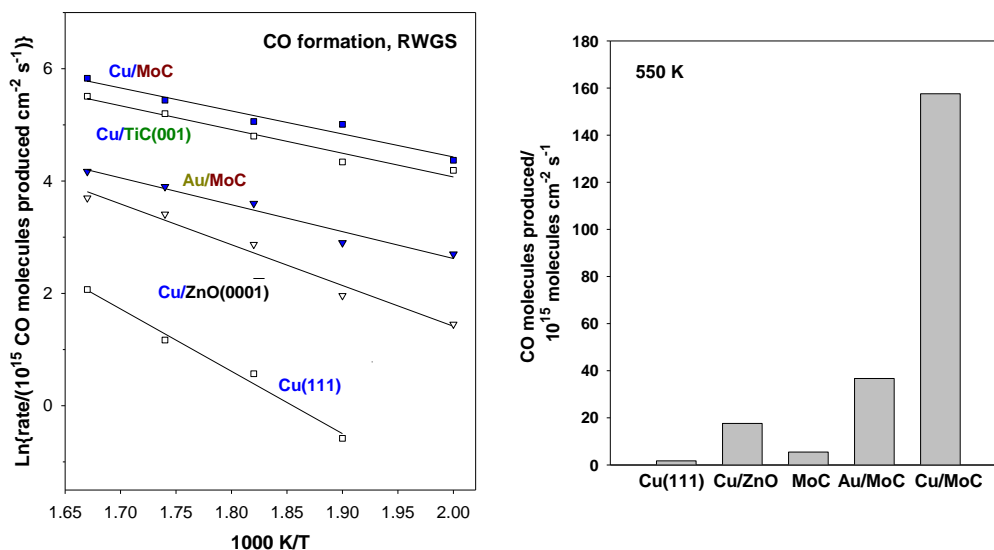


Figure 6.7: Left-side panel: Arrhenius plots for the production of CO by CO₂ hydrogenation on a series of gold- and copper-containing catalysts. The Cu and Au coverages on δ -MoC and TiC (001) were close to 0.2 ML.

Table 1. Apparent activation energies in eV.

Catalyst	CO production /eV	MeOH production /eV
Cu/ δ -MoC	0.39	0.43
Cu/TiC (001)	0.39	0.48
Au/ δ -MoC	0.43	0.52
Au/TiC (001)	0.61	0.57
δ -MoC	0.78	0.74
TiC (001)	0.35	0.91
Cu/ZnO (000 $\bar{1}$) ¹³	0.61	0.69
Cu (111) ¹³	0.95	1.08

On MoC and TiC (001) surfaces, the rate for CO formation was 10^2 - 10^3 times faster than the rate for methanol synthesis. Nevertheless, all these catalysts displayed an activity for methanol synthesis which was much larger than that of Au (111), Cu (111) or a Cu/ZnO catalyst, the catalyst model for the commercial one (Figure 6.8). In this aspect, Cu/ δ -MoC is clearly the best catalyst among the catalysts studied experimentally by the group of Dr. Jose Rodríguez. The apparent activation energy decreases from 1.08 eV on Cu(111)¹³ to 0.69 eV on Cu/ZnO(000 $\bar{1}$)¹³ and to only 0.43 eV on Cu/ δ -MoC. This surface has a catalytic activity that is 8-11 times higher than that of Cu/ZnO(000 $\bar{1}$)¹³ illustrating the advantage in using metal carbides as support. Since catalytic activity of Cu/ δ -MoC is much larger than that of Cu (111) or δ -MoC, the experimentalist hypothesizes that there is a synergy in the copper-carbide interface that favors the adsorption and transformation of CO₂.

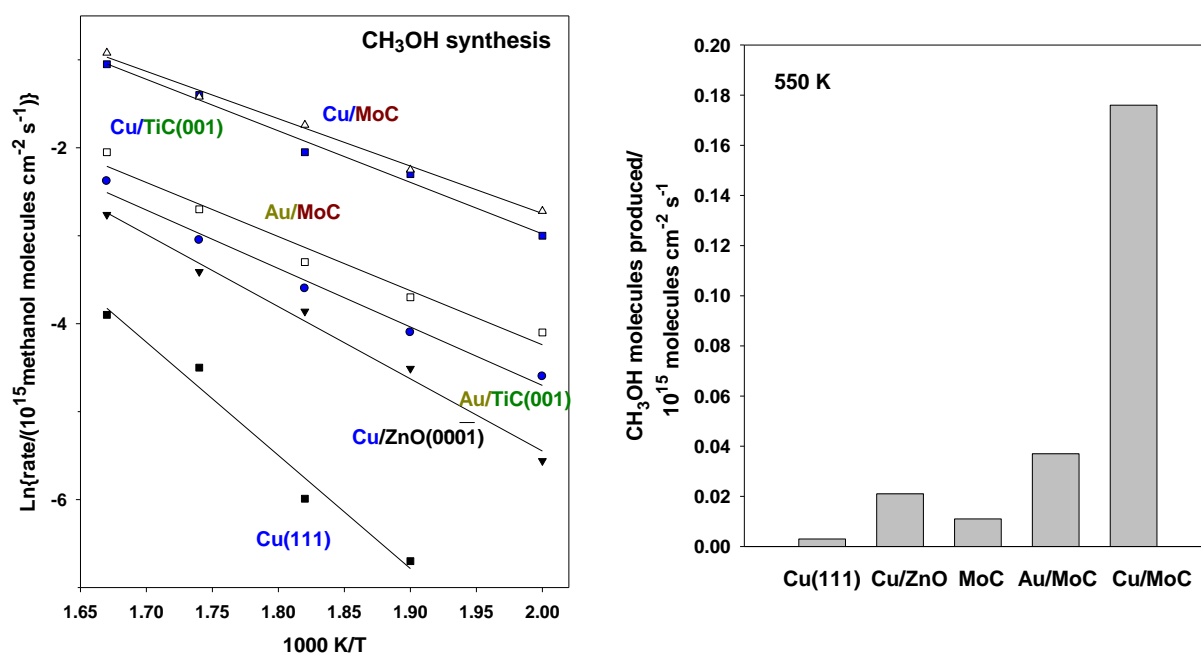


Figure 6.8: Left-side panel: Arrhenius plots for the production of methanol by CO₂ hydrogenation on a series of gold- and copper-containing catalysts. The Cu and Au coverages on MoC and TiC(001) were close to 0.2 ML.

In Table 6.2, the apparent activation energies for MeOH and CO formation on a given surface have similar values, suggesting that CO formation constitutes the rate limiting step in all the metal/carbide systems. Accordingly, CO is likely to be formed first and a fraction of it further converted into MeOH through selective hydrogenation steps.

6.3.2 DFT studies for CO₂ hydrogenation on Cu/MoC (001)

6.3.2.1 CO₂ adsorption on Cu₄/MoC (001) surfaces

To investigate the very large effect observed in the experiments when small Cu clusters are supported on δ -MoC, DFT calculations were performed to model the Cu/MoC systems and study the reaction mechanism. In opposite to orthorhombic Mo₂C, when Cu clusters were deposited on δ -MoC (001) surface they present 3D structure, except for small clusters (Cu₄) where 2D and 3D structures are degenerate in energy as is discussed in Chapter 3. In spite of some limitations due to the choice of the size of the supported clusters, Cu₄ supported on a δ -MoC(001) slab surface model was selected to represent the Cu/ δ -MoC system. Previous works^{12,14} and Chapter 5 of this thesis have corroborated that these models are suitable to describe the tendencies observed by experiments. Furthermore, this choice is justified from the experimental evidence that the Cu clusters on the Cu/ δ -MoC system are small.

The first step was to study the CO₂ adsorption on Cu₄/ δ -MoC, either as pyramidal or rhombus structure, where Top Cu and interface sites were tested. The calculations revealed that upon CO₂ adsorption on the supported Cu₄ pyramidal cluster triggered isomerization to rhombus geometry. As is displayed on Figure 6.9, the adsorption of CO₂ on top of rhombus and pyramidal Cu₄ clusters reach the same minimum structure, with an adsorption energy of -0.66 eV. The CO₂ adsorption on the interface maintained the pyramidal Cu structure, although the adsorption energy was lower, -0.32 eV. Thus, the study of the reaction mechanism was carried out

using the planar Cu₄ structure insomuch as the most favorable site entails the CO₂ activated on top of distorted rhombus cluster.

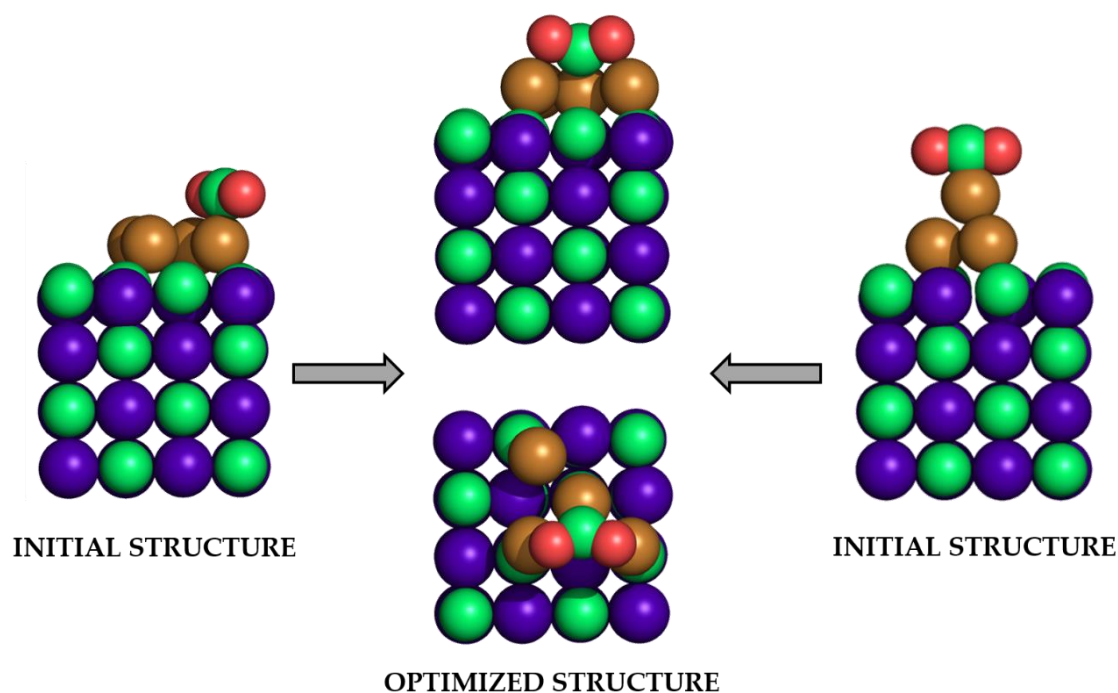


Figure 6.9: Pre-optimized geometries of CO₂ adsorbed on Cu₄ rhombus (left) and pyramid (right). Both structures reach the same minima structure (middle), with CO₂ activated on Cu₄ rhombus structure.

In comparison with bare surface, the CO₂ adsorption on Cu₄ cluster supported on the δ -MoC (001) surface (-0.66 eV) is slightly less favorable. Nevertheless, this difference is small enough to have both types of sites occupied, especially at large coverage where most of the sites of the clean surface will be already occupied. This fact evinces that Cu cluster supported on δ -MoC (001), actively participates on CO₂ activation, in opposite than Cu₄ cluster supported on β -Mo₂C (001), where the adsorption energy is 0.14 eV only. Here, an impact of the metal/carbon ratio of the carbide on the properties of the supported system is clearly observed; it changes the chemical nature of the supported metal cluster opening a completely different reactivity.

6.3.2.2 CO₂ conversion to CO and MeOH on Cu₄/ δ -MoC (001)

Figure 6.10 exhibits the energy profile and the energy barriers of CO₂ hydrogenation on Cu₄/ δ -MoC (001). The first step of reaction mechanism justifies the increase on the activity detected by experiments. Small Cu clusters can perform the adsorption and activation of CO₂ and promote its direct dissociation, which is not a favorable pathway on clean δ -MoC (001). The presence of supported Cu clusters facilitates direct CO₂ dissociation to CO + O with a fairly small activation energy barrier (0.65 eV), which cannot occur on clean δ -MoC (001) surfaces or on extended surfaces of copper such as Cu (111) or Cu (100).¹³ Our DFT calculations suggest that Cu reduces the CO₂ molecule towards CO whereas the water production probably comes from the H₂ oxidation to water, as was observed on previous works using Cu-based catalysts for CO₂ hydrogenation.¹⁵ These results suggest a change in the reaction mechanism, from the associative one on bare δ -MoC (001) surface, to redox path on Cu/ δ -MoC (001). This mechanism causes that the atomic O derived from the CO₂ reduction reacts with a fraction of H₂ to produce water, avoiding an excess of atomic O on the carbide region, which is not detected by experiments.

Therefore, on the Cu/ δ -MoC (001) system, there is synergy between the components of the catalyst and CO production is easier (and likely faster) than on the clean surface, in agreement with the experimental observations. On bare surface, two reaction steps are needed to produce CO, with a rate limiting step of 0.78 eV, whereas Cu₄ supported clusters dissociates directly the CO₂ molecule with an energy barrier of 0.65 eV.

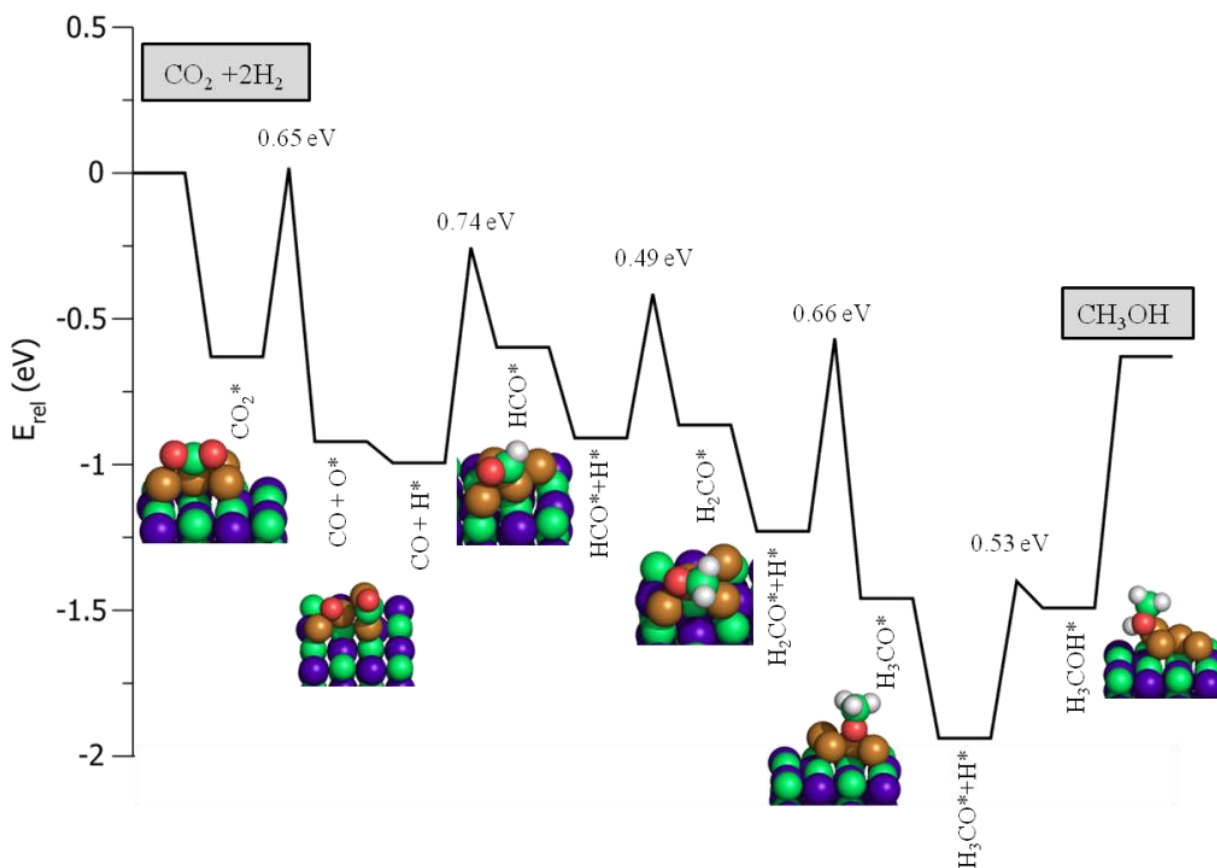


Figure 6.10: Energy profile for the elementary steps involved in CO₂ hydrogenation on Cu₄/ δ -MoC(001) model. Sketches represent the adsorption of CO₂ (I), CO+O (II), HCO (III), H₂CO (IV), H₃CO (V), and CH₃OH (VI).

Note however, that some energy barriers are slightly larger than the same reaction steps on bare δ -MoC (001). For this reason, Figure 6.11, compares total energy and Gibbs free energy profiles at 500 and 600 K and 5 atm for bare and Cu supported surface. Figures 6.11a and 6.11b confirmed the role of the supported Cu cluster in providing an alternative reaction pathway, since the CO₂ hydrogenation to COOH intermediate on top of Cu clusters entails a large energy barrier (1.29 eV, Figure 6.11b) in comparison with direct CO₂ dissociation (0.65, Figure 6.11a). Thus, CO is produced from direct dissociation of CO₂ rather than from prior formation of the COOH intermediate and its subsequent dissociation which is the preferred pathway on the bare δ -MoC(001) surface. Thereby, CO is produced through two different mechanisms depending of the CO₂ adsorption site (Cu or bare surface).

It is worth pointing out that on the supported cluster, at variance of the clean surface, direct CO₂ hydrogenation to formate (HCOO) is likely to occur. This was not unexpected since formate is typically observed on CO₂ hydrogenation using Cu as catalysts.¹⁶⁻¹⁸ Nevertheless, formate decomposition towards HCO intermediate is very unlikely since it is endothermic by 1.39 eV and HCOO hydrogenation towards dioxymethylene (H₂COO) presents a huge energy barrier (1.40 eV). Clearly, reaction pathways *via* formate could be discarded and this species will at most behave as a spectator perhaps poisoning the surface, occupying active sites for CO₂ conversion. Once the main role of Cu supported clusters were disseminated, Figures 6.11c-6.11f exhibit the effect of Cu clusters in comparison with bare surface. The overall study shows that the reaction proceeds at the clean surface *via* the HCO intermediate (Figure 6.10c) after the CO production. While CO is produced mostly at the supported cluster —and also partly at the clean surface— some of the further hydrogenation steps are facilitated by the presence of the support. In fact, compared to the clean surface, CO hydrogenation at Cu and Cu-Mo interface sites entails a higher energy barrier (~0.95 eV). Therefore, the CO produced on Cu₄/MoC (001) would diffuse to clean surface region, which is indeed thermodynamically favorable since adsorption at sites of the clean surface ($E_{\text{ads}} = -1.91$ eV) is preferred to adsorption at Cu sites ($E_{\text{ads}} = -1.15$ eV) and the calculated diffusion energy barriers from the supported cluster to the bare surface region are much smaller (around ~0.30 eV) as is discussed in Chapter 2. Besides its relevant role on triggering CO₂ dissociation, Cu₄ and the Cu-MoC interface sites also play a crucial role on several hydrogenations steps. For instance, the energy barrier of H₂CO formation from HCO is reduced from 0.67 eV on the bare surface to 0.49 eV (Figure 6.11d), and subsequent hydrogenation to H₃CO is also more favorable at Cu sites; the energy barrier decreases from 0.85 eV on the bare surface to 0.66 eV at Cu sites (Figure 6.11e). The profile for last hydrogenation to methanol is displayed on Figure 6.11f and implies an energy barrier larger than on the bare surface (0.53 eV). This is, however, lower than the energy barriers for the previous steps and, furthermore, methanol could

also be formed on the clean region. Eventually, note that temperature and pressure effects affect mainly the desorption step which becomes more favorable, avoiding one of the negative (and critical) points of CO₂ hydrogenation on bare δ -MoC (001).

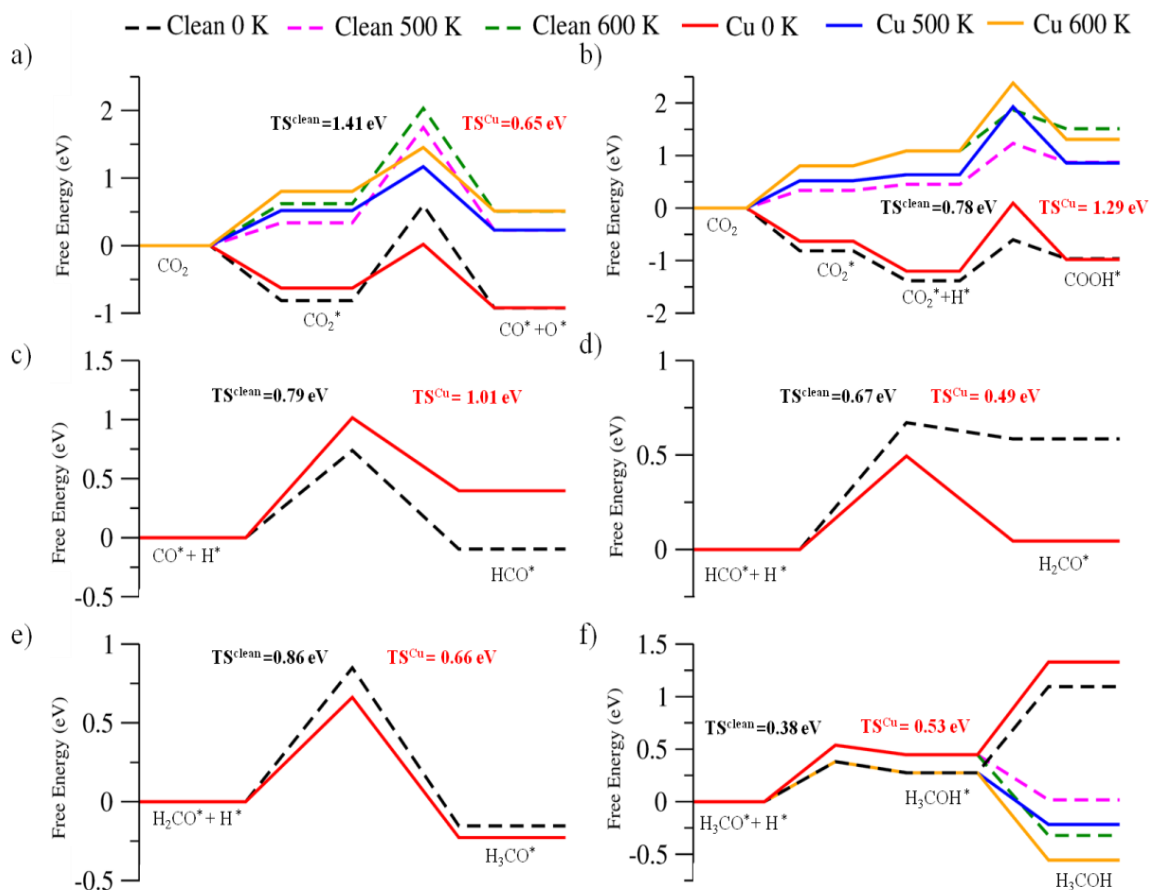


Figure 6.11: Calculated total energy (0 K) and Gibbs free energy (500 and 600 K at 5 atm) profiles for the most relevant elementary steps: (a) CO₂ dissociation, (b) CO₂ hydrogenation, (c) CO hydrogenation, (d) HCO hydrogenation, (e), H₂CO hydrogenation and (f) methanol production.

6.4 Conclusions

In this chapter, the CO₂ hydrogenation mechanism towards CO and methanol was studied using cubic δ -MoC, with metal/carbon ratio of one, as catalysts or support of small Cu nanoparticles. This Chapter is essential to demonstrate the critical role of metal/carbon ratio on the carbide for the catalysts performance.

Experiments on bare surfaces of cubic MoC (001) and orthorhombic Mo₂C (001) acclaim MoC (001) as promising catalyst for CO₂ reduction. Both catalysts displayed similar yields of CO and methanol between 500-600 K, although the selectivity of β -Mo₂C (001) is lower, since CH₄ is also produced. The δ -MoC (001) interacts moderately with CO₂ molecule, favoring the CO₂ activation, although avoiding its direct dissociation. This fact is crucial to the catalyst stability and activity, since the CO₂ dissociation involve the atomic O formation, which re-cover the exposed surface with an O layer, poisoning the catalyst. Theoretical results propose the CO₂ hydrogenation towards COOH intermediate as the fundamental step to produce CO. The role of metal/carbon ratio is critical since these results are in opposite with CO₂ hydrogenation on β -Mo₂C (001) (Chapters 4 and 5) where CO₂ is easily dissociated, and consequently, atomic O is deposited on carbide surface, in agreement with experimental results, where the amount of oxygen on this carbide system after reaction was large than 0.4 ML and increased with time.

In order to increase the catalytic power of these systems, small Au and Cu particles were deposited on both molybdenum carbides. Experiments demonstrated that the catalytic activity of Cu supported particles on δ -MoC (001) towards CO and methanol is superior to Au/MoC and Cu/ZnO (000 $\bar{1}$), a model of commercial catalyst. The metal/carbon ratio also governs the catalytic activity of Cu supported clusters, since on Cu₄/ β -Mo (001) the Cu-CO₂ interaction is weak whilst on Cu₄/ δ -MoC, Cu can activate and dissociate CO₂, promoting a change on the reaction mechanism. DFT calculations provide several clues for the origin of the high activity and selectivity

observed for Cu/ δ -MoC in experimental tests. Our DFT calculations suggest that the Cu/ δ -MoC system works as a bifunctional catalyst, where the supported Cu clusters readily dissociate CO₂ into CO and O and both the clean regions of the δ -MoC substrate and the supported clusters catalyze the main hydrogenation steps towards methanol and water. In this way, the supported Cu clusters open a new route to CO generation without requiring the assistance of COOH intermediate as in a clean δ -MoC (001) surface.

In this sense, the great features of Cu/ δ -MoC in terms of activity, selectivity, and stability for CO₂ conversion is encouraging with possible applications in technical or industrial operations.

6.5 References

- [1] X. M. Liu, G. Q. Lu, Z. F. Yan and J. Beltramini, *Ind. Eng. Chem. Res.* **2003**, *42*, 6518.
- [2] H. H. Hwu and J. G. Chen, *Chem. Rev.* **2005**, *105*, 185.
- [3] P. Liu and J. A. Rodriguez, *J. Phys. Chem. B*, **2006**, *110*, 19418.
- [4] C. Kunkel, F. Viñes and F. Illas, *Energy Environ. Sci.*, **2016**, *9*, 141.
- [5] J. A. Rodriguez, J. Evans, L. Feria, A. B. Vidal, P. Liu, K. Nakamura and F. Illas, *J. Catal.*, **2013**, *307* 162.
- [6] J. R. d. S. Politi, F. Viñes, J. A. Rodriguez, F. Illas, *Phys. Chem. Chem. Phys.*, **2013**, *15*, 12617
- [7] A. B., Vidal, L. Feria, J. Evans, Y. Takahashi, P. Liu, K. Nakamura, F. Illas and J. A. Rodriguez, *J. Phys. Chem. Lett.* **2012**, *3*, 2275.
- [8] J. K. Nørskov, F. Studt, F. Abild-Pedersen and T. Bligaard, *Fundamental Concepts in Heterogeneous Catalysis* Wiley, New Jersey, **2014**.
- [9] J. A. Rodriguez and F. Illas, *Phys. Chem. Chem. Phys.*, **2012**, *14*, 427.
- [10] J. A. Rodriguez, P. Liu, F. Viñes, F. Illas, Y. Takahashi and K. Nakamura, *Angew. Chem., Int. Ed.*, **2008**, *47*, 6685.
- [11] J. A. Rodriguez, P. Liu, Y. Takahashi, K. Nakamura, F. Viñes and F. Illas, *J. Am. Chem. Soc.*, **2009**, *131*, 8595.
- [12] L. Feria, J. A. Rodriguez, T. Jirsak and F. Illas, *J. Catal.*, **2011**, *279*, 352.
- [13] Y. Yang, J. Evans, J. A. Rodriguez, M. G. White and P. Liu, *Phys. Chem. Chem. Phys.* **2010**, *12*, 9909.
- [14] J. A. Rodriguez, P. J. Ramírez, G. G. Asara, F. Viñes, J. Evans, P. Liu, J. M. Ricart and F. Illas, *Angew. Chem. Int. Ed.*, **2014**, *53*, 11270
- [15] M. Gines, A. J. Marchi and C. R. Apesteguia, *Appl. Catal. A*, **1997**, *154*, 155.
- [16] C. Liu, B. Yang, E. Tyo, S. Seifert, J. De Bartolo, B. von Issendorff, P. Zapol, S. Vajda and L.A. Curtiss, *J. Am. Chem. Soc.* **2015**, *137*, 8676.
- [17] F. Studt, M. Behrens, E. L. Kunkes, N. Thomas, S. Zander, A. Tarasov, J. Schumann, E. Frei, J. B. Varley, F. Abil-Pedersen, J. K. Nørskov and R. Schlögl, *Chem. Cat. Chem.* **2015**, *7*, 1105.
- [18] Y. Kim, T. S. B. Trung, S. Yang, S. Kim and H. Lee, *ACS Catal.* **2016**, *6*, 1037.

CHAPTER SEVEN

Water Gas Shift reaction on Cubic δ - MoC and Au/ δ -MoC (001) Surfaces

7.1 Introduction

The results presented in Chapters 4, 5, and 6 have exhibited the excellent properties of orthorhombic β -Mo₂C and cubic δ -MoC (001) surfaces as catalysts and supports of CO₂ hydrogenation towards CO and MeOH, being δ -MoC (001) the most suitable due to its activity, selectivity, and stability.

After these promising results, the last part of this thesis was focused on the study of another green chemistry reaction, the water gas shift (WGS), which has been exhaustively studied from experimental and theoretical sides due to its relevant role in the chemical industry.¹⁻¹⁴ This reaction is fundamental for our society due to economical^{15,16} and environmental reasons,¹⁷ since H₂ is considered an inexhaustible and environmental friendly gas, and it has been proposed as a substitute of gas-oil fuels and biodiesel vehicles fuels.¹⁸

One of the key factors is related with the fact that WGS is exothermic and reversible, and consequently, high temperatures decrease the equilibrium constant, disfavoring the H₂ production.⁷ Nevertheless, due to kinetic reasons, faster reaction rates would be obtained at high temperatures. In fact, it is often necessary to follow two different strategies, working at high and low temperatures, where Fe₂O₃/Cr₂O₃ and Cu/ZnO/Al₂O₃ are employed in industry as catalysts, respectively. Thus, the design of new cost-effective catalysts able to perform the WGS reaction at low temperatures is a chief challenge.

The reaction mechanism of WGS have constituted a large debate. Basically, two different mechanisms have been proposed, the associative and redox ones. In the associative pathway, the hydroxyl moiety (OH) is combined with CO, leading to a controversy about the produced intermediate. Some authors consider that HCOO specie is produced¹⁹ and later decomposes to CO₂ and H₂ whereas there are studies where the COOH is the generated intermediate.^{12,20} Otherwise, redox mechanism consists in the surface oxidation by H₂O, which is reduced to H₂ and the reduction of this oxidized surface by CO, which is oxidized to CO₂. A DFT study of WGS on

several (111) surfaces of transition metals revealed that gold is an excellent candidate to oxidize CO towards CO₂ and the recombination of H atoms to produce H₂. Also, platinum can catalyze efficiently the COOH formation and decomposition to CO₂. Nevertheless, neither Au nor Pt are the suitable catalysts for WGS since the energy barrier for H₂O dissociation, the essential step of WGS, is too large.

In this sense, TMCs appear as an excellent alternative to adsorb and dissociate the H₂O molecule. The extended (001) surface of TiC was proposed as an active catalyst for H₂O dissociation,²¹ although redox and associative intermediate steps present energy barriers close to 1 eV. However, the deposition of small Au nanoparticles on TiC (001) reduces the energy barrier of COOH formation, promoting Au/TiC (001) as an excellent catalyst for WGS reaction.²² Respect to molybdenum carbides, α -Mo₂C and β -Mo₂C were studied as catalysts of WGS reaction, where α -Mo₂C works by redox mechanism²³ and β -Mo₂C is considered as a less reactive catalyst than Cu owing to the fact of the oxycarbide formation from the complete H₂O decomposition.²⁴

In this Chapter, using a combination of experimental and theoretical models, a study of the low temperature WGS reaction on clean δ -MoC and β -Mo₂C (001) surfaces and on Au clusters supported thereon has been accomplished. The addition of Au to the δ -MoC and β -Mo₂C substrates produces an important increase in the amount of H₂ and CO₂ produced during the WGS reaction. Despite of the experimentalists provided results for CO₂ and H₂ production on orthorhombic and cubic phases, only the last one was considered from a computational point of view, since the metal/carbon ratio has a strong effect on the performance of the catalysts, as was observed for CO₂ hydrogenation. Given that the reactants of WGS contain oxygen (H₂O and CO), orthorhombic Mo₂C (001) surface shows a strong adsorbate-support interaction, which involves their dissociation and subsequent deactivation due to the oxycarbide formation.

7.2 Experimental results

As was observed for CO₂ hydrogenation, bare β -Mo₂C (001) surface exhibited higher reactivity than plain δ -MoC (001). The bare β -Mo₂C (001) surface is very reactive towards water,^{25,26} involving the rupture of the O-H bonds. Thus, as was detected after the CO₂ dissociation, a layer of oxygen was formed on top of the carbide surface. One can consider that part of the deposited O may come from the CO dissociation, since the dissociation energy barrier is lower than 1 eV (Chapter 4). Therefore, the active phase of Mo₂C as a catalyst for the WGS is best described as an oxycarbide.^{26,27} Moreover, this strong interaction of water with β -Mo₂C leads to an active catalyst that exhibits short term stability as is displayed on Figure 7.1, where the amount of produced CO₂ molecules decrease as time passes.

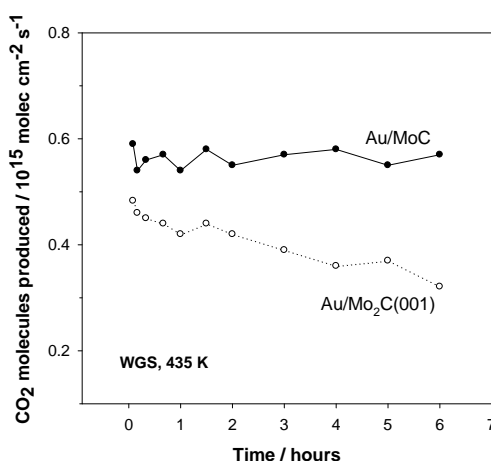


Figure 4: Water-gas shift activity of Au/ δ -MoC and Au/ β -Mo₂C (001) surfaces as a function of time. A coverage of 0.15 ML of gold was deposited on the carbide surfaces and the generated catalysts were exposed to 20 Torr of CO and 10 Torr of H₂O at 435 K.

Results on Figure 7.1 exhibited that the Au/ δ -MoC catalysts did not undergo deactivation with time, although a small amount of oxygen ($\theta < 0.4$ ML) was observed on the catalyst surface with post-reaction XPS characterization. Given that δ -MoC displayed a lower reactivity towards water than β -Mo₂C (001),²⁵ together with the large energy barrier of CO dissociation on δ -MoC, the experimentalist suggested

that this amount of oxygen was produced on intermediate steps. Nevertheless, on δ -MoC, the catalysts deactivation was not observed, probably due to that the O- δ -MoC interactions are lower than the O- β -Mo₂C ones.

In terms of selectivity, both catalysts presented similar tendencies for WGS and CO₂ hydrogenation. Figure 7.2 displays data collected after performing the WGS under hydrogen-rich conditions. On the δ -MoC-based systems, there is only production of CO₂ (and H₂) from the WGS. No CH₄ is detected on δ -MoC or Au/ δ -MoC. However, the β -Mo₂C (001) generates simultaneously CO₂/H₂ and CH₄, *i.e.*, the selectivity decrease. The β -Mo₂C (001) fully dissociates CO into O and C that can be hydrogenated into CH₄ as has been discussed in Chapter 5. Figure 7.2 also revealed the great importance of Au supported clusters, given that the production of CO₂ (and H₂) increase drastically. The Au/ δ -MoC systems exhibited the large number of produced molecules, despite bare δ -MoC is slightly less active than bare β -Mo₂C (001).

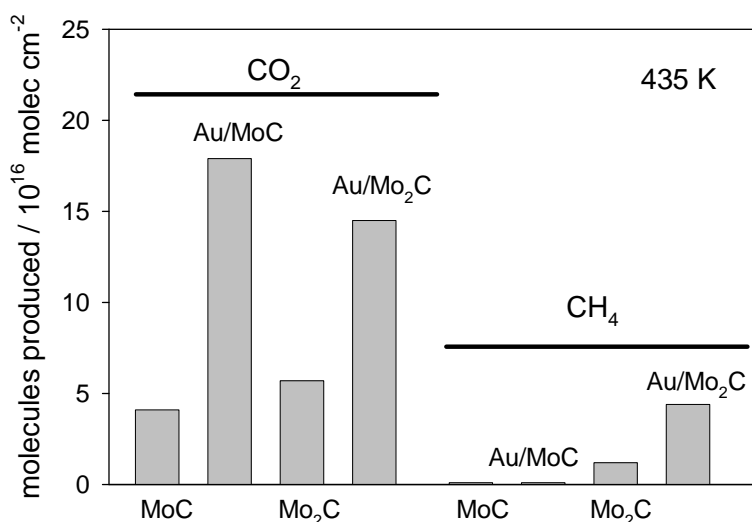
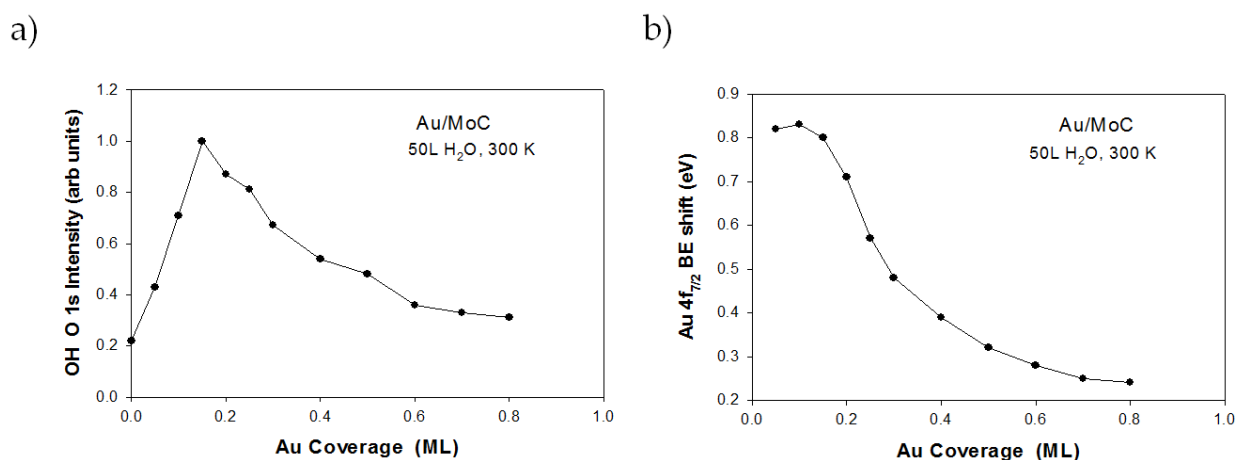


Figure 7.2: Production of CO₂ and CH₄ after exposing a series of metal carbide catalysts to a mixture of CO (20 Torr), H₂O (10 Torr) and H₂ (100 Torr) at 435 K for 5 minutes.

7.2 Experimental results

The synergistic interactions between Au and δ -MoC enhance the dissociation of water. Figure 7.3 summarizes results of XPS obtained after dosing 50 L of water at 300 K to clean δ -MoC and Au/ δ -MoC surfaces. The interaction of water with plain δ -MoC produces an O 1s peak at ~ 531.8 eV that matches the binding energy expected for adsorbed OH on the carbide surface.²⁵ Water does not dissociate on surfaces or unsupported nanoparticles of gold.^{5,13} However, the addition of Au produces an increase in the rate of water dissociation up to an admetal coverage of ~ 0.15 ML. After that point, there is a monotonic decrease in the amount of OH deposited on the surface. At small coverages, the reaction with water produces a binding energy shift of ~ 0.8 eV in the Au $4f_{7/2}$ core level consistent with the formation of Au-OH bonds. A decrease in the Au coverage reduces the amount of OH generated on the surface and the Au $4f_{7/2}$ binding energy shift is reduced in magnitude. The deposition of Au coverages above 0.5 ML probably produces on the carbide surface big Au



particles. ¡Error! Marcador no definido.

Figure 7.3: a) Amount of OH detected with XPS after dosing 50 langmuir (L) of water at 300 K to δ -MoC and Au/ δ -MoC surfaces and b) Corresponding binding shift in the Au $4f_{7/2}$ binding energy.

In Figure 7.4, the WGS activity of Au/ δ -MoC and Au/TiO₂ (110) surfaces is compared. A maximum in the production of H₂ and CO₂ through the WGS was observed at $\theta_{\text{Au}} \sim 0.15$ ML, as observed for H₂O dissociation. The data clearly indicate that δ -MoC is a better support to generate a low-temperature WGS catalyst. The best Au/ δ -MoC catalyst displays an activity that is ~ 8 times larger than that of the top Au/TiO₂ (110) catalyst. This trend was also observed in the Arrhenius plot in Figure 7.5. In the temperature range of 410-465 K, Au/ δ -MoC is clearly the best catalyst. The apparent activation energy for the WGS reaction on Au/ δ -MoC is 0.29 eV, an activation energy which is noticeably lower than the values of 0.37 eV on Au/TiO₂ (110) and 0.66 eV on Cu (111).²⁸ At relatively low temperatures (below 470 K), Au/ δ -MoC has a WGS activity that is observed on Au/oxide and Cu/oxide catalysts (oxide= TiO₂, ZnO, CeO₂, and MgO) only at elevated temperatures (above 500 K).^{22,28}

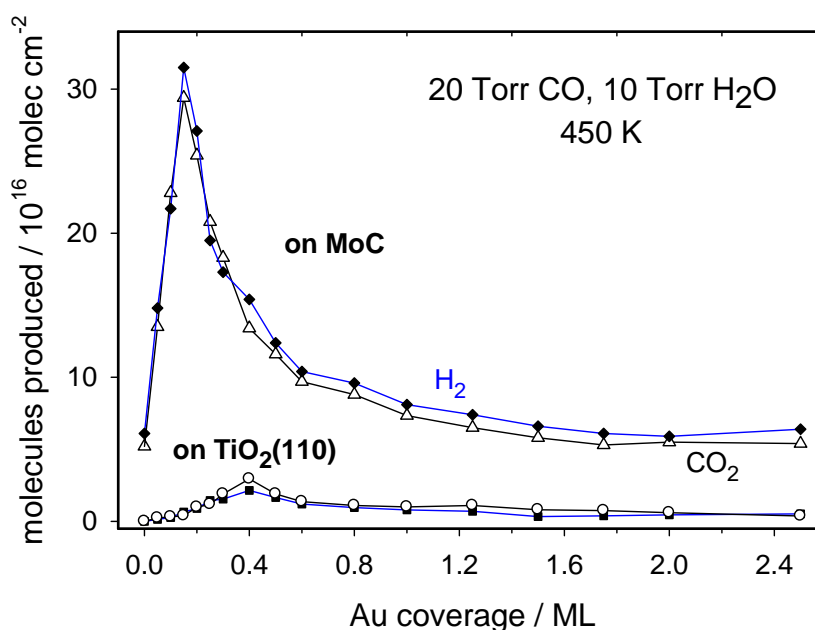


Figure 7.4: WGS activity of Au/ δ -MoC and Au/TiO₂ (110) as a function of Au coverage. The reported values for the production of H₂ (filled symbols) and CO₂ (empty symbols) were obtained after exposing the catalysts to CO (20 Torr) and H₂O (10 Torr) at 450 K for 5 min.

7.2 Experimental results

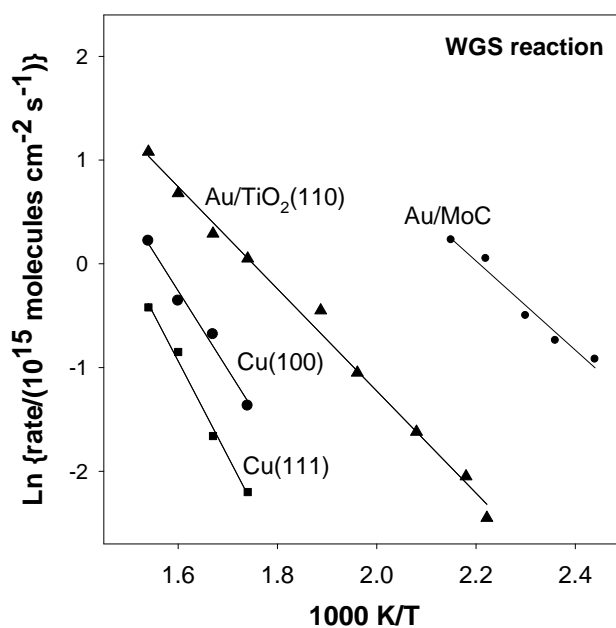


Figure 7.5: Arrhenius plots for the WGS on Cu (111), Cu (100), Au/TiO₂ (110) and Au/ δ -MoC catalysts (CO: 20 Torr; H₂O: 10 Torr). Surfaces for metallic Au are not active for the WGS reaction. The data for Cu (111), Cu (100) and Au/TiO₂ (110) are taken from Refs. 11 and 28. The coverages of Au on TiO₂ (110) and δ -MoC were 0.4 and 0.15 ML, respectively.

Insomuch as the experimental results presented in this section and considering the previous studies about CO₂ hydrogenation reaction discussed in previous chapters, it seems clear that in terms of activity, selectivity, and stability, δ -MoC (001) and Au/ δ -MoC (001) are the proper candidates for WGS reaction. Therefore, only these systems were model to study the properties and the different reaction mechanisms from a computational point of view.

7.3 DFT study of WGS on bare δ -MoC (001)

After the essential H_2O dissociation, many possible mechanisms for the WGS reaction have been proposed in the literature using metal surfaces,^{1,2,3,9,12,13} bare TiC and Au/TiC surfaces,^{10,11} and β - Mo_2C ¹⁴ as catalyst models. Figure 7.6 displays these pathways after the first O-H cleavage. Once the OH^* moiety is produced, it can recombine with the CO molecule towards the carboxyl (COOH^*) intermediate, and its dissociation leads to the CO_2 production (P1). On the other hand, the reaction could follow the redox pathway implying OH dissociation and the subsequent recombination of atomic O^* with CO^* molecule towards CO_2 (P2). Following this redox route, the reaction path could also imply the formate intermediate (HCOO^*) by means of the recombination of CO, and atomic H and O, from the OH moiety dissociation (P3). Furthermore, another possibility involves the reaction between two OH moieties to produce $\text{H}_2\text{O} + \text{O}$ (P4). In this manner, an atomic O is generated which could form CO_2 after the recombination with CO.

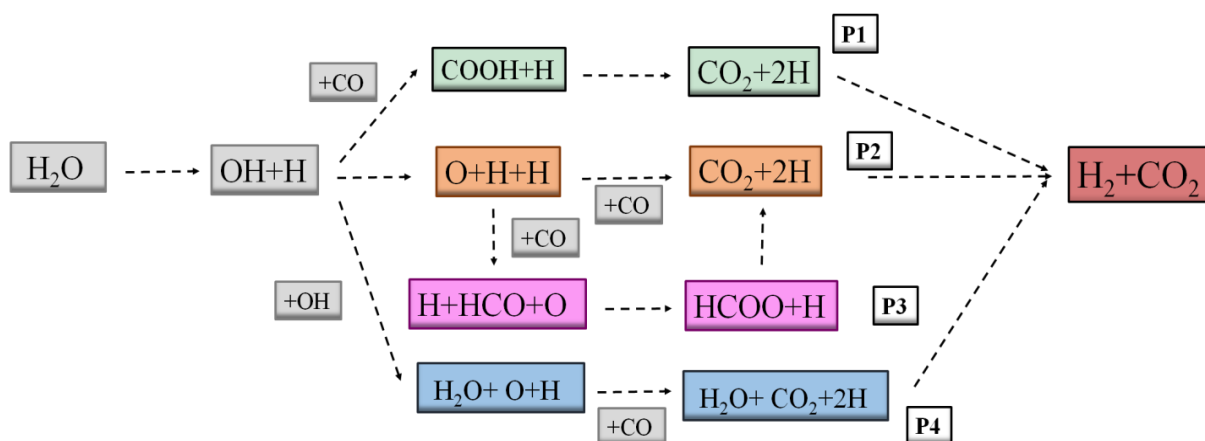


Figure 7.6: Scheme of studied pathways of WGS on δ -MoC (001).

On bare δ -MoC (001), the water molecule is clearly chemisorbed (-0.77 eV) on Top Mo sites with the two H atoms in the same δ -MoC (001) surface plane, pointing to C atoms. The energy barrier of this process included the ZPE correction is 0.53 eV.

7.3 DFT study of WGS on δ -MoC (001)

On bare δ -MoC (001), the water molecule is clearly chemisorbed (-0.77 eV) on Top Mo sites with the two H atoms in the same δ -MoC (001) surface plane, pointing to C atoms. The energy barrier of this process including the ZPE correction is 0.53 eV. Once the H* and OH* moieties are produced, the H atom will recombine with other H atom to produce H₂ with an energy barrier of 0.75 eV, whereas the OH* moiety will be a key reactant to obtain CO₂. Figure 7.7, exhibits the most favorable pathway for the WGS on clean δ -MoC (001). This path (P1) implies the COOH* formation through OH* and CO* recombination. Note that, as was displayed in previous works using TiC (001),^{10,11} the rate limiting step is the COOH* formation since it involves an activation energy of 0.89 eV, in contrast to metal surfaces catalysts, where the water dissociation step normally has the largest barrier.¹³ Once formed, the COOH* intermediate can evolve to CO₂ by overcoming an energy barrier of 0.27 eV. Once formed, the COOH* intermediate can evolve to CO₂ by overcoming an energy barrier of 0.27 eV.

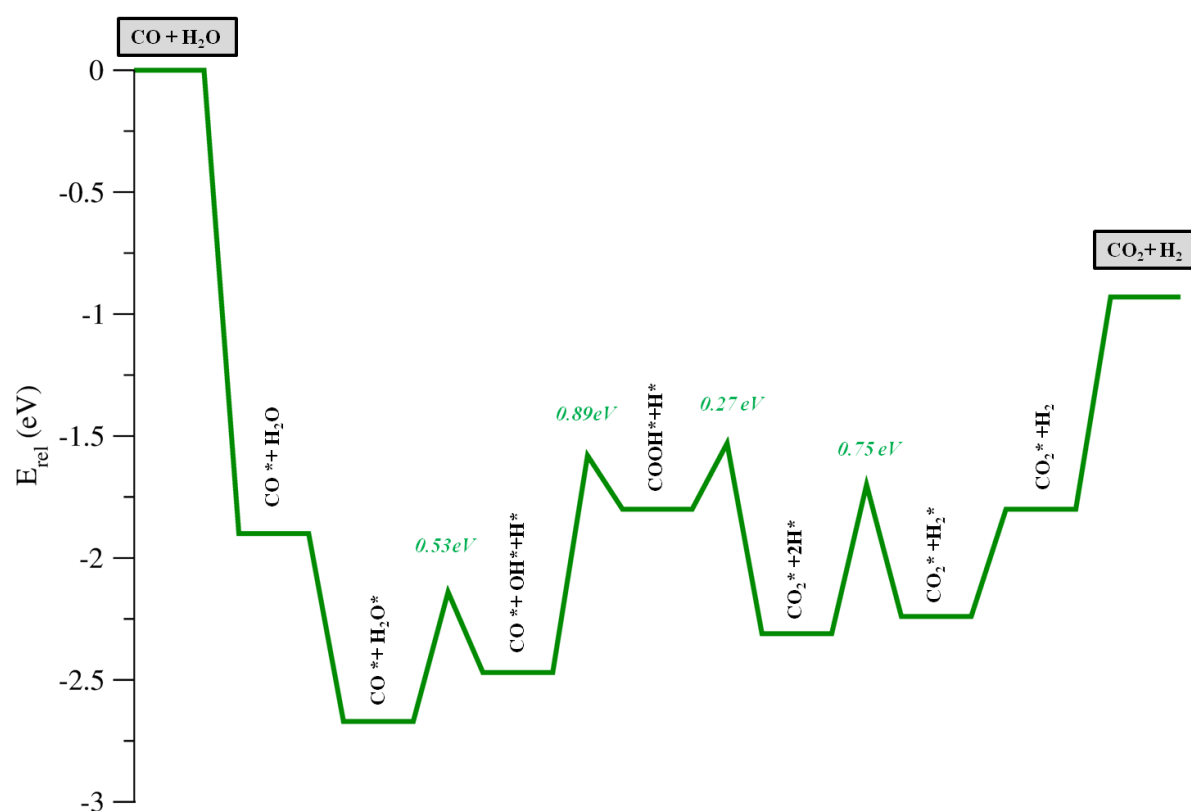


Figure 7.7: Most favorable WGS energy profile on δ -MoC (001) including ZPE correction.

Despite of the fact that the energy barriers of P1 are not excessively high, experiments detect less CO_2 and H_2 than one could expect (see Figure 7.2). This fact is consistent with our theoretical predictions, since on the clean δ -MoC (001) surface some reverse rates are higher (lower energy barriers) than the forward ones (Table 7.1). Once H_2O is dissociated, the OH could evolve towards COOH through $\text{CO} + \text{OH} \rightarrow \text{COOH}$ reaction or it can recombine to H ($\text{H} + \text{OH} \rightarrow \text{H}_2\text{O}$) to produce the H_2O molecule back. The rate of the latter reaction is three orders of magnitude superior ($5.21 \times 10^5 \text{ s}^{-1}$) to the COOH production ($3.31 \times 10^2 \text{ s}^{-1}$). Nevertheless, the H recombination to produce H_2 ($\text{H} + \text{H} \rightarrow \text{H}_2$) competes against H_2O formation, since its rate is only one order of magnitude lower ($5.82 \times 10^4 \text{ s}^{-1}$) than H_2O reverse barrier, *i.e.*, part of the H atoms needed in the H_2O regeneration could evolve to H_2 production, thus allowing the reaction between OH and CO molecule. Besides, once COOH is produced, the reverse rate ($\text{COOH} \rightarrow \text{CO} + \text{OH}$) is two orders of magnitude larger ($3.40 \times 10^{10} \text{ s}^{-1}$) than that of COOH dissociation ($\text{COOH} \rightarrow \text{CO}_2 + \text{H}$, $8.09 \times 10^8 \text{ s}^{-1}$), thus disfavoring CO_2 production.

On the other hand, the products desorption is not a minor issue, since the interaction between them and δ -MoC (001) surface is strong, especially in the case of CO_2 molecule, as it has been discussed in previous Chapters. The CO_2 desorption energy is 0.85 eV, similar to the energy barrier for the rate limiting step for WGS on this surface. Therefore, adsorbed CO_2 can poison, at least in part, the surface due to the difficult desorption. Otherwise, the possible hydrogenation of CO_2 molecule towards COOH on bare δ -MoC (001) has an energy barrier of 0.78 eV, see Chapter 6. Hence, this process competes with both CO_2 desorption and H_2 production (0.75 eV), triggering the reverse water gas shift reaction. These two features lead to a surface collapse, since the difficulty to desorb CO_2 and the constant COOH production through reverse WGS, which does not favor the presence of reactive sites, preventing the rapid dissociation of H_2O .

7.3 DFT study of WGS on δ -MoC (001)

Table 7.1: Transition state theory derived rates (s^{-1}), at 465 K, for the direct (r_d) and reverse (r_r) elementary steps of the WGS mechanism on clean δ -MoC (001).

Step	T= 465 K δ -MoC (001)	
	r_d /s ⁻¹	r_r /s ⁻¹
H ₂ O → H+OH	1.62×10^3	5.21×10^5
OH → O+H	1.54×10^{-4}	4.37×10^{00}
CO+OH → COOH	3.31×10^2	3.40×10^{10}
COOH → CO ₂ +H	8.09×10^8	2.07×10^4
OH + OH → H ₂ O + O	1.98×10^{-10}	6.08×10^{-12}
CO+O → CO ₂	2.81×10^{-4}	4.86×10^{-2}
H + H → H ₂	5.82×10^4	2.29×10^4

In order to gather information for the process under more realistic conditions and establish the role of temperature on the adsorption/desorption process, Figure 7.8 shows the Gibbs free energy profile for WGS on the clean δ -MoC (001) at the minimum and maximum temperatures (410 and 465 K) used in the experiments and at 30 Torr. Note that the Gibbs free energy barriers in the profiles in Figure 7.8 are identical to those reported at 0 K, because calculated Gibbs free energy values neglect the entropic contributions from adsorbed species, as was carried out in Chapter 6. From the results in Figure 7.8 it is clear that the WGS is exergonic at all tested temperatures. The effect of temperature is crucial to favor CO₂ and H₂ desorption and does not significantly hinder the reagents adsorption.

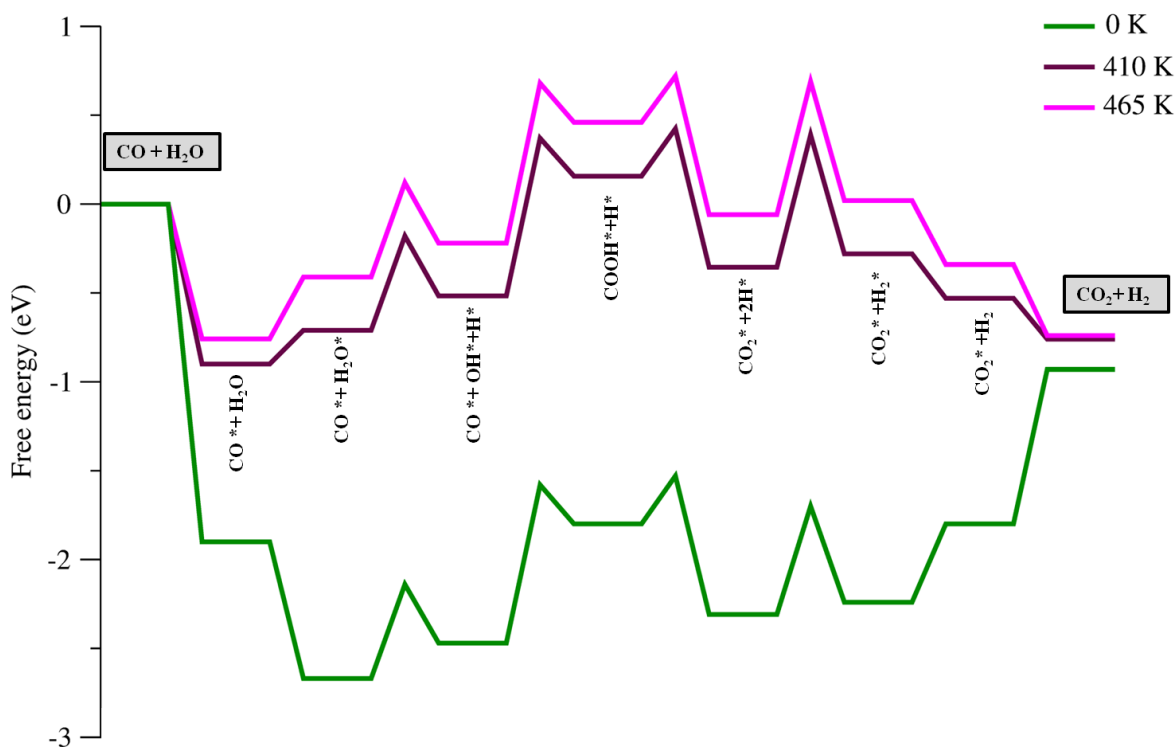


Figure 7.8: Gibbs free energy profile of the most favorable pathway of WGS on δ -MoC (001) including ZPE correction at 410 and 465 K at 30 Torr of pressure.

Aside from P1 reaction mechanism, the other ones portrayed on Figure 7.6, was also studied. Regarding P2 path, the OH dissociation entails an energy barrier of 1.56 eV, *i.e.*, ~ 0.6 eV larger than that corresponding to COOH formation. CO hydrogenation to HCO intermediate (P3), could proceed since its energy barrier is 0.79 eV. Nevertheless, the subsequent steps cannot occur since HCOO intermediate production required the recombination of HCO and atomic O, where the latter is hardly present due to the unlikely dissociation of OH and CO species on bare δ -MoC (001). On the other hand, the improbable traces of HCOO produced cannot dissociate to CO_2 due to their high energy barrier. This is attributed to the strong interaction of HCOO with clean δ -MoC (001), which could result in surface poisoning. Finally, another possibility to produce O, the OH+OH recombination to produce H_2O and atomic O (P4), is also ruled out, which entails an energy barrier

superior to 2 eV. All the sketches of minima and TS structures are reported on Figures 7.9 and 7.10 respectively.

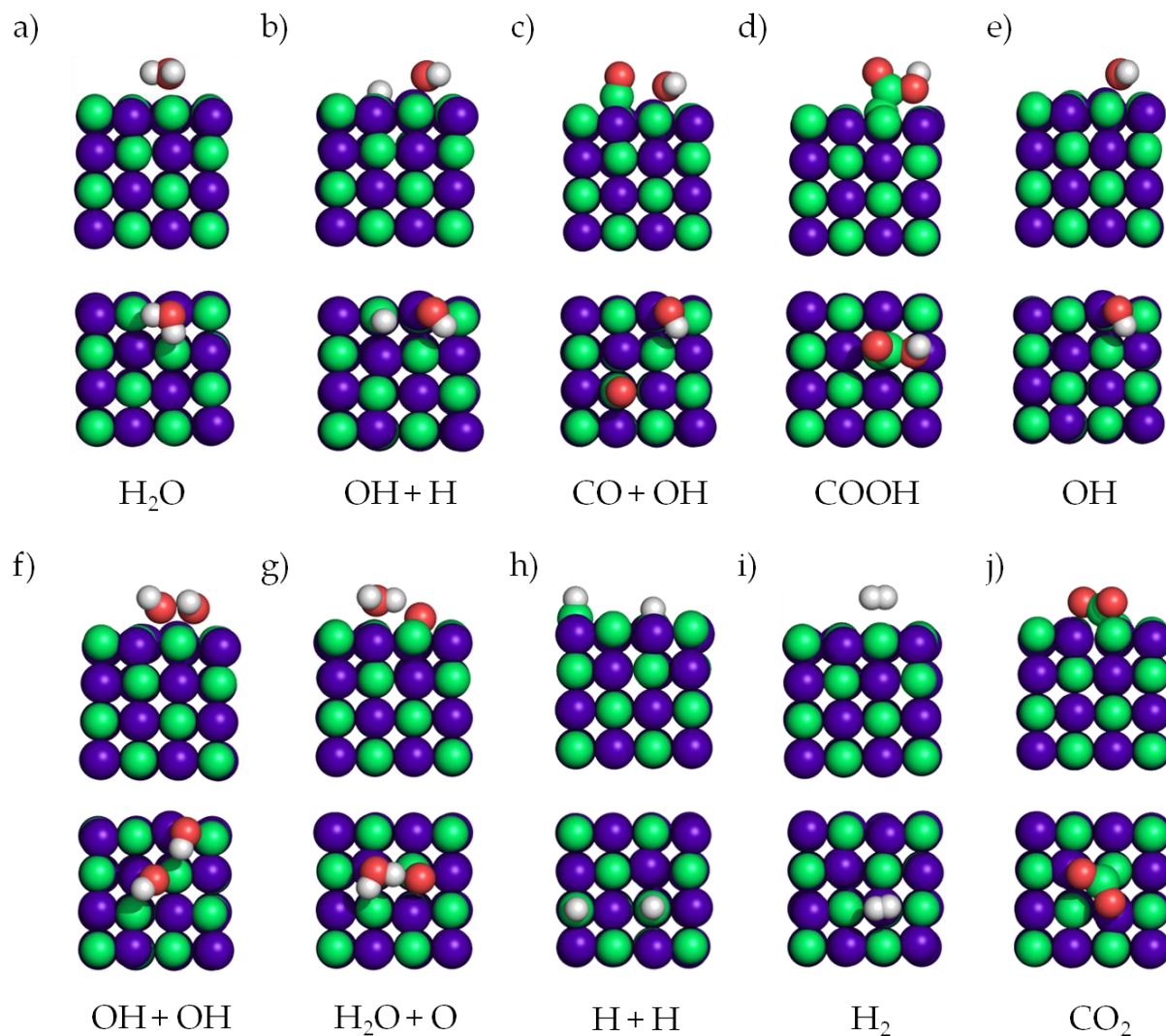


Figure 7.9: Adsorption sketches of reactants, intermediates, and products of WGS on plain δ -MoC (001) surface. Side (top) and top views (bottom) are displayed.

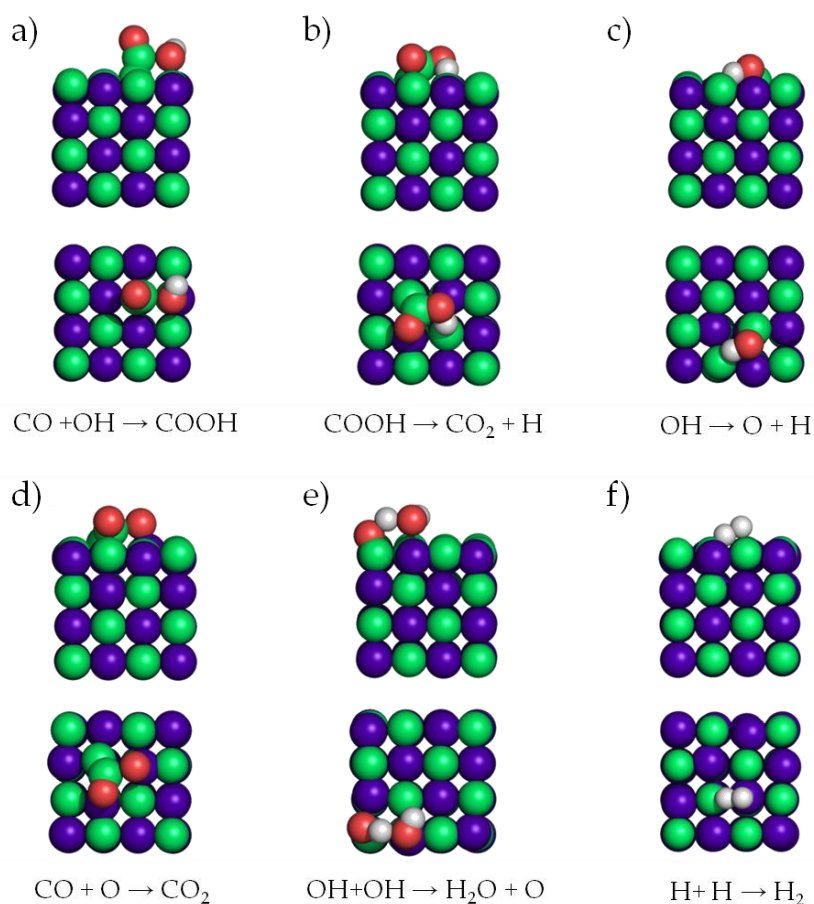


Figure 7.10: TS sketches of different elementary steps of WGS on plain δ -MoC (001) surface. Side (top) and top views (bottom) are displayed.

In conclusion, DFT calculations display that WGS on δ -MoC (001) is produced by means of associative mechanism. The low amount of CO_2/H_2 detected by experiments (Figure 7.2) on bare surface can be justified by our calculations since the rate constants of reverse elementary steps are superior than the forwards ones, suggesting a surface collapse. Nevertheless, our DFT calculations cannot explain the amount of atomic O detected by experiments after the reaction process, since the elementary steps to produce atomic O on P2 ($\text{OH} \rightarrow \text{O} + \text{H}$) and P4 ($\text{OH} + \text{OH} \rightarrow \text{H}_2\text{O} + \text{O}$) present huge energy barriers. Therefore, our calculations suggest that the deposited O detected by experiments ($\theta > 0.4$ ML) is due to the presence of Au supported clusters.

7.4 DFT study of WGS on Au₄/δ-MoC (001)

7.4.1 Choice of model

The first step to investigate the most favorable mechanism for WGS reaction was the choice of appropriate Au_n/δ-MoC (001) model, among the options studied in Chapter 3. The main reasons to select the model were the capability to represent the experimental trends and an agreement between accuracy and computational cost.

Table 7.2 reports the adsorption of different reactants, intermediates, and products of WGS on the most stable geometries of different Au_n supported clusters. These results clearly showed that the similarity of adsorption energy values. Furthermore, the computational cost related with the optimization of Au₉ and Au₁₃ supported systems was also a key factor, since these calculations entailed the use of big supercells ((3×3) and (4×4)). Then, considering that the experimental results in Figures 7.3 and 7.4 which indicate that the highest reactivity is seen for small clusters of gold on MoC, the previous choice discussed in previous Chapters, the previous works of Au clusters supported on TiC (001),¹¹ and the computational cost, the Au₄/δ-MoC (001) was selected.

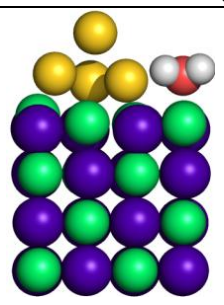
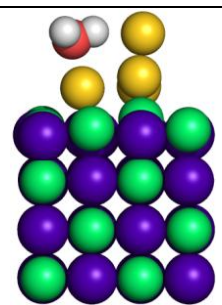
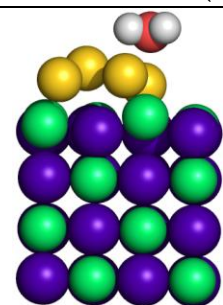
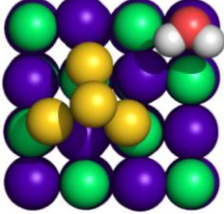
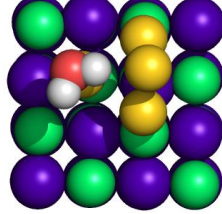
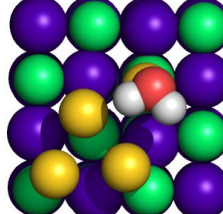
Table 7.2: Adsorption energies of different molecules adsorbed on Au_n/δ-MoC (001) (n= 4,9, and 13).

	E _{ads} H ₂ O /eV	E _{ads} CO /eV	E _{ads} CO ₂ /eV	E _{ads} H ₂ /eV	E _{ads} COOH /eV	E _{ads} OH /eV
Au₄	-0.34	-1.23	-0.10	-0.07	-2.35	-3.38
Au₉	-0.40	-1.24	-0.11	-0.03	-2.34	-3.45
Au₁₃	-0.42	-1.09	-0.10	-0.03	-2.48	-3.46

However, DFT calculations carried out in Chapter 3 revealed five different Au₄ structures supported on δ-MoC (001). Despite of 3D structures are 0.5 eV

favorable than the 2D ones, the work accomplished in chapter 6 exhibited that pyramidal Cu_4 clusters evolve towards planar structure. Notwithstanding, adsorption tests of H_2O , CO , and COOH molecules on $\text{Au}_4/\delta\text{-MoC}$ (001) systems reported on Tables 7.3, 7.4, and 7.5 respectively, showed that this fact did not happen on Au_4 deposited clusters. The most favorable geometries of adsorbed H_2O , CO , and COOH , are in pyramidal Au_4 supported cluster. Therefore, the most stable structure of Au_4 supported cluster corresponds to two degenerate 3D geometries with three atoms at MMC sites. Both structures have been used as model of Au/MoC catalyst for the WGS reaction, although the reactants and intermediates adsorption revealed that the Au_4 cluster reach the same pyramidal geometry after the adsorption.

Table 7.3: Sketches, relative energies, adsorption energy, and O-H bond length of water adsorption on $\text{Au}_4/\delta\text{-MoC}$ (001) surface.

	Pyramid 1 $\text{Au}_4/\delta\text{-MoC}$ (001)	Pyramid 2 $\text{Au}_4/\delta\text{-MoC}$ (001)	Planar $\text{Au}_4/\delta\text{-MoC}$ (001)
Side view			
Top view			
E_{rel} (eV)	0.00	0.10	0.34
E_{ads} (eV)	-0.45	-0.34	-0.63
$d(\text{O-H})$ (Å)	0.98/1.01	0.98	0.98/0.99

7.4 DFT study of WGS on Au₄/δ-MoC (001)

Table 7.4: Sketches, relative energies, and adsorption energy of CO adsorption on Au₄/δ-MoC (001) surface. First and second sketches represent different adsorption sites on Top Au cluster.

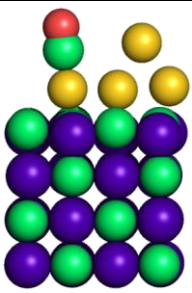
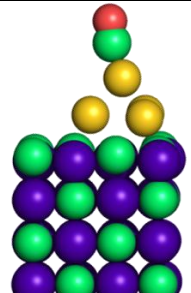
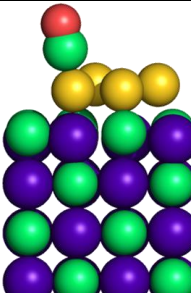
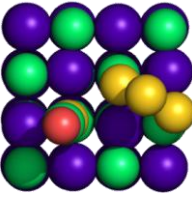
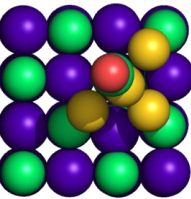
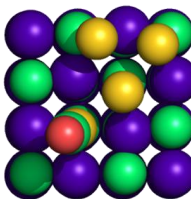
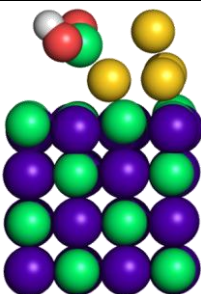
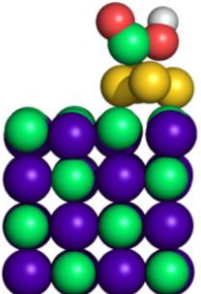
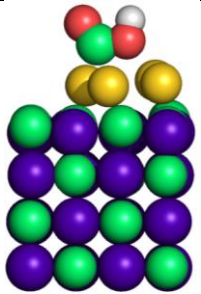
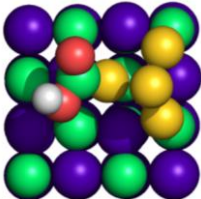
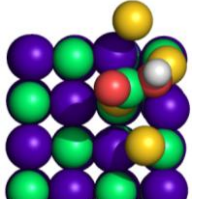
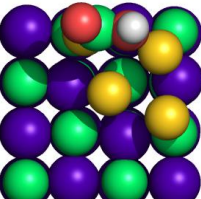
	Pyramid 1 Au ₄ /δ-MoC (001)	Pyramid 1 Au ₄ /δ-MoC (001)	Planar Au ₄ /δ-MoC (001)
Side view			
Top view			
E _{rel} (eV)	0.00	0.43	0.44
E _{ads} (eV)	-1.23	-0.76	-1.28

Table 7.5: Sketches, relative energies, and adsorption energy of COOH adsorption on Au₄/δ-MoC (001) surface. The second and third sketches represent different adsorption sites on planar Au cluster.

	Pyramid 1 Au ₄ /δ-MoC (001)	Planar Au ₄ /δ-MoC (001)	Planar Au ₄ /δ-MoC (001)
Side view			
Top view			
E _{rel} (eV)	0.00	0.25	0.38
E _{ads} (eV)	-2.35	-2.53	-2.48

7.4.2 Reaction mechanisms of WGS

The experimentalists associate the results on Figure 7.3a, with the capability of small Au clusters deposited on δ -MoC (001) to dissociate the H₂O molecule easily than bare δ -MoC (001). Thus, the computational study was focused to investigate the interaction between H₂O molecule and Au₄ supported clusters, either directly above the metallic cluster or at the Au/ δ -MoC interface. Table 7.6 compares calculated results for the interaction of H₂O with clean surface, with sites at the Au/ δ -MoC interface, and on Top of Au supported cluster. Clearly, H₂O \leftrightarrow carbide interaction is stronger than the H₂O \leftrightarrow Au one. Indeed, the adsorption energy decreases when H₂O is closer to Au cluster.

Table 7.6: Sketches, relative energies, and adsorption energy of water on δ -MoC (001) and Au/ δ -MoC (001) surface.

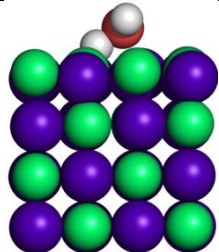
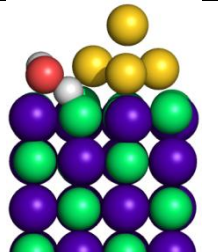
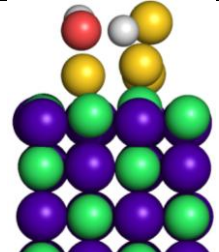
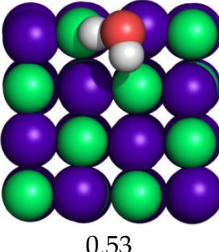
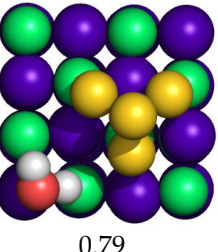
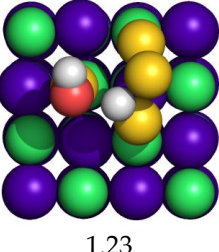
	Bare δ -MoC (001)	Interface Au ₄ / δ -MoC (001)	Top Au ₄ / δ -MoC (001)
Side view			
Top view			
E _{rel} (eV)	-	0.00	0.10
E _{ads} (eV)	-0.77	-0.34	-0.24
d(O-H) (Å)	0.98	0.98/1.01	0.98

Indeed, the same tendency was observed after the energy barrier calculations, see Table 7.7. The energy barrier for water dissociation on the carbide surface is rather low and at the interface is slightly superior. Notwithstanding, one must

7.4 DFT study of WGS on Au₄/δ-MoC (001)

consider the desorption process, which is easier than dissociation (0.34 eV against 0.79 eV) at the interface as is displayed on Table 7.2. Likewise, H₂O dissociation on top of Au cluster is strongly disfavored, implying that H₂O adsorption and dissociation is likely to occur on the clean regions of the surface. Hence, as far as H₂O dissociation is concerned, the presence of Au cluster does not help to the OH moiety production. This is not unexpected since, as already shown by Flytzani-Stephanopoulos *et al.*,^{29,30} pure gold does not play any role on water dissociation. On the contrary, these authors claim that the presence of -OH groups attached to Au species and support (whatever support) is the key to water dissociation.

Table 7.7: Sketches, energy barrier and O-H bond length of H₂O transition state structures on bare and Au₄/δ-MoC (001) surface.

	Bare δ-MoC (001)	Interface Au ₄ /δ-MoC (001)	Top Au ₄ /δ-MoC (001)
Side view			
Top view			
E _{barrier} (eV)	0.53	0.79	1.23
d(O-H) (Å)	0.98/1.37	0.98/1.38	0.98/1.94

According to the preceding discussion, H₂O dissociation takes place in the plain surface, as is represented on Figure 7.11a. Therefore, the reaction mechanisms presented in Figure 7.6 were studied on Au₄/δ-MoC (001) model in order to investigate the role of Au. Figure 7.11b revealed that the role of Au clusters is to facilitate the OH recombination and formation of atomic O involving with energy barrier of only 0.44 eV. This step, not possible on the clean surface, contributes to

increase the quantity of products, since, on one hand, the subsequent CO oxidation to CO₂ implies a very low energy barrier of 0.10 eV and, on the other hand, a new H₂O molecule is produced, which can be recycled for the WGS reaction. Moreover, the atomic O not only oxidizes CO towards CO₂, but also contributes to catalyze the H₂O dissociation. Note that the reverse OH recombination (H₂O + O → 2OH) presents a favorable rate (1.11 × 10⁵ s⁻¹, see Table 7.8), in agreement with a recent work published in *Science* studying the WGS on Au/MoC (111), which justifies the increase of OH production with the generation of atomic O, facilitating the subsequent H₂O dissociation.³¹ Furthermore, DFT calculations were able to explain the O coverage detected by the experimentalists after the process. As our calculations suggested, the carbide support does not play any role in this O production, whereas the deposition of Au clusters changes the reaction mechanism from associative to redox (from P1 to P4). The comparison of rates at 465 K (see Table 7.8) shows that, once the OH moiety is produced, its disproportionation (OH + OH → H₂O + O) on Au₄/ δ -MoC (001) entails a rate of 6.39 × 10⁷ s⁻¹ whereas the reverse rate of H₂O production (OH + H → H₂O) on clean δ -MoC (since on the Au₄/ δ -MoC interface is not available) is 5.21 × 10⁵ s⁻¹. That is, the deposition of Au clearly tunes the activity of δ -MoC (001) more toward the OH disproportionation. All the sketches of minima and TS structures are reported on Figures 7.12 and 7.13 respectively.

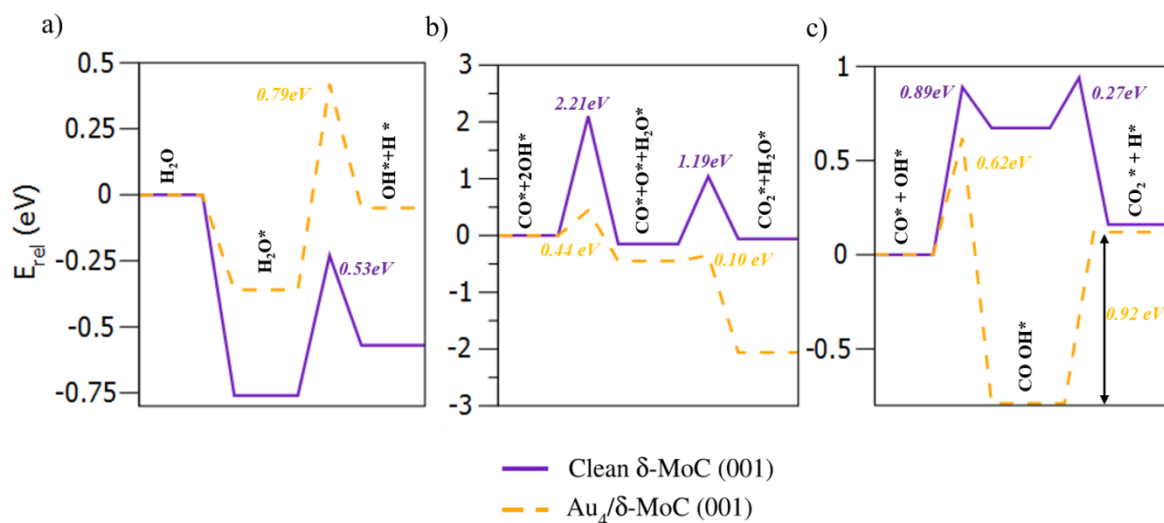


Figure 7.11: Comparison of different steps a) H₂O dissociation, b) OH recombination and CO oxidation, and c) COOH production and dissociation, of WGS on δ -MoC (001) and Au₄/ δ -MoC (001).

7.4 DFT study of WGS on Au₄/δ-MoC (001)

Another important difference between the clean δ-MoC (001) and Au₄/δ-MoC (001) systems regards H₂ and CO₂ desorption. On the former it entails an energy of 0.46 and 0.85 eV respectively, whereas on the latter desorption involves essentially a zero-energy cost. Thus, easiness of products desorption at the Au supported cluster helps in hindering the poisoning by reaction intermediates and maintaining the role of the reactive sites on δ-MoC and at the Au- δ-MoC interface.

For the COOH formation, a key step for the WGS reaction on clean δ-MoC, decreases in energy barrier of ~0.3 eV (Figure 7.11c) and a rate of $1.15 \times 10^5 \text{ s}^{-1}$ are obtained with the deposition of Au cluster, which is two orders of magnitude slower than the O production through OH disproportionation. Although the deposition of Au cluster on δ-MoC can enables a faster COOH production than that on δ-MoC, it is not likely to compete with the O formation via OH disproportionation, *i.e.*, the majority of OH moieties follow the P4 mechanism.

Table 7.8: Transition state theory derived reaction rates (s⁻¹), at 465 K, for the direct (r_d) and reverse (r_r) elementary steps of the WGS mechanism on clean δ-MoC (001) and Au₄/δ-MoC (001) surfaces.

T= 465 K	δ-MoC (001)		Au ₄ /δ-MoC (001)	
Step	r_d /(s ⁻¹)	r_r /(s ⁻¹)	r_d /(s ⁻¹)	r_r /(s ⁻¹)
H ₂ O → H+OH	1.62×10^3	5.21×10^5	2.86×10^3	1.53×10^8
OH → O+H	1.54×10^{-4}	4.37×10^{00}	2.39×10^{-6}	2.65×10^{-6}
CO+OH → COOH	3.31×10^2	3.40×10^{10}	1.15×10^5	4.68×10^{-12}
COOH → CO ₂ +H	8.09×10^8	2.07×10^4	-	-
OH + OH → H ₂ O + O	1.98×10^{-10}	6.08×10^{-12}	6.39×10^7	1.11×10^5
CO+O → CO ₂	2.81×10^{-4}	4.86×10^{-2}	4.69×10^{11}	1.30×10^{-14}
H + H → H ₂	5.82×10^4	2.29×10^4	2.02×10^2	2.61×10^2

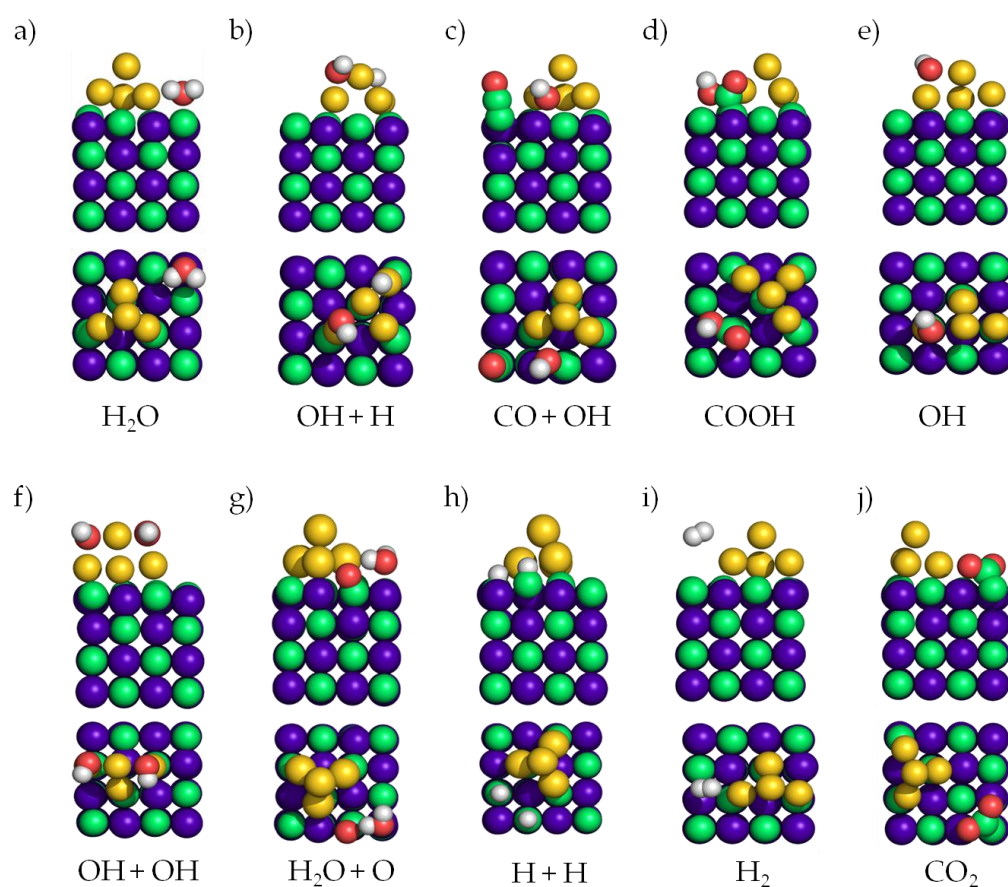


Figure 7.12: Adsorption sketches of reactants, intermediates, and products of WGS on $\text{Au}_4/\delta\text{-MoC}$ (001) surface. Side (top) and top views (bottom) are displayed.

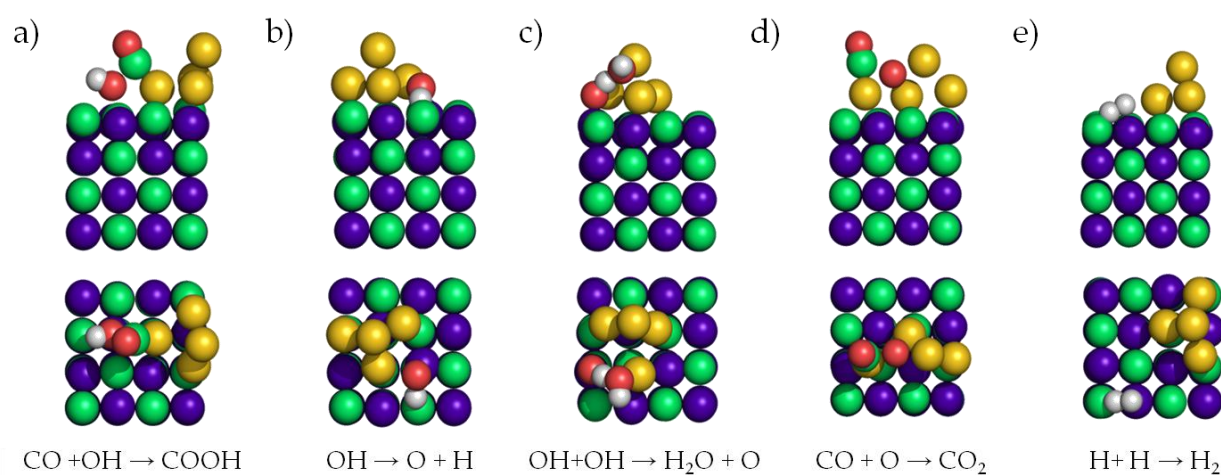


Figure 7.13: TS sketches of different elementary steps of WGS on $\text{Au}_4/\delta\text{-MoC}$ (001) surface. Side (top) and top views (bottom) are displayed.

7.5 Conclusions

The experimental results show that water gas shift reaction is produced on both bare studied surfaces, where on orthorhombic Mo₂C surface the amount of products is (slightly) superior, although the catalyst selectivity is worse due to CH₄ being produced apart from CO₂ and H₂. Unique interactions with the metal carbide support enhance the chemical reactivity of Au on Au/ δ -MoC and Au/ β -Mo₂C making the Au/ δ -MoC the suitable catalyst due to its activity (more CO₂ and H₂ production than Au/ β -Mo₂C and Cu (111)), selectivity (CH₄ is not detected), and stability (oxycarbide is not formed).

Considering the key effect of metal/carbon ratio discussed in previous Chapters, and the experimental results of Au/MoC systems, theoretical calculations were carried out only on series of appropriate models of the suitable and more promising catalysts using in experiments, δ -MoC (001) and Au₄/ δ -MoC (001). Our calculations of the WGS reaction on the bare δ -MoC (001) surface reveals that H₂O easily dissociates and that the most favorable mechanism involves the associative one. Notwithstanding, the energy barriers and rates obtained from the DFT calculations on bare surface, revealed that the reverse energy barriers are lower than the direct ones. This fact, together with the difficult desorption of CO₂ could lead to a surface collapse, justifying the low amount of product detected on the experiments. In summary, one can conclude that plain δ -MoC (001) surface promotes the reverse WGS reaction ($\text{CO}_2 + \text{H}_2 \rightarrow \text{CO} + \text{H}_2\text{O}$), discussed in Chapter 6, instead of the WGS.

The deposition of small Au clusters on δ -MoC (001) increases drastically the amount of CO₂ and H₂, and also, an amount of atomic O is detected on the carbide after the experiments. The synergistic interactions involving the metal and carbide support lead to an overall excellent low-temperature WGS catalyst with high stability. Calculations on appropriate models displayed that supported Au clusters do not help the H₂O dissociation otherwise the presence of the supported cluster contributes to switch the preferred mechanism of WGS reaction from associative to

redox one. In such a way, the recombination of OH moieties towards H₂O and O and the subsequent CO oxidation to CO₂ entail the lowest energy barriers. Moreover, the interaction between products and Au clusters is too weak, which favors the products desorption, avoiding the possible CO₂ hydrogenation and, in turn, favoring the H₂ production and generating new reactive sites on the clean region. These facts justify the increase of products detected by experiments and the amount of detected O, since redox pathway is predominant.

Finally, the present combined theoretical and experimental study illustrates the high impact that the carbon/metal ratio has on the chemical and catalytic properties also on WGS reaction.

7.6 References

- [1] C. V. Ovesen, B. S. Clausen, J. Schiøtz, P. Stolze, H. Topsøe and J. K. Nørskov, *J. Catal.* **1997**, *168*, 133.
- [2] N. Akiya and P. E. Savage, *Chem. Rev.*, **2002**, *102*, 2725.
- [3] J. Nakamura, J. M. Campbell and C. T. Campbell, *J. Chem. Soc. Faraday Trans.*, **1990**, *86*, 2725.
- [4] J. A. Rodriguez, P. Liu, J. Hrbek, J. Evans and M. Perez, *Angew. Chem. Int. Ed.*, **2007**, *46*, 1329.
- [5] P. Liu and J. A. Rodriguez, *J. Chem. Phys.*, **2007**, *126*, 164705.
- [6] A. A. Gokhale, J. A. Dumesic and M. Mavrikakis, *J. Am. Chem. Soc.*, **2008**, *130*, 1402.
- [7] R. M. Navarro, M. A. Peña and J. L. G. Fierro, *Chem. Rev.*, **2007**, *107*, 3952.
- [8] L. C. Grabow and M. Mavrikakis, *ACS Catal.*, **2011**, *1*, 365.
- [9] L. C. Grabow, A. A. Gokhale, S. T. Evans, J. A. Dumesic and M. Mavrikakis, *J. Phys. Chem. C*, **2008**, *112*, 4608.
- [10] F. Viñes, J. A. Rodríguez, P. Liu and F. Illas, *J. Catal.*, **2008**, *260*, 103.
- [11] J. A. Rodriguez, P. J. Ramirez, G. G. Asara, F. Viñes, J. Evans, P. Liu, J. M. Ricart and F. Illas, *Angew. Chem. Int. Ed.*, **2014**, *53*, 11270.
- [12] H. Prats, P. Gamallo, R. Sayós and F. Illas, *Phys. Chem. Chem. Phys.*, **2016**, *18*, 2792.
- [13] C. H. Lin, C. L. Chen and J. H. Wang, *J. Phys. Chem. C*, **2011**, *115*, 18582.
- [14] P. Liu and J. A. Rodriguez, *J. Phys. Chem. B*, **2006**, *110*, 19418.
- [15] U.S. Department of Energy Hydrogen, Fuel Cells and Infrastructure Technologies Program, Hydrogen Posture Plan, U.S. Department of Energy, 2006
- [16] J. D. Holladay, J. Hu, D. L. King and Y. Wang, *Catal. Today*, **2009**, *139*, 244.
- [17] U.E.I. Administration, International Energy Outlook 2013, Washington DC, 2013; <http://www.eia.gov/forecasts/ieo/pdf/0484%282013%29.pdf>.
- [18] R.D. Cortright, R.R. Davda and J.A. Dumesic, *Nature*, **2002**, *418*, 964.
- [19] A. A. Gokhale, J. A. Dumesic and M. Mavrikakis, *J. Am. Chem. Soc.*, **2008**, *130*, 1402.
- [20] R. J. Madon, D. Braden, S. Kandoi, P. Nagel, M. Mavrikakis, J. A. Dumesic, *J. Catal.*, **2011**, *281*, 1.
- [21] P. Liu and J. A. Rodriguez, *J. Phys. Chem. B*, **2006**, *110*, 19418.
- [22] J. A. Rodriguez, P. Liu, J. Hrbek, J. Evans and M. Perez, *Angew. Chem. Int. Ed.*, **2007**, *46*, 1329.
- [23] H. Tominaga and M. Nagai, *J. Phys. Chem. B*, **2005**, *109*, 20415.
- [24] N. M. Schweitzer, J. A. Schaidle, O. K. Ezekoye, X. Pan, S. Linic and L. T. Thompson, *J. Am. Chem. Soc.*, **2011**, *133*, 2378
- [25] J. A. Rodriguez, P. J. Ramirez and R. A. Gutierrez, *Catal. Today*, **2017**, *289*, 47.
- [26] P. Liu, J. A. Rodriguez, T. Asakura, J. Gomes, and K. Nakamura, *J. Phys. Chem. B*, **2005**, *109*, 4575.
- [27] K. D. Sabnis, Y. Cui, M. C. Akatay, M. Shekhar, W.-S. Lee, J. T. Miller, W. N. Delgass, and F. H. Ribeiro, *J. Catal.*, **2015**, *331*, 162.
- [28] J. A. Rodriguez, J. Evans, J. Graciani, J. B. Park, P. Liu, J. Hrbek and J. F. Sanz, *J. Phys. Chem.*, 2009, **113**, 7364.
- [29] M. Flytzani-Stephanopoulos, *Acc. Chem. Res.* 2014, **47**, 783.
- [30] M. Yang, L. F. Allard and M. Flytzani-Stephanopoulos, *J. Am. Chem. Soc.*, 2013, **135**, 3768.

- [31] S. Yao, X. Zhang, W. Zhou, R. Gao, W. Xu, Y. Ye, L. Li, X. Wen, P. Liu, B. Chen, E. Crumlin, J. Guo, Z. Zuo, W. Li, J. Xie, L. Lu, C. J. Kiely, L. Gu, C. Shi, J. A. Rodríguez and D. Ma, *Science*, **2017**, 357, 389.

CHAPTER EIGHT

General Conclusions

General conclusions

In this thesis, theoretical calculations have been used to investigate and propose the reaction mechanism for the studied green chemistry reactions and to elucidate the role of the catalyst. The specific conclusions for each of the green chemistry reactions investigated in this thesis have been presented at the end of the corresponding chapter. Nevertheless, some more general conclusions have been reached that are worth to highlight. From the point of view of modeling, the results presented in this thesis show that DFT and periodic calculations are a very useful tools for modeling surfaces and to carry out the study of reaction mechanism of heterogeneous catalytic reactions. The computational models used in this thesis have been able to describe the key trends of experiments, contributing to explain the particular role of metal particles and support in order to provide essential data to improve the catalyst performance. In particular, DFT calculations have unveiled the catalytic role of molybdenum and carbon terminations. More specifically, the interpretation of experiments by means of the theoretical calculations presented in this thesis show that:

- The (001) surface of the Mo₂C orthorhombic phase is an excellent catalyst for CO₂ reduction towards CO without the H₂ assistance.
- The high interaction between β -Mo₂C (001) and CO₂ and oxygen containing molecules (CO, H₂O, ...), leads to the oxycarbide formation, which involves a decrease in the catalyst activity and the possible catalyst deactivation.
- The strong interaction of CO₂ and CO on β -Mo₂C (001) provokes a decrease in the catalyst selectivity due to the atomic carbon deposition, which hydrogenates towards methane, becoming in the major product on CO₂ hydrogenation.
- The deposition of small copper and gold particles on the carbide surface increases the catalyst activity, changing the reaction mechanism.
- The metal/carbon ratio on the carbide plays a key role on the catalyst performance, in terms of activity, selectivity, and stability.

General conclusions

- The cubic δ -MoC (001), with metal/carbon ratio of one, becomes the most promising catalyst for CO₂ hydrogenation and WGS reaction.
- Cu/ δ -MoC (001) exhibits a production of CO and MeOH larger than that of models of commercial catalyst for MeOH production, and similar production than Cu/ β -Mo₂C (001). Respect to WGS, Au/ δ -MoC (001) produces more CO₂ and H₂ than Au/ β -Mo₂C (001).
- The carbide with metal/carbon ratio of two generates methane on both studied reactions whilst cubic δ -MoC (001) only produces CO and MeOH on CO₂ hydrogenation, and CO₂ and H₂ on WGS.
- Oxycarbide formation have been detected by experiments and confirmed by DFT calculations on β -Mo₂C (001), which lead to the catalyst deactivation, whereas on δ -MoC (001) (and metal cluster supported on thereon) the catalyst activity remains constant.

RESUM EN CATALÀ

Pròleg

La catàlisi és un fenomen conegut des de temps molt antics, encara que els seus fonaments no es van conèixer fins al segle XIX. El primer concepte de catàlisi no va ser introduït fins a 1836, per Berzelius.¹ Més tard, Ostwald va redefinir el terme tal com ho coneixem avui dia: "la catàlisi és l'acceleració d'una reacció química a través de la presència d'una substància externa, que pot participar en la reacció, però no es consumeix".²

La catàlisi es diu homogènia o heterogènia en funció de l'estat físic de totes les substàncies implicades. En la catàlisi homogènia, els reactius i el catalitzador es troben en el mateix estat físic mentre que la catàlisi heterogènia engloba els estudis de materials capaços d'accelerar les reaccions químiques en fase gas o líquida sobre catalitzadors sòlids. Un dels avantatges dels catalitzadors heterogenis respecte als homogenis és la facilitat per separar el catalitzador i el producte de reacció final. Molts esforços en el món de la química s'han centrat en la catàlisi heterogènia degut al seu gran impacte en la nostra societat. La majoria de les reaccions industrials importants, del present i del passat, estan o han estat catalitzades per catalitzadors heterogenis. No obstant, molts dels catalitzadors comercials utilitzats industrialment contenen metalls de transició, el que fa augmentar el cost de la síntesi, i per tant, del producte final.

Motivació: Química, medi ambient i societat

Canvi climàtic i energia són dues cares de la mateixa moneda: bona part de les emissions de gasos d'efecte hivernacle provenen del sector energètic (incloent transport). L'ús d'energies no renovables, com els combustibles fòssils, no només genera problemes per no apostar per les energies renovables, sinó que és molt perjudicial pel medi ambient. De fet, el diòxid de carboni (CO₂) és el gas d'efecte hivernacle més abundant a l'atmosfera de la Terra a causa de les excessives

emissions derivades de les activitats humanes relacionades amb els combustibles fòssils.³ Les emissions han augmentat des dels anys seixanta fins a un nivell actual superior a 400 ppm (Figura S1). A més, les prediccions indiquen que les emissions de CO₂ continuaran augmentant al 2040 amb conseqüències devastadores per al medi ambient.⁴

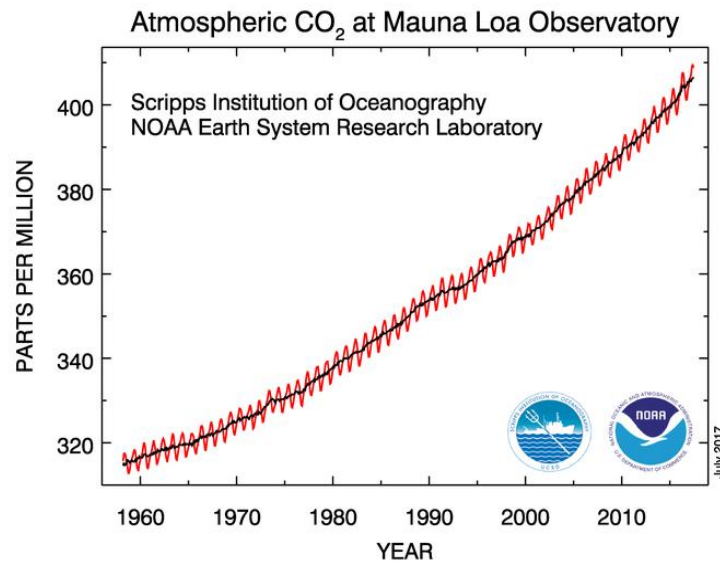


Figura S1: Augment de la concentracions de CO₂ a l'atmosfera durant els últims seixanta anys. Les línies vermelles i negres indiquen els valors mitjans mensuals i la mitjana per temporada, respectivament. Adaptat de <https://www.esrl.noaa.gov/gmd/ccgg/trends/full.html>.

És per això que la solució al problema passa per un canvi fonamental en el sistema energètic, ja sigui amb una major participació de les energies renovables i/o amb una nova política de captura i reutilització dels gasos d'efecte hivernacle en productes útils per a la nostra societat.

Aquesta tesi es basa en la recerca de catalitzadors capaços de convertir substàncies nocives per al medi ambient en combustibles eficients i ambientalment respectuosos. Aquest treball és un repte per a la catàlisi heterogènia en particular i per a la ciència en general. En aquesta tesi s'ha estudiat l'activació i conversió del CO₂ en productes com el monòxid de carboni (CO), el metanol (MeOH) i altres hidrocarburs utilitzats com a combustibles, i també la reacció de "water gas shift" (WGS), per generar hidrogen (H₂) a partir de CO i aigua.

Respecte a l'ús del CO_2 , la Figura S2 resumeix tres camins per a la seva conversió; la reducció del CO_2 s'ha convertit en una opció interessant ja que el CO produït podria utilitzar-se com a matèria primera en la síntesi Fisher-Tropsch.⁵ Es tracta d'un procés catalític industrial conegut des dels anys 40 per produir hidrocarburs sintètics per a ser utilitzats com a combustibles, tot i que cal destacar que la seva viabilitat econòmica està estretament relacionada amb el preu del cru. A més, el CO és també un ingredient clau del gas de síntesi, una barreja de CO, CO_2 i H_2 que s'utilitza en molts processos industrials per produir tones de productes químics com el metà (CH_4)^{6,7} o el metanol (MeOH).⁸ En aquest sentit, la conversió de CO_2 a MeOH sorgeix com la forma més important per a la utilització del CO_2 , ja que és la ruta més directa per a la seva reutilització. El MeOH és un combustible per a bateries i precursor de molts productes químics interessants per a la nostra societat i és molt notable que l'ús del MeOH com a combustible de transport presenta avantatges econòmics similars a les piles de combustible basades en hidrogen.⁹ Finalment, la hidrogenació directa de CO_2 a alcans (CO_2 -Fisher-Tropsch) és possible en un reactor, ja que és termodinàmicament més fàcil que la reversió de la reacció de *water gas shift*, ja que el procés general és exotèrmic.¹⁰ Aquest pas només és la conversió directa de CO a hidrocarburs després de la reducció de CO_2 .

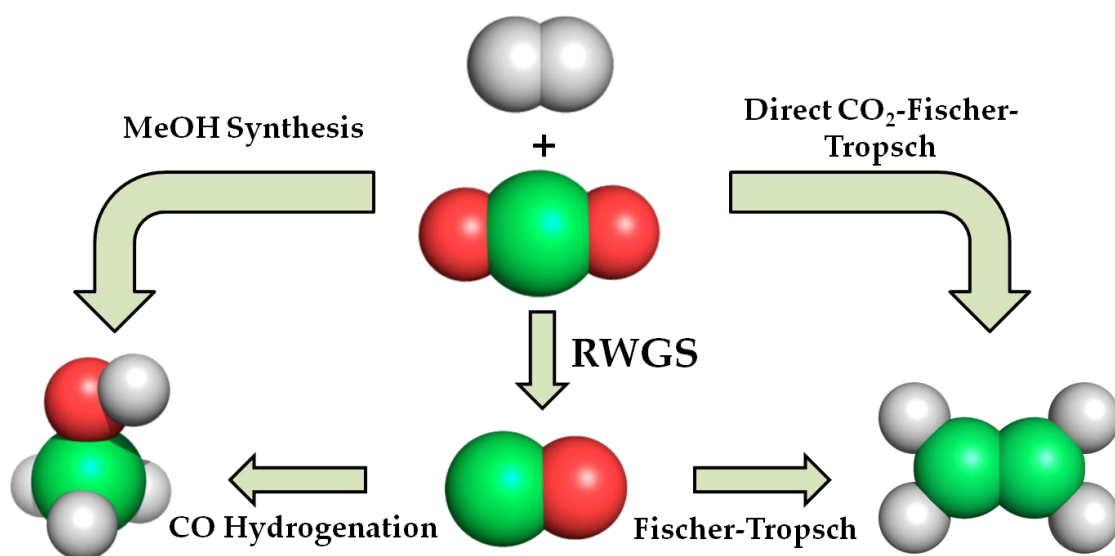


Figura S2: Esquema dels diferents camins per a la conversió del CO₂.

Pel que fa a l'hidrogen, és considerat com una font inesgotable i un gas amigable amb el medi ambient i s'ha proposat com a substitut dels combustibles de gasoil i dels combustibles per a biodièsel.¹¹ Tot i ser un dels elements més abundants de la Terra, no es troba en fase gasosa (H₂), sinó en aigua i molècules orgàniques com hidrocarburs o proteïnes. La principal aplicació del H₂ es basa en fer amoníac,¹² un component important dels fertilitzants i un producte molt utilitzat en la neteja domèstica. Les refineries utilitzen la segona major quantitat d'hidrogen per a processos químics com l'eliminació de sofre de la gasolina i la conversió d'hidrocarburs pesats en gasolina o gasoil. A més, cal tenir en compte que la demanda d'hidrogen, tant per a usos tradicionals com per a noves piles de combustible, augmentarà en les pròximes dècades. La indústria genera uns 48 milions de tones mètriques d'hidrogen cada any a nivell mundial a partir de combustibles fòssils. A més, l'H₂ es pot produir a partir de diferents fonts com la biomassa¹³ o els combustibles líquids derivats de la biomassa (MeOH, EtOH,^{14,15} biodièsel ...), així com de l'aigua. Una altra reacció exhaustivament estudiada per produir H₂ des dels vessants experimentals i teòrics a causa de la seva funció rellevant en la indústria química és la reacció WGS.¹⁶⁻²⁵ Aquesta reacció va ser descoberta per Felice Fontana al 1780, però va ser a principis del segle XX amb el desenvolupament del procés Haber-Bosh per a la producció d'amoníac, quan va començar a tenir un ús pràctic real.²⁶ A partir d'aquest moment, la WGS ha guanyat importància a causa del seu paper crucial en la producció d'hidrogen pur per a les aplicacions de piles de combustible i s'ha convertit en una part inseparable de diversos processos industrials.²⁷⁻²⁹

Els catalitzadors

Desafortunadament, durant molts anys, el disseny de catalitzadors heterogenis es va realitzar mitjançant la tècnica de "prova i error", que comporta

testejar tots els possibles catalitzadors al laboratori. És evident que aquesta tècnica és millorable ja que no considera el raonament químic.³⁰ Afortunadament, en els últims temps, la fructífera col·laboració entre els experiments i els càlculs computacionals ha provocat un salt endavant en el coneixement dels processos catalítics. La simulació computacional de la catàlisi, ja sigui com a complement d'estudis experimentals o com a eina predictiva,³¹ és una tècnica útil per reduir la quantitat d'experiments i centrar els esforços cap els materials més prometedors.

La majoria dels catalitzadors utilitzats en la indústria per a una gran quantitat de reaccions químiques utilitzen nanopartícules de metalls preciosos com pal·ladi o platí com una fase activa que es recolza tant en òxids com en sulfurs.³² No obstant, l'ús de metalls preciosos com el platí és un dels principals problemes alhora del disseny de nous catalitzadors, degut principalment al seu alt cost. Actualment, un dels principals reptes en el camp de la catàlisi és el disseny de nous catalitzadors per a la producció de combustibles ecològics i de reaccions de química verda, que minimitzin la utilització de compostos cars. En la recerca de nous catalitzadors econòmics i actius, els carburs de metall de transició (TMC) es poden considerar com uns excel·lents candidats. Els TMC tenen propietats físiques i químiques úniques, que combinen les propietats característiques de tres classes diferents de materials: mostren l'extrema duresa i fragilitat dels sòlids covalents, la temperatura de fusió alta i les estructures cristal·lines senzilles, típiques en cristalls iònics i propietats electròniques i magnètiques similar als metalls de transició.³³⁻³⁵ Tot i que pot semblar sorprenent, l'estudi i el coneixement d'aquests materials és molt nou, malgrat que les excel·lents propietats de l'acer (ferro amb un 0,03-2,14% de carboni) era coneguda.³⁶ De fet, el nombre de publicacions relacionades amb TMC va ser molt baix fins a principis del segle XX. Quin va ser el factor que va canviar aquesta tendència? La catàlisi!

Es podria pensar que la crisi econòmica mundial ha tingut un paper destacat en la recerca creixent de TMC, donada la necessitat imperiosa de substituir els

catalitzadors més cars, que normalment inclouen metalls preciosos, per altres més econòmics i igual o més eficients. Les propietats dels TMC els posicionen davant dels metalls de transició per a ser utilitzats com a catalitzadors. Per una banda, la seva abundància redueix dràsticament el cost. Per altra banda, la presència del carboni a l'estructura del catalitzador redueix lleugerament el poder catalític del metall, que tot i que pugui semblar contraproductiu, és necessari per reduir les fortes interaccions entre els metalls i les molècules adsorbides, que pot donar lloc a una difícil separació entre el catalitzador i els productes i a la contaminació i desactivació del catalitzador. Els TMC eviten l'enverinament de carboni o sofre detectat en metalls, tot i que poden ser enverinats i, en conseqüència, desactivats, a causa de l'adsorció d'oxigen i la posterior formació de l'oxicarburi, que no presenta la mateixa activitat catalítica que TMC pur.³⁷

El primer i principal referent en aquest tema va ser el treball de Levy i Boudart, que va suggerir que els carburs de tungstè presentaven un comportament semblant al platí en diverses reaccions catalítiques com ara reaccions d'hidrogenació, deshidrogenació, isomerització i dessulfuració.³⁸⁻⁴⁰ Es va trobar que el WC i el W₂C eren catalitzadors potencials per a la conversió de l'alcohol i els electrocatalitzadors per a les piles de combustible d'alcohol.⁴¹⁻⁴³ A més, el carburi de titani (TiC), un dels TMCs que ha generat més interès en els últims temps, es va proposar com un excel·lent catalitzador per dissociar la molècula d'H₂ i oxidar CO.⁴⁴⁻⁴⁶

Una de les propietats més prometedores d'alguns TMC és la capacitat de modificar l'estructura electrònica de petites partícules metàl·liques suportades i augmentar dràsticament la seva activitat catalítica a través de fortes interaccions de suport metàl·lics.⁴⁷ Motivats pel treball inicial d'Ono i Roldán-Cuenya sobre l'activitat catalítica d'Au/TiC cap a l'oxidació CO de baixa temperatura,⁴⁸ el grup del Dr. José Rodríguez i el grup del Prof. Francesc Illas van iniciar un estudi detallat de la interacció d'Au amb TiC (001), mostrant que aquests sistemes són actius per a moltes reaccions..⁴⁹⁻⁵⁵ No obstant això, es va trobar la dificultat d'obtenir

nanopartícules catalíticament actives en condicions de treball sobre el TiC. Com es pot observar a la figura S3, només les partícules petites ofereixen un rendiment i una obtenció elevada de productes, mentre que les nanopartícules grans suportades en TiC, que són fàcils de sintetitzar, no tenen interès catalític degut a la seva baixa activitat. En aquest sentit, els carburs de molibdè, en particular, la fase cúbica (δ) MoC, ortoròmbica (β) Mo₂C i hexagonals (α) Mo₂C, han sorgit com una excel·lent alternativa perquè són més actius i no requereixen condicions especials per a la seva síntesi.

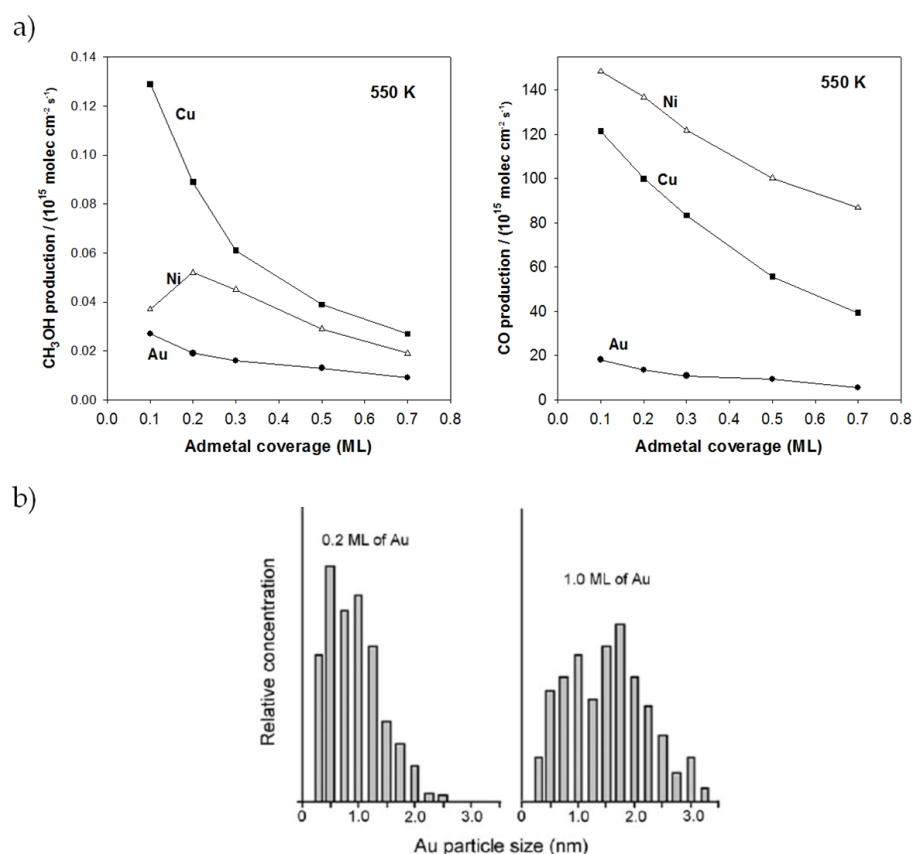


Figura S3: a) Producció de Metanol (esquerra) i CO (dreta) depenent del recobriment de nanopartícules metàl·liques sobre la superfície de TiC (001) a 550 K i b) Experiments STM de la grandària de nanopartícula Au suportada en TiC (001) en dos recobriments diferents.

Objectius

En aquesta tesi es desenvoluparà un treball computacional com a complement dels experiments per a estudiar la hidrogenació de CO₂ cap a MeOH ($\text{CO}_2 + 3\text{H}_2 \rightarrow \text{CH}_3\text{OH} + \text{H}_2\text{O}$) i la reacció de *water gas shift* ($\text{CO} + \text{H}_2\text{O} \rightarrow \text{CO}_2 + \text{H}_2$), dos exemples clars de com generar recursos energètics a partir de substàncies perilloses, utilitzant carbur de molibdè com a catalitzador o com a suport de petites nanopartícules metàl·liques.

Els objectius d'aquesta tesi són conèixer la capacitat dels carburs de molibdè en l'activació del CO₂ en primera instància per a posteriorment realitzar un ampli estudi del mecanisme de reacció sobre la conversió del CO₂ cap a productes útils com el CO i el MeOH. El compliment d'aquest objectiu, unit als treballs experimentals duts a terme pel grup del Dr. José Rodríguez al Brookhaven National Laboratory, van permetre extreure una imatge global de com té lloc el procés. A més, la hidrogenació del CO₂ s'ha estudiat sistemàticament en les fases cúbica ($\delta\text{-MoC}$) i ortoròmbica ($\beta\text{-Mo}_2\text{C}$) del carbur de molibdè per tal d'avaluar el rol de l'estructura, morfologia i estequiometria del catalitzador, amb l'objectiu de determinar els punts clau de les interaccions del substrat-catalitzador, analitzant qualitativament els descriptors de catalitzadors típics com l'activitat, la selectivitat i l'estabilitat. Els coneixements adquirits per assolir aquest primer objectiu conformen un rerefons de coneixements fonamentals sobre el comportament dels carburs de molibdè, la seva estructura i la seva estabilitat.

Posteriorment a aquest estudi, l'objectiu era modelitzar els sistemes de nanopartícules metàl·liques suportades en les superfícies del carbur de molibdè, per tal de simular els sistemes experimentals. En el cas de la hidrogenació del CO₂, els experiments predeien que el coure era el metall més actiu i per tant, va ser l'escollit. La reacció d'hidrogenació del CO₂ va ser estudiada sistemàticament en les diverses

fases del carbur de molibdè, per investigar els diferents rols de les partícules metàl·liques segons la fase en la qual es depositen.

Aquests objectius ambiciosos van centrar el desenvolupament de la tesi doctoral, per tal de trobar fase més activa dels carburs de molibdè. El compliment dels objectius explicats prèviament va permetre investigar la reacció de “*water gas shift*” només en una de les superfícies proposades, ja que els resultats previs amb la hidrogenació del CO₂ van demostrar que la fase cúbica presentava millors resultats en termes d’activitat, selectivitat i estabilitat. Aquest fet, unit a que els experiments també mostraven aquesta tendència, van donar lloc a que la reacció de WGS només s’estudiés sobre la fase cúbica, ja sigui com a catalitzador o com a suport de petites nanopartícules d’or.

Amb tot, les dades que es recullen en aquesta tesi són només la punta de l’iceberg. Hi ha encara moltíssim treball per tal d’investigar el paper del carbur de molibdè i altres carburs de metalls de transició en altres reaccions de química verda.

Metodologia i models computacionals

Per entendre les propietats d’un material cal conèixer la seva estructura a nivell atòmic. Un dels problemes més simples de descriure i alhora més difícils de resoldre en química computacional és la determinació de l’estructura electrònica. L’aplicació de qualsevol mètode computacional per estudiar qualsevol tipus de sistema requereix d’un model matemàtic a través del qual es pugui calcular l’energia del sistema. La precisió i la idoneïtat del model dependrà de la seva qualitat. Per a sistemes de pocs àtoms, és possible emprar mètodes basats en la mecànica quàntica. En aquesta tesi, els càlculs computacionals s’han dut a terme mitjançant la teoria funcional de la densitat (DFT), molt útil per avaluar l’energia i altres propietats d’un sistema polieletrònic. El mètode DFT proposa utilitzar la densitat electrònica $\rho(r)$ per incloure la correlació electrònica en la solució de l’equació de Schrödinger.

Aquest fet redueix dràsticament el cost computacional, ja que, per a un sistema aleatori amb N electrons, la funció d'ona depèn de coordenades espacials de cada electró més l'spin, mentre que l'ús de $\rho(r)$ depèn només de tres coordenades espacials.

La teoria DFT indica que l'energia es defineix per mitjà de la seva densitat electrònica.⁵⁶ Així, l'energia és un funcional de la densitat, i coneixent el funcional exacte es podria resoldre exactament l'equació d' Schrödinger. Malauradament, es desconeix l'expressió matemàtica exacta del funcional universal, cosa que descobreix el punt més feble de la teoria DFT. Per tant, la qualitat del càlcul va estretament relacionada amb la precisió de l'aproximació del funcional utilitzat. En aquesta tesi, tots els càlculs s'han realitzat utilitzant un funcional dins de l'aproximació del gradient generalitzat, el funcional PBE. Estudis previs sobre les propietats dels TMC utilitzen PW91 com funcional perquè descriu bé les seves característiques,⁵⁷ tot i que PBE i PBE revisat (RPBE) són adequats per a la descripció del *bulk* i superfícies de tots els TMC estudiats prèviament i els metalls de transició en general.⁵⁸ Tots els detalls respecte als mètodes computacionals es troben al capítol 2.

Pel que fa als models, per simular els catalitzadors experimentals s'ha utilitzat un model de superfície. El treball de Politi i col·laboradors,⁵⁹ va optimitzar la malla de punts k per a diferents supercel·les i la quantitat de capes necessàries per descriure apropiadament els models. Les propietats de les superfícies dels TMC es poden descriure correctament utilitzant models de quatre capes, amb les dues capes més exteriors completament relaxades i les altres dues fixes, simulant el *bulk* (aproximació de 2+2). En el cas de β -Mo₂C, els nostres col·laboradors experimentals sintetitzen monocristalls de la superfície (001). Pel que fa a la fase cúbica, la superfície (001) va resultar ser la superfície més estable. Aquest resultat adquireix una gran importància en les simulacions computacionals, ja que des d'un punt de vista experimental, el δ -MoC és policristal·lí i els càlculs DFT van revelar que (001) és la terminació superficial més exposada. Per tant, vam utilitzar una superfície cúbica

MoC (001) per reproduir teòricament els resultats experimentals en MoC. La figura S4 mostra les superfícies emprades.

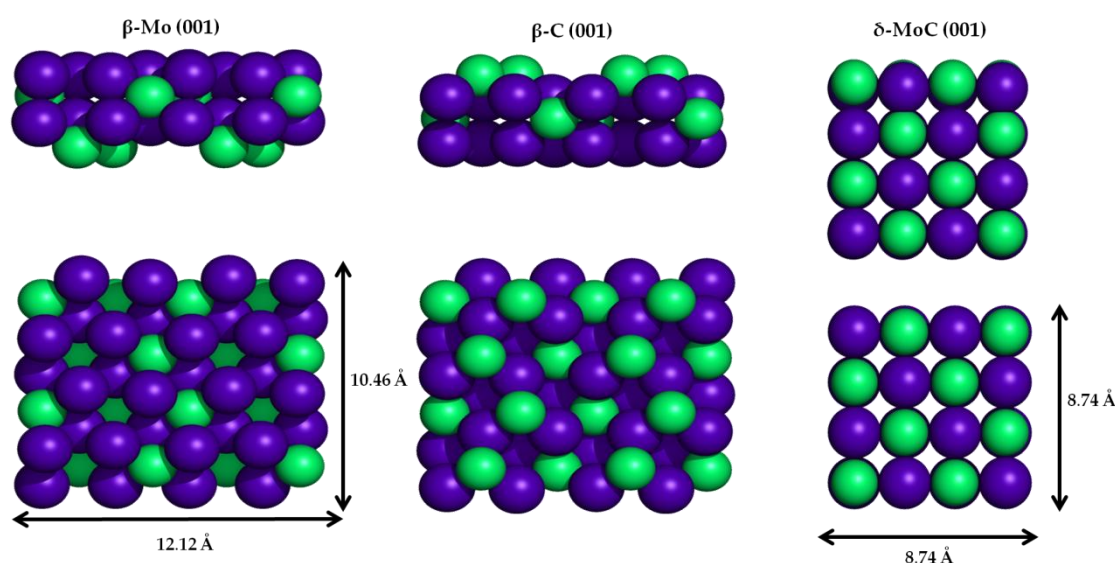


Figura S4: Vista de perfil (dalt) i planta (baix) de les tres superfícies (001) emprades en aquesta tesi. A l'esquerra, la superfície ortoròmbica acaba en molibdè, al centre la superfície ortoròmbica acaba en carboni i a la dreta la superfície cubica MoC.

D'altra banda, es van modelitzar també els sistemes formats per nanopartícules metàl·liques suportats en les superfícies esmentades del carbur de molibdè. Els experiments van determinar que per a la hidrogenació del CO_2 , el coure és el metall que més bons resultats té, mentre que per a la WGS, és l'or. Per a les superfícies polars β - Mo_2C (001), els resultats van mostrar que, malgrat la seva diferent terminació en àtoms de molibdè o carboni, les partícules de coure suportades tendien a convertir-se en estructures bidimensionals, malgrat que els clústers de coure aïllats majors de set àtoms són tridimensionals. A la superfície

acabada de Mo, les partícules suportades tendien a ser reduïdes, mentre que a la superfície C, la partícula suportada tendeix a ser oxidada. Aquesta diferència podia donar lloc a una reactivitat diferent i suggereix que és possible controlar el caràcter donant o acceptor de la partícula metàl·lica suportada mitjançant les característiques del carbur. Per a la superfície δ -MoC (001), es van considerar petits clústers de coure ($n = 4, 6$ i 7). Les tendències van indicar que les partícules més grans probablement adopten una estructura tridimensional i seran sensibles a l'oxidació, mentre que les partícules de 4 àtoms presenten la mateixa energia en partícules bidimensionals i tridimensionals.

Respecte als clústers d'or, l'estudi de la deposició només es va dur a terme en δ -MoC (001), ja que les investigacions experimentals van revelar que és el catalitzador adequat per a la reacció WGS. La deposició de clústers d'or petits ($n = 4, 9$ i 13) va demostrar que les partícules suportades tendien a convertir-se en tridimensionals. Això contradeia als treballs anteriors, ja que al depositar clústers de quatre àtoms de diferents metalls sobre TiC (001),⁶⁰ aquests adoptaven una estructura plana. Els càlculs DFT van concloure que aquest desacord es devia a l'ús de diferents funcionals de GGA. Per aprofundir més en el disseny dels models, consultar el capítol 3.

Interacció del CO₂, CO, H₂ i CH₄ amb els carburs de molibdè (Capítol 4)

Objectius

L'objectiu en aquesta secció era explorar i examinar des d'un punt de vista experimental i computacional la interacció i activació de les molècules de CO₂ i H₂ a les superfícies (001) del δ -MoC i β -Mo₂C i veure si la activació del CO₂ i la dissociació de H₂ es produeixen, com a passos preliminars i necessaris per a l'ús de carburs de molibdè com a catalitzadors en la conversió de CO₂. També es volia determinar com

l'activitat cap a l'activació de CO₂ i H₂ canvia amb la relació metall/carboni en el carbur.

Resultats

Els experiments d'espectroscòpia de fotoelectrons emesos per raigs X (XPS) a la regió de l'orbital 1s de l'oxigen, mostraven senyals molt febles per a la superfície δ -MoC, fet que indica la no dissociació del CO₂ en aquesta superfície com s'observa a la figura S5a. En canvi, dues senyals, apareixen a la superfície β -Mo₂C (001). La més intensa, correspon a oxigen atòmic, mentre que la menys intensa correspon al CO (Figura S5b). Aquests resultats indiquen que la superfície β -Mo₂C dissocia el CO₂ completament ($\text{CO}_2^* \rightarrow \text{CO}^* + \text{O}^*$; $\text{CO}^* \rightarrow \text{C}^* + \text{O}^*$). Respecte a la hidrogenació de CO₂ a les dues superfícies estudiades del carbur de molibdè (Figura S5c), van revelar que els principals productes en β -Mo₂C (001) són CO i CH₄, mentre que la quantitat de MeOH és clarament menor i també es van trobar traces de C₂H₆, CH₃OCH₃ i C₂H₅OH. D'altra banda, la Figura S5c va mostrar que en MoC policristal·lí, la hidrogenació del CO₂ produïa només CO i MeOH. Ambdues superfícies mostren activitats molt similars per a la producció de CO i MeOH.

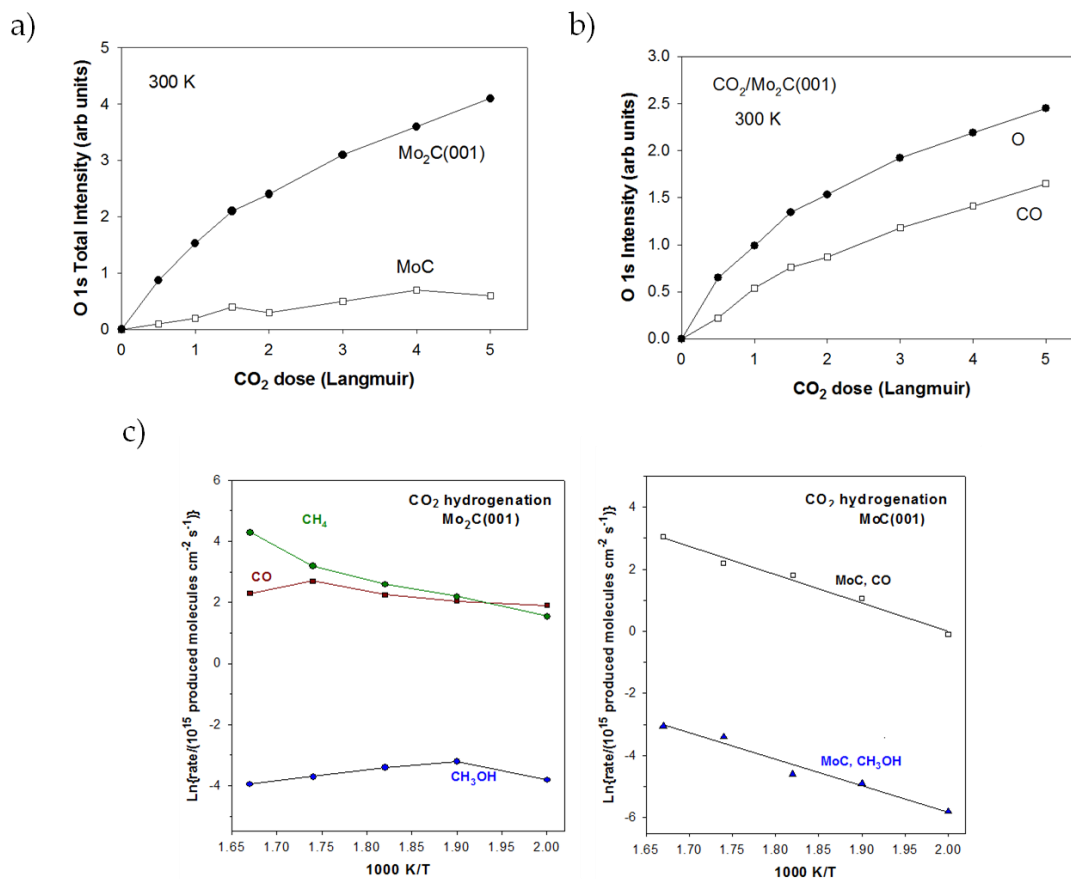


Figura S5: a) Variació del senyal O 1s total després de l'adsorció de CO₂ a MoC policristal·lí i una superfície β -Mo₂C (001). b) Intensitat d' O i CO després de diverses dosis de CO₂ adsorbits a la superfície β -Mo₂C (001) a 300 K. c) Gràfics d'Arrhenius per a la producció de CO, metà i metanol en β -Mo₂C (001) (esquerra) i MoC (001) (dreta).

Els càlculs DFT van corroborar els experiments. L'adsorció del CO₂ va ser estudiada sobre les dues terminacions en molibdè i carboni de la superfície β -Mo₂C (001), a les quals ens referirem com a β -Mo i β -C. Ambdues terminacions activen i dissocien el CO₂ sense la necessitat de ser assistit per hidrogen, en especial la terminació en molibdè, amb una barrera d'energia molt baixa, només 0.21 eV. Per altra banda, els càlculs van determinar que la superfície β -Mo és la responsable de la dissociació del CO format, amb una barrera d'energia de 0.86 eV, mentre que aquest no dissocia a la superfície β -C. Aquest fet aporta una justificació a la formació de CH₄ observada als experiments, ja que la dissociació completa del CO₂ genera la producció de carboni atòmic, que pot ser hidrogenat a metà. D'altra banda, els càlculs també justifiquen els resultats experimentals per a la superfície δ -MoC (001),

ja que la dissociació del CO_2 presenta una barrera molt alta (1.41 eV), tot i que s'activa degut a la transferència de càrrega de la superfície a la molècula. Aquests resultats suggereixen que el CO i el MeOH es produeixen a partir de la hidrogenació del CO_2 . La diferent selectivitat observada en ambdues superfícies també va ser corroborada pels càlculs DFT, ja que al contrari que la superfície ortoròmbica, la superfície δ -MoC (001) no és capaç de dissociar el CO i per tant la formació de carboni atòmic queda descartada, evitant la formació de CH_4 .

Pel que fa a l'adsorció i activació de l' hidrogen, ambdues terminacions de la superfície ortoròmbica dissocien l' hidrogen de manera espontània, amb una barrera inferior a 0.1 eV. Per altra banda, la superfície δ -MoC (001) també es capaç de dissociar l' hidrogen, tot i que la barrera d'energia és una mica superior (0.60 eV). Aquests resultats confirmen que el procés d'hidrogenació no és un pas limitant a la reacció d'hidrogenació del CO_2 .

Per altra banda, considerant els resultat experimentals obtinguts, es va considerar oportú realitzar un estudi sobre l'adsorció i activació del CH_4 sobre les superfícies estudiades. Pel que fa a la superfície β , el CH_4 no s'activa i s'adsorbeix amb una energia molt baixa. Aquesta interacció tan feble dona lloc a una ràpida desorció del CH_4 un cop es produeix, ja que aquest procés serà sempre favorable a qualsevol altre reacció lateral que es pugui produir. Aquesta interacció és lleugerament superior amb la superfície δ -MoC (001), tot i que no és una interacció prou forta per a promoure la superfície δ -MoC (001) per a l'activació del CH_4 .

Conclusions

Les conclusions generals d'aquest capítol són les següents:

- Les superfícies (001) cúbica i ortoròmbica del carbur de molibdè són capaces d'activar la molècula de CO_2 i promoure la seva conversió cap a CO, MeOH i CH_4 .

- Els experiments mostren una activitat similar d'ambdues superfícies, però una selectivitat diferent, ja que a la superfície β -Mo₂C (001) es produeix CO, CH₄ com a productes principals i el MeOH com a producte secundari, mentre que a la superfície δ -MoC (001), només CO i MeOH van ser detectats.
- L'efecte del ràtio metall/carboni esdevé clau en l'activitat del catalitzador i en el camí de reacció.

Pel que fa a la superfície β -Mo₂C (001):

- Ambdues terminacions en molibdè i carboni dissocien el CO₂ directament.
- La terminació en molibdè és responsable de la formació del CH₄, ja que també dissocia el CO, donant lloc a la formació de carboni atòmic, que pot hidrogenar a CH₄.

Respecte a la superfície δ -MoC (001):

- Els experiments i els càlculs computacionals mostren que aquesta superfície no és capaç de dissociar el CO₂ sense l'assistència d'hidrogen.
- No obstant, la superfície δ -MoC (001) activa el CO₂ promovent la seva hidrogenació.

Hidrogenació del CO₂ a les superfícies β -Mo₂C (001) i Cu/ β -Mo₂C (001) **(Capítol 5)**

Objectius

L'objectiu d'aquest capítol és estudiar el mecanisme de reacció de la hidrogenació de CO₂ a la superfície neta i amb coure suportat de la fase ortoròmbica, amb un ràtio metall/carboni de 2. Es vol determinar quin és el rol de les nanopartícules de coure i el seu efecte en l'activitat i la selectivitat de la reacció.

Resultats

La figura S6a mostra com la deposició del coure a la superfície β -Mo₂C (001) augmenta la producció de CO i metanol, mentre que la producció de CH₄ es redueix dràsticament. Els experiments també mostren que si la mida de la nanopartícula de coure augmenta, la quantitat de CH₄ produïda baixa (Figura S6b), és a dir, que el coure bloca els llocs de la superfície on es produeix el CH₄.

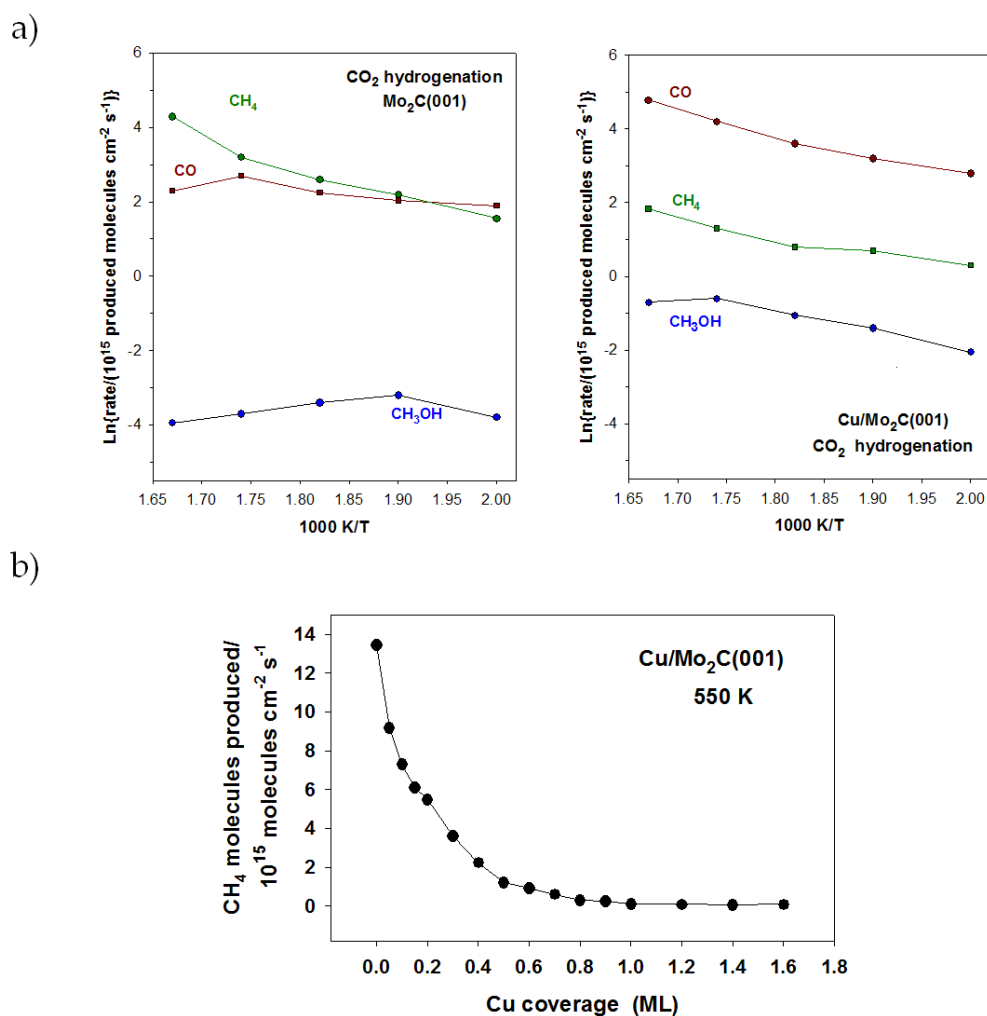


Figura S6: a) Gràfics d'Arrhenius per a la producció de CO, metà i metanol en la superfície β -Mo₂C (001), panell esquerre, i una superfície pre-coberta amb 0,4 ML de coure, panell dret. b) Taxa per a la producció de metà en superfícies Cu/Mo₂C (001) en funció del recobriment de coure.

Els càlculs DFT es van dur a terme sobre la superfície neta i sobre les nanopartícules suportades. A la superfície neta acabada en molibdè (Figura S7)

s'observa que la producció del CO és molt favorable degut a la dissociació directa del CO₂. Un cop es produeix el CO, aquest pot hidrogenar cap a MeOH o dissociar, generant carboni atòmic que posteriorment hidrogenarà a CH₄. Els càlculs confirmen els resultats experimentals, on la quantitat de CH₄ produïda és molt superior a la de MeOH. Això és degut a que la dissociació del CO és lleugerament més favorable que la hidrogenació, tot i que, aquesta diferència no justifica la gran diferència trobada als experiments entre el CH₄ i el MeOH. No obstant, els càlculs DFT mostren com la hidrogenació de MeOH es veu desfavorida als últims passos. Per una banda, l'últim pas per a formar MeOH, la hidrogenació de l'intermedi CH₃O*, presenta una barrera lleugerament superior a la seva dissociació, la qual genera l'intermedi CH₃*, que hidrogena cap a CH₄, corroborant així la diferència entre el CH₄ i el MeOH. Per altra banda, la forta interacció entre el MeOH i el catalitzador dificulta la seva desorció, afavorint la reacció inversa. D'altra banda, la terminació en carboni és molt poc activa, ja que només genera CO. No és capaç ni de dissociar-lo ni d'hidrogenar-lo.

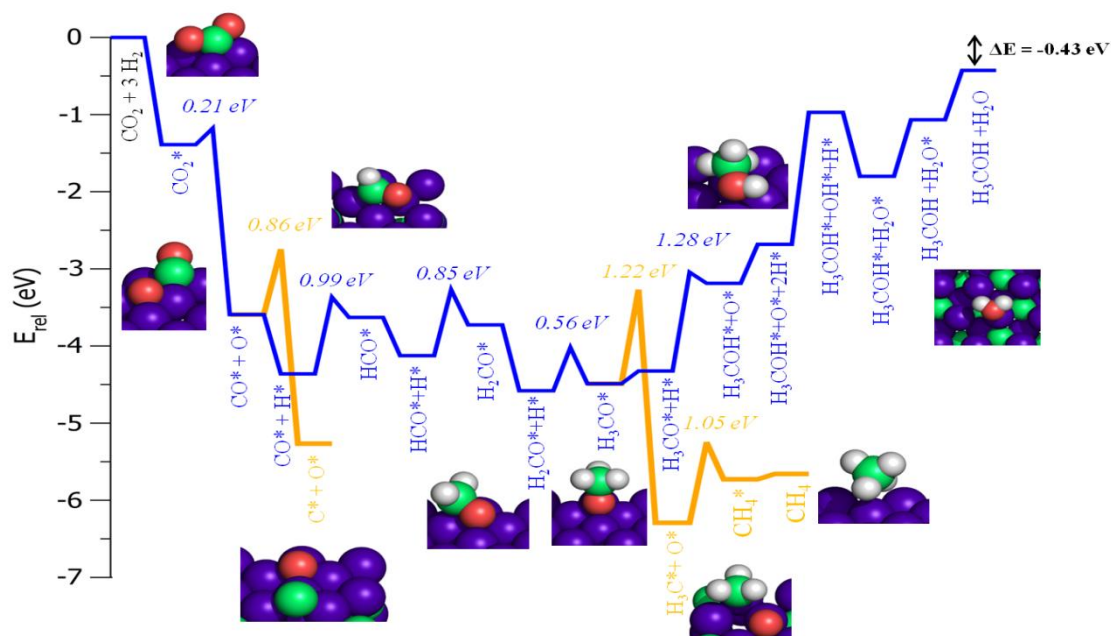


Figura S7: Perfil d'energia calculat per a la hidrogenació de CO₂ a la superfície neta β -Mo₂C (001)-Mo termination.

Per a modelitzar les nanopartícules suportades, es va fer un estudi amb diverses mides de partícula. Per raons de cost computacional i considerant els resultats inclosos a la figura S8, es va escollir un model de Cu₄ ja que mostrava les mateixes tendències, valor d'energia d'adsorció i barrera d'energia que models més grans. Com en el cas de la superfície neta, el coure suportat sobre la terminació en carboni no és actiu. En canvi, sobre la terminació en molibdè, el coure es mostra actiu. L'activació del CO₂ a les nanopartícules és molt menor que a la superfície neta (Figura S9), per tant, no catalitza la seva dissociació directa. Això també es va observar per al CO, cosa que corrobora els resultats experimentals. El coure bloca llocs de la superfície i evita la dissociació del CO, que implica un decreixement en la producció de CH₄. D'altra banda, el canvi de selectivitat entre el CH₄ i el MeOH és degut a la nanopartícula de coure, que és capaç d'hidrogenar el CO₂ cap a formar (HCOO*), un intermedi de reacció molt comú en la hidrogenació del CO₂, especialment si s'utilitza coure com a catalitzador. Aquest intermedi, després de diverses hidrogenacions i dissociacions, forma el MeOH a la interfase entre la superfície i la nanopartícula (HCOO* → H₂COO* → H₂CO* → H₃CO* → CH₃OH*). A més, el coure també evita la dissociació de l'intermedi H₃CO* a CH₃*, com s'observa a la superfície neta.

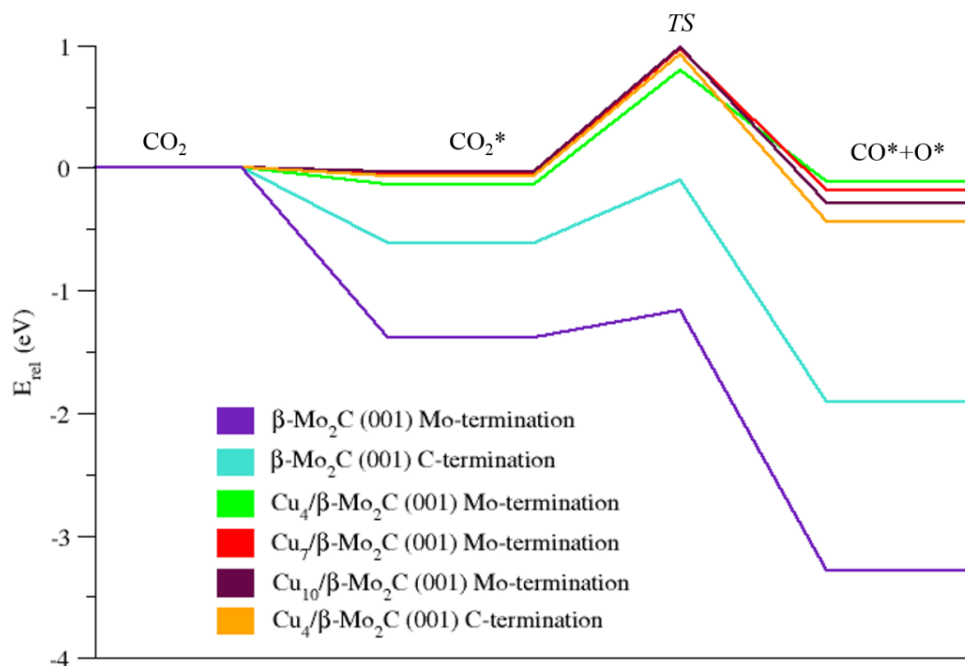


Figura S8: Perfil d'energia per a la dissociació de CO_2 a les superfícies netes de $\beta-Mo_2C$ (001) i en diferents models de superfícies $Cu_n/\beta-Mo_2C$ (001) ($n = 4, 7, 10$).

En general, es pot dir que el coure suportat a la superfície (001) de la fase ortoròmbica, especialment la terminació en molibdè, és un catalitzador actiu per a la hidrogenació del CO_2 . No obstant, no és tracta d'un catalitzador selectiu i per altra banda, la gran activitat cap a la dissociació completa del CO_2 dona lloc a la disposició d'oxigen atòmic a la superfície del carbur, formant el que s'anomena oxicarburi, que fa disminuir l'activitat del catalitzador.

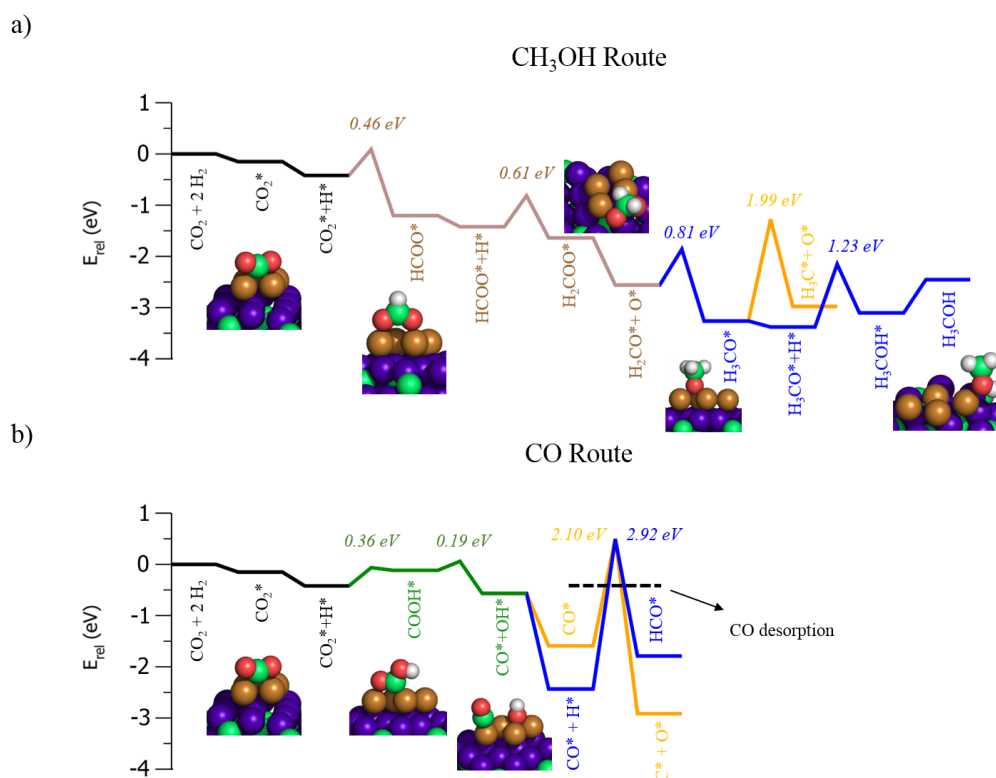


Figura S9: a) Perfil d'energia per a la formació de metanol en la superfície Cu₄/β-Mo. b) Perfil d'energia per a la formació de CO en la superfície Cu₄/β-Mo.

Conclusions

Les conclusions d'aquest capítol són les següents:

- Els càlculs DFT mostren com el CO es forma a partir de la dissociació directa del CO₂, mentre que el CH₄ i el MeOH es formen a partir de la hidrogenació del carboni atòmic i el CO respectivament.
- Els càlculs justifiquen la selectivitat trobada en els experiments.
- La deposició de petites nanopartícules de coure fan decreixer la quantitat de CH₄ produïda, degut a que bloca els llocs de la superfície per a la dissociació del CO.
- El coure canvia el mecanisme de la reacció, on el CO₂ s'hidrogena cap a HCOO*, i d'aquí, es forma el MeOH.

- La superfície β -Mo₂C (001) és un catalitzador actiu per a la hidrogenació del CO₂, però és poc selectiu i es desactiva amb el temps degut a la deposició d'oxigen atòmic.

Hidrogenació del CO₂ a les superfícies δ -MoC (001) i Cu/ δ -MoC (001) (Capítol 6)

Objectiu

Els objectius d'aquest capítol són l'estudi del mecanisme de reacció de la hidrogenació del CO₂ a la superfície δ -MoC (001) i Cu/ δ -MoC (001). Amb això es pretén determinar si l'efecte del ràtio metall/carboni juga un paper clau en el rendiment del catalitzador.

Resultats

Els experiments mostren una millor selectivitat del catalitzador δ -MoC (001) respecte a la superfície β -Mo₂C (001), ja que només el CO i el MeOH es detecten com a productes. La deposició de coure sobre δ -MoC (001) incrementa la producció de CO i MeOH, com s'observa a la figura S10. A més, aquest catalitzador presenta una activitat superior al model de catalitzador comercial Cu/ZnO(000 $\bar{1}$).⁶¹

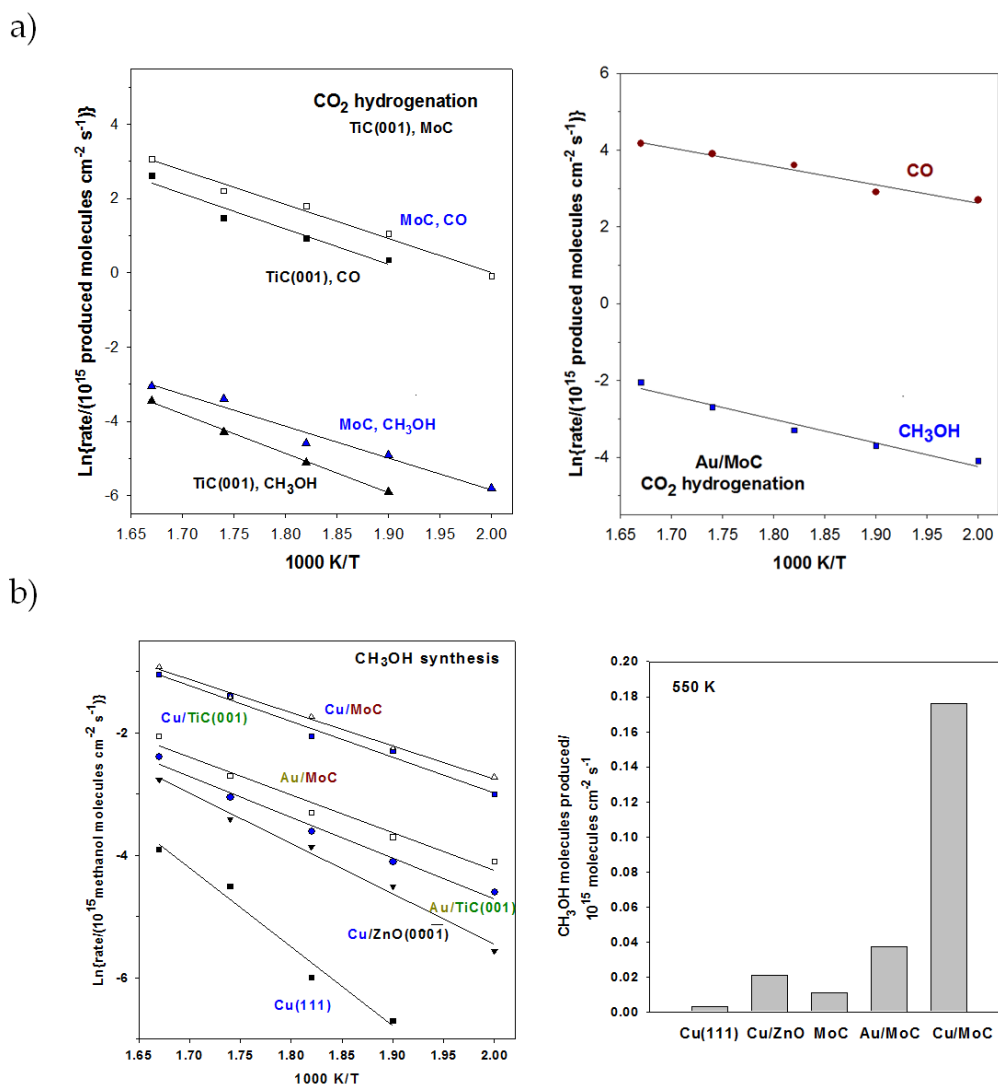


Figura S10: a) Perfil d'energia per a la formació de metanol en la superfície Cu₄/β-Mo. b) Perfil d'energia per a la formació de CO en la superfície Cu₄/β-Mo.

Els càlculs DFT a la superfície neta mostren com el CO₂ necessita ser hidrogenat a l'intermedi carboxil (COOH*) per a iniciar la reacció. Posteriorment, el COOH* dissocia a CO, el producte principal de la reacció. El MeOH es forma a partir de la hidrogenació de la fracció de CO que no desorbeix. Aquesta superfície mostra unes barreres d'energia lleugerament superiors a les obtingudes amb la superfície β-Mo₂C (001), però mostra una millor selectivitat i una estabilitat major. El fet que la dissociació del CO no es produeixi, evita la deposició d'oxigen atòmic a la superfície, és a dir, no es forma l'òxicarbur. Per tant, la superfície δ-MoC (001) no es desactiva

amb el pas del temps, el que fa que la producció de CO i MeOH sigui similar a l'obtinguda amb el catalitzador β -Mo₂C (001).

La deposició de petites partícules de coure, provoca un canvi de mecanisme de reacció (Figura S11). Al contrari que a la superfície amb un ràtio metall/carboni de 2, el coure suportat a la superfície δ -MoC (001) és capaç d'activar el CO₂, donant lloc a la dissociació directa cap a CO. Aquest pas redueix la barrera d'energia per produir CO, fet que augmenta la seva producció i també la de MeOH, sent superior al model de catalitzador comercial.

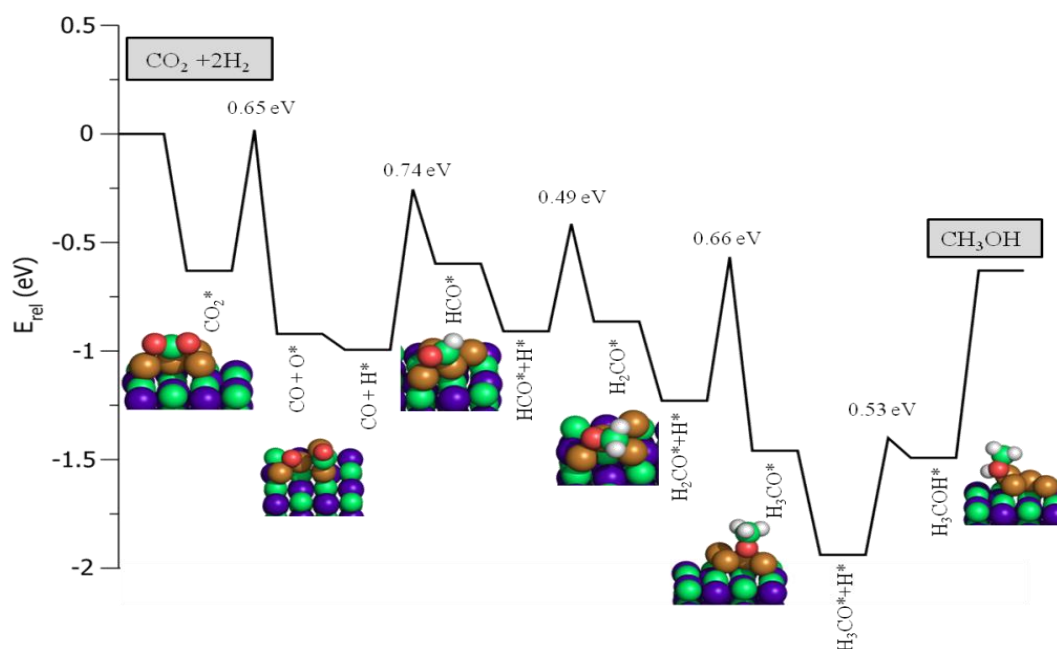


Figura S11: Perfil d'energia per als passos elementals que intervenen en la hidrogenació de CO₂ en el model Cu₄/ δ -MoC (001). Esbossos representen l'adsorció de CO₂ (I), CO + O (II), HCO (III), H₂CO (IV), H₃CO (V) i CH₃OH (VI).

Aquest estudi mostra la importància del ràtio metall/carboni, ja que no només modifica el mecanisme de reacció, sinó que també modifica el rol de les partícules metàl·liques depositades.

Conclusions

Les conclusions d'aquest capítol són les següents:

- La hidrogenació del CO₂ a la superfície δ -MoC (001) segueix un mecanisme assertiu, que implica la formació de l'intermedi COOH*. El CO es forma a partir de la ràpida dissociació de l'intermedi i el MeOH a partir de la hidrogenació del CO.
- La deposició de petites partícules de coure incrementa dràsticament la producció de CO i MeOH.
- El rol del coure és canviar el mecanisme de reacció, dissociant el CO₂ directament amb una barrera d'energia més baixa que a la superfície neta.
- El ràtio metall/carboni del carbur juga un rol clau en la reactivitat del catalitzador.
- La superfície δ -MoC (001) neta i amb coure suportat és un catalitzador molt prometedor per a la hidrogenació de CO₂. El catalitzador de coure suportat en carbur de molibdè amb ràtio metall/carboni d'1 presenta avantatges respecte al carbur amb ràtio de 2, en termes d'activitat (la producció de CO i MeOH és superior), selectivitat (només produeix CO i el MeOH) i estabilitat (la superfície Cu/ δ -MoC (001) no es desactiva, mentre que la superfície de Cu/ β -Mo₂C (001) es forma l'oxicarbur, que desactiva el catalitzador).

Reacció de *water gas shift* sobre les superfícies δ -MoC (001) i Au/ δ -MoC (001) (Capítol 7)

Objectiu

L'objectiu d'aquest capítol és aplicar tota la recerca i els coneixements adquirits per a la hidrogenació del CO₂, per tal d'investigar la idoneïtat dels carburs de molibdè per catalitzar la reacció de *water gas shift*.

Resultats

Els resultats experimentals resumits a la figura S14 mostren que la superfície neta β -Mo₂C (001) és més activa que la superfície δ -MoC (001). No obstant, com va ser observat per a la reacció d'hidrogenació del CO₂, la superfície β -Mo₂C (001) és menys selectiva, ja que a part dels productes comuns de la reacció de WGS (CO₂ i H₂), també es va detectar la formació de CH₄.

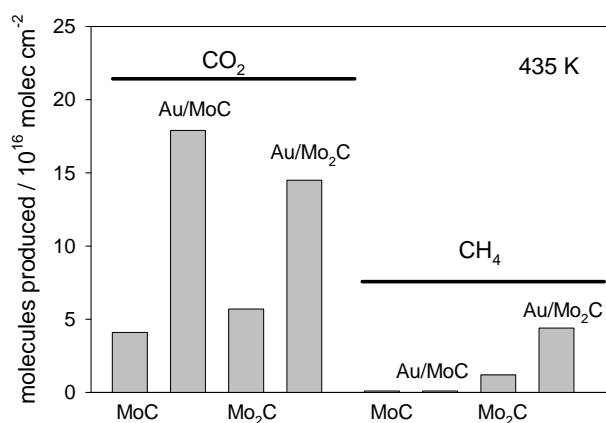


Figura S12: Producció de CO₂ i CH₄ després d'exposar una sèrie de catalitzadors de carbur de molibdè a una barreja de CO (20 Torr), H₂O (10 Torr) i H₂ (100 Torr) a 435 K durant 5 minuts.

D'altra banda, la deposició de petits clústers d'or incrementen la producció de CO_2 i H_2 , causat principalment a un augment de la concentració del radical OH^* (Figura S13), que els experimentals van associar a una dissociació de l'aigua més favorable degut a la presència dels clústers d'or. En aquest cas, el catalitzador Au/ δ -MoC (001) esdevé com el més actiu i selectiu, ja que d'una banda, presenta el major índex de producció de CO_2 i H_2 , i per altra banda, és el catalitzador més selectiu, ja que només és detecten aquests dos productes.

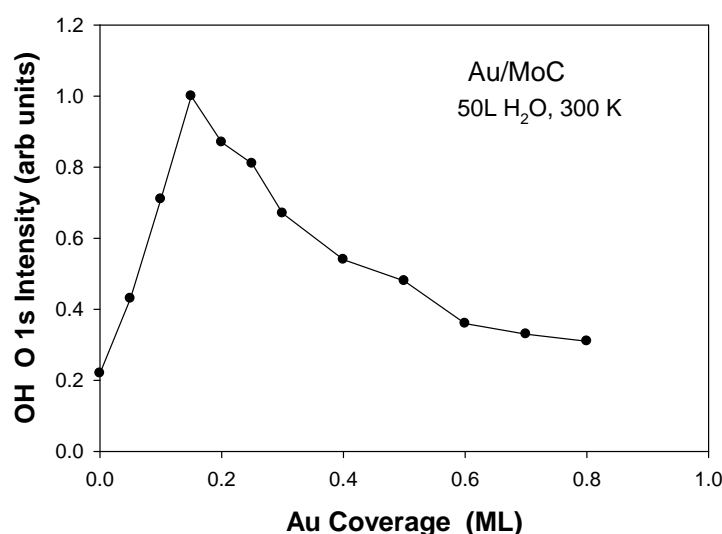


Figura S13: Experiments XPS sobre l'oxigen de l'OH, després de 50 L d'aigua a 300 K a superfícies δ -MoC i Au/ δ -MoC.

A més a més, com s'observa la figura S14, l'estabilitat és un altre punt a favor d'aquest catalitzador. Mentre que el catalitzador Au/ β -Mo₂C (001) disminueix la seva producció amb el temps degut a la formació de l'oxicarbur, aquest fet no afecta al catalitzador d'or suportat sobre δ -MoC (001), ja que tot i detectar la deposició d'oxigen en aquesta superfície, l'oxicarbur no es forma i com a conseqüència, el catalitzador no es desactiva. Per tant, els experiments proposen el catalitzador Au/ δ -MoC (001) com un excel·lent catalitzador en termes d'activitat, selectivitat i estabilitat. Considerant els resultats experimentals presentats en aquest apartat i els

resultats obtinguts al bloc 2 respecte la hidrogenació del CO₂, es va decidir modelitzar només el sistema Au/ δ -MoC (001).

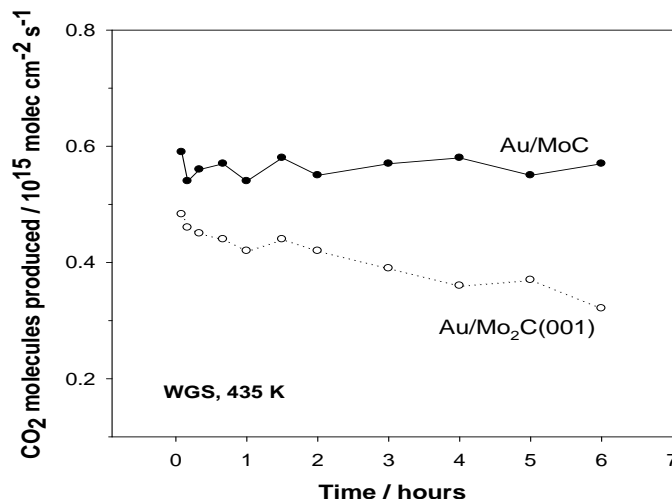


Figura S14: Activitat de la reacció de water gas shift de les superfícies Au/ δ -MoC i Au/ β -Mo₂C (001) en funció del temps. Es va dipositar una recobriments de 0.15 ML d'or sobre les superfícies de carbur i els catalitzadors generats es van exposar a 20 Torr de CO i a 10 Torr de H₂O a 435 K.

Com en el cas del coure suportat, un model de clúster d'or amb quatre àtoms va ser l'escollit per a la modelitzar el catalitzador experimental. Aquest, va mostrar resultats similars que clústers d'or més grans.

Els càlculs DFT per a la superfície neta van determinar que el camí de reacció més favorable implicava la dissociació de l'aigua ($\text{H}_2\text{O}^* \rightarrow \text{H}^* + \text{OH}^*$) i la formació de l'intermedi carboxil (COOH^*) a partir del CO^* i el radical OH^* (Figura S15). Posteriorment, el carboxil dissocia a CO₂, mentre que l'hidrogen molecular es forma a partir dels àtoms d'hidrogen que provenen de la dissociació de l'aigua i del carboxil. No obstant, es va trobar que les barreres inverses eren més favorables que les barreres directes, cosa que provoca un col·lapse a la superfície, que explica la producció tan baixa de CO₂ i H₂ trobada als experiments. A més, els càlculs DFT suggereixen que la presència d'oxigen atòmic detectada als experiments no és degut a la superfície neta sinó que ha de ser generat degut a la deposició del clúster d'or.

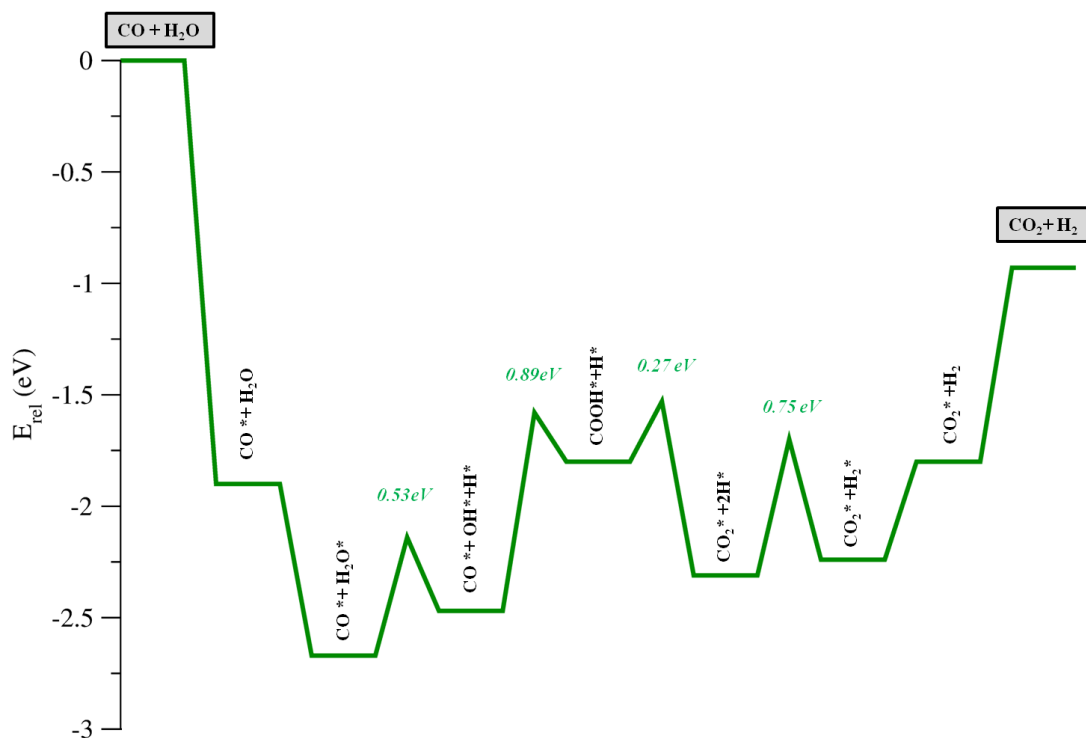
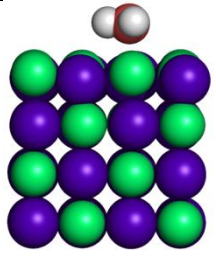
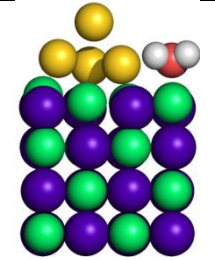
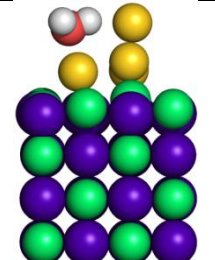
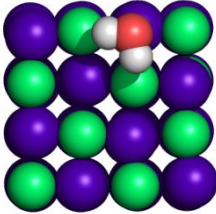
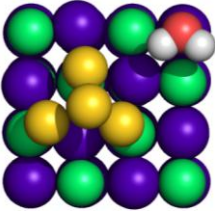
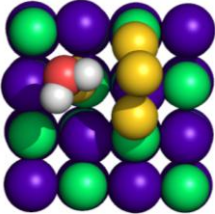


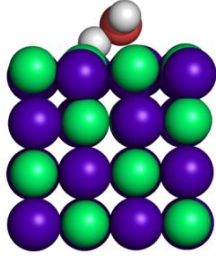
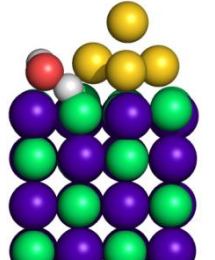
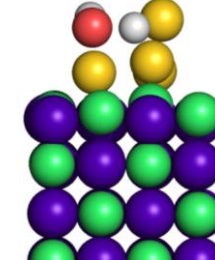
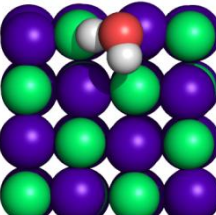
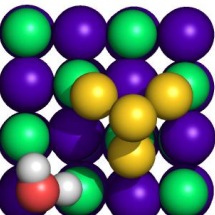
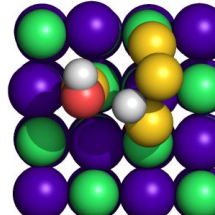
Figura S15: Perfil d'energia de la reacció de WGS en δ -MoC (001) inclouent correcció ZPE.

Els càlculs sobre el model $\text{Au}_4/\delta\text{-MoC}$ (001), van descartar la hipòtesi experimental que indicava que les petites nanopartícules afavorien la dissociació de l'aigua. La taula S1 mostra com l'aigua s'adsorbeix més favorablement al carbur, mentre que la taula S2 mostra com la barrera d'energia de la dissociació és més favorable al carbur que a la interfase o al clúster d'or.

Taula S1: Esbossos, energies relatives, energia d'adsorció i longitud d'enllaç O-H a la superfície Au₄/δ-MoC (001).

	δ-MoC (001)	Interfase Au ₄ /δ-MoC (001)	Top Au ₄ /δ-MoC (001)
Perfil			
Alçat			
E _{rel} (eV)	-	0.00	0.10
E _{ads} (eV)	-0.77	-0.34	-0.24
d(O-H) (Å)	0.98	0.98/1.01	0.98

Taula S2: Esbossos, barrera d'energia i longitud d'enllaç O-H de les estructures de l'estat de transició de la dissociació d'H₂O a la superfície Au₄/δ-MoC (001).

	δ-MoC (001)	Interfase Au ₄ /δ-MoC (001)	Top Au ₄ /δ-MoC (001)
Perfil			
Alçat			
E _{barrier} (eV)	0.53	0.79	1.23
d(O-H) (Å)	0.98/1.37	0.98/1.38	0.98/1.94

Es van estudiar els diferents mecanismes de reacció fins a trobar el rol dels clústers d'or. Com s'observa a la figura XX, els clúster d'or canvien el mecanisme de

reacció del assertiu al redox. Els clústers d'or afavoreixen la recombinació de dos radicals OH^* per a produir una nova molècula d'aigua i oxigen atòmic, justificant així les observacions experimentals. A més, la formació de l'oxicarburi no s'observa ja que l'oxigen atòmic oxida el CO amb una barrera de 0.1 eV.

Conclusions

Les conclusions d'aquest capítol són les següents:

- L'efecte del ràtio metall/carboni torna a ser decisiu en termes d'activitat, selectivitat i estabilitat per demostrar que el sistema Au/ δ -MoC (001) com a un catalitzador més idoni que l'Au/ β -Mo₂C (001).
- Les reaccions inverses a la superfície neta són més favorables que les barreres directes. Aquest fet dificulta la formació dels productes i justifica la baixa producció observada pels experiments.
- La deposició de petits clústers d'or no ajuda a la dissociació de l'aigua, com suggerien els experiments, sinó que canvien el mecanisme de reacció, disminuint l'efecte de les barreres inverses i afavorint la desorció dels productes.

Referencies

- [1] J. Berzelius, *Annales chimie physiques*, **1836**, 61, 146.
- [2] W. Ostwald, Nobel Lecture: On Catalysis, **1909**.
- [3] X. Lim, *Nature*, **2015**, 526, 628.
- [4] Intergovernmental Panel on Climate Change, *Climate Change 2013 – The Physical Science Basis.*, Cambridge University Press, 1st edn., **2014**.
- [5] Y. F. Zhang, F. Viñes, Y. J. Xu, Y. Li, J. Q. Li and F. Illas, *J. Phys. Chem. B*, **2006**, 110, 15454.
- [6] S. Wang, G. Q. Lu and G. J. Millar, *Energ. Fuels*, **1996**, 10, 896.
- [7] A. Caballero and P. J. Perez, *Chem. Soc. Rev.*, **2013**, 42, 8809.
- [8] X. M. Liu, G. Q. Lu, Z. F. Yan and J. Beltramini, *Ind. Eng. Chem. Res.*, **2003**, 42, 6518.
- [9] G. A. Olah, A. Goepfert and G. K. S. Prakash, *Beyond Oil and Gas: The Methanol Economy*, Wiley- VCH Verlag GmbH & Co. KGaA: Weinheim, **2006**.
- [10] Green Carbon Dioxide: Advances in CO₂ Utilization, ed. G. Centi and S. Perathoner, John Wiley & Sons, Hoboken, NJ, **2014**.
- [11] R.D. Cortright, R.R. Davda and J.A. Dumesic, *Nature*, **2002**, 418, 964.
- [12] M. Halmann and A. Steinfeld, *Energy*, **2006**, 31, 3171.
- [13] D. B. Levin, L. Pitt, and M. Love, *Int. J. Hydrogen Energy*, **2004**, 29, 173.
- [14] A. N. Fatsikostas and X. E. Verykios, *J. Catal.*, **2004**, 225, 439
- [15] J. Llorca, P. R. de la Piscina, J. Sales and N. Homs, *Chem. Commun.*, **2001**, 0, 641
- [16] C. V. Ovesen, B. S. Clausen, J. Schiøtz, P. Stolze, H. Topsøe and J. K. Nørskov, *J. Catal.* **1997**, 168, 133.
- [17] N. Akiya and P. E. Savage, *Chem. Rev.*, **2002**, 102, 2725.
- [18] J. Nakamura, J. M. Campbell and C. T. Campbell, *J. Chem. Soc. Faraday Trans.*, **1990**, 86, 2725.
- [19] J. A. Rodriguez, P. Liu, J. Hrbek, J. Evans and M. Perez, *Angew. Chem. Int. Ed.*, **2007**, 46, 1329.
- [20] P. Liu and J. A. Rodriguez, *J. Chem. Phys.*, **2007**, 126, 164705.
- [21] A. A. Gokhale, J. A. Dumesic and M. Mavrikakis, *J. Am. Chem. Soc.*, **2008**, 130, 1402.
- [22] R. M. Navarro, M. A. Peña and J. L. G. Fierro, *Chem. Rev.*, **2007**, 107, 3952.
- [23] L. C. Grabow, A. A. Gokhale, S. T. Evans, J. A. Dumesic and M. Mavrikakis, *J. Phys. Chem. C*, **2008**, 112, 4608.
- [24] J. A. Rodriguez, P. J. Ramírez, G. G. Asara, F. Viñes, J. Evans, P. Liu, J. M. Ricart and F. Illas, *Angew. Chem. Int. Ed.*, **2014**, 53, 11270.
- [25] C. H. Lin, C. L. Chen and J. H. Wang, *J. Phys. Chem. C*, **2011**, 115, 18582.
- [26] C. Ratnasamy and J. P. Wagner, *Catal. Rev.*, **2009**, 51, 325.
- [27] Q. Fu, W. Deng, H. Saltsburg, M. Flytzani-Stephanopoulos, *Appl. Catal. B*, **2005**, 56, 57.
- [28] G. Jacobs, E. Chenu, P.M. Patterson, L. Williams, D. Sparks, G. Thomas and B.H. Davis, *Appl. Catal. A*, **2004**, 258, 203.
- [29] D. Andreeva, V. Idakiev, T. Tabakova, L. Ilieva, P. Falaras, A. Bourlinos, A. Travlos, *Catal. Today*, **2002**, 72, 51.
- [30] P. Ball, *Nature*, **2006**, 442, 500.
- [31] J. K. Nørskov, T. Bligaard, J. Rossmeisl and C. H. Christensen, *Nature Chem.*, **2009**, 1, 37.
- [32] M. Fernández-García and J. A. Anderson, *Supported Metals in Catalysis*, Catalytic Sciences Series, Vol. 5, Imperial College Press, London, **2005**; A. Wieckowski, E. Savinova, and C. G.

- Vayenas, *Catalysis and Electrocatalysis at Nanoparticle Surfaces*, Marcel Dekker, New York, **2003**.
- [33] L. E. Toth, *Transition Metal Carbides and Nitrides*; Academic Press: New York, **1971**.
- [34] S. T. Oyama, *Catal. Today*, **1992**, *15*, 179.
- [35] S. T. Oyama, *The Chemistry of Transition Metal Carbides and Nitrides*; Blackie Academic and Professional: Glasgow, **1996**.
- [36] J. Chipman, *Metallurgical Transactions*, **1975**, *3*, 1972.
- [37] H. H. Hwu and J. G. Chen, *Chem. Rev.*, **2005**, *105*, 185.
- [38] H. C. Woo, K. Y. Park, Y. G. Kim, I. S. Nam, J. S. Chung and J. S. Lee, *Appl. Catal.*, **1991**, *75*, 267
- [39] B. Dhandapani, T. St Clair and S. T. Oyama, *Appl. Catal. A*, **1998**, *168*, 219.
- [40] J. R. Kitchin, J. K. Nørskov, M. A. Barteau and J. G. Chen, *Catal. Today* **2005**, *105*, 66
- [41] D. Ham and J. Lee, *Energies*, **2009**, *2*, 873.
- [42] E. C. Weigert, M. B. Zellner, A. L. Stottlemeyer and J. G. Chen, *Top. Catal.*, **2007**, *46*, 349.
- [43] A. Serov and C. Kwak, *Appl. Catal., B*, **2009**, *90*, 313.
- [44] J. A. Rodriguez, P. Liu, F. Viñes, F. Illas, Y. Takahashi, K. Nakamura, *Angew. Chem., Int. Ed.*, **2008**, *47*, 6685.
- [45] J. A. Rodriguez, P. Liu, Y. Takahashi, K. Nakamura, F. Viñes, F. Illas, *J. Am. Chem. Soc.*, **2009**, *131*, 8595.
- [46] J. A. Rodriguez, P. Liu, Y. Takahashi, K. Nakamura, F. Viñes, F. Illas, *Top. Catal.*, **2010**, *53*, 393.
- [47] J. A. Rodriguez, F. Viñes, F. Illas, P. Liu, Y. Takahashi and K. Nakamura, *J. Chem. Phys.*, **2007**, *127*, 211102.
- [48] L. K. Ono and B. Roldán-Cuenya, *Catal. Lett.*, **2007**, *113*, 8.
- [49] J. A. Rodriguez, P. Liu, F. Viñes, F. Illas, Y. Takahashi and K. Nakamura, *Angew. Chem., Int. Ed.*, **2008**, *47*, 6685.
- [50] J. A. Rodriguez, P. Liu, Y. Takahashi, K. Nakamura, F. Viñes and F. Illas, *J. Am. Chem. Soc.*, **2009**, *131*, 8595.
- [51] L. Feria, J. A. Rodriguez, T. Jirsak and F. Illas, *J. Catal.*, **2011**, *279*, 352.
- [52] J. A. Rodriguez, P. Liu, Y. Takahashi, K. Nakamura, F. Viñes and F. Illas, *Top. Catal.*, **2010**, *53*, 393.
- [53] J. A. Rodriguez, P. Liu, Y. Takahashi, F. Viñes, L. Feria, E. Florez, K. Nakamura and F. Illas, *Catal. Today*, **2011**, *166*, 2.
- [54] J. A. Rodriguez, L. Feria, T. Jirsak, Y. Takahashi, K. Nakamura and F. Illas, *J. Am. Chem. Soc.*, **2010**, *132*, 3177.
- [55] E. Florez, T. Gomez, P. Liu, J. A. Rodriguez and F. Illas, *ChemCatChem*, **2010**, *2*, 1219
- [56] P. C. Hohenberg and W. Kohn, *Phys. Rev.*, **1964**, *136*, 864.
- [57] F. Viñes, *PhD Thesis*, 2008.
- [58] P. Janthon, S. M. Kozlov, F. Viñes, J. Limtrakul, F. Illas, *J. Chem. Theo. Comput.*, **2013**, *9*, 1631.
- [59] J. R. d. S. Politi, F. Viñes, J. A. Rodriguez, F. Illas, *Phys. Chem. Chem. Phys.*, **2013**, *15*, 12617.
- [60] G. G. Asara, F. Viñes, J. M. Ricart, J. A. Rodriguez, and F. Illas, *Surf. Sci.* **624**, 32 (2014).
- [61] Y. Yang, J. Evans, J. A. Rodriguez, M. G. White, P. Liu, *Phys. Chem. Chem. Phys.* **2010**, *12*, 9909.

LIST OF PUBLICATIONS

List of publications

"The bending machine: CO₂ activation and hydrogenation on δ -MoC (001) and β -Mo₂C(001) surfaces", **S. Posada-Pérez**, F. Viñes, P. J. Ramirez, A. B. Vidal, J. A. Rodriguez and F. Illas, *Physical Chemistry Chemical Physics*, **2014**, *16*, 14912-14921.

"Fundamentals of methanol synthesis on metal carbide based catalysts: Activation of CO₂ and H₂", **S. Posada-Pérez**, F. Viñes, J. A. Rodriguez and F. Illas, *Topics in Catalysis*, **2015**, *58*, 159-173.

"Methane capture at room temperature: adsorption on cubic δ -MoC and orthorhombic β -Mo₂C molybdenum carbide (001) surfaces" **S. Posada-Pérez**, J. R. d. S. Politi and F. Illas, *RSC Advances*, **2015**, *5*, 33737-33746.

"Structure and electronic properties of Cu nanoclusters supported on Mo₂C (001) and MoC (001) surfaces" **S. Posada-Pérez**, F. Viñes, J. A. Rodriguez and F. Illas, *Journal Chemical Physics*, **2015**, *143*, 1114704.

List of publications

"The conversion of CO₂ to methanol on orthorhombic β -Mo₂C and Cu/ β -Mo₂C catalysts: mechanism for admetal induced change in the selectivity and activity", **S. Posada-Pérez**, P. J. Ramirez, R. A. Gutierrez, D. J. Stacchiola, F. Viñes, P. Liu, F. Illas and J. A. Rodriguez, *Catalysis Science & Technology*, **2016**, 6, 6676-6777.

"Highly active Au/ δ -MoC and Cu/ δ -MoC catalysts for the conversion of CO₂: The metal/C ratio as a key factor defining activity, selectivity, and stability", **S. Posada-Pérez**, P. J. Ramirez, J. Evans, F. Viñes, P. Liu, F. Illas and J. A. Rodriguez, *Journal of the American Chemical Society*, **2016**, 138, 8269-8278.

"Adsorption and dissociation of molecular hydrogen on orthorhombic β -Mo₂C and cubic δ -MoC (001) surfaces", **S. Posada-Pérez**, F. Viñes, R. Valero, J. A. Rodriguez and F. Illas, *Surface Science*, **2017**, 656, 24-32.

"Highly active Au/ δ -MoC and Au/ β -Mo₂C catalysts for the low-temperature water gas shift reaction: effects of the carbide metal/carbon ratio on the catalysts performance", **S. Posada-Pérez**, R. A. Gutierrez, Z. Zuo, P. J. Ramirez, F. Viñes, P. Liu, F. Illas and J. A. Rodriguez, *Catalysis Science & Technology*, **2017**, 7, 5332-5342.

